Reactivity Studies of Electron Poor Titanium Amides

Tara N. Williams

Submitted for the degree of Doctor of Philosophy
University of Sussex
October 2010

Declaration

I hereby declare that this thesis has not been and will not be submitted in whole or in part to another University for the award of any other degree.

Signature:

Tara N. Williams

UNIVERSITY OF SUSSEX

TARA N. WILLIAMS, DOCTOR OF PHILOSOPHY

REACTIVITY STUDIES OF ELECTRON POOR TITANIUM AMIDES

SUMMARY

Abstract

Chapter One presents an overview of olefin polymerisation, which provides the context for the majority of the work described in later chapters. Both Ziegler-Natta and late transition metal systems are described.

Chapter Two describes the synthesis and reactivity of *tris*amido titanium complexes with the diarylamido fragments derived from diphenylamine and di-*p*-tolylamine. These complexes have been thoroughly studied using NMR spectroscopy. This chapter also presents the syntheses of two rare examples of *tris*amido methyl complexes. In addition, an improved synthetic route to the cocatalyst, $KB(C_6F_5)_4$ and the structures of $[B(C_6F_5)_3{\cdot}C_4H_8O]$ and $[Mg(C_6F_5)_2(Et_2O)(dioxane)]$ are described.

Chapter Three describes the polymerisation activity of the catalysts derived from $(R_2N)_3TiCl$, $(R_2N)_3TiMe$, and $[(R_2N)_3Ti]^+$ with the cocatalysts MAO, $B(C_6F_5)_3$, and $KB(C_6F_5)_4$. Data was recorded for each of the catalysts, and the consumption of propene over time was plotted. Rate constants were found for each of the polymerisation reactions. The mechanism for the polymerisation of each of these was also examined.

Chapter Four presents the synthesis and reactivities of new *tris*amido complexes using 10,11-dihydro-dibenz(*b*,*f*)azepinyl, hereafter abbrievated as dda, as the amide fragment. Specifically, syntheses of $(dda)_3TiCl$, $(dda)_3TiMe$ and $(dda)_3TiBH_4$ are described and their characterisation by NMR spectroscopy and X-ray crystallography is presented. The use of these complexes in synthetic approaches to $(dda)_3TiH$ are described. Initial steps in the characterisation of hydride transfer to CO_2 from $(dda)_3TiH$ are also presented.

Chapter Five presents details for the experimental work and Appendices are included, containing selected experimental data.

Acknowledgements

First and foremost I would like to thank my supervisor Dr. John Turner without whom I would have never had this amazing experience of living and working in England. Thank you for always believing in my abilities, even when I didn't believe in them myself. Thank you for all the late night chats about chemistry and life and most of all for being an amazing friend. I will never forget what you have done for me, both for my career and my life, and I hope that our friendship continues to grow for many years to come.

I would also like to thank my mother, Judy. Thank you mom for always believing in me and encouraging me to do whatever I felt was right, including the decision to move to England. You have and always will be my best friend and the best mother anyone could ask for. I would also like to thank my father Gary. Thank you dad for always pushing me to do my best in everything, even if that means not finishing first, or being the best. I would also like to thank my brother Ryan for always setting the bar high, and pushing me to excel in everything I do. Your work ethic has always been something for me to strive for, and I hope to reach that goal in the future.

I would also like to thank Kelly Salih. Thank you for being such a good friend the last three years, and putting up with me while I've been crazily writing my thesis. Our friendship has made moving across the world worthwhile. Thank you for all the dancing and singing moments, the laughter, the dinners, and most of all the conversation.

I would also like to thank my tea-time buddies-Lewis, Noel, James, Paul, Lee, and Rich. Our morning conversations have been something I have always looked forward to and will be one of the things I miss the most. A special thanks to Lewis-you have been an amazing friend, and our talks about anything and everything will stay with me forever. You will be the person I miss the most while I'm in America.

Contents

0.1 Abbreviations

Ar	aromatic ring
$BArF_3$	*tris*(pentafluorophenyl)borane
$BArF_4^+$	*tetrakis*(pentafluorophenyl)borate
dpa	diphenylamine
dpta	di-*p*-tolylamine
dda	10,11-dihydro-5*H*-[*b*,*f*]-azepine
Me	methyl
THF	tetrahydrofuran
Et_2O	diethyl ether
Cp	cyclopentadienyl
Cp'	methylcyclopentadienyl
TMS	tetramethylsilane
TBS	$tert$-butyldimethylsilyl
TIPS	triisopropylsilyl

Chapter 1

Introduction

This thesis describes synthetic explorations of *tris*amido complexes of titanium with a focus on small molecule activation. Specifically, olefin polymerisation catalysis and reactions related to fundamental steps in CO_2 functionalisation are explored with details being given in later chapters. This chapter presents the context of this work.

1.1 Applications of metal-amido chemistry

1.1.1 Olefin polymerisation

Polymerisation catalysis is one of the most important topics in chemistry today. Both academia and industry have intensively studied single-site metallocene catalysts used in olefin polymerisation. As both precursor and cocatalyst technology have advanced over the years, it is now possible to specifically design the properties of the polymer produced, including the microstructure.[1] The progress made in polymerisation precursors and cocatalysts are outlined in the sections below.

The first catalysts used in polymerisation were aluminium alkyls, including trialkylaluminiums and alkylaluminium chlorides, used in homogenous Ziegler-Natta catalysis.[2,3] These cocatalysts were used in the polymerisation of olefins with vanadium[4,5] to produce syndiospecific polypropene at low temperatures. The three types of polymer stereochemistries are shown below in Figure 1.1. Isotatic polymer has identical stereochemistry at each carbon atom. Syndiotactic polymer has alternating stereochemistry at each carbon atom, while atactic polymer has no stereoregulation. Chromium[6] and nickel[7] precursors were also used with aluminium alkyl cocatalysts for diene polymerisation and ethene oligomerization.

The first Cp system used for ethene polymerisation, Cp_2TiCl_2, was activated with diethylaluminium chloride Et_2AlCl.[8,9] The role of Et_2AlCl in polymerisation was studied extensively to investigate the generation of the active species.[10–18] These studies identified ligand exchange

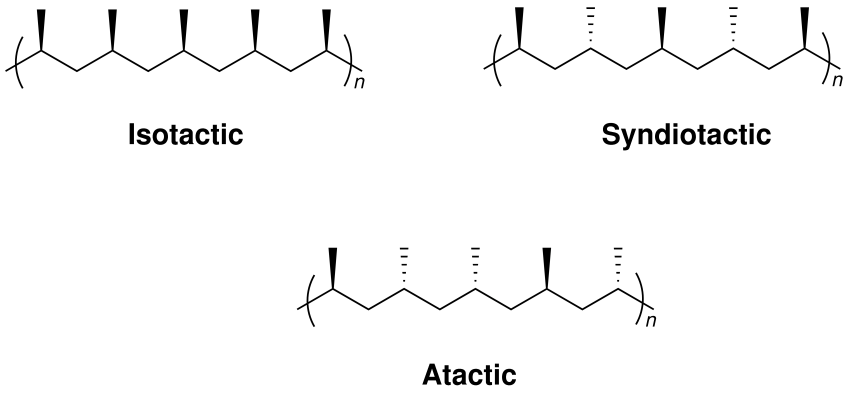

Figure 1.1: Possible Stereochemistries of Polymers

between the precursor species Cp_2TiCl_2, and the cocatalyst species R_2AlCl, in the complex, Cp_2TiRCl. Ethene was then inserted into the Ti-R bond of the alkylaluminium halide activated complex. These initial findings paved the way for Cossée's insertion mechanism[19–21] for heterogenous Ziegler-Natta catalysis. A subsequent mechanistic study by Shilov in 1961,[22] suggested the cationic species Cp_2TiMe^+ participated in the catalysis. Another study, on the reaction of $Cp_2Ti(R)Cl$ with $AlRCl_2$, by Dyachkovskii *et al*[23] indicated that after abstraction of a Cl^- atom, the cationic titanium complex, Cp_2Ti^+-R remained. Ethene then inserts at the titanium centre. The generation of this cationic species if shown in Figure 1.2.

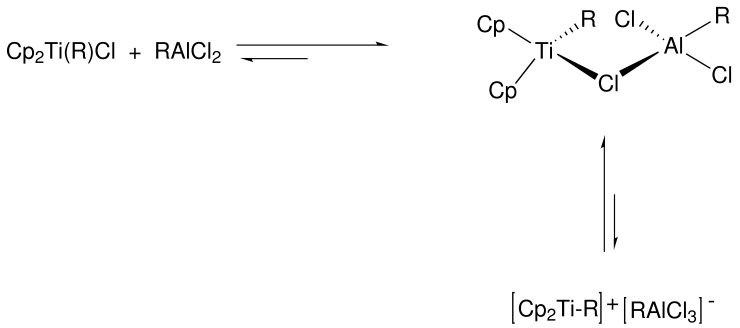

Figure 1.2: Cationic titanium centre for ethene insertion proposed by Dyachkovskii *et al.*

The titanium and zirconium metallocene precursors activated by alkylaluminium cocatalysts were only able to polymerise ethene, not propene or higher α-olefins. The ethene polymerisation activity for these systems was low to medium, with limited product molecular weight distributions. The catalysts in these systems also deactivated quickly. Many attempts were made to increase the rate of ethene polymerisation in these systems. Rate enhancement was accomplished when Reichert and Meyer[24] added water to $Cp_2TiEtCl/AlEtCl_2$. Long and Breslow[25] and Sinn and Kaminsky[26] followed by adding water to the otherwise inactive $Cp_2TiCl_2/AlEtCl_2$ and

$Cp_2ZrMe_2/AlMe_3$ systems. The increased activities of these systems after the addition of water, suggested that a stronger Lewis acid was formed. Methylaluminoxane, otherwise known as MAO, had been inadvertently discovered.[27,28]

1.1.2 Polymerisation Cocatalysts

The function of cocatalysts in metal-catalyzed polymerisation is two-fold. The cocatalyst is used to activate the transition metal precursor. In order for activation to be successful, the cocatalyst chosen must have key essential features that influence the kinetics and thermodynamics of the reaction. After activation, the cocatalyst becomes the counter ion to the catalytic transition-metal cation. This pair has significant influence over the activity, lifetime, stability, and solubility of the catalyst, whilst also affecting the properties of the polymer produced.[1]

Structurally Indistinct Initiators

MAO is prepared by the controlled hydrolysis of $AlMe_3$, and yields highly active catalysts with group IV metallocenes to produce polyethene, polypropene, and higher α-olefins.[29] MAO is an alkylaluminoxane, with the general formula $[-Al(Me)-O-]_n$. Aluminoxanes are defined as species which contain at least one bridging oxo group between two aluminium centers.[30] The exact structure of MAO has eluded both industrial and academic groups, even though extensive research has been carried out in this area.[31,32] NMR characterization has been difficult due to the oligomerization of MAO in solution. The presence of both "free" and "associated" trimethylaluminium in MAO has also hindered characterization.[33] X-ray diffraction is not a useful tool in the structural identification of MAO either; crystalline samples have yet to be isolated. Since the structure of MAO remains ambiguous, its exact mechanistic role is still unclear. The proposed one and two-dimensional structures for MAO are shown in Figure 1.3.

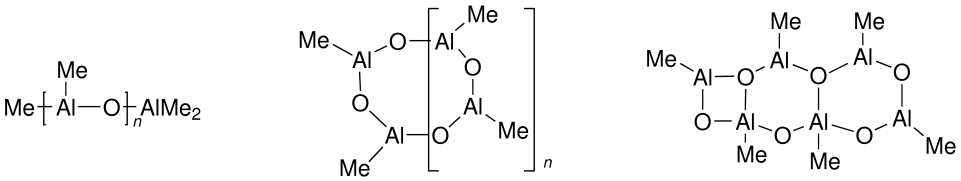

Figure 1.3: Proposed Structures for MAO

Structural evidence suggests that it is unlikely for MAO to be a chain structure.[34] In the proposed structure, the aluminium atoms are three-coordinate. Aluminium atoms often have a coordination number of four or more, achieving this higher coordination through bridging ligands, forming dimers and trimers.[34] In order for the aluminium atoms in methylaluminoxane to acheive

a coordination number of four, four or six membered rings must exist in the structure. Support for this theory was published by Pasynkiewicz[33] and Atwood, *et al.*[35] who crystallographically determined the structure of $[Al_7O_6Me_{16}]^-$, which is shown in Figure 1.4.

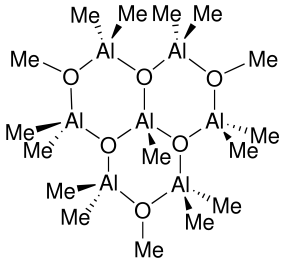

Figure 1.4: Structure of $[Al_7O_6Me_{16}]^-$

The possibility that MAO could be a three-dimensional cluster complex, and not a linear or two-dimensional aluminoxane, has been confirmed by Barron,[36] who characterized the aluminoxane complexes $[Al(O)_x(OH)_y(X)_z]_n$ where X = $OSiR_3O_2CR$. Barron[37] compared the multinuclear NMR, IR, X-Ray photoelectron spectroscopy, and single crystal X-ray diffraction data of $Al_{10}(OH)_{16}(OSiEt_3)_{14}$ to the $[AlO_x]$ core of the minerals, boehmite and diaspore. These minerals contain six-coordinate aluminium atoms, and have the formula, $[Al(O)(OH)]_n$. The core of the minerals is shown in Figure 1.5. The spectroscopic observation of the two complexes indicate that they are isostructural, demonstrating that a three-dimensional cluster structure for aluminoxanes, such as MAO, is possible. The fact that main group elements, specifically those of group 13, are prone to cluster or cage formation, also supports a cluster structure.[36]

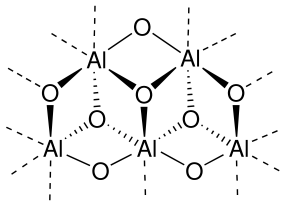

Figure 1.5: Isostructural Core of Boehmite and Diaspore

Results from Barron's work on gallium chalcogenide cage compounds,[38–40] and previous work in the literature on nonalkylalumoxanes,[37] prompted the synthesis of Al−O analogues for comparison to Ga−S clusters. The hydrolysis of $Ga(^tBu)_3$ results in the isolable $[(^tBu)_2Ga(\mu{-}OH)]_3$, produced in quantitative yield.[36] When the aluminoxane $Al(^tBu)_3$ is hydrolyzed, $[(^tBu)_2Al(\mu{-}OH)]_3$ (**1**) is isolated in yields from 20 to 55%. The additional side-products of this reaction have not been isolated. In an effort to keep side-products to a minimum, partial hydrolysis of $Al(^tBu)_3$ was achieved with $Al_2(SO_4)_3{\cdot}18\,H_2O$. One major product, $[(^tBu)_2Al[\mu{-}OAl(^tBu)_2]_2$ (**2**), and one

minor product (**3**), were isolated after fractional crystallisation. The two hydrolysis routes are shown in Scheme 1.1.

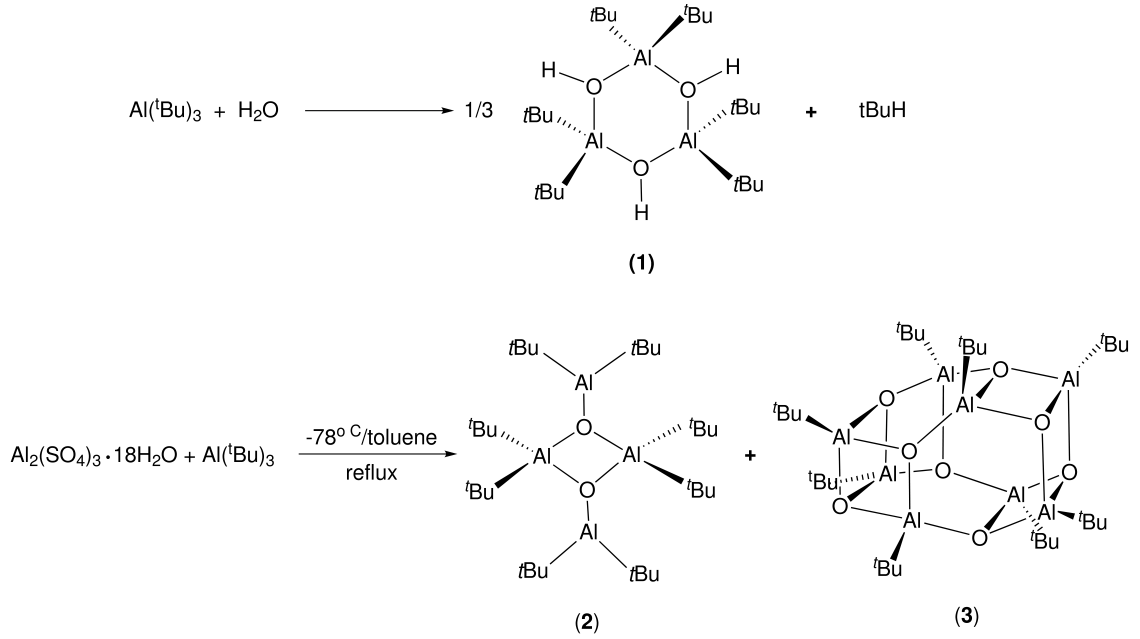

Scheme 1.1: Routes to the Hydrolysis of aluminium Alkyls

The mass spectrum of **(3)** was consistent with an octameric aluminoxane $[(^t\text{Bu})\text{Al}(\mu_3{-}\text{O})]_8$, but crystals suitable for X-ray diffraction were not obtained. The structure of two different *tert*-butyl aluminium-bound environments were found by ^{1}H and ^{13}C experiments performed on **(2)**. The ^{27}Al spectra confirmed that both a four-coordinate and a three-coordinate aluminium centre were present in **(2)** by comparison to other known compounds in similar coordination environments, R_2AlO_2 and R_2AlO.[39] The peak observed in the ^{17}O spectrum also fell within range of other observed tricoordinate oxo ligands. The NMR resonances for **(1)**, **(2)**, and **(3)** are shown in Table 1.1.

Compound	^{1}H	^{13}C	^{27}Al	^{17}O
(1)	2.02, 1.10	31.34	1.0	139.0
(2)	1.174, 1.169	32.14,	75.0	142.0
(3)	1.23, 1.18	29.74, 29.07	–	–
MAO	–	–	149	55.00

Table 1.1: NMR resonances for (1), (2), (3), and MAO

Barron's work on *tert*-butyl aluminoxanes has provided valuable information on possible struc-

tural features of MAO. The NMR experiments performed on the hydrolysis of *tert*-butyl aluminium provided ^{1}H, ^{13}C, ^{17}O, and ^{27}Al spectra for direct comparison to the spectra of comercially synthesised MAO. Unsurprisingly, ^{1}H and ^{13}C NMR data verify the presence of CH_3 groups bound to aluminium. The peaks are very broad, indicating a fluxional system. The ^{27}Al and ^{17}O spectra give insight into the coordination environments of the aluminium and oxygen atoms in MAO. These data is summarised in Table 1.2 and discussed below.

Aluminium	Oxygen
3-coordinate R_2AlO	3-coordinate oxo ligand
3-coordinate $RAlO_2$	3-coordinate OH moiety
4-coordinate $RAlO_3$	–
4-coordinate R_2AlO_2	–

Table 1.2: Possible MAO coordination environments

The ^{27}Al spectrum of MAO does not indicate as to whether the structure contains either three-coordinate aluminium [R_2AlO], or four-coordinate aluminium [R_2AlO_2], that is seen in structure **(1)**. There were broad resonances found between δ 149-152 ppm, which do indicate the previously published three-coordinate aluminium environment as found in $RAlO_2$. This coordination environment is generally found at 100 ppm.[33,39] The resonance found in the ^{17}O spectrum of MAO is indicative of a three-coordinative oxo ligand, or three-coordinate hydroxide moiety. The hydroxide groups were ruled out by IR and ^{1}H spectroscopy, confirming that three-coordinate oxo ligands are indeed present in the structure of MAO. Even though the hydrolysis of $Al(^tBu)_3$ and not $AlMe_3$ was studied, the crystallographic data and various NMR spectra of the aluminoxanes, $(RAlO)_n$, are indicative of cluster structures with four-coordinate aluminium centres, and an oxygen coordination environment with three bridging aluminium atoms. The conclusions from the structural data obtained from these experiments were beneficial, yet the structure of MAO has still not been proven.[36]

MAO has now become the industrial standard as a cocatalyst in olefin polymerisation. The structural 'plasticity' of MAO has prevented its mechanism from being extensively studied. A large excess of MAO must be used in the precatalyst activation process, with ratios typically 10^2 to 10^4:1. The large stoichiometric quantity of MAO used in activation prevents the catalytically active species from being characterized, therefore preventing the characterization of the overall activation process. The structural ambiguity of MAO is not the only drawback for its use as a polymerisation cocatalyst. The polymerisation activity of MAO activated precursors is depend-

ent on the hydrated salt used as the synthetic H_2O source, and the reaction conditions present. These obstacles led to the development of other cocatalyst systems, which exhibited the same or greater catalytic activity. These systems also showed greater characterizability, which improved the mechanistic understanding of cocatalysts in polymerisation.[1]

Structurally Distinct Initiators *Tris*(pentafluorophenyl)borane, $B(C_6F_5)_3$, was first synthesised by Massey and Park in 1964,[41] though it was not used as a cocatalyst for polymerisation until the early 90's. $B(C_6F_5)_3$ was initially used as a polymerisation initiator and cocatalyst when other strong Lewis acids were being assessed as abstracting agents. Other strong Lewis acids were also considered, but were not suitable for various reasons. BF_3 is not sufficiently strong to abstract the alkyl group in all cases, which is necessary to generate a vacant site and may also act as a fluoride transfer reagent, generating a relatively strong and inert metal-fluorine bond. $B(CF_3)_3$ has high Lewis acidity, but decomposes violenty above -78°C. $B(C_6H_5)_3$ is a good abstracting agent, but it is not a strong Lewis acid and can also act as an alkylating reagent.

$B(C_6F_5)_3$ is a strong Lewis acid. Although there is no crystal structure of uncoordinated $B(C_6F_5)_3$, there are many crystal structures of its adducts. The strength of the Lewis acidity derives from two sources. Firstly the inductive withdrawal of charge density from B by the C_6F_5 rings raises the effective charge on B. Secondly, the steric bulk of the fluorinated rings forces them to be tilted out of the plane, providing the propeller-like structure seen in Figure 1.6. This canted disposition of the rings limits the amount of π-overlap between the C_6F_5 π-system and the boron atom.[42,43]

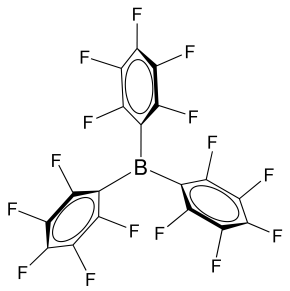

Figure 1.6: The propeller structure of *tris*(pentafluorophenyl)borane

Marks[44] and Ewen[45,46] discovered that $B(C_6F_5)_3$ could be used as a cocatalyst with group IV metallocene alkyls to produce crystallographically characterizable single-site cationic metallocene complexes.[47] Marks[44] studied the reactions of a variety of zirconocene complexes with $B(C_6F_5)_3$ to yield methyltriarylborate complexes. The various reactions are shown in Scheme 1.2.

All of the cationic zirconocene species were found to be catalytically active towards ethene.

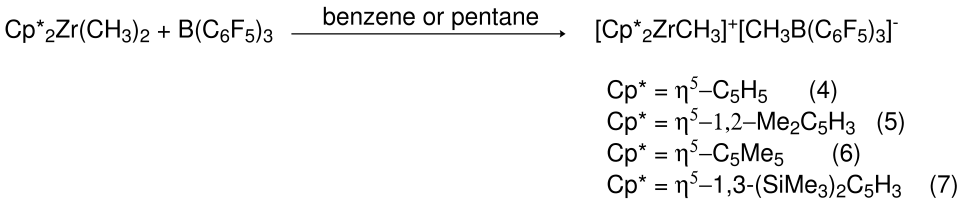

Scheme 1.2: The reaction of $B(C_6F_5)_3$ with a variety of zirconocene complexes

Complexes **4**, **5**, and **6** were catalytically active towards propene. The activity of these species were dependent on a few factors. The coordination environment for the cationic species is much more open after abstraction than the original dimethyl or dihydrido species. The crystallographic studies of the various cationic species also showed that the $CH_3B(C_6F_5)_3^-$ is coordinated weakly to the zirconium centre, implying that stabilisation in the absence of monomer can occur. Both of these effects contribure to making them very reactive polymerisation catalysts.[44]

Marks' findings that $B(C_6F_5)_3$ worked well as a cocatalyst for polymerisation was an important discovery for both academia and industry. Unlike MAO, $B(C_6F_5)_3$ does not have to be used in large excess in order to produce highly active catalytic species. The structural disadvantages encountered with the use of MAO as a cocatalyst are not seen either. The catalytically active species involved in the polymerisations with $B(C_6F_5)_3$ were crystallographically characterizable cationic species, with one of two possible binding modes shown in Figure 1.7. The crystallographic data would therefore support the $B(C_6F_5)_3$ binding in (8). The ^{1}H NMR data supports the binding in (8) as well, with a C−H coupling constant of 118 Hz, indicating the carbon is not bound to the metal center. The ^{13}C NMR shows very little zirconium-carbon interaction, providing further proof that the $CH_3B(C_6F_5)_3^-$ is weakly bound to the metal, and most likely binding through the hydrogen atoms of the bridging methyl group.[44] The results from this study provided further evidence and mechanistic insight into cationic metallocene polymerisation catalysts.

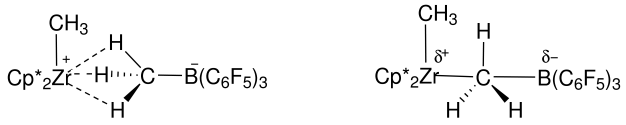

Figure 1.7: Possible Binding Modes of $B(C_6F_5)_3$ to Zirconocene Cation Complexes

The success of $B(C_6F_5)_3$ prompted other perfluoroarylborane and bifunctional borane activators to be synthesised. Piers[48] synthesised bis(pentafluorophenyl)borane, $[HB(C_6F_5)_2]_2$ in quantitative yield, as seen in Scheme 1.3. $[HB(C_6F_5)_2]_2$ was found to be an excellent reagent for hydrob-

oration; it is highly electrophilic in non-coordinating solvents.[49] Despite its strong electrophilicity and fast kinetics, this reagent was also found to be more regio and chemo-selective than others used in hydroboration.

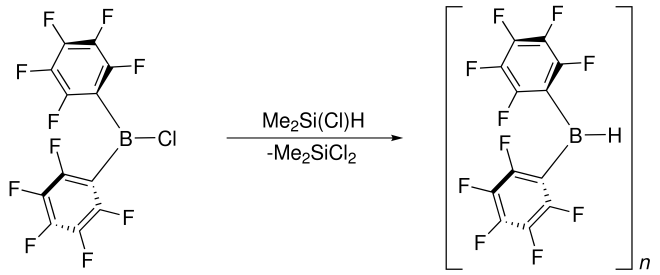

Scheme 1.3: Synthesis of *bis*(pentafluorophenyl)borane

$[HB(C_6F_5)_2]_2$ was treated with the dialkyl zirconocenes Cp_2ZrR_2 where R=CH_3, $CH_2C_6H_5$, and CH_2SiMe_3. These reactions are shown in Scheme 1.4. There are two distinct reaction pathways, the first of which is dependent on the sterics of the ligands bound to zirconium. In the first pathway, Cp_2ZrR_2 and $HB(C_6F_5)_2$ undergo alkyl-hydride exchange. The newly formed hydride, $Cp_2ZrR(H)$, then consumes another equivalent of $HB(C_6F_5)_2$, forming the dihydrido-bis(pentafluorophenyl)borate zirconium shown in Scheme 1.4.

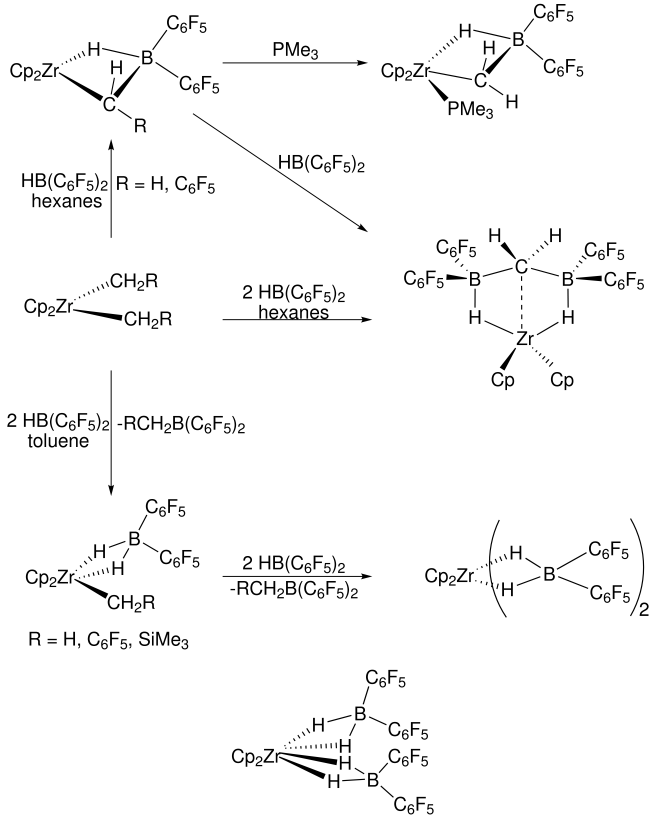

Scheme 1.4: Reactions of $HB(C_6F_5)_2$ with dialkyl zirconocenes

The dihydrido complexes were formed when the R group on zirconium was sterically bulky. In the second pathway, an alkylidene derivative was formed when an RH group was lost from Cp_2ZrR_2 via a Lewis-acid induction.[49] These alkylidene derivatives were stabilised by $HB(C_6F_5)_2$. This reaction pathway is similar to that of the Tebbe's reagent, when Cp_2TiMe is reacted with $AlMe_3$ to form $Cp_2Ti{=}CH_2$. This alkylidene derivative was found to be a very reactive species, further reacting with $HB(C_6F_5)_2$ to form $Cp_2Zr\{\eta^3{-}CH(C_6H_5)[(\mu{-}H)B(C_6F_5)_2]\}$. This complex contains two $HB(C_6F_5)_2$ fragments bonded to the methylene carbon. The crystal structure of this compound revealed that there is bonding between the methylene carbon and the zirconium centre. The Zr$-$C bond length of the alkylidene is 2.419 Å, similar to the Zr$-$C bond length of 2.27 Å, for the Zr$-$Me bond in $Cp_2Zr(CH_3)_2$. The methylene carbon in this complex would therefore be five-coordinate. The complexes from Scheme 1.4 are very reactive, yet they show strong metal-borate interactions. The strongly coordinating $HB(C_6F_5)_2$ limits the ability of these complexes to be highly active polymerisation catalysts.

The sterically encumbered perfluoroarylboranes, *tris*(2,2',2"-perfluorobiphenyl)borane (PBB),[50] *bis*(pentafluorophenyl)(2-perfluorobiphenyl)borane (BPB),[51] and *tris*(β-perfluoronaphthyl)borane (PNB)[52] were also synthesised. These perfluoroboranes, similar in structure to $B(C_6F_5)_3$, were also used as initiators to synthesise cationic metallocene complexes. The polymerisation activities and reaction characteristics of these cationic species were examined for comparison to their $B(C_6F_5)_3$ analogues. These perfluorarylboranes are shown in Figure 1.8 and are discussed in detail below.[50]

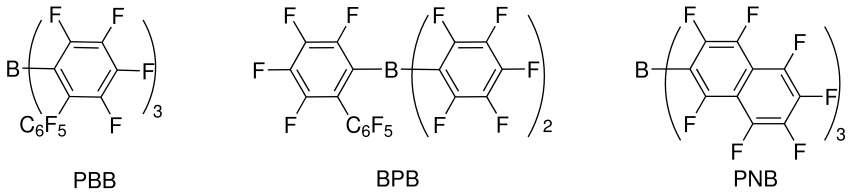

Figure 1.8: Sterically encumbered perfluoroarylboranes

The cationic complexes in Scheme 1.5 are synthesised when *tris*(2,2',2"-perfluorobiphenyl)borane, or (PBB), is reacted with group IV or thorium methyl complexes. Complexes (**10**) and (**15**-**18**) indicate a downfield shift in the ^{13}C NMR spectrum, indicative of a M^+-$^{13}CH_3$ cationic complex. The ^{19}F spectrum of these complexes has nine resonances, while the ^{19}F spectrum of PBB has seven. This difference in number of resonances implies restricted rotation of the C_6F_5 group.

The ion-pair relationship between PBB and the precursor was examined to measure the strength of anion coordination. The coordination strength of the $MePBB^-$ anion was then compared to the known coordination strength of $MeB(C_6F_5)_3{}^-$.[44] The $MePBB^-$ anion was found to be more

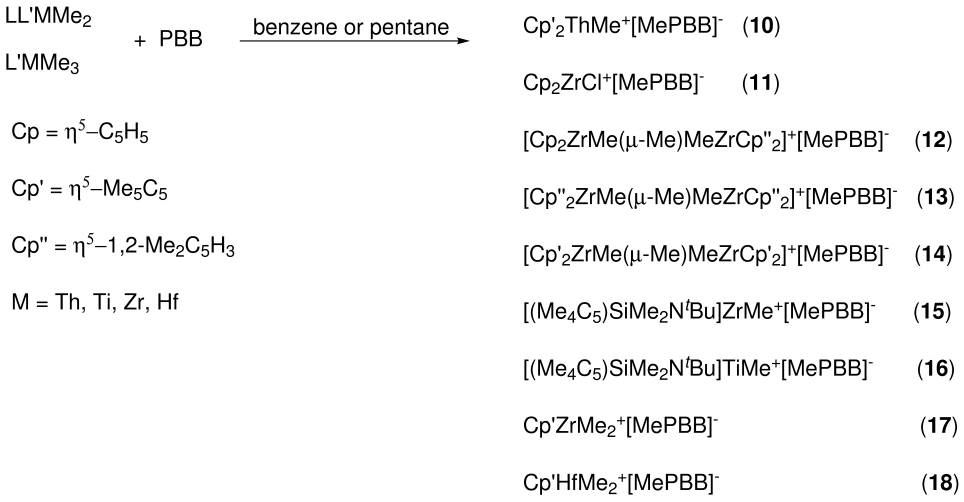

Scheme 1.5: Cationic complexes formed on reaction of PBB with group IV or thorium methyl complexes

weakly coordinated. As there were no significant differences in the ^{1}H NMR spectrum of the countercations versus the MePBB^{-} anion, dynamic NMR studies were performed on complex (**15**) of the MePBB^{-} coordinated systems. Previous data found the ΔG of the same Me(C$_6$F$_5$)$_3^{-}$ system to be 2.6 kcal/mol higher, indicating this system is more strongly coordinated to the metal centre.[44] The ^{19}F spectra of (**10**), (**12**), (**15**), and (**17**) show magnetic equivalence of the three MePBB^{-}C$_6$F$_5$C$_6$F$_4$ groups, a further indication that these complexes are weakly coordinated.

When Cp'$_2$ThMe$_2$, where Cp' is η^5-Me$_5$C$_5$ and Cp$_2$ZrClMe were reacted with B(C$_6$F$_5$)$_3$, the products were not separable, or catalytically active.[44] These precursors were activated with PBB, underwent methyl abstraction, and formed complexes (**10**) and (**11**). Dimeric μ-Me complexes (**12**-**14**) were formed when PBB was reacted with group IV dimethyl metallocenes. Dimeric cationic species of this nature had been previously observed, but were not characterisable by x-ray diffraction.[52]

When comparing complexes (**12**-**14**) that were activated with B(C$_6$F$_5$)$_3$, these catalysts showed the same polymerisation activity towards ethene as those initiated with PBB. The precursors activated with PBB produced higher molecular weight polyethenes. When the previously reported precursors to complexes (**15**-**16**) were initiated with B(C$_6$F$_5$)$_3$, the catalysts produced were slightly active with zirconium, and only marginally active with titanium. When these precursors were initiated with PBB, the catalysts produced are highly active with both ethene and 1-hexene.[50]

As discussed above, group IV dimethyl precursors initiated with PBB, produce dinuclear complexes. Monomeric species are not produced when excess PBB is added to the precursor, or when the reaction is heated.[53] They are only produced at high temperatures *in situ*. The activation time

for these systems is often quite slow. To try and solve both the activation and structural problems associated with PBB, *bis*(pentafluorophenyl)(2-perfluorobiphenylyl)borane, or BPB was synthesised.[51] BPB was investigated because it contained substituents with steric and electronic properties between PBB and $B(C_6F_5)_3$. The synthesis of BPB is shown in Scheme 1.6.

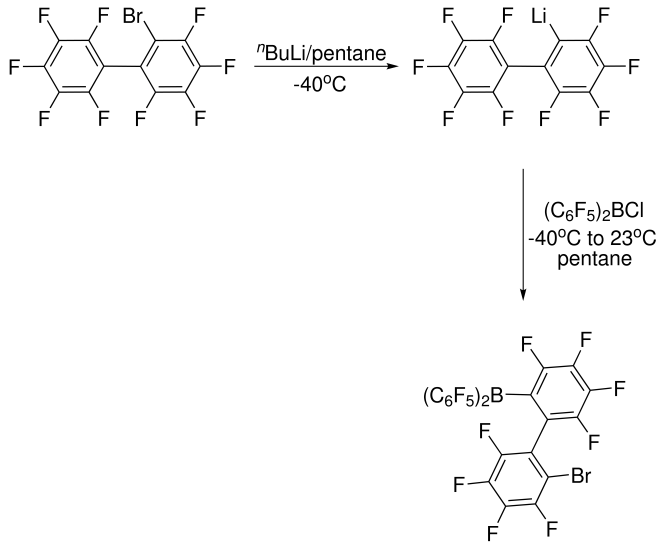

Scheme 1.6: The synthesis of BPB

Cationic monomeric species were produced when BPB was reacted with dimethylmetallocenes. These species have the general formula, $L_2ZrMe^+MeBPB^-$, and are shown in Scheme 1.7. Unlike PBB, only one equivalent of initiator was needed for the reaction to go to completion. These complexes were isolated, and characterized by NMR spectroscopy and elemental analysis. BPB initiated precursors showed the same or higher polymerisation activities than those initiated with $B(C_6F_5)_3$. The cationic complex (**19**) showed the same activity with ethene, and produced polyethene with similar molecular weight and polydispersities. Complex (**22**) is a constrained geometry catalyst, or CGC, and showed three times the activity of the $B(C_6F_5)_3$ initiated precursor. Complex (**22**) also showed higher activities when reacted with ethene and 1-hexene.

Tris(β-perfluoronapthyl)borane (PNB) was also investigated as a cocatalyst in olefin polymerisation.[52] PNB was investigated alongside PBB and BPB as an alternative to the use of $B(C_6F_5)_3$ as a cocatalyst. The steric and electronic properties of PNB provided another viable alternative to $B(C_6F_5)_3$. The synthesis of PNB is shown in Scheme 1.8.

Like PBB and BPB, PNB was reacted with various dimethyl metallocenes to produce the metallocene cations shown in Scheme 1.9. A 1:1 ratio of dimethyl metallocene to PNB, resulted in monomeric cationic species with the formula $L_2ZrMe^+MePNB^-$. In order to form the dimeric species with the general formula, $[L_2ZrMe(\mu{-}Me)MeZrL_2]^+MePNB^-$, a 2:1 ratio was used.

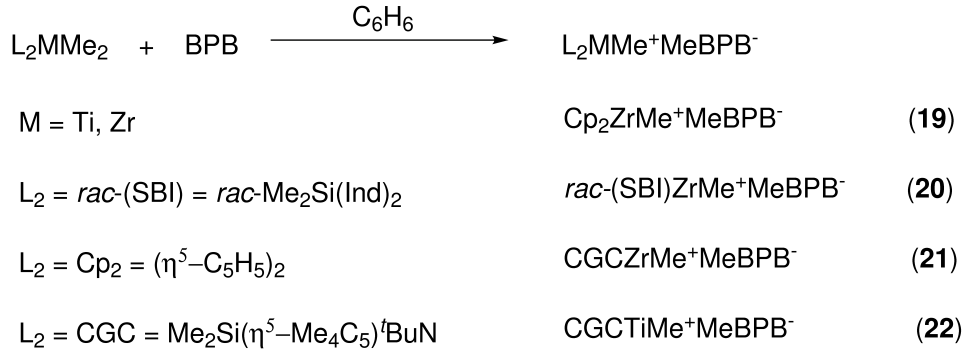

Scheme 1.7: Metallocenium cations generated from reaction of BPB and dimethylmetallocenes

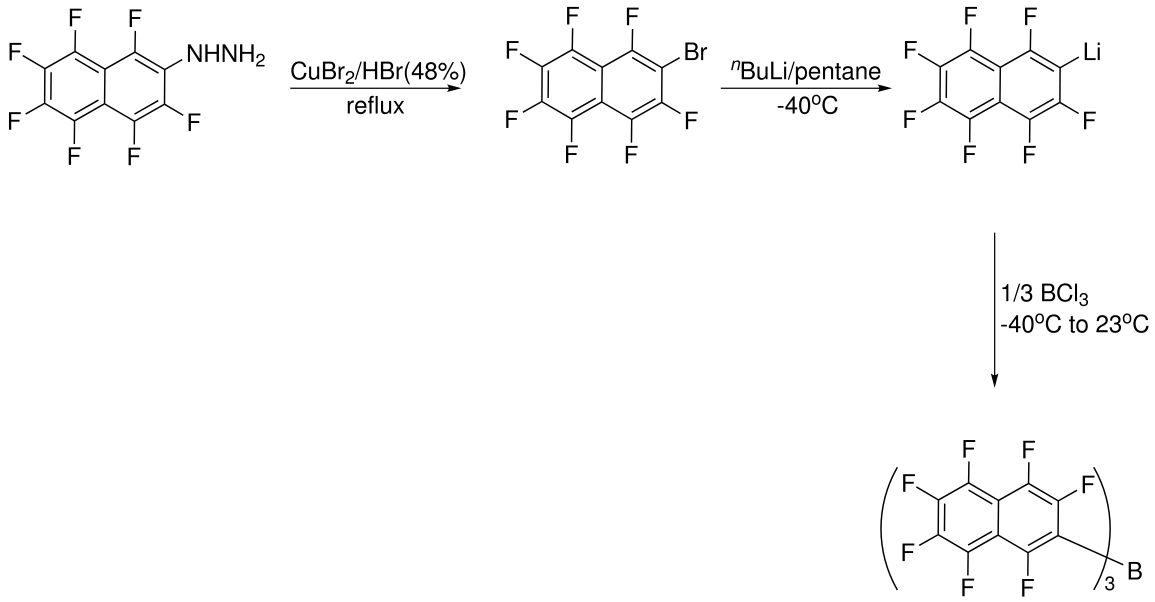

Scheme 1.8: The synthesis of PNB

After the success of polymerisation catalysis with the initator $B(C_6F_5)_3$ and its derivatives, scientists began to test the ability of other pentafluorophenylboranes. Alternatively, Marks[54] and a few others[55–58] directed their attention to the Lewis acidic cocatalyst involved in the reactions. These cocatalysts were studied to better understand the metallocenium-fluoroaryl ion pairing, and the mechanism for polymerisation.

The studies performed on the cocatalysts $B(C_6F_5)_3$, PNB, PBB, and BPB, evinced they were strongly coordinating anions. The next logical step was to search for strongly Lewis acidic non-coordinating anions. The cationic centre formed upon coordination with the counteranion was a highly Lewis basic system, extremely succeptable to electrophilic attack. Previous studies showed that in order to be successful, the counteranion must therefore be chemically robust, and resistant to electrophilic attack.[59–62] The charge on the anion was also very important. In order to be weakly

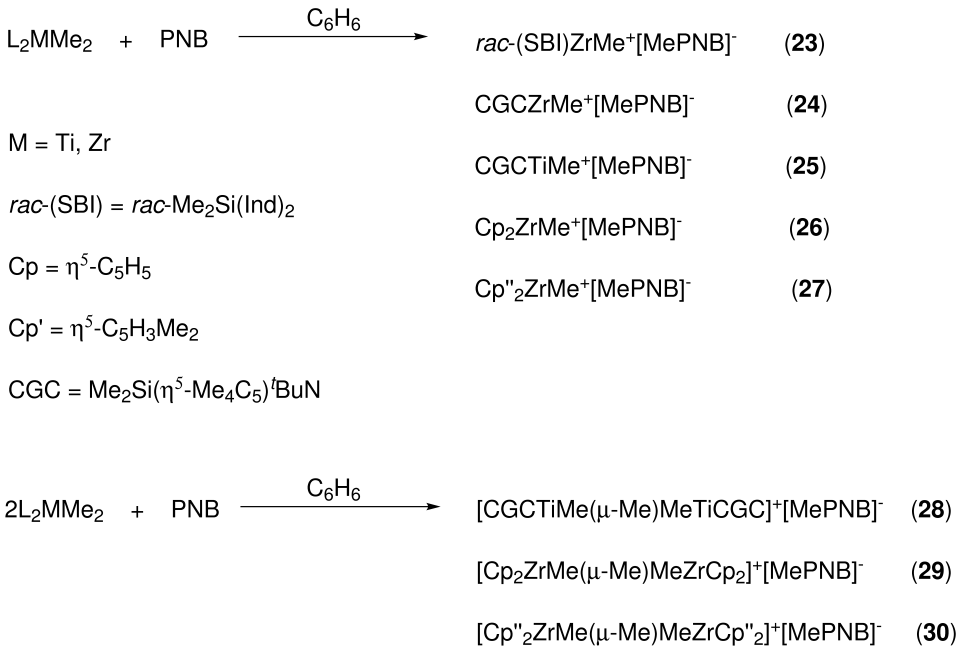

Scheme 1.9: Metallocenium cations formed from the reaction of PNB and dimethyl metallocenes

coordinating, the anion must have a -2 or -1 charge, with the latter being preferred. The charge on the anion should also be delocalized entirely. For obvious reasons, larger anions are preferred. The charge is then delocalized over a larger surface, providing a weaker coordination sphere. It is also important to have only weakly basic atoms available for cation binding. Fluorine or hydrogen atoms are therefore preferred over chlorine or oxygen atoms. That being said, anions containing fluorine atoms must be kinetically stable enough in order to avoid fluoride ion abstraction.[60]

In order to minimize the cation-anion coordination seen in polymerisation catalysis using $B(C_6F_5)_3$ as a cocatalyst, the (*tetrakis*)pentafluorophenylborate anion, $B(C_6F_5)_4^-$, was examined for its use as supporting anion. There are some fundamental differences between the role of $B(C_6F_5)_3$ and the other fluoroborate anions used as cocatalysts. $B(C_6F_5)_3$ both abstracts an alkyl group or hydride, and supports the cationic metal centre. $C(C_6H_5)_3^-$ is also used as an alkyl/hydride abstracting agent.[63] $B(C_6F_5)_4^-$ abstracts an alkyl or hydride, and supports the cationic centre. $B(C_6F_5)_4^-$ is only weakly coordinated to the cationic metal centre, unlike $B(C_6F_5)_3$.

Metallocenium borate ion pairs can be synthesised one of three ways. The first is the formation of ion pairs using redox reactions. One example from the literature is Ag^+X^-.[64] The second method utilises protonolytic reagents, such as $Bu_3NH^+B(C_6F_5)_4^-$.[64–66] The third method is the use of alkyl or hydride abstractors, such as $Ph_3C^+X^-$.[63]

The $B(C_6F_5)_4^-$ anion proved to be an excellent supporting anion, producing catalytically active transition metal cations, but not coordinating to the metal centre. Some examples from

Marks[54] are shown in Scheme 1.10. The polymerisation activities of the above examples using the $B(C_6F_5)_4^-$ as a supporting anion, were some of the highest activities published. Unfortunately, these reactions produced cationic species that were insoluble, oily, and were unable to be isolated from a variety of different products. In order to isolate the catalytically active centre to study the mechanism of reaction, the transition metal used as a precursor, and the ligands attached to the metal centre were replaced.

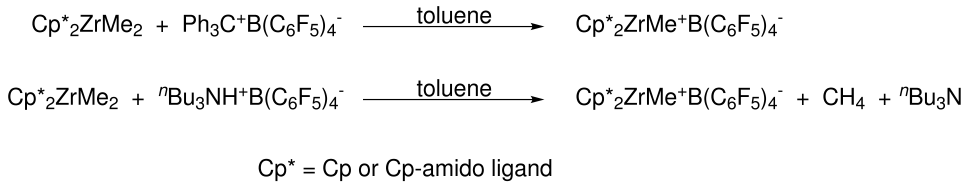

Scheme 1.10: Cationic Zirconium Complex with $[B(C_6F_5)_4]^-$ Anion

In order to promote product isolation and crystal growth, alternatives to the standard trityl and ammonium borate cocatalysts were also investigated.[54] The electron-withdrawing and sterically shielding cocatalysts $B(C_6F_4TBS)_4$ and $B(C_6F_4TIPS)_4$ where TBS = *tert*-butyldimethylsilyl and TIPS = triisopropylsilyl, were chosen in order to stabilise the highly electrophilic cationic zirconium centres. These ligands can be seen in Figure 1.9. These cocatalysts also showed increased solubility in nonpolar solvents. Coordination comparison to the previously studied $B(C_6F_5)_4^-$ were also studied. Scheme 1.11 shows the synthesis of the ligands TBS and TIPS.

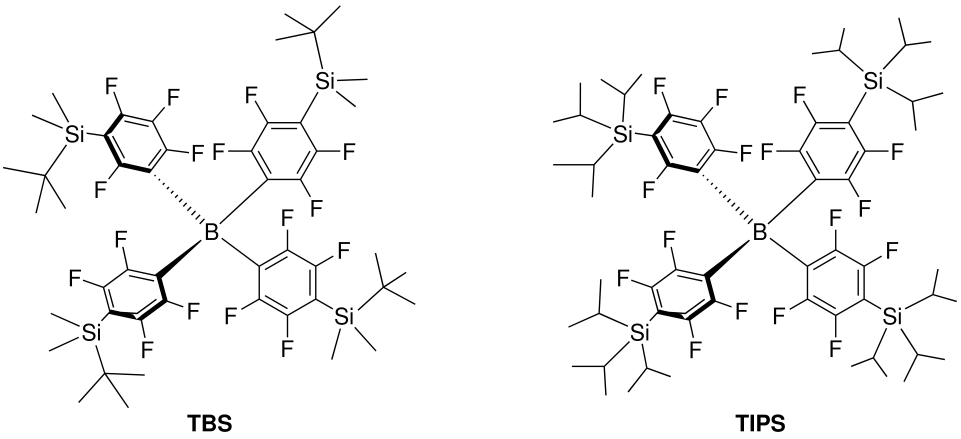

Figure 1.9: The ligands TBS and TIPS

A series of zirconium and thorium borate complexes were synthesised in order to study the strength of the anion coordination. This series is shown in Scheme 1.12. Of the above mentioned synthetic methods, the methide or hydride abstraction using $[C(C_6H_5)_3]^+$ was chosen as Ph_3CMe is soluble in hydrocarbon solvents, allowing clean isolation of the metallocenium species.[54]

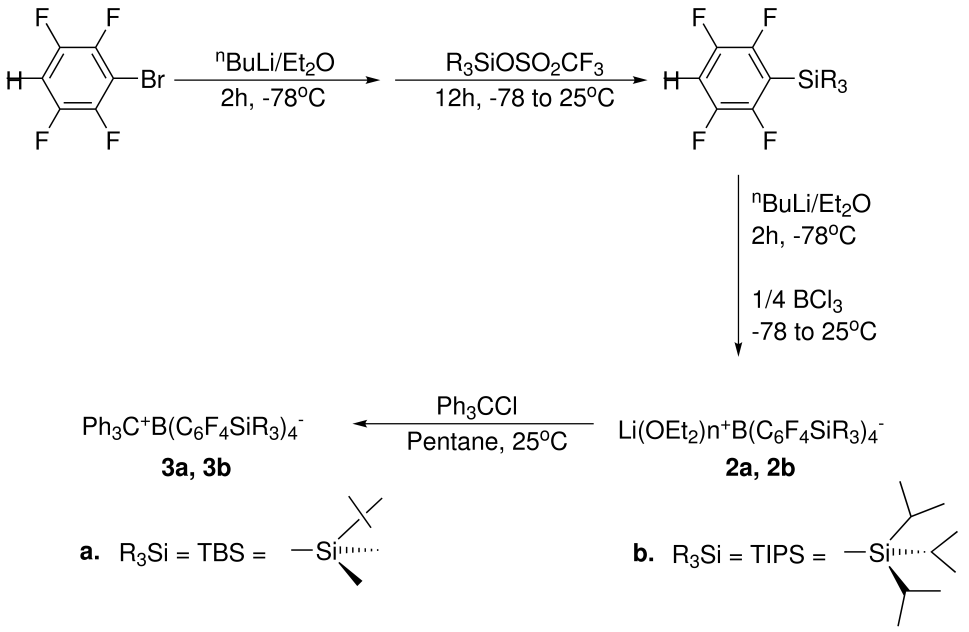

Scheme 1.11: The synthesis of the carbenium salts TBS and TIPS

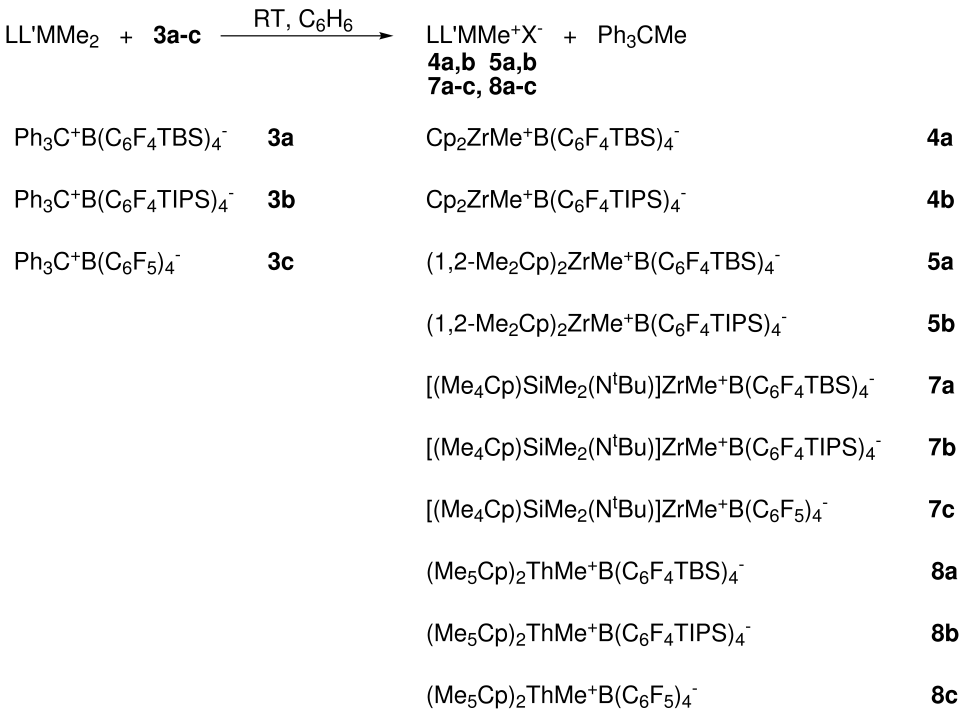

Scheme 1.12: A series of cationic ion-paired zirconium and thorium (fluoroaryl)borate complexes

When the transition metal used in the precursor was changed from zirconium to thorium, isolation was possible, and crystals of $[(Me_5Cp_2)ThMe]^+[B(C_6F_5)_4]^-$ were characterised. The molecular structure is shown in Figure 1.10. Crystallographic studies show the structure consists of the loosely bound cation, $[(Me_5Cp)_2ThMe]^+$ and anion, $[B(C_6F_5)_4]^-$. The structure of the

cationic species, $[(Me_5Cp_2)ThMe]^+$, is a bent sandwich configuration, similar to other transition-metal metallocenes. The measured Th−Me distance and the average Th−C_{ring} distances are shorter than those found in other cationic thorium complexes containing different counterions or Lewis bases. The decrease seen in the bond distances indicates decreased electron density and coordinative unsaturation at the thorium centre. The crystal structure also shows one aryl ring of the $B(C_6F_5)_4^-$ unit in close proximity of the cationic thorium centre, with two fluorine atoms of the ring closest to the metal centre. These fluorine atoms, labeled F18 and F19, have Th−F bond distances of 2.757 Åand 2.675 Å. The sum of the ionic radii of Th^{4+} and F^- is significantly shorter, 2.28 Å. The average C−F bond distance in the $B(C_6F_5)_4^-$ are slighty smaller than the C−F bond distances for C_{43}−F_{18} and C_{44}−F_{19}, 1.325 Å, and 1.344 Å. The other C−F lengths fall within the mean length of a typical C−F bond. These appear to be the only cation-anion interactions,[67] clearly indicating that the $B(C_6F_5)_4^-$ unit is weakly coordinated to the metal centre.

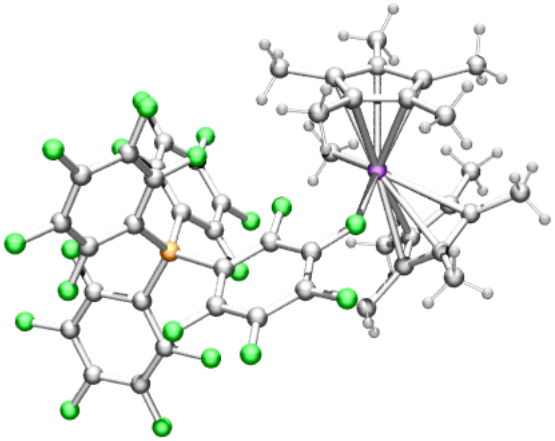

Figure 1.10: Molecular structure of $(Me_5Cp_2)ThMe^+B(C_6F_5)_4^-$

A comparative study on the coordination ability of the anions, $B(C_6F_5)_4^-$, $B(C_6F_4TBS)_4^-$, $B(C_6F_4TIPS)_4^-$, and $Me(C_6F_4)_3^-$ to the zirconium centre was performed using NMR spectroscopy. The activation energy of the various systems, $(1,2\text{-}Me_2Cp)_2ZrMe^+X^-$, where X is one of the anions listed above, was calculated. These complexes undergo an ion-pair reorganization of the ground state indicated by the the alternation of two methyl groups on the ring, as seen in Figure 1.11. The activation energies were measured using variable-temperature NMR spectroscopy. The activation enthalpies, entropies, and rate constants were also measured using dynamic NMR studies and are tabulated below in Table 1.3.[54,68] These calculations were then used in order to

compare the ion-pair dissociation of the previously calculated (1,2-$Me_2Cp)_2ZrMe^+MeB(C_6F_5)_3^-$ system[68,69] to the complexes using $B(C_6F_5)_4$ anions.

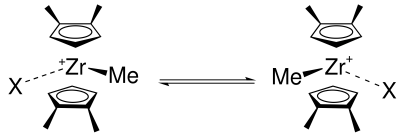

Figure 1.11: Ion-Pair Reorganization

X^-	$\Delta H^\ddagger$/ kcal/mol	$\Delta S^\ddagger$/ kcal/mol	$\Delta G^\ddagger_{coal}$/ kcal/mol	T_c ° C
$MeB(C_6F_5)_3^-$	24(1)	17(2)	18.3(2)	80(1)
$B(C_6F_4TBS)_4^-$	18.6(8)	11(1)	15(1)	56(1)
$B(C_6F_4TIPS)_4^-$	19.2(4)	10(1)	15.8(7)	65(1)

Table 1.3: Activation energy parameters for the ion pair reorganization process

The activation enthalpy for ion-pair reorganization of (1,2-$Me_2Cp)_2ZrMe^+MeB(C_6F_5)_3^-$ is much higher than for (1,2-$Me_2Cp)_2ZrMe^+B(C_6F_4TBS)_4^-$ and (1,2-$Me_2Cp)_2ZrMe^+B(C_6F_4TIPS)_4^-$, indicating that the $MeB(C_6F_5)_3^-$ is more tightly bound to the metal centre. The activation entropies of the systems employing $B(C_6F_5)_4$ anions are also lower, indicating the ground states of these ion-pairs are more disordered, providing further evidence that $MeB(C_6F_5)_3^-$ is more tightly associated than the $B(C_6F_5)_4^-$ systems. From crystallographic and NMR studies, it can be stated that the coordination ability of fluroarylborates with respect to metallocene catalysts can be ranked with $MeB(C_6F_5)_3^-$ having the strongest coordination. (1,2-$Me_2Cp)_2ZrMe^+B(C_6F_4TBS)_4^-$ and (1,2-$Me_2Cp)_2ZrMe^+B(C_6F_4TIPS)_4^-$ have weaker coordination, but are about the same in comparison to each other; $B(C_6F_5)_4^-$ therefore has the weakest coordination ability.[54]

The ^{19}F spectra of these systems provides additional support for the strength of anion coordination in these complexes. There are no significiant changes in the chemical shifts or line shapes in the ^{19}F spectrum of those complexes using $MeB(C_6F_5)_3^-$ as the anion. The anion-cation interaction is not affected by the fluoroaryl groups, as the contact with the metal centre is largely through the methyl group.[44] This interaction is shown in Figure 1.12. When the anion is changed to $B(C_6F_5)_4^-$, or in this case, $B(C_6F_4TBS)_4^-$ or $B(C_6F_4TIPS)_4^-$, the ^{19}F spectrum is significantly altered. These alterations are indicative of direct metal-fluorine interactions. From these observations, the strength of anion coordination can be inferred.

No substantial changes are seen in the room temperature ^{19}F spectrum of the system, Me_5-$(Cp)_2ThMe^+B(C_6F_5)_4^-$. Even at temperatures as low as $-80°C$, only minor line broadening

was seen in the spectrum. These data would therefore suggest that the anion is coordinated very weakly to the cation. The molecular structure and C−F bond lengths provided above support the weak coordination evinced by the ^{19}F spectrum. In contrast, there is severe line broadening and chemical shift changes seen in the ^{19}F spectra of the same thorium complexes, when the anion is either $B(C_6F_4TBS)_4^-$ or $B(C_6F_4TIPS)_4^-$. These anions therefore have stronger coordinating ability. These spectra confirm the ranking of anionic strength outlined above.

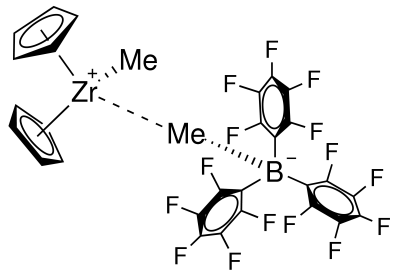

Figure 1.12: Cation-anion interaction seen in $MeB(C_6F_5)_3$ systems

The polymerisation experiments performed using $B(C_6F_5)_4^-$ as a supporting anion showed excellent activity towards ethene. The methyl cationic catalysts are thermally sensitive, however, and decompose at elevated temperatures commonly used in industrial polymerisation. The $B(C_6F_5)_4^-$ cocatalysts therefore exhibit the highest catalytic activity when they are initially synthesised. The catalytic activities of $(1,2\text{-}Me_2Cp)_2ZrMe^+B(C_6F_4TBS)_4^-$, $(1,2\text{-}Me_2Cp)_2ZrMe^+B(C_6F_4TIPS)_4^-$, and $(1,2\text{-}Me_2Cp)_2ZrMe^+B(C_6F_5)_4^-$, were all similar to each other, but were much higher than the previously studied $(1,2\text{-}[Me_2Cp)_2ZrMe]^+[MeB(C_6F_5)_3]^-$.[44] Polymerisation experiments were carried out on the same catalysts, substituting thorium in for zirconium. These catalysts also exhibited high catalytic activity, but were suprisingly much lower than the zirconium analogues using the same reaction conditions. The catalytic activity for the zirconium complexes using $B(C_6F_5)_4^-$, $B(C_6F_4TBS)_4^-$, and $B(C_6F_4TIPS)_4^-$ as cocatalysts was not as varied when exposed to propene. The thorium complexes did not catalyse propene. These complexes form an η^3-allyl complex and give off methane when reacted stoichiometrically with propene.[44] Similar complexes have been produced when the lanthanides were exposed to propene.[70–72]

The experimental work performed using various $B(C_6F_5)_4$ anions as polymerisation cocatalysts, has provided more information on both the structure and reactivity of catalytically active transition metal cations. This study has proven that the anionic cocatalyst used in polymer activation is as important as the transition metal precursor chosen. Spectroscopic experiments performed have proven that weakly-coordinated cocatalysts such as $B(C_6F_5)_4^-$, $B(C_6F_4TBS)_4^-$, and $B(C_6F_4TIPS)_4^-$ show higher polymerisation activities than more strongly-coordinated cocatalysts

such as $MeB(C_6F_5)_3^-$.[44]

1.1.3 Heterogenous Catalysis

Olefin metathesis polymerisation can be facilitated by either a heterogenous or homogenous catalyst. Heterogenous catalysis takes place at the surface of the material. This catalysis is therefore more difficult to study than homogenous catalysis, where the catalyst is in the same phase as the reactants.

Ziegler-Natta Catalysis

Organolithium and organoaluminium compounds were the first catalysts used by Karl Ziegler for olefin insertion reactions. There are two separate industrial processes used for olefin insertion. In this first process, oligomerisation and polymerisation of ethene and propene occurs when the monomer is added to alkyls of lithium or aluminium. The metal carbon bond is regenerated and the chain is extended when the unsaturated hydrocarbon is inserted into the metal alkyl linkage. This "chain-growth" reaction has an unlimited number of polymer chains, whose length is only terminated when the elimination of a M−H occurs. This reaction is referred to as the *Aufbau* reaction and is shown in Scheme 1.13.[73] The LiH species is insoluble and inactive, but the R_2AlH species remains active after hydroalumination occurs and reforms the trialkyl species.

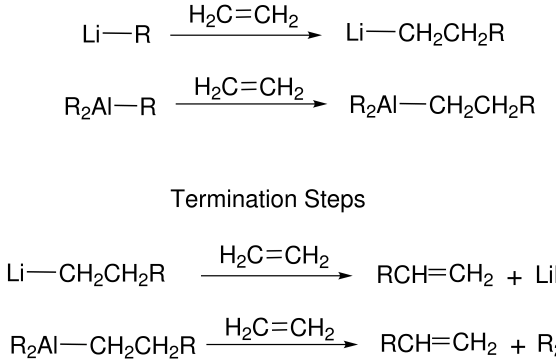

Scheme 1.13: *Aufbau* reactions using lithium and aluminium catalysts

In the second process, ethene and other alkenes are used with the transition metal polymerisation catalyst $TiCl_4$-$AlEt_3$ to produce high-density polyethene at much lower temperature and pressure. This process is known as the Mülheim normal-pressure polyethene process. The Mülheim process produced mixtures of amorphous and crystalline polyethenes and polypropenes. Giulio Natta used the same catalyst and conditions with propene to create stereoregular isotactic polypropene. Polyethene and polypropene produced in this manner have a higher density, hard-

ness, and tensile strength, making them very durable polymers for industrial use.[74] Natta also found that α-$TiCl_3$- $AlEt_3$ produced products that were more crystalline in nature than the Ti (IV) system. This catalyst was also able to polymerise styrene and 1-butene into stereoregular polymers. A vanadium catalyst, VCl_4-$AlEt_2Cl$, was also used to produce syndiotactic polypropene if the reaction mixture was kept below -78°C.

1.1.4 Homogenous Catalysis

Ansa-Cyclopentadienyl-Amido Catalysts

For many years, metallocene complexes, especially of titanium and zirconium, were the main source of catalysts used in olefin polymerisation. These MAO initated metallocenes were found to be extremely active polymerisation catalysts.[75–77] The success of metallocene catalysts in polymerisation led to the development of other homogenous catalysts. One of the pivotal advantages of homogenous catalysis over heterogenous catalysis is that there is only one active site for polymerisation to occur. When there are multiple active sites, there is less control over the characteristics of the polymer produced. Extensive research of metallocene catalysts led to the discovery that the symmetry of the zirconocene held significant influence over the microstructure of the polymer produced. Some examples of the effects of catalyst symmetry and the structure of the polymer are shown in Figure 1.13.[75] Though these catalysts give significant control over the polymer microstructure, they have limited temperature stability and tend to produce only low molecular weight polymers.

Research groups in both industry and academia began to look at group IV metallocene analogues for their use as polymerisation catalysts. *Ansa*-monocyclopentadienyl-amido complexes, or CpA's, were developed by both Dow and Exxon.[75] Figure 1.14 shows a generalized structure for the CpA catalyst. These catalysts employ zirconium and titanium but were originally suggested by Bercaw[78,79] for organoscandium olefin polymerisation. The titanium CpA complex was first published by Okuda[80] in 1990, and patents indicate that Dow and Exxon began to investigate the activity of these catalytic systems soon after in 1991.[81–85]

CpA catalysts are unique in that they have the ability to copolymerise ethene with other olefins. The lack of steric hindrance at the active site allows these catalysts to polymerise ethene with hexene, octene, and norbornene.[86–101] CpA catalysts are also one of the only catalysts able to incorporate styrene into polyethene.[87,95,102–104] These catalysts are more stable than Cp metallocenes when MAO is used as an initiator, and at higher temperatures. Higher molecular weight polymers are also produced when CpA is used as a catalyst.[105]

There are a few possible synthetic routes to CpA ligands. These routes are shown in Scheme

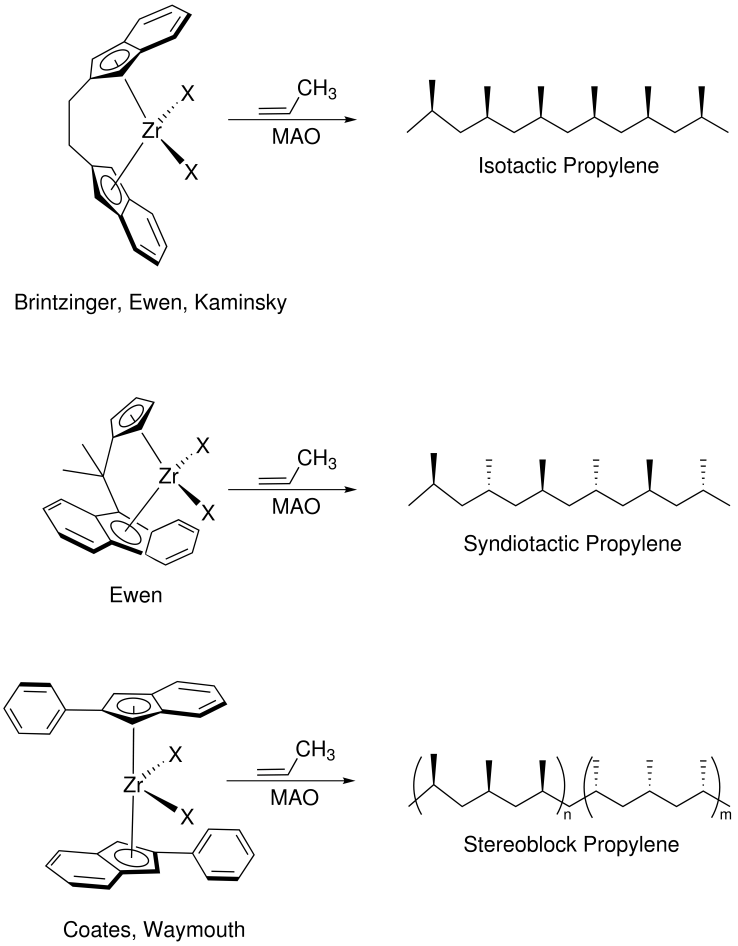

Figure 1.13: Catalysts for stereospecific propene polymerisation

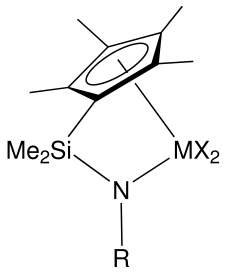

Figure 1.14: The general structure for the CpA catalyst

1.14. The first route is the addition of both the silyl bridge and the amine to the Cp fragment. There are purification problems with this route however. Even when an excess of silyl chloride is added to the reaction, there is Cp'$_2$SiMe$_2$ in the product. It is often necessary to sublime Cp'SiMe$_2$Cl by distillation or sublimation. The loss of Cp'SiMe$_2$Cl is also observed, as the reaction rarely occurs in quantitative yield.

Polyethene is grouped into one of three categories. Low-density polyethene, or LDPE, is

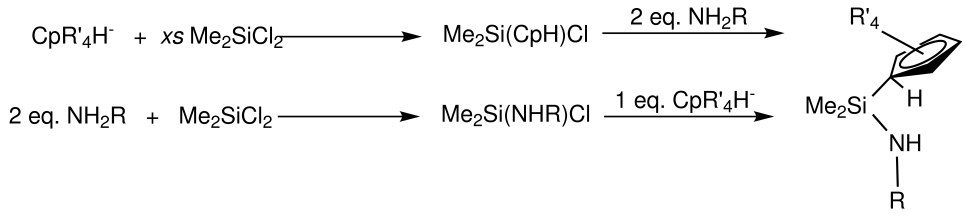

Scheme 1.14: Synthetic routes to the CpA ligand

produced in a high-pressure and temperature environment. The occurence of side-branching in this polymer significantly increases the ability to process it. High-density polyethene, or HDPE, has poor processability but increased strength, as it is a linear polymer. Polyethene produced by CpA catalysts is unique in that it possesses the properties of two types of polyethene. Linear low-density polyethene, or LLDPE, is produced when low levels of α olefins are integrated into the backbone of HDPE.[75]

CpA catalysts are unique in their ability to successfully copolymerise various olefins. These catalysts have copolymerised ethene and various long chain α-olefins to produce polymers with both LLDPE and LDPE characteristics.[86,87,89,96] These polymers combine the strength and toughness of LLDPE and the increased processability of LDPE. The copolymerisation of ethene and styrene in ratios of up to 50% has also been observed with the use of CpA catalysts. This successful copolymerisation is important since traditional Ziegler-Natta catalysts, such as bis-Cp metallocenes, typically incorporate less than one percent styrene in ethene.[106–110]

1.2 Non-metallocene olefin polymerisation catalysts

The successful polymerisation of olefins using group IV metallocene and mono-Cp derivatives prompted other transition metal systems to be explored for their use in catalysis. Other heterogenous and homogenous polymerisation systems have been successful with late transition metals such as iron and nickel. A variety of ligands with different structural and electronic properties have also been explored, and will be discussed in the following sections.

1.2.1 Alternative group IV polymerisation catalysts

Many alternative non-metallocene group IV complexes were examined for their use as olefin polymerisation catalysts. A few examples of such catalysts will be discussed in this section. Chelating diamide complexes of titanium were examined by Scollard and McConville.[111,112] MAO was used to activate the precatalysts, $[RN(CH_2)_3NR]TiMe_2$ where R is either 2,6-$^{i}PR_2C_6H_3$ or 2,6-$Me_2C_6H_3$. These catalysts were very efficient for the polymerisation of 1-hexene. There was

some chain transfer to the aluminum atom, causing the chain to subsequently terminate. The cocatalyst $B(C_6F_5)_3$ was chosen to replace MAO in order to stop chain termination. When the titanium precatalyst and the cocatalyst $B(C_6F_5)_3$ were added in equimolar amounts, polymerisation of α-olefins occurred. These catalysts are shown in Scheme 1.15 and were the first examples to polymerise α-olefins at room temperature.

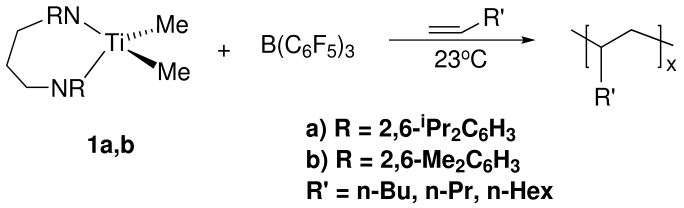

Scheme 1.15: Diamide catalyst used for olefin polymerisation

Spectroscopic analysis of the catalytically active species was attempted, but was unsuccessful as the catalyst system was extremely reactive with chlorinated solvents and insoluble in aromatic solvents. The polymers generated by these systems were high in molecular weight, with a small molecular weight distribution. Higher molecular weight polymers were observed when the polymerisation reactions were performed using $CHCl_2$, possibly due to the polarity of charge separation between the cationic titanium pre-catalyst, and the anionic cocatalyst.[113,114] When the polymerisation reactions were performed in toluene, a tenfold decrease in activity and subsequently molecular weight of the polymer was seen, suggesting that the only some of the catalyst is active in toluene. Competitive binding between toluene and polymer is possible, as the catalyst is assumed at be a cationic alkyl complex. This competition is unsurprising given the low coordination number of these complexes. Chain termination or transfer is not observed in these catalytic systems.

Other group IV catalysts have been synthesised to emulate the electronic and structural properties of metallocene catalysts. Imido ligands $[NR]^{2-}$ are isolable with Cp, and have been used in the design of new catalysts.[115–118] The imido complexes, $Ti(N^tBu)(Me_3[_9]aneN_3)R_2$, where R = Me or CH_2SiMe_3, $CH_2{}^tBu$ or CH_2Ph were synthesised by Mountford for their use as pre-catalysts in order to study the polymerisation of ethene. The synthesis of these complexes is shown in Scheme 1.16.[119]

The cocatalyst $[Ph_3C][B(C_6F_5)_4]$, which was chosen as a methide ion abstraction reagent, was reacted with the titanium alkyls to produce *tert*-butyl imido cations for polymerisation. The ethene polymerisation experiments were performed in toluene with initiation taking place at room temperature. In the the catalytic systems, the steric bulk of the ligands was directly proportional to the activity of the catalyst. The catalysts with the largest amount of steric bulk produced the

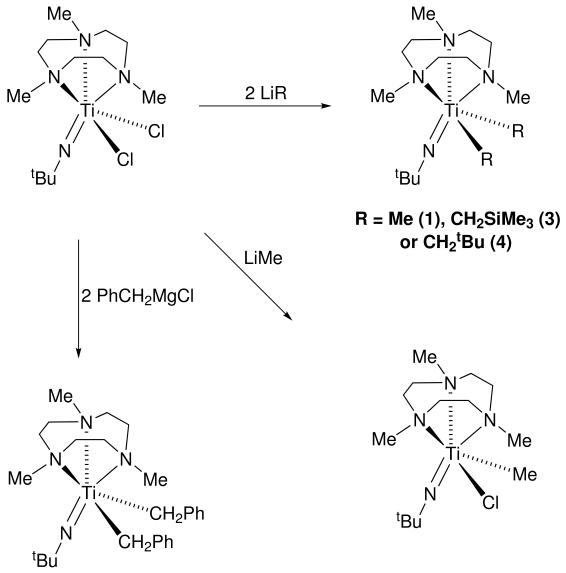

Scheme 1.16: Synthesis of *tert*-Butyl imido titanium alkyl compounds

highest polymerisation activity. The polyethene produced possesed a polydispersity index value of 2.0, which is consistent with single-site catalysts. The catalyst, $Ti(N^tBu)(Me_3[_9]aneN_3)R_2$, where R = Me produced approximately 1750 polyethene chains per metal centre. The imido group in these catalysts were found to have two functions. The first function is to stabilise the dialkyl precatalyst to degradation, while the second function is to inhibit the formation of catalytically inactive heterobimetallic or homobimetallic complexes.[119]

1.2.2 Shell Higher Olefin Process

Most late transition metal catalysts are only able to dimerise or oligomerise alkenes. Chain growth is terminated due to β-hydride elimination. A system which exemplifies this behavior is $NiCl_2$/$EtAlCl_2$, where a nickel hydride is thought to be the active catalyst. Ethene is inserted, and a ethyl complex is produced. This complex can insert into another ethene or can β-eliminate. If insertion takes place, the cycle begins again, i.e. the complex can continue insertion or β-eliminate. The chain length therefore depends on the rate of insertion versus the rate of β-elimination.[120,121]

Catalysts synthesised by Keim *et. al* were among the first successful late transition metal oligomerisation catalysts.[122,123] These heterogenous nickel based catalysts were used to oligomerise ethene, producing alkenes of chain length C_6-C_{20}. It is obvious in these systems that the rate of insertion is faster than the rate of β-elimination. This process is known as the Shell higher olefins process, or SHOP, and is shown in Scheme 1.17.

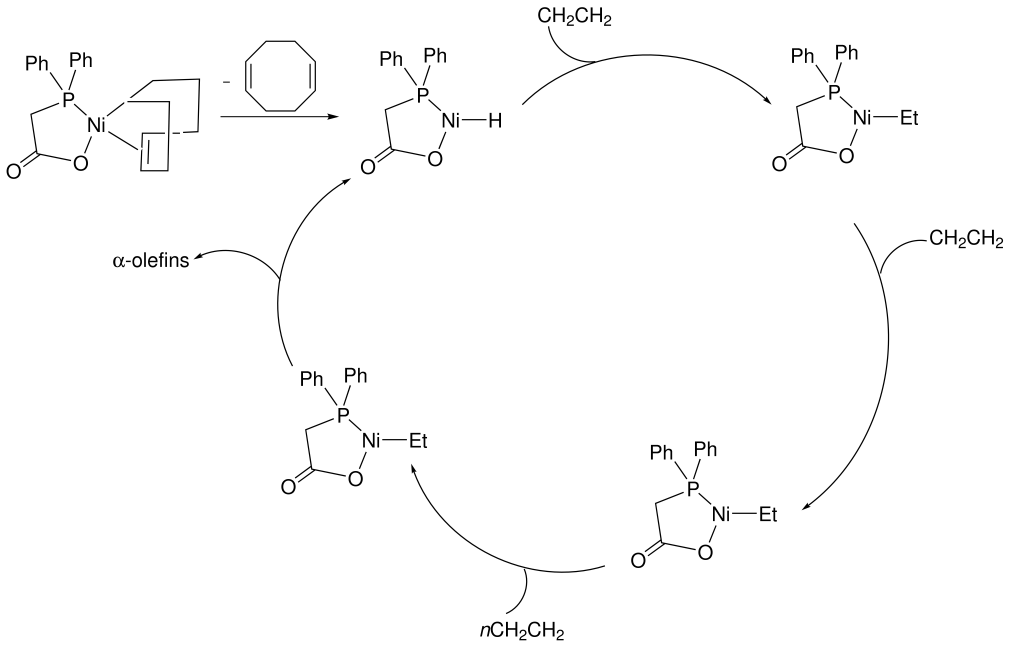

Scheme 1.17: The Shell Higher Olefin Process

1.2.3 Brookhart's systems

Brookhart also began to look at the reactivity of late transition metals as catalysts.[124] These catalysts were Ni(II) or Pd(II) with diimine ligands. These late transition metal catalysts are shown in Figure 1.15. When the Pd catalysts were reacted with ethene, propene, or 1-hexene, high molecular weight polymers are produced. The polyethene produced displays severe branching in the ^{1}H and ^{13}C spectroscopic data. This amorphous polyethene was found to be a new form of polyethene, as it was far more branched than traditonal low-density polyethene. The Ni catalysts were activated with MAO and reacted with ethene to produce highly linear to moderately branched polyethenes. The degree of branching in the polymer is a function of temperature and pressure. When higher pressure is applied, the polymer produced is linear, while at higher temperatures, the degree of branching increases. Linear polymer is produced at low temperatures, due to the preference of the position of the aryl rings. If these rings block the position of the incoming ethene, no branching can occur, and only linear polymer can be produced.

Iron catalysts were also investigated for their use in ethene oligomerisation to produce linear α-olefins.[125] The pyridinebisimine ligand used for catalysis are shown in Figure 1.16. The pyridinebisimine ligands used were chosen to reduce the steric bulk in order to increase the activity of the catalyst. These catalysts performed better than the previous tridentate pyridinebisimine ligands.[126,127] These catalysts were activated with modified MAO and were shown to oligomerise ethene to α-olefins. The turnover frequency of these catalysts was also dependent on temperature

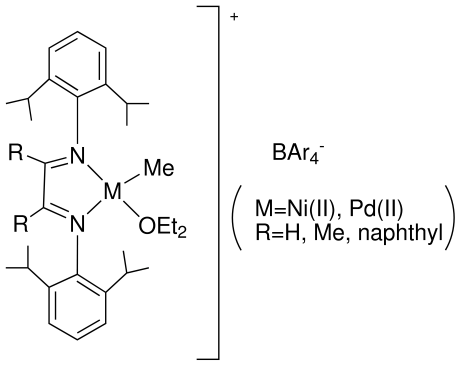

Figure 1.15: Nickel and palladium based catalysts synthesised by Brookhart

of the reaction mixture, and pressure of the system. The activity of these catalysts increased with pressure and temperature.

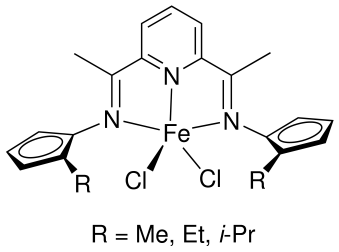

Figure 1.16: Iron-based Brookhart/Gibson catalyst

1.3 Mechanistic aspects of Ziegler-Natta catalysts

The stereoregularity of the polymer produced by both heterogenous and homogenous Ziegler-Natta catalysts make them invaluable to olefin polymerisation. The mechanism that demonstrates polymer chain growth and subsequent stereoregulation of this chain is still under speculation. There are several models which describe the mechanistic studies of Ziegler-Natta catalysis. The most widely accepted models are the Cossée-Arlman mechanism and the modified Green-Rooney mechanism.

1.3.1 Cossée-Arlman mechanism

Metal-mediated Ziegler-Natta systems have four key steps in their mechanism. The first step is the alkylation of a surface titanium ion. Abstraction of a group from the titanium centre occurs at the same time. The Lewis acid used in this mechanism is either $AlEt_3$ or $AlEt_2Cl$. The abstraction takes place *cis* to the alkyl or polymer chain. Formation of the active site is shown in

Figure 1.17. The propene then coordinates into the vacant site, inserting into the Ti-C bond *via* a metallocyclobutane intermediate. The alkyl chain then migrates forming a new metal-alkyl bond, and the polymer chain begins to grow. A new coordination site is formed *cis* to the alkyl or polymer chain, and polymer binding begins again. This rationale behind this mechanism is dependent on the vacant site being *cis* to the alkyl chain.

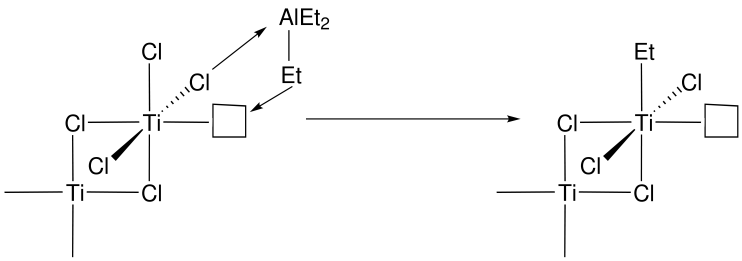

Figure 1.17: Formation of the active site in Ziegler-Natta catalysis

Steric interactions between the monomer and polymer influence the stereochemistry of the polymer. The use of electron poor titanium ions are significant in Ziegler-Natta catalysis. Isotactic polymer is produced when α-$TiCl_3$, which has a lattice structure that is layered, is used as the catalyst. This lattice consists of a close-packed array of Cl^- ions, and Ti^{3+} ions that occupy two-thirds of the octahedral holes in the lattice. The titanium ions on the inside of the lattice are therefore octahedrally coordinated, while the titanium ions at the surface of the lattice are not. Insertion into the titanium-alkyl and coordination of the subsequent ion brings the reactants close enough together so that a ligand transfer reaction occurs. Stereochemical control is influenced by the methyl group on the α-olefin *anti* to the growing polymer chain. The incoming alkyl group will therefore always be *anti* to the chain, producing stereochemically controlled polymer.[19,20,128–131] The Cossée-Arlman mechanism is shown in Scheme 1.18.

1.3.2 Modified Green-Rooney mechanism

As the Cossée-Arlman mechanism is based on interactions at the surface of the metal, this mechanism is only considered for the use of heterogenous catalysts. A new mechanism had to be found that would make sense for both homogenous and heterogenous catalysts. The reason for retention of the configuration of the polymer with respect to the vacant site is not clear from the Cossée-Arlman mechanism. A new mechanism, formulated by Green and Rooney, addresses the retention of polymer configuration.

The term agostic bond was formulated by Green *et al.* to describe the interaction between a C−H bond and a transition metal centre to form a two-electron three-centre bond. This interac-

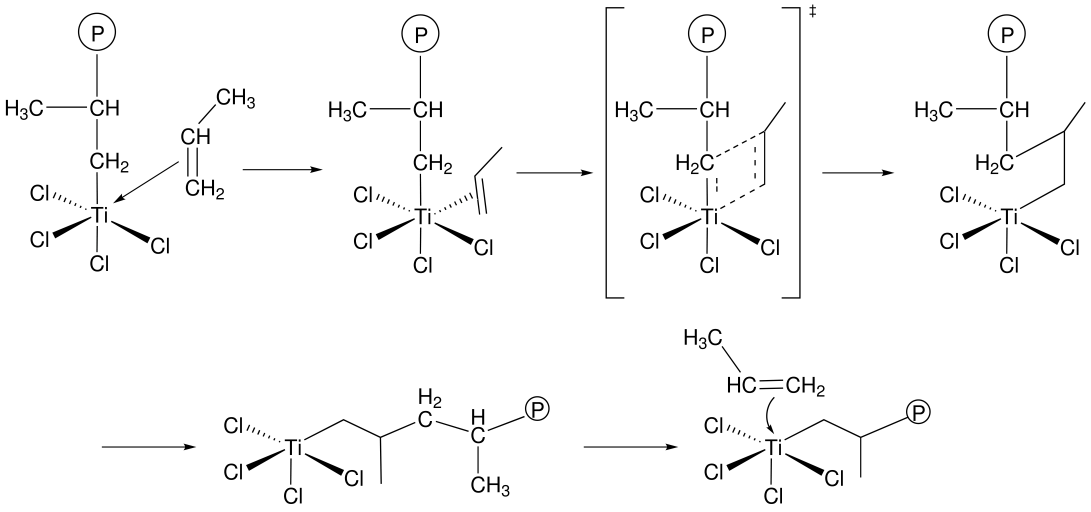

Scheme 1.18: Cossée-Arlman mechanism

tion is surprising, as C−H bonds were thought to be inert. "*The word agostic is used to refer specifically to situations in which a hydrogen atom is covalently bonded simultaneously to both a carbon atom and to a transition metal atom.*"[132] An example of an agostic interaction is shown in Figure 1.18. In the complex $[(Me_2PCH_2CH_2PMe_2)TiEtCl_3]$, the Ti−C−C angle is 86.3°.[133,134] In other reported 16 to 18 electron transition methyl or ethyl complexes, the average M−C−C bond angle is in the range of 108-123°.[135–137] The bond angle of 86.3° indicates severe distortion of the methyl group. This group is therefore being drawn towards the titanium, giving proof of an agostic interaction. One of the hydrogens on the ethyl moiety is also close to the titanium centre, with a bond length of 2.29 Å. The bond lengths and angles resolved by the molecular structure of $[(Me_2PCH_2CH_2PMe_2)TiEtCl_3]$ demonstrate that there is an agostic interaction between the titanium and C−H of the methyl group. Agostic interactions increase the electron count of the complex by 2 electrons, as they are counted as an L ligand.[138] These interactions are therefore only observed in transition metal complexes with a lower electron count as the donation of the C-H bond to the transition metal centre alleviates low electron density seen in early transition metal complexes.

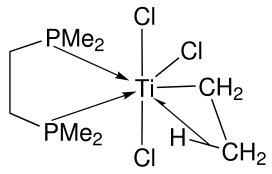

Figure 1.18: Green's $[(Me_2PCH_2CH_2PMe_2)TiEtCl_3]$

The Cossée-Arlman mechanism proposed no direct involvement of the C−H bonds of the

alkyl chains in the formation of C−C bonds. Green therefore looked to agostic interactions for the mechanism of Ziegler-Natta catalysis. It was hypothesised that the α-H of the growing alkyl side-chain in the mechanism could form an agostic interaction with a C−H bond forming an agostic C−H−Ti bridge. The formation of the C−C bond would therefore be more likely as the other atoms on the α-carbon would move away in preparation of the approaching carbon of the olefin. The agostic interaction is also more likely as the steric inhibition of the C−C bond forming step would be reduced by the formation of an α-bridging hydrogen of the alkyl group. The Ti−H−C agostic interaction could also provide a reason for the incoming olefin to be controlled by the stereochemistry of the alkyl group.[132]

There are two problems with the original Green-Rooney mechanism. It was identified that this mechanism would not work with most active catalysts, as they are usually d^0, and can not accomodate the reductive elimination step required. The metallocycle observed in this mechanism could also eliminate to the second Ti−C bond. This step would produce a branched polymer, while linear polymers are most often produced. The mechanism was modified to include an agostic C−H interaction to replace the alkylidene hydride.[134] The modified Green-Rooney mechanism is shown in Scheme 1.19.

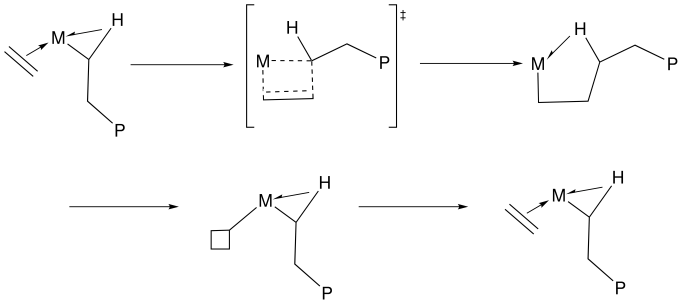

Scheme 1.19: The modified Green-Rooney mechanism

Chapter 2

Synthesis and reactivity of the *tris*(amido)titanium platform

2.1 Ligand Syntheses

2.1.1 Synthesis of diphenylamido lithium (dpaLi) (1)

Deprotonation of the diphenylamine ligand is accomplished in one step: 1.2 equivalents of t-butyllithium are added to 1.0 equivalent of diphenylamine in hexane, yielding the lithium amide salt in approximately 95-98% yield. Diphenylamine is soluble in hexane, while its lithium salt is not. The salt is collected on the frit when the reaction mixture is filtered. The product is then dried under reduced pressure producing a very fine white powder, that is extremely water and oxygen sensitive. If oxygen is introduced in small concentrations, the salt begins to turn light green, then dark green with the addition of more oxygen. The structure and purity of (1) was confirmed by NMR spectroscopy. The synthesis of (1) is shown in Scheme 2.1.

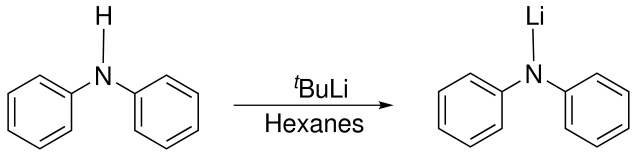

Scheme 2.1: The synthesis of dpaLi (1)

The ^{7}Li NMR spectrum of this compound was also analysed as is shown below in Figure 2.1. This spectrum shows one lithium resonance at 2.2 ppm, indicating there is only one magnetic environment present on this timescale. The ^{6}Li spectrum of diphenylamide found in the literature exhibits a resonance at 0.25 ppm. The literature also confirms that diphenylamide is dimeric in ethereal solutions.[139,140]

The ^{13}C NMR resonances of (1) are shifted slightly downfield to the resonances of dpaH. The resonances at 124.6 ppm and 130.4 ppm are assigned to the *ortho* and *meta* carbons. The resonance at 127.0 ppm is assigned to the *para* carbon, and the resonance at 151.2 ppm is assigned to the *ipso* carbon. The carbon assignments are collated in Table 2.1.

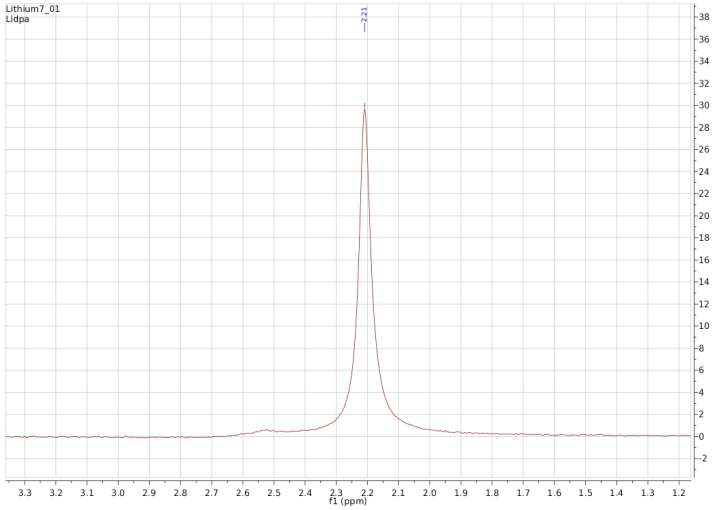

Figure 2.1: The ^{7}Li spectrum of (1)

Carbon Assignment	δ/ppm
ortho	112.6
meta	119.7
para	129.0
ipso	159.9

Table 2.1: ^{13}C NMR spectral resonances of (1)

This compound is insoluble in hydrocarbon solvents, extremely soluble in ethereal solvents, and slightly soluble in toluene and benzene. Electron Impact mass spectrometry found the parent ion for this complex at 168 m/z. Elemental analysis confirmed the purity of this product.

2.1.2 Synthesis of *tris*(diphenylamido)titanium chloride ((dpa)$_3$TiCl) (2)

The reaction of three molar equivalents of (1) with one equivalent of $TiCl_4$·2THF yields (2) in approximately 80% yield. Both reactants are slurried in toluene. The dpaLi slurry is added dropwise to the $TiCl_4$·2THF slurry. When the first drop is added, the reaction mixture begins to turn dark-red, and the reaction is essentially complete after twelve hours. The reaction mixture is filtered,

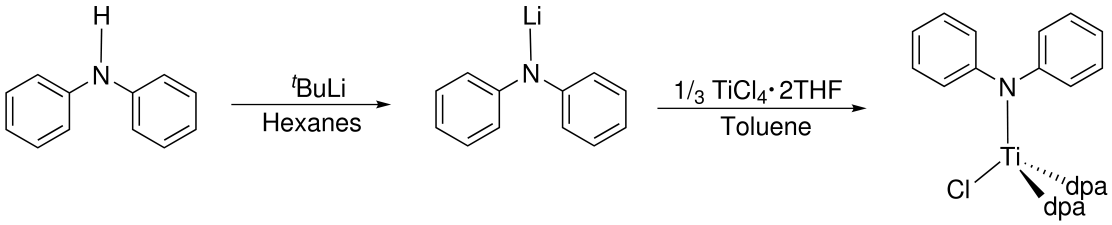

Scheme 2.2: The synthesis of $(dpa)_3TiCl$ (2)

and recrystallized from a mixture of toluene and hexane, at which time drying under reduced pressure yields a dark-red powder. The synthesis of (2) is shown in Scheme 2.2.

The stability of (2) is poor. This compound begins to decompose at room temperature overnight in an argon-filled glove box. This complex is stable for a short time at -40°C. This complex is also very water sensitive. Similar to compound (1), complex (2) decomposes to a dark green colour upon oxygenolysis.

The ^{1}H spectrum of (2) has resonances in the conventional aromatic region, with extensive coupling amongst aromatic protons. Coupling between the protons on the ring could give various spectroscopic results, depending on the equivalence of the hydrogen atoms. Figure 2.2 shows the H,H couplings that take place in the ligand, diphenylamine, where X = nitrogen.[141]

The obvious coupling occurs between H_a and H_b, which should produce a doublet. H_b, however is coupled to both H_a and H_c, which should produce a doublet of doublets. H_c is also coupled to H_b, which should produce a doublet. There are also multiple bond couplings that can occur. H_a can couple through two bonds to H_c, producing a doublet of doublets. The various coupling amongst these aromatic protons, produces various multiplets in the aromatic region of a ^{1}H spectrum. Due to extensive coupling among aromatic protons in ligands such as diphenylamine, assignment of the aromatic region in a ^{1}H spectrum can be difficult.

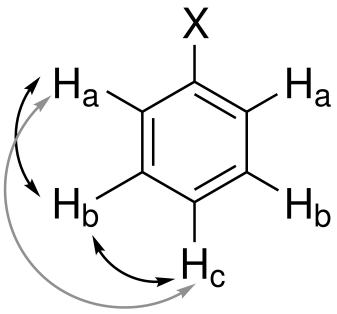

Figure 2.2: Example of H,H couplings in aromatic ligands

Integration of the aromatic resonances gives a 2:1:2 ratio, which is resolved as *ortho*:*para*:*meta*.

The resonances in the ^{1}H spectrum integrate to 2:1:2. The resonance at 7.1 ppm is a multiplet, and is assigned to the *meta* protons. This resonance should be a doublet of doublets, but is seen in the spectrum as a multiplet due to the roofing effect. "*The roofing effect is illustrated in spectroscopic data when the intensities of the lines in a strongly coupled multiplet tilt upwards from the multiplet of the coupled spin, making a roof.*"[142] These resonances will be referred to as multiplets, as they are observed to be so in the ^{1}H spectrum. The resonance at 6.9 ppm is also a triplet, and is assigned to the *para* protons. The resonance at 6.8 ppm is a doublet and is assigned to the *ortho* protons. The aromatic region of $(dpa)_3TiCl$ is shown in A.4. Table 2.2 contains the ^{1}H data for (2).

Proton Assignment	δ/ppm	Coupling Pattern	H-H coupling constant/Hz
ortho	6.8	doublet	7.9
meta	7.1	multiplet	7.7
para	6.9	triplet	7.3

Table 2.2: ^{1}H NMR spectral resonances of (2)

The ^{13}C spectrum of (2) is straightforward to assign when looking at the Heteroatom Single Quantum Coherence spectrum, abbreviated as HSQC. This spectrum is shown in Figure 2.3. The quaternary carbon is found at 151.1 ppm, shifted due to its close proximity to the nitrogen atom. The resonances at 130.3 and 124.6 ppm are assigned the *ortho* and *meta* carbons on the ring, easily seen as they are the same intensity. The *ortho* carbon is also shifted downfield due to its closer proximity to the nitrogen atom. The resonance at 127.0 ppm is assigned to the *para* carbon. The ^{13}C resonances are collated in Table 2.3.

The solubility of (2) is very high. It is soluble in all hydrocarbon solvents and ethers. Electron impact mass spectrometry also confirmed the purity of this product. The parent ion was found at 587 m/z. Elemental analysis confirmed the purity of this compound.

Carbon Assignment	δ/ppm
ortho	124.6
meta	130.3
para	127.0
ipso	151.1

Table 2.3: ^{13}C NMR spectral resonances of (2)

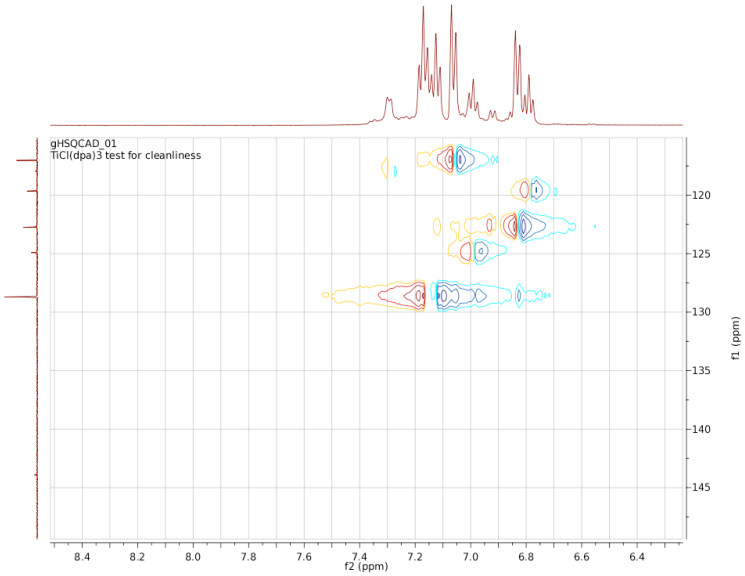

Figure 2.3: The HSQC spectrum of (2)

2.1.3 Synthesis of di-*p*-tolylamido lithium (dptaLi) (3)

In order to carry out further NMR spectroscopic studies on subsequent compounds, a new amido ligand with reduced coupling on the aromatic rings had to be chosen. An aromatic ring system with reduced coupling would provide for easier resonance assignment and coupling constants. NMR spectroscopic data that is easily interpreted on the starting material would also assist in the product assignment of further reactions. Di-*p*-tolylamine, or dptaH, was chosen as the new ligand. The *para* tolyl group breaks up the coupling in the ring, producing two doublets in the aromatic region, and a methyl group in the aliphatic region. The synthesis of compound (3) is shown in 2.3.

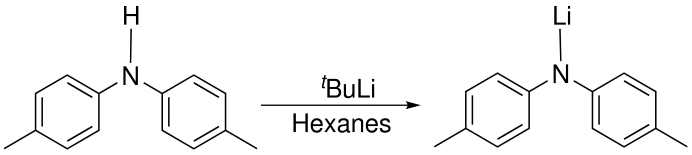

Scheme 2.3: The synthesis of dptaLi (3)

The synthesis of (3) is accomplished in the same manner as (1). The lithium salt, (3) is yielded in 95-98%. Di-*p*-tolylamine shows the same solubility as diphenylamine. This lithium salt is a very fine, cream-coloured powder. (3) is also extremely water and oxygen sensitive, turning green with the addition of oxygen. This compound also shows similar solubility to (1).

The structure and purity of (3) was confirmed by ^{1}H NMR spectroscopy in d_8-THF. The aromatic region of this compound is simple yet surprising. This region contains one doublet at 6.5

ppm. Before the deprotonation of dpta, the aromatic region contains two doublets. When (3) is used to synthesize $(dpta)_3TiCl$, the two doublets return to the spectrum. Since the number of doublets is reduced, there must be fluxionality of one or both of the rings when di-*p*-tolylamine is deprotonated. "*Fluxional molecules are molecules that undergo dynamics such that some or all of their atoms interchange between symmetry equivalent positions.*"[142] Due to fluxionality, protons on the *ortho* and *meta* positions on the ring are inequivalent. Previous NMR studies[139,140] have shown that, unsurprisingly, (1) is clustered or dimeric in ethereal solution. There is also a singlet at 2.0 ppm for the methyl group on the rings. The ^1H spectrum is shown in Figure A.2.

The ^{13}C NMR spectroscopic resonances of this compound are at 156.8 ppm for the *ipso* carbon bound to the nitrogen, 118.4 ppm for the *ortho* carbons, 128.5 ppm for the *meta* carbons, and 19.7 ppm for the methyl group bound to the *para* carbon on the ring. Even after increasing the number of scans significantly, there is not a signal shown for the quaternary carbon bound to the methyl group. Electron impact mass spectrometry of this compound also confirmed the purity of this product. The parent ion was found at 196 m/z. The ^{13}C data are collated below in Table 2.4.

Carbon Assignment	δ/ppm
ortho	118.4
meta	128.5
ipso	156.8
para methyl	19.7

Table 2.4: ^{13}C NMR spectral resonances of (3)

2.1.4 Synthesis of *tris*(di-*p*-tolylamido)titanium chloride ($(dpta)_3TiCl$) (4)

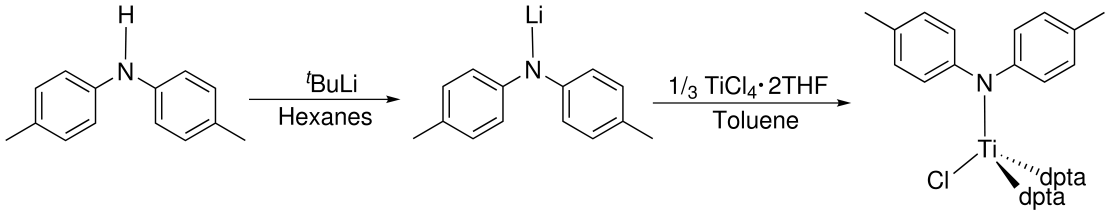

Scheme 2.4: The synthesis of $(dpta)_3TiCl$ (4)

The synthesis of (4) is achieved in the same way as (2). The reaction of three molar equivalents of (3) with one equivalent of $TiCl_4{\cdot}2THF$ yields (4) in approximately 70% yield. The reaction mixture is recrystallized from a mixture of toluene and hexane, and produces a bright red powder.

The synthesis of (4) is shown in Scheme 2.4.

The ^{1}H spectrum of (4) has resonances in the conventional aromatic region, but is much easier to interpret than the spectrum of (2). The presence of a methyl group on the *para*-carbon produces a very straight-forward spectrum. Due to now minimized coupling on the aromatic rings, there are two doublets for the *ortho* and *meta* protons, and one isolated singlet for the methyl on the *para* carbon. The resonances integrate to 2:2:3. Since the *ortho* and *meta* protons are doublets, it is impossible to assign these protons without two-dimensional spectra. The HSQC spectrum indicates which carbon is assigned to which proton, but does not indicate which doublet is assigned the *ortho* protons, and which doublet is assigned the *meta* protons. The Heteronuclear Multiple Bond Correlation spectrum, or HMBC, which shows through bond coupling was then consulted. This spectrum makes the assignment straightforward. The doublet at 6.8 ppm is assigned to the *meta* protons. The doublet at 7.0 ppm is therefore assigned to the *ortho* protons, as there is no other coupling. The singlet at 1.9 ppm is assigned to the protons of the methyl group on the *para* carbon. The HMBC spectrum is shown in Scheme 2.4. The spectrum of (4) is much easier to assign than (2), and is shown in Figure A.6. The resonances are collated in Table 2.5.

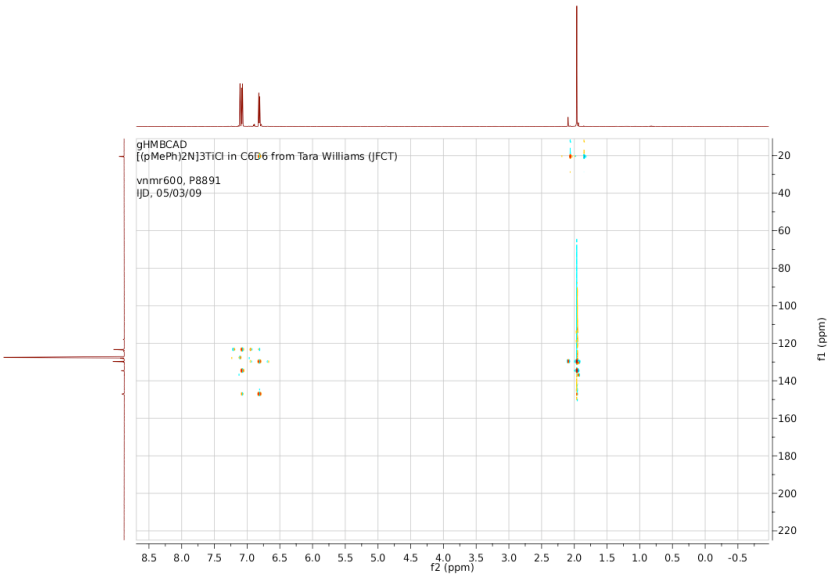

Figure 2.4: The HMBC spectrum of (4)

The ^{13}C spectrum of (4) is also straightforward to assign, when looking at the HSQC spectrum, which is shown in Figure 2.5. The resonance at 147.0 ppm is assigned to the *ipso* carbon attached to the nitrogen. The resonances at 129.8 ppm and 123.5 ppm are assigned to the *meta* and *ortho* carbons on the ring, easily identified as the resonances are in a 1:1 ratio. The the resonance at 134.7 ppm is assigned to *ipso* carbon bound to the methyl, and the resonance at 20.2 ppm is the carbon of the methyl group. These resonances are collated in Table 2.6.

Proton Assignment	δ/ppm	Coupling Pattern	H-H coupling constant/Hz
meta	6.8	doublet	8.1
ortho	7.0	doublet	8.3
para methyl	1.9	singlet	-

Table 2.5: ^{1}H NMR spectral resonances of (4)

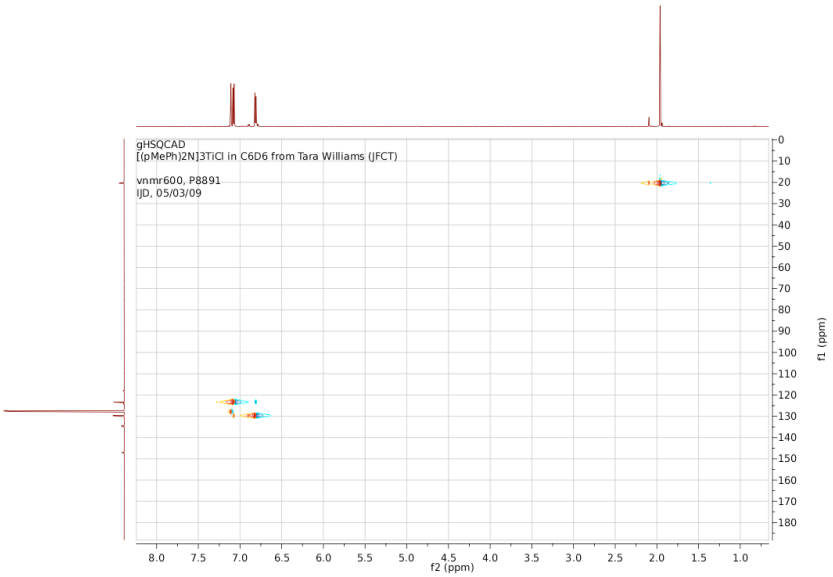

Figure 2.5: The HSQC spectrum of (4)

Carbon Assignment	δ/ppm
ortho	129.8
meta	123.5
N-ipso	147.0
C-ipso	134.7
para methyl	20.2

Table 2.6: ^{13}C NMR spectral resonances of (4)

The solubility of (4) is very high. This compound is soluble in all hydrocarbon solvents, THF, and ethers. Electron impact mass spectrometry also confirmed the parent ion for this compound at 673 m/z. The purity of this compound was confirmed by elemental analysis.

2.1.5 Synthesis of *tris*(diphenylamido)titanium methyl ($(dpa)_3TiMe$) (5)

Treatment of (2) with one equivalent of LiMe, slurried in toluene with a few drops of Et_2O added to increase the solubility, provides a route to (5). A toluene slurry of (2) is prepared, at which time both of these reactants are placed in the -40°C freezer for at least an hour. After an hour, the LiMe/toluene/Et_2O mixture is added to the $(dpa)_3TiCl$/toluene mixture. The $(dpa)_3TiCl$ solution is dark red in colour before addition of LiMe. After addition, the solution is a dark orange. The mixture is allowed to warm to room temperature while being stirred for a period of three hours. The solution is then filtered through a fine frit to remove any LiCl. The dark orange solution is then concentrated to half its volume, at which time an equal amount of hexane is added to the solution. The solution is put in the -40°C freezer overnight, at which time, a bright orange microcrystalline powder precipitates out of solution. The solution is then filtered, and the product is formed in approximately 70% yield. The synthesis of (5) is shown in Scheme 2.5.

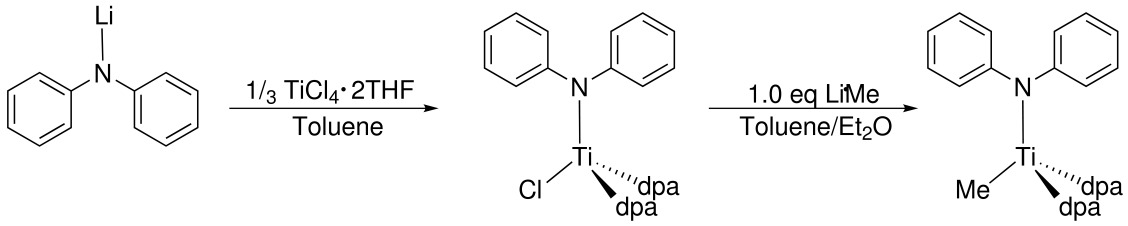

Scheme 2.5: The synthesis of $(dpa)_3TiMe$ (5)

As expected, the ^1H spectrum of (5) is very similar to the ^1H spectrum of (2). The sample of (5) was dissolved in d_8-toluene for solubility purposes. The presence of toluene resonances in the aromatic region of the spectrum do not affect the assignments however. The doublet at 7.6 ppm is assigned to the *ortho* protons. The triplet at 6.9 ppm is assigned to the *meta* protons are assigned. The triplet found at 6.8 ppm is assigned to the *para* protons. The methyl group bound to the titanium is assigned to the resonance at 0.4 ppm. The resonance assignments are collated in Table 2.7.

Proton Assignment	δ/ppm	Coupling Pattern	H-H coupling constant/Hz
ortho	7.1	doublet	7.5
meta	7.0	triplet	7.7
para	6.8	triplet	7.3
methyl	0.4	singlet	-

Table 2.7: ^1H NMR spectral resonances of (5)

The carbon spectrum is easy to assign when the HSQC spectrum is analysed. The HSQC spectrum is shown in Figure 2.6. The carbon assignments are as follows, and are collated in Table 2.8. The resonance at 123.6 ppm is assigned to the *ortho* carbons. The resonance at 129.5 ppm is assigned to the *meta* carbons. The *para* carbon was harder to locate in the HSQC spectrum because this resonance is very close to the toluene resonance. It is assigned to the resonance at 126.0 ppm. The resonance at 65.1 ppm is assigned to the *ipso* carbon, and the resonance at 65.1 ppm is assigned to the methyl carbon.

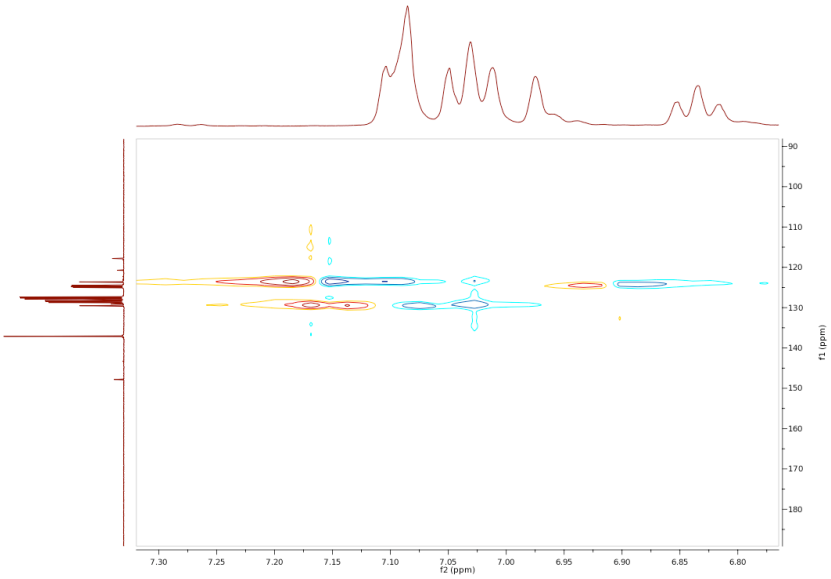

Figure 2.6: HSQC of (5)

Carbon Assignment	δ/ppm
ortho	123.6
meta	129.5
para	126.0
ipso	147.8
methyl	65.1

Table 2.8: ^{13}C NMR spectral resonances of (5)

The solubility of (5) shows a signficant change when the methyl group is coordinated to the titanium centre. This complex, $(dpa)_3TiMe$, is soluble in ethers, insoluble in hydrocarbon solvents, and sparingly soluble in toluene and benzene. The parent ion is for this compound is found at 553 m/z using Electron Impact mass spectrometry. Elemental analysis confirmed the purity of this

compound.

2.1.6 Synthesis of *tris*(di-*p*-tolylamido)titanium methyl ((dpta)$_3$TiMe) (6)

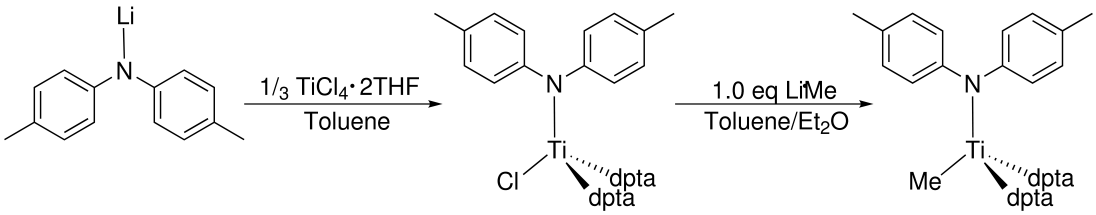

Scheme 2.6: The synthesis of (dpta)$_3$TiMe

The synthesis of (6) is achieved in the same way as (5). One molar equivalent of LiMe is reacted with (4), to produce (6) in approximately 60% yield. The product is recrystallized from a toluene/hexane mixture, at which time a dark orange microcrystalline powder is collected upon filtration of the solution. The synthesis of (6) is shown in Figure 2.6.

The ^{1}H spectrum of (6) is easily interpreted. In order to verify where the *ortho* and *meta* resonances are located, two-dimensional spectra were consulted. The HMBC spectrum, shown in Figure 2.7 shows that the *ortho* and *meta* resonances are in the same positions as in the (dpta)$_3$TiCl spectrum. The resonances at 7.2 ppm and 6.9 ppm are assigned to the *ortho* and *meta* protons. The resonance for protons on the *para* carbon is at 2.0 ppm. The resonance for the methyl group bound to the titanium is assigned to the singlet at 0.3 ppm. These resonance assignments are collated in 2.9.

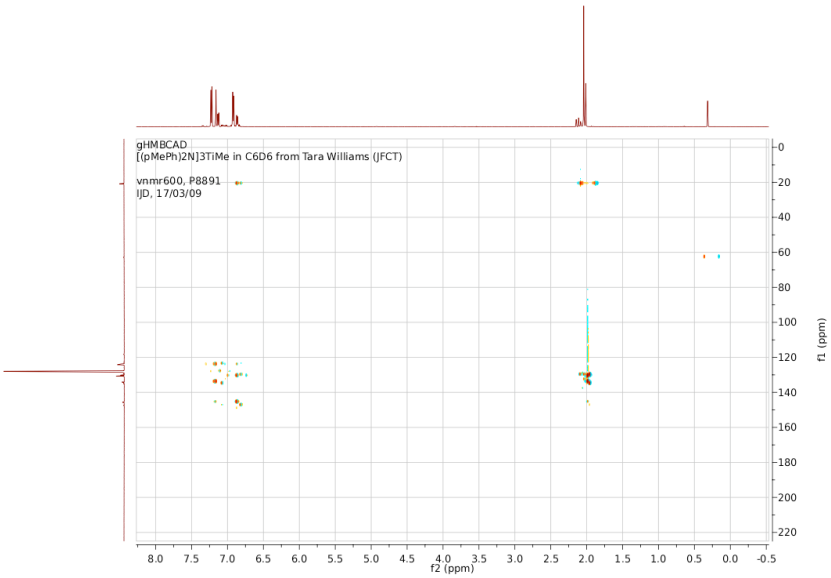

Figure 2.7: HMBC of (6)

Proton Assignment	δ/ppm	Coupling Pattern	H-H coupling constant/Hz
ortho	7.2	doublet	8.3
meta	6.9	doublet	8.1
para-methyl	2.0	singlet	-
methyl	0.3	singlet	-

Table 2.9: ^{1}H NMR spectral resonances of (6)

The HSQC spectrum makes assignment of the carbon straight-forward. This spectrum is shown in Figure 2.8, and the carbon assignments are collated in Table 2.10. The resonances at 130.5 ppm and 125.2 ppm are assigned to the *ortho* and *meta* carbons. The the resonance at 148.8 ppm is assigned to the *ipso* carbon bound to the nitrogen. The resonance at 134.1 ppm is assigned to the *ipso* carbon. The resonance at 20.8 ppm is assigned to the methyl carbon bound to the *para* carbon. The resonance at 62.7 ppm is assigned to the methyl group bound to the titanium.

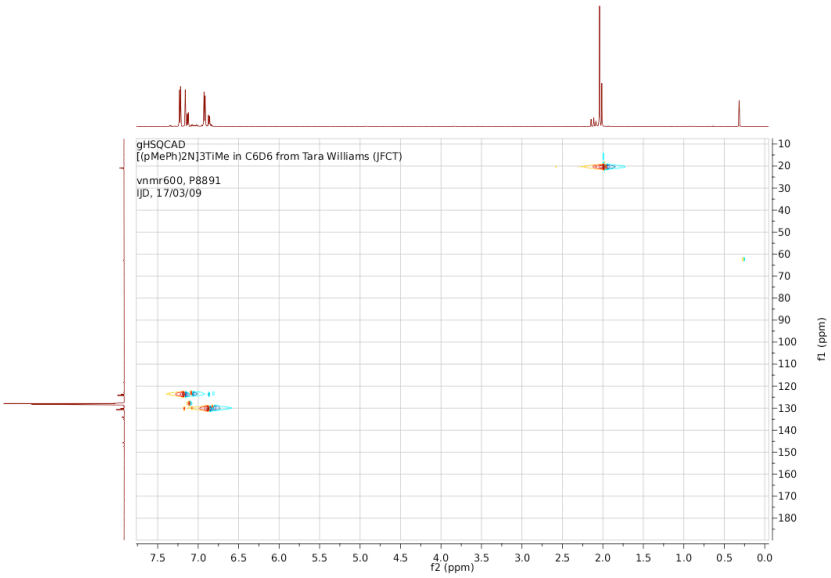

Figure 2.8: HSQC of (6)

The solubility of (6) is similar to the solubility of (5). This compound is soluble in ethers, insoluble in hydrocarbon solvents, and slightly soluble in toluene and benzene. The parent ion is found at 636 m/z using Electron Impact mass spectrometry. Elemental analysis confirm the purity of this product.

Carbon Assignment	δ/ppm
ortho	130.5
meta	125.2
N-ipso	148.8
C-ipso	134.1
para methyl	20.8
methyl	62.7

Table 2.10: ^{13}C NMR spectral resonances of (6)

2.1.7 Syntheses of $(dpa)_3TiMeB(C_6F_5)_3$) (7) and $(dpta)_3TiMeB(C_6F_5)_3$) (8)

Complexes (7) and (8) were synthesised for their possible use as polymerisation catalysts; one equivalent of $B(C_6F_5)_3$ was added to complexes (5) and (6). The use of $B(C_6F_5)_3$ as a cocatalyst in polymerisation is discussed in the first chapter. The precatalysts used by Marks[44] were dialkyl zirconocene complexes that were reacted with one equivalent of $B(C_6F_5)_3$ in order to abstract an alkyl group. The zirconium alkyl bond is sufficiently weakened, and insertion of an olefin occurs. Therefore, if the methyl group is abstracted from (5) or (6), the complexes become 12 electron systems, which should show activity as polymerisation catalysts. These complexes also contain a metal-alkyl bond, necessary for insertion of the olefin.

There are three possible products to illustrate how $B(C_6F_5)_3$ can bind to (5). These binding possibilities are shown in Scheme 2.7. The first binding mode, (a), is more likely for steric reasons. The diphenylamido groups should be sterically bulky enough to prevent the $B(C_6F_5)_3$ group from bonding to a diphenylamido ligand.

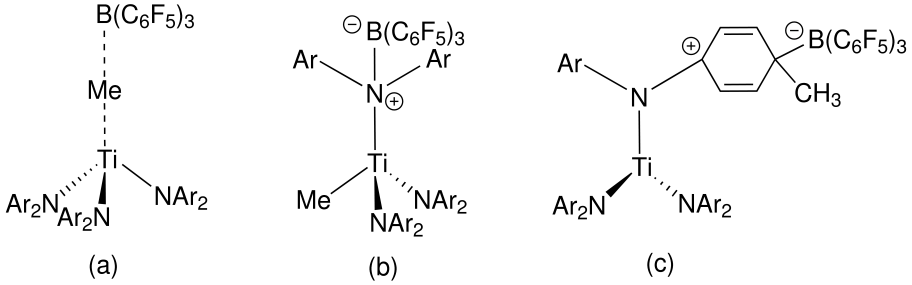

Scheme 2.7: The possible binding in (5) and (6)

It is easy to synthesise (7) and (8) *in situ*. Since these products are adducts, there should be no side products. One molar equivalent of $B(C_6F_5)_3$ in hexane is added to one molar equivalent

of either (5) or (6) in hexane. A small amount of benzene is added to the $B(C_6F_5)_3$ in order to increase the solubility. After the addition of $B(C_6F_5)_3$ is complete, the dark red solutions turn dark purple. These reactions are allowed to stir for a period of three hours, at which time the solvent was removed under reduced pressure, producing dark purple powders.

The methyl resonance is shifted in the ^1H spectrum from 0.4 ppm in (5) to 0.9 ppm in (7). This is a total shift of 0.5 ppm. This downfield shift is indicative for alkyl abstraction seen in the zirconocene complexes mentioned above. Marks[47] observed a chemical shift of between 0.08 ppm and 0.3 ppm in similar complexes. The direction of the shift is in the same sense to those observed by Marks in the zirconocene systems.

There is also a change in the ^{13}C spectra. The methyl resonance appears at 76.7 ppm in (7). This resonance is seen at 65.1 ppm in the spectrum for (5). These shifts are therefore more evidence for partial methyl abstraction, which would also support the binding seen in structure (a). In the ^1H spectrum of (8), the methyl resonance is found at 0.9 ppm, shifted from 0.3 ppm in the spectrum of (6). This is a downfield shift of 0.6 ppm. The ^{13}C resonance is found at 76.6 ppm for (8), shifted from 62.7 ppm in the spectrum of (6).

There are also differences observed in the aromatic region of ^1H spectrum of these compounds after the addition of $B(C_6F_5)_3$. In the ^1H spectrum of both (5) and (6), the resonances are relatively straightforward to assign. After addition of $B(C_6F_5)_3$, there are more resonances in the aromatic region, indicating that there is more coupling occurring in these compounds. There are no new resonances observed in the HSQC spectrum or COSY spectrum, however. There should only be a change observed in the aromatic region of the ^1H spectrum if there is direct contact occurring between the $B(C_6F_5)_3$ and the amido ligands. A stacked plot for each of these reactions is shown in Figure 2.9 and Figure 2.10.

The $(R_2N)_3TiMe{-}B(C_6F_5)_3$ adducts are soluble in hydrocarbon solvents and ethers. These products are very air and water sensitive. The dark purple powders degrade very quickly above 2.0 ppm of oxygen. The parent ions for these products were unable to be found due to their sensitivity in air. The samples decomposed before they could be analysed. Elemental analysis confirmed the purity of these products. ^{11}B, ^{19}F, and two-dimensional NMR spectra were also run for these products. X-Ray quality single crystals of these products have been grown, and are currently awaiting diffraction.

2.1.8 Synthesis of *tris*(diphenylamido titanium) $[(dpa)_3Ti]^+[B(C_6F_5)_4]^-$ (9)

Given the potential development of cationic character at titanium in the abstraction reaction between either $(dpa)_3TiMe$ or $(dpta)_3TiMe$ and $B(C_6F_5)_3$, full abstraction of the chloride should ensure

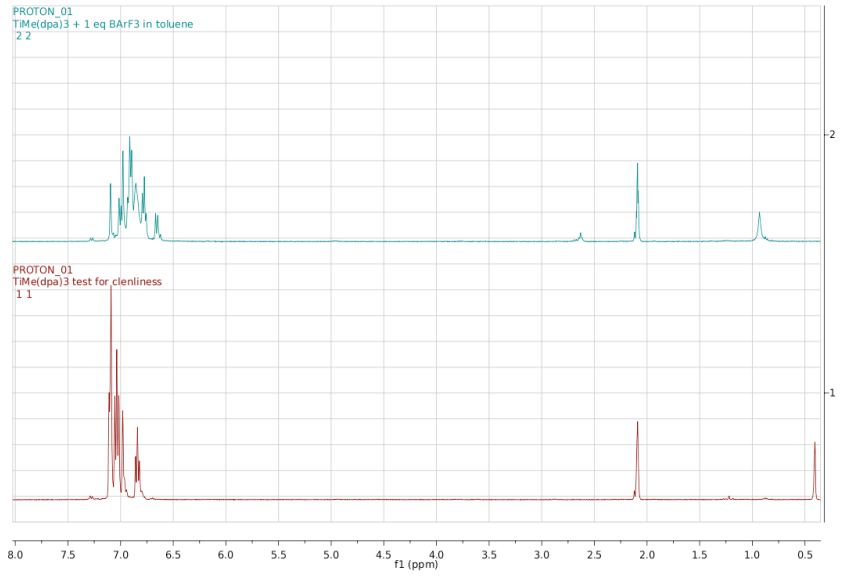

Figure 2.9: Stacked plot of the ^{1}H spectrum of (5) (below) and (5) + $B(C_6F_5)_3$ (above)

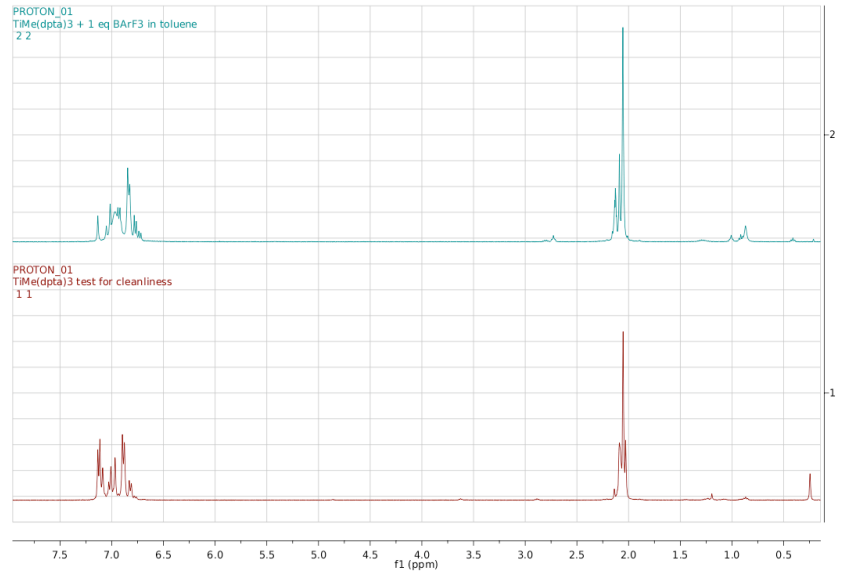

Figure 2.10: Stacked plot of the ^{1}H spectrum of (6) (below) and (6) + $B(C_6F_5)_3$ (above)

full development of the charge, resulting in the formation of a cationic titanium amido complex. Such a species would be a $[L_3X_3]^+$, or L_2X_4 system,[138] with 12 electrons. The synthesis of $[(dpa)_3Ti]^+[B(C_6F_5)_4]^-$ is shown in Scheme 2.8.

The cationic complex, (9), is synthesised by abstraction of Cl^- from (2) using $KB(C_6F_5)_4$. $KB(C_6F_5)_4$ is dissolved in benzene, and added to one equivalent of (2) in benzene. Upon addition, the solution turns from a dark red to a dark purple. The solution was stirred at room temperature for three hours, at which time it was allowed to settle. The solution was then filtered to remove

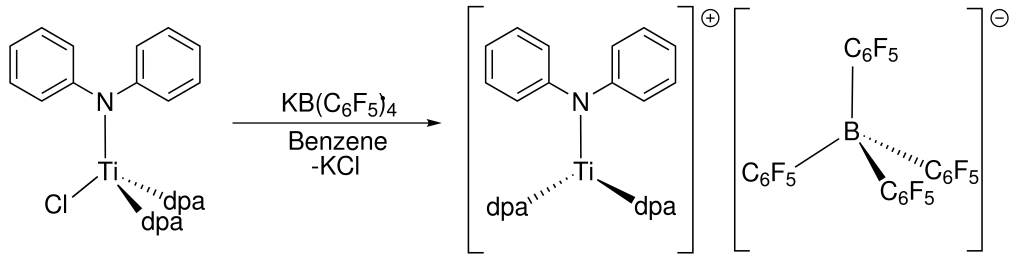

Scheme 2.8: The synthesis of $[(dpa)_3Ti]^+[B(C_6F_5)_4]^-$ (9)

any remaining KCl, and the frit was washed twice with hexane. The solvent was removed under reduced pressure, producing a reddish/purple solid in approximately 40% yield. Due to the low electron count on the titanium centre, this complex is extremely air and water sensitive, and will decompose in concentrations of less than 2.0 ppm. This complex is also ether sensitive. Binding of the ether to the titanium centre will occur even in low concentrations.

As expected, the ^{1}H spectrum of (9) is very similar to the ^{1}H spectrum of (2). The ^{1}H spectrum of (9) is shown in Figure A.13. The resonances at 6.9 ppm and 7.0 ppm are assigned to the *ortho* and *meta*. The resonance at 6.8 ppm is assigned to the *para* protons. There are some small differences however. There are now a few resonances in the aliphatic region of the spectrum. There are also resonances at 1.8 and 3.6, that suggest THF coordination. These resonances are at 0.9 ppm and 3.2 ppm. The resonance assignments are collated in Table 2.11.

Proton Assignment	δ/ppm	Coupling Pattern	H-H coupling constant/Hz
ortho	7.0	doublet	7.6
meta	6.9	triplet	7.7
para	6.8	triplet	7.3

Table 2.11: ^{1}H NMR spectral resonances of (9)

The ^{13}C spectrum is easily assigned using the HSQC spectrum shown in Figure 2.11. The resonances at 123.4 ppm and 129.4 ppm are assigned to the *ortho* and *meta* carbons. The resonance at 125.5 ppm is assigned to the *para* carbon, and the resonance at 150.0 ppm is assigned to the *ipso* carbon. These resonances are collated in Table 2.12.

The solubility of the cationic complex (9) is similar to complex (2). This cationic complex is soluble in toluene and benzene, but shows much lower solubility in hydrocarbon solvents. The parent ion of this complex was unable to found by Electron Impact mass spectrometry. The extreme sensitivity of this complex lead to decomposition before the sample could be analysed. Elemental analysis confirmed the purity of this product.

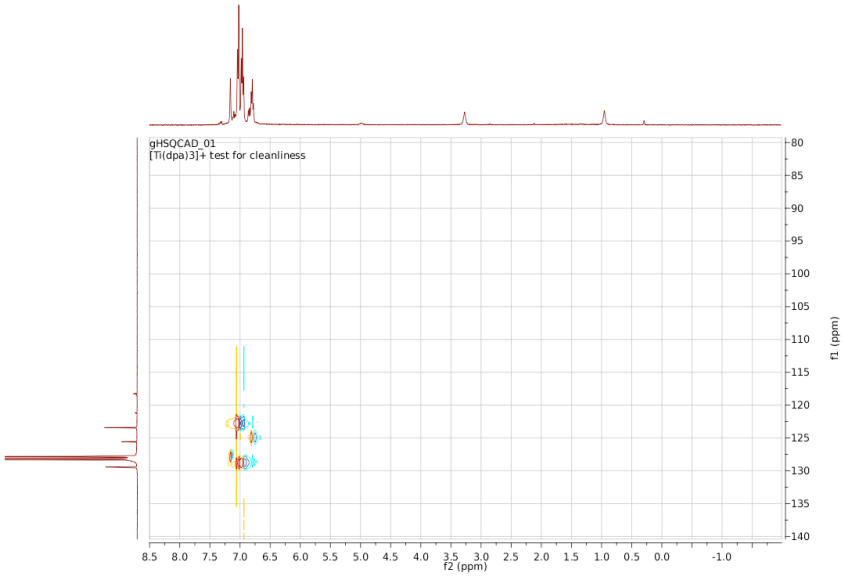

Figure 2.11: The HSQC spectrum of (9)

Carbon Assignment	δ/ppm
ortho	123.4
meta	129.4
para	125.5
ipso	150.0

Table 2.12: ^{13}C NMR spectral resonances of (9)

2.1.9 Synthesis of *tris*(di*p*-tolylamido)titanium $[(dpta)_3Ti]^+[B(C_6F_5)_4]^-$ (10)

The synthesis of (10) is achieved in the same way as (9). A benzene solution containing one molar equivalent of $KB(C_6F_5)_4$, is added to a benzene solution containing one molar equivalent of (4). Upon addition, the solution turns from a bright red to a darker red. The solution was stirred at room temperature for three hours, at which time it was stopped, and allowed to settle. The solution was then filtered to remove any remaining KCl, and the frit was washed twice with hexane. The solvent was removed under reduced pressure, producing a reddish/purple solid in approximately 55% yield. This product is also extremely air, water, and ether sensitive. The synthesis of (10) is shown in Scheme 2.9.

The ^{1}H spectrum of (10) is shown in Figure A.12. The resonances at 7.1 ppm and 6.8 ppm are assigned to the *ortho* and *meta* protons. The resonance at 2.0 ppm is assigned to the *para*-methyl protons. This spectrum also contains resonances in the aliphatic region, similar to (9). These

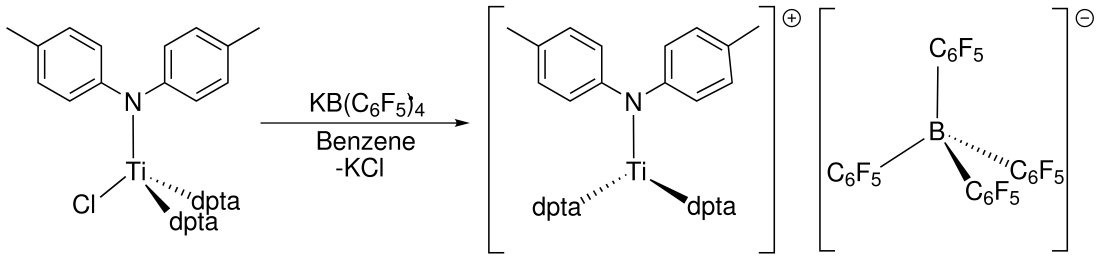

Scheme 2.9: The synthesis of $[(dpta)_3Ti]^+[B(C_6F_5)_4]^-$ (10)

resonances have the same chemical shift in both cationic spectra. The proton assignments are collated in Table 2.13.

Proton Assignment	δ/ppm	Coupling Pattern	H-H coupling constant/Hz
ortho	7.1	doublet	8.3
meta	6.8	doublet	8.7
para-methyl	2.0	singlet	-

Table 2.13: ^{1}H NMR spectral resonances of (10)

The ^{13}C spectrum is easily assigned using the HSQC spectrum shown in Figure 2.12. The resonances at 130.1 ppm and 123.7 ppm are assigned to the *ortho* and *meta* carbons. The resonance at 20.8 is assigned to the *para*-methyl carbon, and the resonance at 147.4 ppm is assigned to the *N-ipso* carbon. The resonance at 136.1 ppm is assigned to the *C-ipso* carbon. These resonance assignments are collated in Table 2.14.

Carbon Assignment	δ/ppm
ortho	130.1
meta	123.7
N-ipso	147.4
C-ipso	136.1
para methyl	20.8

Table 2.14: ^{13}C NMR spectral resonances of (10)

The solubility of this complex is increased in benzene and toluene, but not in most hydrocarbon solvents. The parent ion for this complex was unable to be found using Electron Impact mass spectrometry, due to immediate decomposition in air. Elemental analysis confirmed the purity of

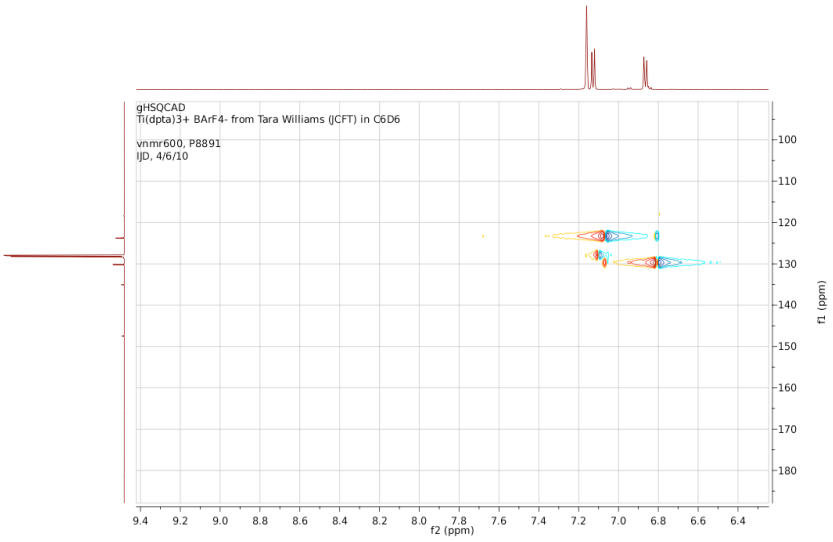

Figure 2.12: The HSQC spectrum of (10)

this product.

2.1.10 Synthesis of potassium *tetrakis*(perfluorophenylborate) ($KB(C_6F_5)_4$) (11)

Due to the high cost of *tetrakis*(perfluorophenylborate) salts, such as $NaB(C_6F_5)_4$ and $KB(C_6F_5)_4$ a novel route to the synthesis of $KB(C_6F_5)_4$ was explored. A novel method for this synthesis was found. The first step of this method can be seen in Scheme 2.9.

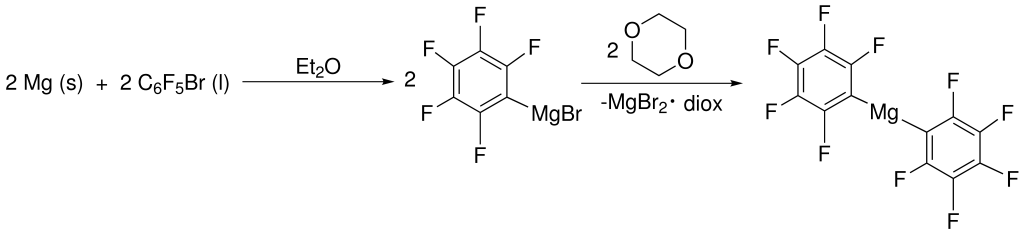

Scheme 2.10: The synthesis of $Mg(C_6F_5)_2$

A standard Grignard synthesis was implemented; two equivalents of magnesium were reacted with two equivalents of bromopentafluorobenzene in diethyl ether, to produce $MgBrC_6F_5$. The BrC_6F_5 in Et_2O was added dropwise to the Mg in Et_2O. The Mg/Et_2O solution was stirred slowly during the addition, until bubbles rose from the Mg turnings, indicating the reaction was taking place. The solution slowly turned brown upon addition. By the end of the addition, the solution was dark brown in colour. The reaction was allowed to stir overnight, was filtered, and 1,4-dioxane, $C_4H_8O_2$, was added in order to shift the Schlenk equilibrium (*vide infra*), and pre-

cipitate out the dihalide, $MgBr_2 \cdot 2diox$. The dihalide began to precipitate out immediately. The reaction was filtered, and large crystals were grown in a -80°C freezer overnight. The solution was filtered from the crystals, and the crystals were dried under light vacuum, producing $[Mg(C_6F_5)_2(Et_2O)(dioxane)]$. Diffraction data was collected from the crystals, and the molecular structure is shown in Figure 2.13.

The complex, $[Mg(C_6F_5)_2(Et_2O)(dioxane)]$, crystallises in space group P21/c and the crystal group is monoclinic. The lattice parameters for this structure are a = 14.3835(5) Å, b = 17.2946(7) Å, c = 17.5981(4) Å, $\alpha = \gamma = 90°$, and $\beta = 102.943(2)°$. This is a rare structure with magnesium being bound to two ethers, dioxane and Et_2O. The average Mg−C bond length in this structure is 2.22 Å, while average Mg−O bond length is 2.17 Å. A search of the CCSD[143] gave an average bond length of 2.20 Å, for Mg−C, and 2.07 Å, for the Mg−O bond to the dioxane. The bond lengths for the molecular structure of $[Mg(C_6F_5)_2(Et_2O)(dioxane)]$ are therefore unexceptional. The C−F bond lengths are comparable to the C−F bond lengths in *tris*pentafluorophenylborane·THF, which is unsurprising as the fluorinated rings are in the same environment for both structures.

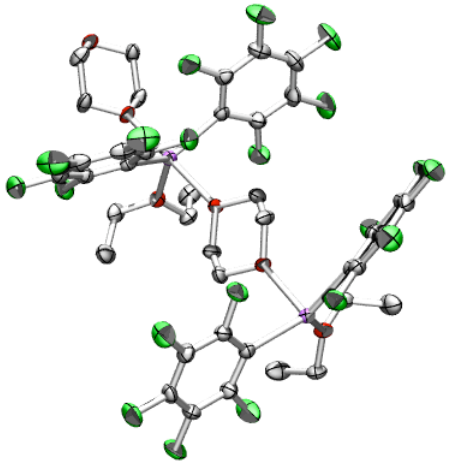

Figure 2.13: Molecular Structure of $[Mg(C_6F_5)_2(Et_2O)(dioxane)]$ 50% ellipsoid with hydrogen atoms omitted for clarity

The Schlenk equilibrium takes place in the ethereal solutions of Grignard reagents. On the left side of the equilibrium lies two equivalents of either an alkyl or aryl halide, RMgX. One equivalent of alkyl or aryl magnesium, and one equivalent of magnesium halide lie to the right of the equilibrium. An example of the Schlenk equilibrium is shown in Scheme 2.11.[144] Dioxane is used to shift the equilibrium to the right of the reaction, producing the diaryl complex, MgR_2.

This shift in equilibrium can also be seen in Scheme 2.11.

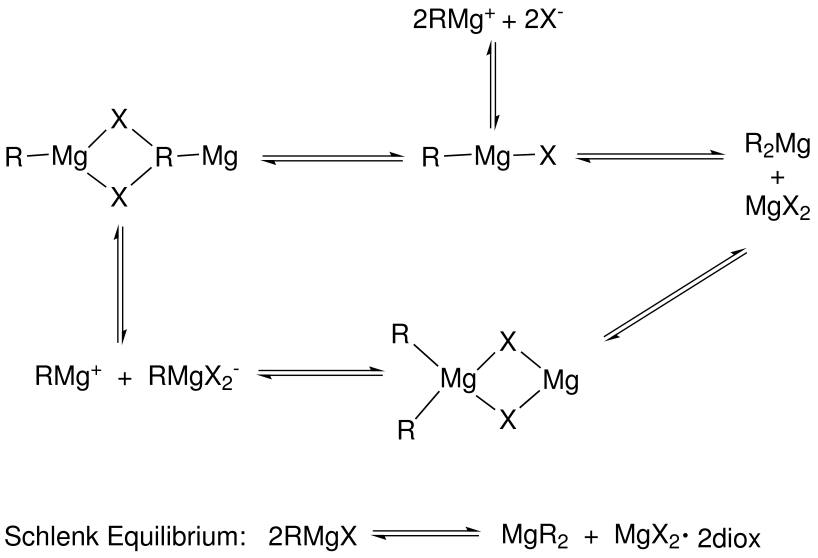

Scheme 2.11: The Schlenk equilibrium

The ^{19}F spectrum of $Mg(C_6F_5)_2$ is shown in Figure 2.14, and the spectroscopic assignments are tabulated below in Table 2.15. The *ortho* fluorines on the ring integrate to 2.0 and are assigned to the resonance at -114.0 ppm. The *meta* fluorines on the ring also integrate to 2.0 and are assigned to the resonance at -161.2 ppm. The *para* fluorine on the ring integrates to 1.0 and is assigned to the resonance at 157.1 ppm.

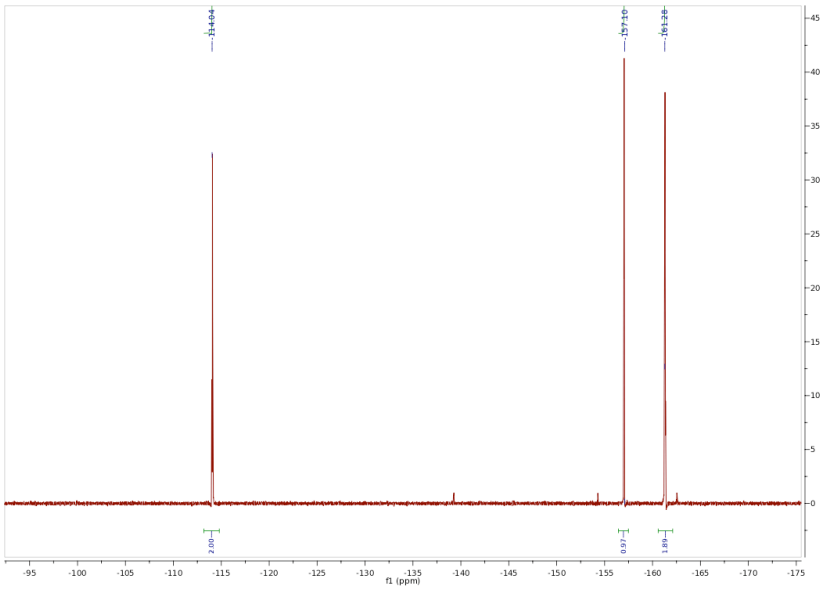

Figure 2.14: The ^{19}F spectrum of $Mg(C_6F_5)_2$

The second step to the synthesis of (11) is shown in Figure 2.12. Two equivalents of $Mg(C_6F_5)_2$

Fluorine Assignment	δ/ppm
ortho	-114.0
meta	-161.2
para	-157.1

Table 2.15: ^{19}F NMR spectral resonances of $Mg(C_6F_5)_2$

in Et_2O were added to one equivalent of KBF_4 in Et_2O at room temperature. This reaction was allowed to stir overnight. After twelve hours the stirrer was turned off, and the reaction was allowed to settle. The reaction was filtered through a fine frit. The frit was then washed with Et_2O twice, and solvent was removed under reduced pressure, producing a cream-coloured powder. The first few attempts at the synthesis of $KB(C_6F_5)_4$ were unsuccessful, and a new synthetic method for $KB(C_6F_5)_4$ had to be devised. The synthetic literature preparation attempted was a 1:1 addition of a C_6F_5Br solution in anhydrous butylic ether to an alkyllithium.[145]

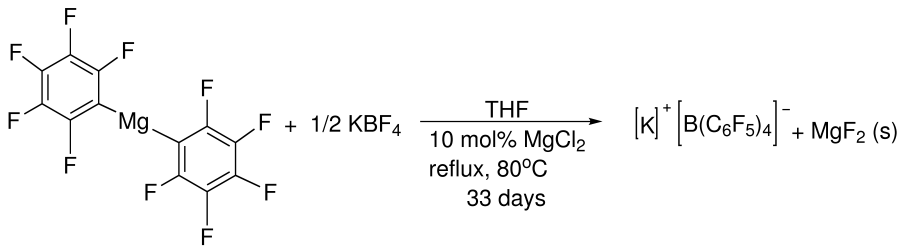

Scheme 2.12: The synthesis of $KB(C_6F_5)_4$ (11)

The reaction was attempted in THF, and allowed to stir for 2-4 days. There was no change in the ^{19}F spectrum, the resonances had the same chemical shift as $Mg(C_6F_5)_2$. The reaction mixture was refluxed in Et_2O for a few days, producing the same result. Finally the reaction mixture was refluxed in THF in an ampoule under vacuum with 10 mol% $MgCl_2$.

An aliquot of this sample was taken everyday to test the conversion in the ^{19}F spectrum between $Mg(C_6F_5)_2$ and $KB(C_6F_5)_4$ over the 33 days required for reaction. During this process, there were many resonances in the ^{19}F. The reaction was not stopped until there were three resonances remaining, with different chemical shifts than $Mg(C_6F_5)_2$, indicating that the reaction had fully gone to completion. A stacked plot of the ^{19}F spectroscopic data that show the conversion between $Mg(C_6F_5)_2$ and $KB(C_6F_5)_4$ is shown in Figure 2.15.

After the reaction mixture had cooled and settled, it was filtered. The solvent was removed under reduced pressure, producing a sticky brown solid. This solid was washed 7 times with 50 mL pentane to remove all traces of THF, producing a fine cream powder.

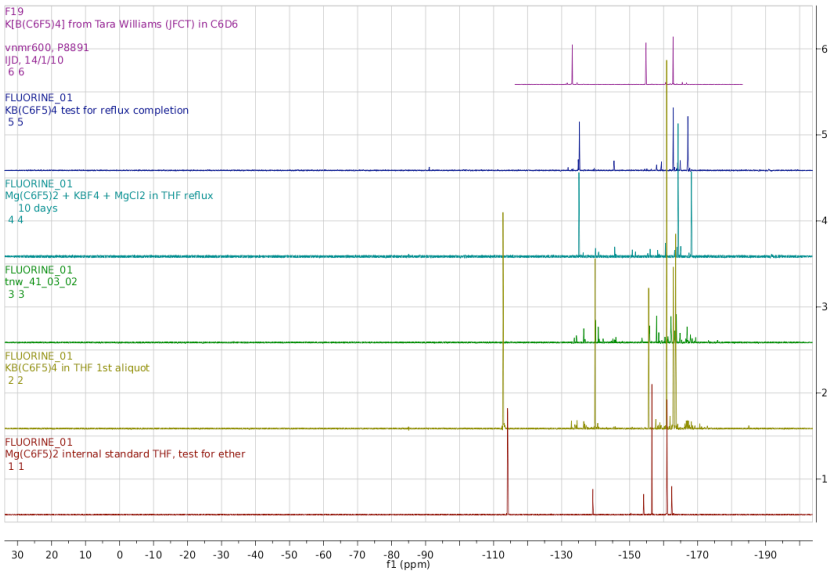

Figure 2.15: The conversion of $Mg(C_6F_5)_2$ to $KB(C_6F_5)_4$

2.1.11 Crystal structure of *tris*(pentafluorophenyl)borane·THF

Crystalline specimens of $BArF_3$·d_8-THF, where $BArF_3$ is $(C_6F_5)_3$, were grown by evaporation of solvent from an NMR sample. The perhydro isotopomer was rationally synthesized by addition of h_8-THF to a solution of $BArF_3$ in toluene, followed by evaporation of the solution over twelve hours. Spectroscopic data, including ^{11}B, ^{19}F, and ^{1}H NMR data were consistent with the formulation of this compound.

The structures *tris*(pentafluorophenyl)borane·THF $[B(C_6F_5)_3{\cdot}C_4H_8O]$ and $[B(C_6F_5)_3{\cdot}C_4D_8O]$ have been determined. An interesting arene-arene interaction can be seen in the unit cell of these structures. A comparatively longer than average boron-oxygen bond distance of 1.5845(19) Å, is seen, most likely due to the zwitterionic nature of the molecule.

Despite its utility, no crystal structure of tris(pentafluorophenyl)borane has been reported, and structural information for this system is confined to adducts of the form $L{-}BArF_3$. In structurally characterized complexes of this general type, boron is usually ligated by elements from the first row of the main group and of these, carbon dominates. There are a few purely anionic structures recorded for $[FBArF_3]^-$ and $[ClBArF_3]^-$ with a variety of organic or transition metal-containing counterions and a smaller number of formally zwitterionic systems with O or N as the ligating atom. The number of structurally characterized complexes in which boron is ligated by an atom from the second or lower rows of the main group is very much smaller.

The lattice parameters for the hydrogenated version are a = 14.2579(4) Å, b = 11.2188(2) Å, c = 14.7039(4) Å, $\alpha = \gamma = 90°$, and $\beta = 115.919(1)°$. A structure of the hydrogenated version

of $BArF_3{\cdot}d_8$-THF was found by Lorber *et al.*[146] A comparison was made between the lattice parameters of the structures, A (the hydrogenated version) and the literature values. The lattice parameters of structure A and the literature values were not significantly different, with values of a = 14.26 Å, b = 11.22 Å, c = 14.70 Å, $\alpha = \gamma = 90°$, and $\beta = 115.97°$. These values fall within SUS values, with a difference of 0.0072 Å, for a, 0.0038 Å, for b, and 0.0149 Å, for c.

The asymmetric unit is one molecule with the rest of the cell contents being elaborated from the centre of inversion and glide planes. Inspection of the packing of [$BArF_3{\cdot}$THF] molecules shows that there are several close intermolecular interactions which serve as the structural driver for the crystal structure. There is a close contact between two of the arene rings that lie coplanar to each other in the unit cell; the rings are therein related by the centre of inversion. There is an interaction between two of the fluorinated rings, and the unit cell has a clear centre of inversion. The arene-arene ring interaction appears to maximize the charge density arrangements of the C_6F_5 ring, placing a fluorine atom over the approximate centre of the positive charge density polarization of the C_6F_5 ring. Similar interactions can be seen in the Cambridge Structural Database[143] particularly in the structure [$B(C_6F_5)_3{\cdot}C_4H_8S$], where the only difference in the structure is found in the replacement of a furan ring with a thiane ring. This interaction is unusual; there are only ninety-four such structures found in the Cambridge Structure Database containing [$B(C_6F_5)_3$] that share this same polarization from the arene-arene ring interaction. Of these structures, the majority of these arene-arene interactions can be seen in structures containing fluorinated benzene rings, specifically $[B(C_6F_5)_4]^-$ and [$B(C_6F_5)_3$]. This interaction can also be seen in the unit cells of crystal structures containing the C_6F_5 moiety with elements as diverse as sulfur, gallium, palladium, gold, and phosphorus.

The bond length for the boron−oxygen bond in tris(pentafluorophenyl)borane·THF was found to be 1.5845(1) Å, which is elongated on average in comparison with the same bond in a three coordinate aryl−boron−oxygen system. Larger boron−oxygen bond lengths are encountered in aryl borane systems that are zwitterionic. A search of the Cambridge Structural Database for tricoordinate aryl−boron−oxygen systems yielded 163 structures with an average boron−oxygen bond length of 1.53712(9) Å. When comparing the oxygen-boron-carbon bond angle in tris(pentafluorophenyl)b with the similar compounds on the Cambridge Structural Database, the average oxygen-boron-carbon bond angle for the tetrahydrofuran adduct is 107.206(6)°, while the average oxygen-carbon-boron bond angle for the above-mentioned compounds is 107.475(9)°.

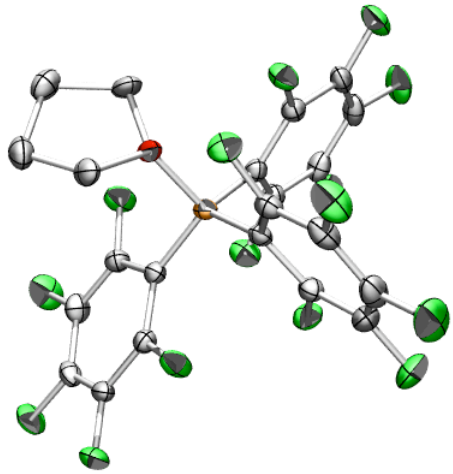

Figure 2.16: Molecular Structure of *tris*pentafluorophenylborane·THF

2.2 Results and Discussion

Synthesis of $(dpa)_3TiCl$ and $(dpta)_3TiCl$ provided a synthetic entrance for all other products in this chapter. These complexes are intrinsically electron-poor, with a coordination sphere composition of L_3X_4 and an electron count of 14 electrons at Ti^{IV}, in contrast to the majority of Ti complexes, which have an electron count of 16 electrons. Metathesis of the chloride with methyl afforded a pair of rare 14 electron titanium methyls. Despite the low electron count, partial abstraction of the methyl group with $B(C_6F_5)_3$ took place cleanly and, in the absence of structural data in the solid state, it is reasonable to assume that a 3-centre-2-electron bond similar to that found in $[Cp_2ZrMe]^+[MeB(C_6F_5)_3]^-$ has been installed; spectroscopic data from both $(dpa)_3TiMeB(C_6F_5)_3$ and $(dpta)_3TiMeB(C_6F_5)_3$ are consistent with similar trends in NMR data observed when Me is abstracted from zirconocene dimethyls.

Although $(dpa)_3TiMeB(C_6F_5)_3$ and $(dpta)_3TiMeB(C_6F_5)_3$ are likely to be close ion pairs, a formal electron count of either species in the neutral class results in a L_2X_4 formulation for the coordination sphere at Ti^{IV}. There are very few complexes with such a low electron count in the early transition metals, one example being shown in Scheme 2.13, where a methyl group was abstracted from $(TMS_2N)_3MMe$ (M = Zr, Hf)[147] where TMS is tetramethylsilane, to form the ion pair shown.

Abstraction of chloride to explicitly form such a species also was successful and it may be assumed that the charge separation in $[(dpa)_3Ti]^+[MeB(C_6F_5)_3]^-$ and $[(dpta)_3Ti]^+[MeB(C_6F_5)_3]^-$ is even more stringent.

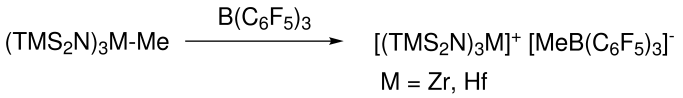

Scheme 2.13: Formation of $[(TMS_2N)_3M]^+[MeB(C_6F_5)_3]^-$ (M = Zr, Hf)

2.3 Conclusions

The complexes synthesised in this chapter provide a platform for the polymerisation reactions discussed in chapter three. Titanium was chosen because it is an early transition metal, and will most often be coordinatively unsaturated. These complexes will therefore have a gap in the coordination sphere, and will be able to accomodate a higher electron count. This increase in electrons is typically indicative of an increase in the number of ligands, or the change in the MLX character of the ligands. Two different amine complexes were used as ligands, diphenylamine (dpa), and di-*p* tolylamine (dpta). These ligands both act as LX ligands, providing three electrons each per ligand to the metal centre. These ligands were chosen for their electronic flexibility. Since these complexes are all electron poor, there will be empty dπ orbitals available to accept electron density from the amido ligands. Amido ligands also provide steric bulk for stability, while not preventing polymerisation chain growth at the titanium centre.

The two methyl complexes, $(dpa)_3$TiMe and $(dpta)_3$TiMe are rare examples of *tris* amido methyl complexes. $B(C_6F_5)_3$ was added to the methyl complexes for their use as polymerisation catalysts. Analysis of the ^{1}H spectrum of these complexes infers that $B(C_6F_5)_3$ successfully partially abstracts a methyl group from these complexes, providing the systems $[(dpa)_3Ti]^+[MeB(C_6F_5)_3]^-$ and $[(dpta)_3Ti]^+[MeB(C_6F_5)_3]^-$. Two rare examples of 12 electron *tris* amido complexes were also synthesised, $[(dpa)_3Ti]^+[B(C_6F_5)_4]^-$ and $[(dpta)_3Ti]^+[B(C_6F_5)_4]^-$.

The purification and syntheses of general polymerisation cocatalysts, such as $KB(C_6F_5)_4$ and $B(C_6F_5)_3$, provided interesting crystallographic results. *Tris*(pentafluorophenyl)borane·THF crystals were grown, and the molecular structure was deduced by X-ray diffraction. A new route for the synthesis of $KB(C_6F_5)_4$ was also formulated. The molecular structure of one of the intermediates in this synthesis, $[Mg(C_6F_5)_2(Et_2O)(dioxane)]$ was also deduced.

Chapter 3

Alkene polymerisation at *tris*(amido)titanium centres

3.1 Introduction

Traditional polymerisation catalysts, such as Cp_2ZrMe^+ are formally $[L_4X_3]^+$ or L_3X_4, 14 electron systems.[138] Before cocatalyst abstraction, or polymerisation occurs, these systems begin as Cp_2ZrMe_2, and are L_4X_4, 16 electron systems. The *tris* amido titanium systems synthesised in this chapter, $(R_2N)_3TiCl$ and $(R_2N)_3TiMe$, begin as L_3X_4, 14 electron systems. These amido complexes are therefore electronically suitable for use as polymerisation cocatalysts in principle.

Additionally $[(dpa)_3Ti]^+[B(C_6F_5)_4]^-$ and $[(dpta)_3Ti]^+[B(C_6F_5)_4]^-$, are formally $[L_3X_3]^+$ or L_2X_4 systems. These complexes have only 12 electrons, and are therefore extremely electron deficient. This deficiency, along with coordinative unsaturation at the metal centre provided for by the amido ligands, makes these complexes potential candidates for single site polymerisation catalysis.

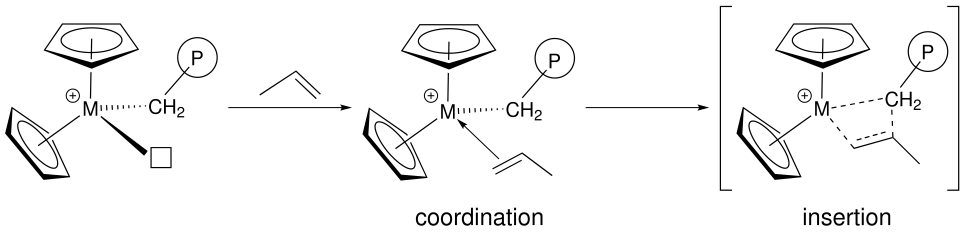

Figure 3.1: Coordination and insertion steps in Ziegler-Natta catalysis

Conventional Ziegler-Natta systems contain two structural features: a vacant coordination site, usually containing the weakly coordinating anion in the absence of monomer, and a metal-carbon bond to the alkyl or polymer chain into which insertion takes place. The essential steps that require

these structural features are shown in Figure 3.1.

Although the methyl complexes formally contain a metal alkyl bond and have an identical electron count to species such as Cp_2ZrMe^+ at 14 electrons, the orbital arrangements are very different. Moreover, the cation has a lower electron count and no metal-carbon bond. Thus the related methyl/cation pairs come close to containing the two required features in a conventional Ziegler-Natta system but in two separate species. These systems therefore break the conventional requirement for Ziegler-Natta catalysts. Since these cationic complexes are unconventional, it is unlikely that they will follow the traditional modified Green-Rooney mechanism for polymerisation. A new mechanism for polymerisation growth in these systems may need to be introduced. Previous work has demonstrated that these *tris*(diphenylamido) titanium complexes can act as homogeneous olefin polymerisation catalysis, reactivity which complements previously patented heterogeneous applications of related systems.[148–153]

3.2 General polymerisation Procedures

Polymerisation catalysis in industry utilizes pressures greater than atmospheric, ranging from 5 atm to 100 atm, and temperatures from 0°C to 150°C in order to increase the rate of reaction.[154,155] Polymerisation studies in this section were conducted at sub-ambient temperatures and pressures, in order to characterize the rates of reaction. The concentrations of all titanium amido catalysts were extremely low, (1.5 x 10^{-5} mol Ti), in order to easily detect deactivation. To keep the data consistent, the number of moles of titanium remained at 1.5 x 10^{-5} for all catalytic reactions.

A volume-calibrated high-vacuum line, equipped with a PTX1400-Pressure transducer, was used in order to monitor the pressure of a known volume of gas added to the catalyst. A picture of the apparatus is shown in Figure 3.2. The calibration of the high vacuum line occurred as follows. A schematic of the high vacuum line was drawn, separating the line into 7 parts. Each part of the line was filled with nitrogen separately, evacuated, and then opened again, in order to calibrate the line section by section. Each additional calibration included the calibration of the section before, i.e. calibration two would include the calibration of section one and section two. The calibration was finished when all seven sections were calibrated together. All reaction ampoules and their adaptors were also volume calibrated.

Solid catalyst and activator were added to an ampoule fitted with a high-vacuum adaptor (approximately 90 mL volume) in the glove box. The ampoule was attached to the line and approximately 15 mL of toluene (standing over K) was vacuum transferred into the polymerisation ampoule. Dry monomer was expanded from the source tank into the volume of line, approximately 961 mL. The polymerisation vessel was cooled to 0.0°C in an ice bath, and the vessel was

opened to monomer feed, which was at a pressure of approximately 710 mbar. Time recording began when the ampoule was exposed to the monomer. The pressure was monitored every 30 seconds until the monomer was consumed. After a time period of 20 minutes, the polymerisation reaction was complete.

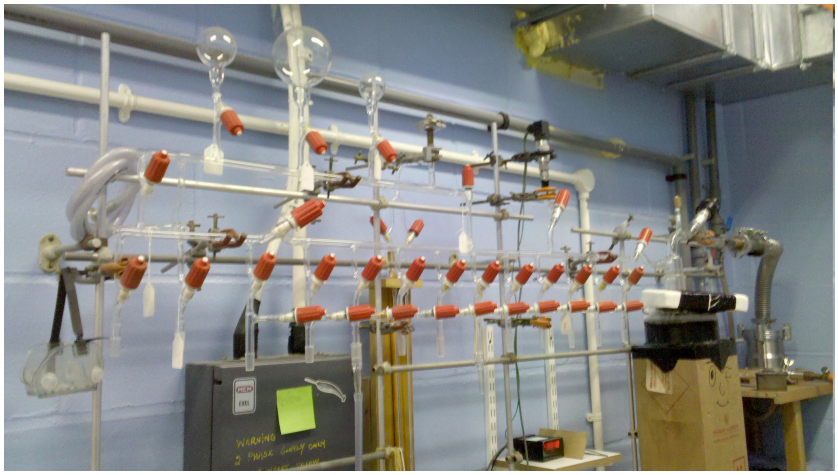

Figure 3.2: High vacuum apparatus used for polymerisation reactions

When polymerisation was complete, the reactions were quenched with a 1:1 methanol:HCl mixture, neutralizing any active catalyst remaining in the ampoule. Solvent was removed under reduced pressure, yielding polymer. Liquid products were washed with methanol:HCl and, filtered, and solvent was removed under reduced pressure. Characterization of the polymers produced was performed by ^{1}H Nuclear Magnetic Resonance spectroscopy.

3.3 Activation of $(dpa)_3TiCl$ and $(dpta)_3TiCl$ with MAO

$(dpa)_3TiCl$ (8.82 mg, 1.5×10^{-5} mol, 1 eq) was added to an ampoule in the glovebox. Excess MAO (21.8 mg, 3.75 x 10^{-4} mol, 25 eq) was added in the dry box. The ampoule was evacuated on the high vacuum line, ($\sim 10^{-6}$ mbar), at which time 8.21 g (9.47 mL) of toluene was vacuum distilled into the ampoule, 30.3 mmol of propene without purification, was expanded into the line with a volume of 961 mL at a pressure of 717 mbar. The frozen solution was allowed to thaw and warmed in an ice bath to 0.0°C. The gas was expanded into the ampoule, and the temperature was kept at 0.0°C during the experiment. When the ampoule is first opened to the monomer, the pressure drops roughly 320 mbar as the monomer expands into the ampoule and begins to polymerize. The rate began to settle after around 330 seconds as the monomer is consumed. The polymerisation reaction yielded 146 mg of polypropene.

In a representative reaction, $(dpta)_3TiCl$ (10.1 mg, 1.5×10^{-5} mol, 1 eq) was added to an

ampoule in the glovebox. Excess MAO (21.8 mg, 3.75 x 10^{-4} mol, 25 eq) was added on top of the catalyst in the dry box. The ampoule was evacuated on the high vacuum line, ($\sim 10^{-6}$ mbar), after which 8.01 g (9.24 mL) of toluene was vacuum distilled into the ampoule, 30.3 mmol of propene without purification, was expanded into the line with a volume of 961 mL at a pressure of 716 mbar. The frozen solution was allowed to thaw and warmed in an bath to 0.0°C. The gas was expanded into the ampoule, and the temperature was kept at 0.0°C during the experiment. When the ampoule is first opened to the monomer, the pressure drops roughly 310 mbar as the monomer expands into the ampoule and begins to polymerize. The rate begins to settle after around 510 seconds as the monomer is consumed. The polymerisation reaction yielded 171 mg of polypropene.

When comparing the polymerisation results between the two diarylamido systems activated with MAO, there are only slight differences that require explanation. In the representative reactions mentioned above, *tris*(di-para-tolylamido)titanium (IV) chloride yielded more polypropene. The *tris*(diphenylamido)titanium (IV) chloride exhibited slightly faster initial activation when exposed to propene. A plot of the rate of propene consumption of the catalysts, *tris*(di-para-tolylamido)titanium (IV) chloride and *tris*(diphenylamido)titanium (IV) chloride with the initiator MAO is shown in Figure 3.3.

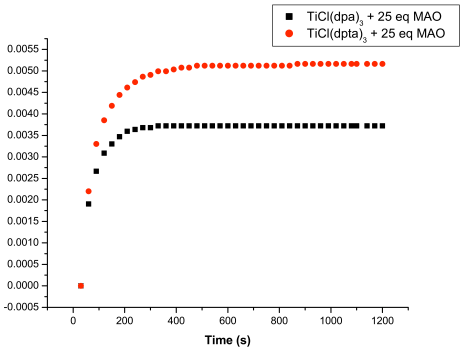

Figure 3.3: Rate of propene consumption of $(dpa)_3TiCl$ and 25 eq. of MAO vs. $(dpta)_3TiCl$ and 25 eq. of MAO

Samples of polypropene produced from the MAO-activated polymerisation reactions were sent to the University of Tennessee to be analysed.[156] GPC was run on a Polymer Laboratories GPC-220 in trichlorobenzene at 145°C with refractive index (RI), Light Scattering (LS15 and LS90), and viscometer detector (UV). Samples were prepared at a concentration of 1.0 mg/ml. DSC was run on a Mettler-Toledo DSC821 from -50°C to 250 °C at a ramp 10°C/min. Each sample was run three times to eliminate thermal history. The NMR experiments were done on the Bruker

400MHz spectrometer in Trichlorobenzene spiked with deuterated DMSO as the lock solvent at 120 °C. The polypropene was found to be atactic for the reaction $(dpta)_3TiCl$ + 25 eq. of MAO, and atactic for $(dpa)_3TiCl$ + 25 eq. of MAO though the sample shows a lot of isotacticity as well. The results are tabulated below in Table 3.1.

Catalyst	M_w	M_n	PDI	Average T_g/°C	AverageT_m/°C
$(dpa)_3TiCl + 25$ eqMAO	1,804,508	646,597	2.790	-6.65	155.16
$(dpta)_3TiCl + 25$ eqMAO	1,265,927	469,483	2.696	-5.89	155.10

Table 3.1: Polypropene data obtained from the analysis of polymer samples

3.4 Activation of $(dpa)_3TiMe$ and $(dpta)_3TiMe$ with $B(C_6F_5)_3$

Polymerisation reactions using the catalysts $(dpa)_3TiMe$ and $(dpta)_3TiMe$, with the cocatalyst, $B(C_6F_5)_3$, were prepared in advance and *in situ*. Since there are no side products in the reactions between the methyl complexes and $B(C_6F_5)_3$, the complexes $TiMe(dpa)_3B(C_6F_5)_3$ and $TiMe(dpta)_3B(C_6F_5)_3$ are easy to isolate and characterize. Using $B(C_6F_5)_3$ as a cocatalyst also has the advantage that only one equivalent is required for activation, unlike the excess used for the activation with MAO.

$(dpa)_3TiCl$ (8.51 mg, 1.5×10^{-5} mol, 1 eq) was added to a volume calibrated ampoule, and $B(C_6F_5)_3$ (7.70 mg, 1.5×10^{-5} mol, 1 eq) was added in the glovebox. The ampoule was evacuated under high vacuum ($\sim 10^{-6}$ mbar) and 7.76 g (8.948 mL) of toluene was vacuum distilled into the ampoule, 30.3 mmol of propene without purification, was expanded into the line with a volume of 961 mL at a pressure of 717 mbar. The frozen solution was allowed to thaw and warm to 0.0°C. The colour of the activated catalyst in solution was dark purple. The gas was expanded into the ampoule, and the temperature was kept at 0.0°C during the experiment. When the catalyst is exposed to the monomer, the pressure drops approximately 290 mbar and the polymerisation begins. The polymerisation reaction yielded 48.2 mg of polypropene.

$(dpta)_3TiCl$ (9.8 mg, 1.5×10^{-5} mol, 1 eq) was added to a volume calibrated ampoule, and $B(C_6F_5)_3$ (7.70 mg, 1.5×10^{-5} mol, 1 eq) was added on top of the catalyst in the glovebox. The ampoule was evacuated under high vacuum ($\sim 10^{-6}$ mbar) and 7.15 g (8.25 mL) of toluene was vacuum distilled into the ampoule, 30.4 mmol of propene without purification, was expanded into the line with a volume of 961 mL at a pressure of 718 mbar. The frozen solution was allowed to thaw and warm to 0.0°C. The colour of the activated catalyst in solution was dark purple. The gas was expanded into the ampoule, and the temperature was kept at 0.0°C during the experiment.

When the catalyst is exposed to the monomer, the pressure drops approximately 240 mbar and the polymerisation begins. The polymerisation reaction yielded 26.7 mg of polypropene.

The $(dpa)_3TiMe$ and $(dpta)_3TiMe$ catalysts activated with $B(C_6F_5)_3$ show similar initial activity to the $(dpa)_3TiCl$ and $(dpta)_3TiCl$ catalysts activated with MAO. The polymerisation reactions initiated with $B(C_6F_5)_3$ show activity for a much longer period of time. The rates of reaction for these systems do not significantly decrease until 13.5 minutes have passed, when the rate of reaction approaches zero.

$(dpa)_3TiMeB(C_6F_5)_3$ and $(dpta)_3TiMeB(C_6F_5)_3$ were also reacted with propene. These experiments were performed in order to test the consistency of the polymerisation reactions carried out with the *in situ* $(dpa)_3TiMe$ and $(dpta)_3TiMe$ reactions with $B(C_6F_5)_3$. The pre-made catalyst, $(dpa)_3TiMeB(C_6F_5)_3$ showed a higher initial activity than the *in situ* catalyst. The *in situ* catalyst stayed active for 810 seconds, whilst the pre-made catalyst only stayed active for 540 seconds. The opposite behaviour was observed for the di-para-tolylamido system. The *in situ* system showed a higher initial activity, and stayed active for 1020 seconds, whilst the pre-made $(dpta)_3TiMeB(C_6F_5)_3$ catalyst only remained active for 960 seconds.

When comparing the diphenylamido and di-para-tolylamido catalysts, $(dpa)_3TiMeB(C_6F_5)_3$ showed higher initial activities. $(dpta)_3TiMeB(C_6F_5)_3$ stayed active for an average of approximately 525 seconds longer than $(dpa)_3TiMeB(C_6F_5)_3$. $(dpa)_3TiMeB(C_6F_5)_3$ also produced more polypropene on average. The plots seen in Figure 3.4 compare the rates of propene consumption between the *in situ* and pre-made catalysts. Matrix-assisted laser desorption/ionization, or MALDI, mass spectrometry is traditionally used to characterise polymers. This technique is used as conventional methods tend to fragment large organic molecules. MALDI could not be used to characterise any of the samples in this chapter, however, as the molecular weights of these polymers exceed the limitations of the instrument.

Figure 3.5 is a plot of the rate of propene consumption of all of the catalysts examined thus far.

3.5 Polymerisation activity of $[(R_2N)_3Ti]^+[B(C_6F_5)_4]^-$

$KB(C_6F_5)_4$ was used to abstract the Cl atom and provides the anion required to support the cation, while also increasing its Lewis acidity. The cationic titanium centre is also alkyl free, and is responsible for polymerisation. All other single-site Ziegler-Natta catalysts require a metal-alkyl bond from which to activate, and then abstract. This abstraction leaves a vacant site open for the polymer chain to be introduced and for chain growth to be initiated. Without this metal-alkyl bond, these polymerisations would therefore not follow any of the traditional single-site polymerisation

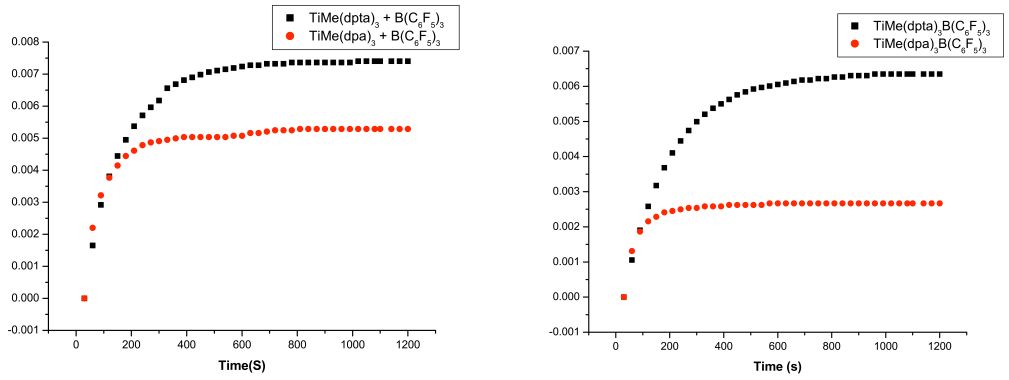

(a) (b)

Figure 3.4: Rate of propene consumption for (a): $(dpa)_3$TiMe with $B(C_6F_5)_3$ vs $(dpta)_3$TiMe with $B(C_6F_5)_3$ and (b): $(dpa)_3$TiMe$B(C_6F_5)_3$ vs $(dpta)_3$TiMe$B(C_6F_5)_3$

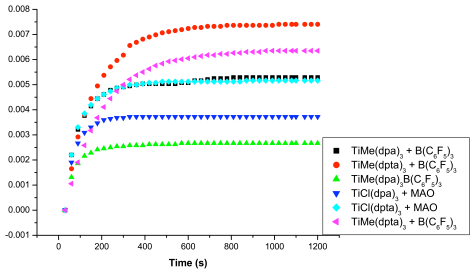

Figure 3.5: Rate of propene consumption for MAO and $B(C_6F_5)_3$ activated catalysts

mechanisms. A new mechanism would therefore need to be hypothesised.

$(dpa)_3$TiCl, (8.80 mg, 1.5×10^{-5} mol, 1 eq) was added to a volume calibrated ampoule, and $KB(C_6F_5)_4$ (10.80 mg, 1.5×10^{-5} mol, 1 eq) was added on top of the catalyst in the glovebox. The ampoule was evacuated under high vacuum ($\sim 10^{-6}$ mbar) and 10.85 g (12.51 mL) of toluene was vacuum distilled into the ampoule, 30.3 mmol of propene without purification, was expanded into the line with a volume of 961 mL at a pressure of 715 mbar. The frozen solution was allowed to thaw and warm to 0.0°C. The colour of the activated catalyst in solution was dark red. The gas was expanded into the ampoule, and the temperature was kept at 0.0°C during the experiment. When the catalyst is exposed to the monomer, the pressure drops approximately 185 mbar and the polymerisation begins. Even after the rate settles, the colour of the catalyst in solution remains dark red, even after deactivation. The polymerisation reaction yielded 21.7 mg of polypropene.

$(dpta)_3$TiCl, (10.1 mg, 1.5×10^{-5} mol, 1 eq) was added to a volume calibrated ampoule, and $KB(C_6F_5)_4$ (10.8 mg, 1.5×10^{-5} mol, 1 eq) was added on top of the catalyst in the glovebox. The

ampoule was evacuated under high vacuum ($\sim 10^{-6}$ mbar) and 9.96 g (11.48 mL) of toluene was vacuum distilled into the ampoule, 30.3 mmol of propene without purification, was expanded into the line with a volume of 961 mL at a pressure of 715 mbar. The frozen solution was allowed to thaw and warm to 0.0°C. The colour of the activated catalyst in solution was dark red. The gas was expanded into the ampoule, and the temperature was kept at 0.0°C during the experiment. When the catalyst is exposed to the monomer, the pressure drops approximately 185 mbar and polymerisation ensues. The polymerisation reaction yielded 34.4 mg of polypropene.

The *in situ* $(dpa)_3TiCl$ and $(dpta)_3TiCl$ catalysts activated with the supporting anion $KB(C_6F_5)_4$ show similar initial activity to the other catalysts. These reactions do not show the large initial uptake of propene. These catalysts do however stay active longer than the other catalysts activated with MAO or $B(C_6F_5)_3$. When $KB(C_6F_5)_4$ was used as a supporting anion, the catalysts stayed active for over twenty minutes. Like the other reactions, the colour of the solutions remained blood-red, indicating that the catalysts were still active.

The catalysts, $[(dpa)_3Ti]^+[B(C_6F_5)_4]^-$ and $[(dpta)_3Ti]^+[B(C_6F_5)_4]^-$, were also reacted with propene. These experiments were performed in order to test the consistency of the polymerisation reactions carried out with the *in situ* $(dpa)_3TiCl$ and $(dpta)_3TiCl$ reactions with $KB(C_6F_5)_4$. The *in situ* catalyst stayed active for 1590 seconds, whilst the pre-made catalyst stayed active for 1320 seconds. The opposite was true for the diphenylamido system. The pre-made catalyst showed a higher activity, and stayed active for 1380 seconds, whilst the *in situ* catalyst only remained active for 1200 seconds.

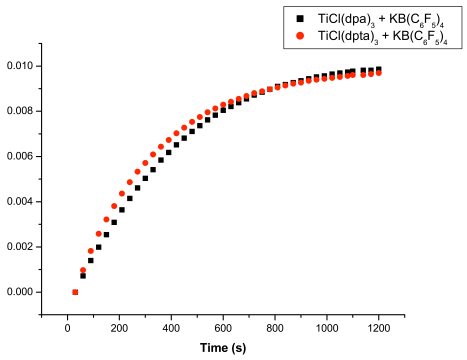

Figure 3.6: Rate of propene consumption for $(dpa)_3TiCl+KB(C_6F_5)_4$ vs $(dpta)_3TiCl+KB(C_6F_5)_4$

The diphenylamido and di-*p*-tolylamido catalysts, $(dpa)_3TiCl + KB(C_6F_5)_4$ and $(dpa)_3TiCl + KB(C_6F_5)_4$ catalysts showed higher initial activities. The catalysts, $[(dpta)_3Ti]^+[B(C_6F_5)_4]^-$ and $[(dpta)_3Ti]^+[B(C_6F_5)_4]^-$ stayed active for an average of approximately 120 seconds longer than the $(dpa)_3TiCl + KB(C_6F_5)_4$ and $(dpta)_3Ti + KB(C_6F_5)_4$ catalysts. The catalyst, $(dpta)_3TiCl +$

$KB(C_6F_5)_4$, produced more polypropene on average. The plots seen in Figures 3.6 and 3.7 compare the rates of propene consumption between the *in situ* and pre-made catalysts.

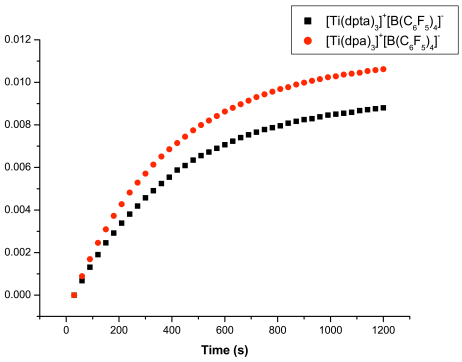

Figure 3.7: Rate of propene consumption for $[(dpa)_3Ti]^+[B(C_6F_5)_4]^-$ with $[(dpta)_3Ti]^+[B(C_6F_5)_4]^-$

Figure 3.8 shows a plot of the direct comparison between the pre-made catalysts, $(dpa)_3TiCl + KB(C_6F_5)_4$ and $(dpta)_3TiCl + KB(C_6F_5)_4$, and the *in situ* catalysts. Figure 3.9 is a plot of the rate of propene consumption of all of the catalysts examined thus far.

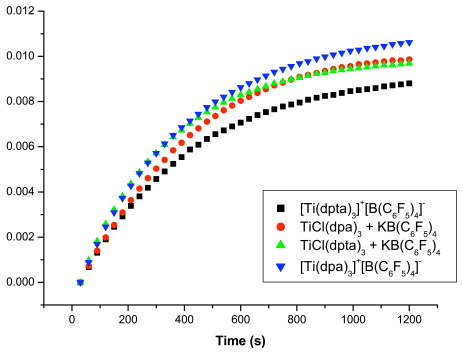

Figure 3.8: Rate of propene consumption for all $TiCl(NAr_2)_3$ + $KB(C_6F_5)_4$

3.6 Kinetics of the various polymerisation reactions

3.6.1 Establishment of the order and rate of polymerisation reactions

In order to establish rate constants for each of the catalytic reactions, the pressure change was plotted over time for each catalyst. The best fit line chosen for the plots was a first-order exponential decay. Given that

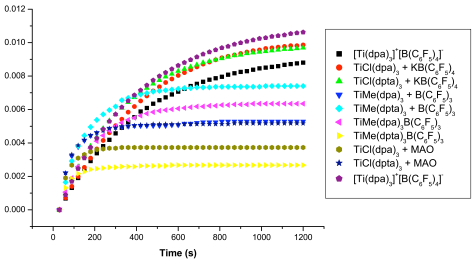

Figure 3.9: Rate of propene consumption for MAO, $B(C_6F_5)_3$ and $KB(C_6F_5)_4$ activated catalysts

$$P(t) = P_0 e^{-kt} \tag{3.6.1}$$

then

$$\frac{P(t)}{P_0} = e^{-kt} \tag{3.6.2}$$

and therefore

$$\ln\left(\frac{P(t)}{P_0}\right) = -kt \tag{3.6.3}$$

The best way to verify that a reaction is indeed first order is to plot the $\ln P$ *vs.* time. This best fit line should be linear if the kinetics are first order. The slope of the line can then be extrapolated, as the slope at $P = P_0$ is proportional to k.

Given that the experimental rate law for the reaction is given by

$$\nu = k[\mathrm{C_3H_6}][\mathrm{TiP}_n] \tag{3.6.4}$$

where $[\mathrm{TiP}_n]$ represents the titanium catalyst attached to an n-monomer polymer chain. First order conditions will occur when $[\mathrm{TiP}_n]$ is approximately constant and so

$$\nu = (k[\mathrm{TiP}_n])\,[\mathrm{C_3H_6}] \approx k'[\mathrm{C_3H_6}] \tag{3.6.5}$$

where $k' = k[\mathrm{TiP}_n]$.

If the catalyst concentration is not constant, then k' will vary and the graph of $\ln P$ *vs.* t will deviate from linearity in a manner that reflects the change in the concentration of the catalyst. The plot of $\ln P$ *vs.* t for polymerisation using $(\mathrm{dpta})_3\mathrm{TiCl} + \mathrm{KB}(\mathrm{C_6F_5})_4$ is shown in Figure 3.10 and shows behaviour that is typical of the other reactions. Plots for each of the other catalysts are included in Appendix C. A straight line was not seen when the $\ln$ of pressure over the time of reaction was plotted.

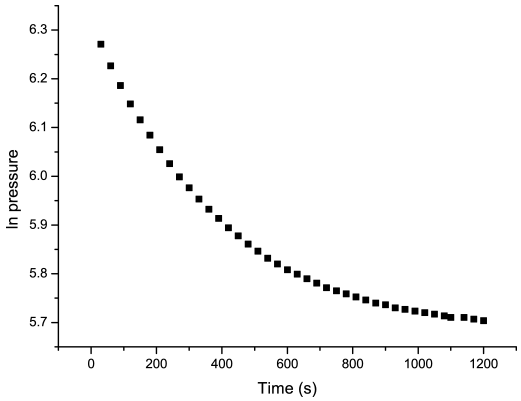

Figure 3.10: ln pressure vs. time plot for the catalyst $(dpta)_3TiCl + KB(C_6F_5)_4$

Assuming that the reaction between the monomer and titanium species is first order and that the deviation from linearity in Figure 3.10 is wholly due to the change in concentration of the catalytic species then Figure 3.10 represents the rate of decay of the catalytic species.

Fitting these data to two or three exponentials, representing two or three first order processes, resulted in non-physical parameters or failed to fit entirely. A single exponential fitted the data well with a confidence of determination $R^2 = 0.99984$, yielding a rate constant for catalyst decay given by $k_{dec} = 0.0025\ \mathrm{s}^{-1}$.

The catalysts could be decomposing due to contamination with water or oxygen as these systems are extremely air and water sensitive. However, all the precatalysts used change colour upon decomposition to an intense dark green on exposure to oxygen. No colour change was observed during the reaction with monomer, indicating that decomposition route is either not taking place or is not dominant.

Hydrolysis is another possibility. However, in experiments using the pre-made cations, the polymerisation could be restarted by addition of another aliquot of propene, showing that the system is still active. Given the sensitivity of $[(R_2N)_3Ti]^+[B(C_6F_5)_4]^-$ and low concentration of the catalyst, hydrolysis seems unlikely in light of the ability to reactivate the catalysts.

One mechanism of termination for conventional Ziegler-Natta catalysts is *via* β-hydride elimination to form the alkene and a metal hydride:

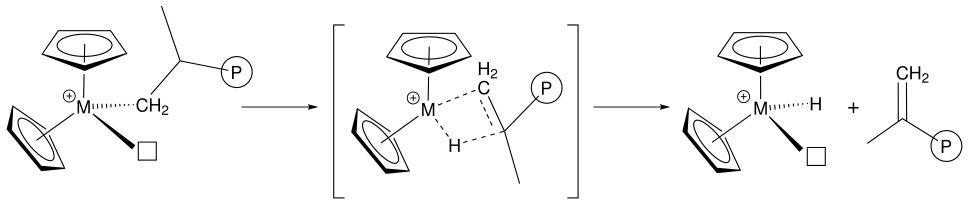

Figure 3.11: A termination reaction in conventional Ziegler-Natta catalysis to form a metal hydride

Whereas a species such as the hypothetical $(R_2N)_3TiEt$ could decompose to the hydride *via*

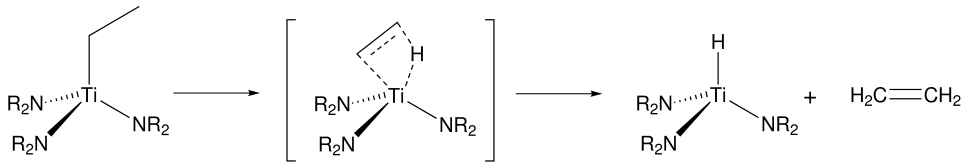

The inclusion of a charge on a species such as $[(R_2N)_3TiCH_2CH(Me)P_n]^+[B(C_6F_5)_4]^-$ should effectively prevent the elimination of a neutral hydrocarbon chain, which would leave a positive Ti-H species such as $[(R_2N)_3TiH]^+[B(C_6F_5)_4]^-$ for a coordination sphere composition of $L_3X_4^+$ or a neutral class of L_2X_5 implying a non-physical Ti^V species. Moreover, as described in Chapter 4, rationally synthesised hydride species based on the *tris*amido titanium platform are exceedingly unstable, liberating hydrogen almost immediately.

Given the observation that the catalytic systems can be cycled, catalytic activity is retained and that single first order process appears to govern the change in rate in the $\ln P$ *vs.* t plot, then a change in the catalyst structure is likely. Calculations using Density Functional Theory, or DFT, were performed by Kayla Keller[157] in order to elucidate a possible mechanism for the change in the structure of the catalyst. When one equivalent of propene was added to the catalyst, $[(dpa)_3Ti]^+$, the propene attaches to the titanium centre. When a second equivalent of propene was added, the polymer chain attaches to the nitrogen atom from one of the diphenylamido ligands. The chain then undergoes rearrangement and a cation is once again created at the titanium centre, forming an open site for the next incoming propene. A hypothesised mechanism for the polymerisation is shown in Figure 3.12.

3.6.2 Stoichiometric reactions of $[(dpa)_3Ti]^+[B(C_6F_5)_4]^-$ with propene

Clearly polymerisation of propene by $[(R_2N)_3Ti]^+[B(C_6F_5)_4]^-$, does not fit the conventional model for Ziegler-Natta polymerisation. There is not a metal-alkyl bond for insertion, and there is no possible intermediate involving a Me group. This catalyst does polymerise olefins, therefore

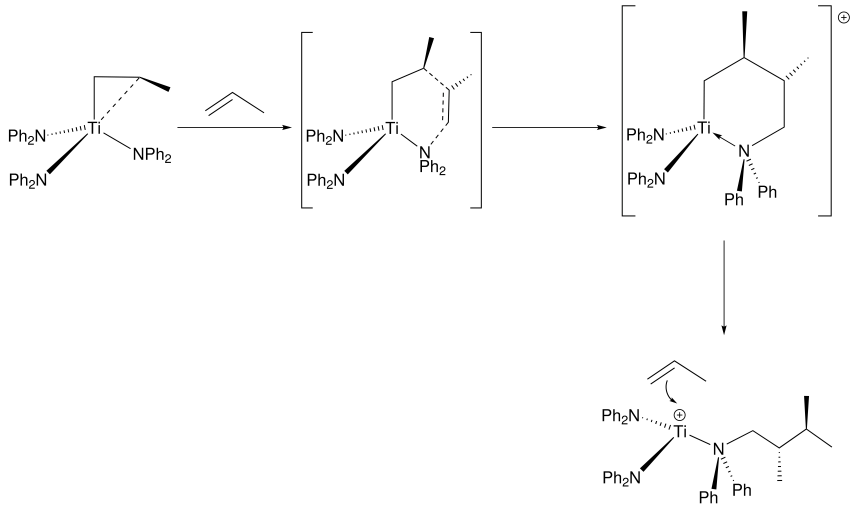

Figure 3.12: Hypothesised mechanism for the structural change of catalysts

a new mechanism must be occurring. In order to assess the binding of propene to the cation, the methyl complex and the methylborate complex, experiments were conducted with stoichiometric quantities of propene on an NMR scale. With 1, 2 and 3 molar equivalents of propene, only free propene was observed in all cases, together with some polymer formation in the case of 2 and 3 molar equivalents in the presence of the cation. However, no bound species was observed.

3.7 Conclusions

$[(R_2N)_3Ti]^+[B(C_6F_5)_4]^-$ and $(R_2N)_3TiMeB(C_6F_5)_3$ are active propene polymerisation catalysts, as is $(R_2N)_3TiCl$ when activated by methylaluminoxane. Rate data collected by measurement of the pressure in the reaction vessel allowed overall rates to be calculated, the rate constants for which are given in Table 3.2.

Catalyst	k / s^{-1}	Catalyst	k / s^{-1}
$(dpta)_3TiCl + KB(C_6F_5)_4$	0.0013	$(dpa)_3TiCl + KB(C_6F_5)_4$	0.0013
$[(dpta)_3Ti]^+[B(C_6F_5)_4]^-$	0.0012	$[(dpa)_3Ti]^+[B(C_6F_5)_4]^-$	0.0009
$(dpta)_3TiCl + MAO$	0.0023	$(dpa)_3TiCl + MAO$	0.0018
$(dpta)_3TiMe + B(C_6F_5)_3$	0.0021	$(dpa)_3TiMe + B(C_6F_5)_3$	0.0013
$(dpta)_3TiMeB(C_6F_5)_3$	0.0013	$(dpa)_3TiMeB(C_6F_5)_3$	0.0012

Table 3.2: Rate constants for the various catalysts

Although these reactions are effectively first order, the rate is complicated by structural changes

in the catalytic system, the interconversion being almost certainly first order itself. The structural change in the catalyst also generates an active catalyst and the rate constants given in Table 3.2 are overall rate constants.

Of the three systems which contain elements of the necessary features of a conventional Ziegler-Natta catalyst, $(R_2N)_3TiMe$, a 14 electron Ti methyl, is inactive with respect to propene polymerisation. This is almost certainly due to the incorrect symmetry of the acceptor orbitals on titanium, coupled with a low Lewis acidity due to the absence of a formal positive charge.

When activated by $B(C_6F_5)_3$ to form the methylborate, or when a full formal positive charge is present, the *tris*amido titanium complexes do polymerise.

Chapter 4

Metathetical reactivity of *tris*(amido)titanium centres

4.1 Formation of C−H and C−C bonds

4.1.1 Peak oil and climate change

Fossil fuels are the main source of energy used today and a large part of the world's energy, approximately 80%, is supplied by the combustion of hydrocarbons. The advantage of storing energy in hydrocarbons is due to the low free energy of formation and the high free energy of combustion, as alkanes are made entirely of very strong C−C and C−H bonds. The strengths of these bonds make hydrocarbons very difficult to use as reactants, as their low energy orbitals are filled, and their high energy orbitals are empty. Consequently, there are no orbitals available to participate in the reaction.[158] Hydrocarbons will react with O_2 in a kinetically blocked reaction which releases the stored free energy and forms CO_2 and H_2O. An example of the combustion of a generic hydrocarbon, C_xH_y, is shown in Scheme 4.1. The emission of CO_2 in to the atmosphere is also very dangerous to the environment (*vide infra*).

$$C_xH_{y\,(g)} + \left(\frac{4x+y}{4}\right) O_{2\,(g)} \longrightarrow x\,CO_{2\,(g)} + \frac{y}{2}\,H_2O_{(l)}$$

Scheme 4.1: Combustion reaction of any hydrocarbon C_xH_y

Fossil fuels are also the dominant source of hydrogen used in industry today. There are two industrial processes used for the production of hydrogen. These reactions are known as the steam reforming reaction, and the water-gas shift reaction, and are shown in Scheme 4.2. The most important use of hydrogen gas is in the Haber-Bosch process, where ammonia is produced from the

reaction of hydrogen gas with nitrogen gas. Ammonia is the main source of the world's fertilizers. The industrial production of ammonia led to the "Green Revolution," where an increase in crop yields led to a significant increase in the rise of global population.

$$\mathrm{CH_{4\,(g)} + H_2O_{(g)} \longrightarrow CO_{(g)} + 3\,H_{2\,(g)}} \qquad \text{Steam reforming}$$
$$\mathrm{CO_{(g)} + H_2O_{(g)} \longrightarrow CO_{2\,(g)} + H_{2\,(g)}} \qquad \text{Water gas shift reaction}$$

Scheme 4.2: Industrial processes for the production of hydrogen, exemplified for methane

Fossil fuels are not an unlimited resource. In the future, the extraction of fossil fuels will peak, at which time a permanent decline in these natural resources will begin. This phenomenon is known as peak oil. When peak oil occurs, the cost of products that depend on fossil fuels and subsequently hydrocarbons for their existence, such as fertilizers and polymers, will increase. There will also be a rise in energy prices for transportation and heating. Finding an alternate source of fuel such as CH_3OH, is very important for the future.

The combustion of hydrocarbons emits approximately 2.7 $\times 10^{10}$ tons, or 6.135 $\times 10^{14}$ moles, of CO_2 in to the atmosphere every year. The current inability to efficiently functionalise CO_2 is the major reason why the carbon cycle is effectively open, given the uncontrolled release from combustion and other industrial sources. Functionalisation of CO_2 is one approach to the closure of the carbon cycle and catalytic conversion technologies are therefore needed.

These routes are necessarily reductive and thus require the formation of C−H and C−C bonds. Reducing CO_2 is very difficult because it is the thermodynamic sink for combustion, with a $\Delta G^{\ominus}$ of -393.4 kJ/mol. Moving up the free energy surface to oxygenates such as formaldehyde, formic acid, and methanol are therefore uphill thermodynamic reactions.

4.1.2 Overview of the work

The metathetical reactions performed in this chapter, including the synthesis of *tris*$(NR_2)_3$titanium hydrides, *tris*$(NR_2)_3$titanium alkyls, *tris*$(NR_2)_3$titanium formates, and *tris*$(NR_2)_3$titanium, are all key intermediates for the synthesis of oxygenates. Titanium was chosen as the transition metal because it has a low electron couple. This single electron couple, is sufficient for the difference in free energy between CO_2 and CH_3OH, or any other oxygenate intermediates. Titanium is also a relatively cheap metal, with a large abundance in nature. Amide ligands were chosen for the platform because they allow for electronic flexibility, and for an electron deficient metal centre. In order for a suitable reduction to occur at the metal centre, it must be electron deficient. The main focus for this chapter was the synthesis of a *tris*$(NR_2)_3$titanium hydride. The syntheses, react-

ivities, and molecular structures of several *tris*(NR_2)$_3$titanium complexes used for the attempted synthesis of the *tris*(NR_2)$_3$titanium hydride are also addressed in this chapter.

4.2 Ligand Syntheses

4.2.1 Synthesis of ddaLi (12)

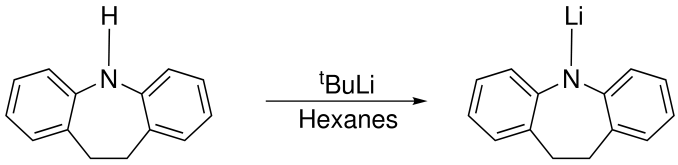

Scheme 4.3: The synthesis of ddaLi (12)

10,11-dihydro-5*H*-[*b*,*f*]-azepine, better known as iminodibenzyl, was the amide ligand chosen for the metathetical results reported in this chapter. For clarity in schemes and figures, this ligand will be referred to as dda from this point forward. The synthesis of ddaLi is accomplished in the same manner as the other Li salts in Chapter 2. The synthesis of (12) is shown in Scheme 4.3. The salt is produced in approximately 98% yield. This salt is insoluble in hydrocarbon solvents, and is only partially soluble in toluene and benzene.

4.2.2 Room temperature NMR studies of (12)

The presence of (12) was confirmed by ^{1}H NMR spectroscopy in d_8-THF. Similar behaviour seen in the aromatic region of this compound is seen in the aromatic region of (dpta)$_3$TiCl. Before the deprotonation of dda, there are two doublets and two triplets seen in the aromatic region of the ^{1}H spectrum. After the salt is deprotonated, the aromatic region contains a multiplet at 6.5 ppm. Similar to dptaLi, the ^{1}H spectrum also indicates clustering or dimeric behaviour in ethereal solution.[139,140] The ^{1}H spectrum is shown in A.4. There is also a singlet at 7.3 ppm. The hydrogen atoms on the backbone of the nitrogen ring are assigned to the singlet at 2.8 ppm. There is also a residual amine resonance at 6.0 ppm. This compound was washed multiple times, but the residual amine remained.

To show the assignment of the carbons on (12), the numbering system on Figure 4.1 was followed.

The ^{13}C NMR spectroscopic resonances for this compound are assigned to 165.6 ppm for the *ipso* carbon bound to the nitrogen, and 112.5 ppm for the carbons *ortho* to the nitrogen. The resonance at 126.8 ppm is assigned to carbons *meta* to the nitrogen, and the resonance at 124.0 ppm

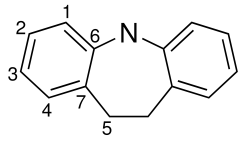

Figure 4.1: Numbering system for the carbon assignment of dda systems

is assigned to the carbons *para* to the nitrogen. The *ipso* carbon bound to the nitrogen is assigned to the resonance at 165.6 ppm, while the *ipso* carbon bound to the carbon on the nitrogen ring is assigned to the resonance at 130.7 ppm. The carbons on the backbone of the seven-membered nitrogen ring is assigned to the resonance at 40.1 ppm. The ^{13}C data are collated in Table 4.1.

Carbon	δ / ppm	Carbon	δ / ppm
C_1	112.5	C_5	40.1
C_2	126.8	C_6	165.6
C_3	124.0	C_7	130.7
C_4	132.7		

Table 4.1: ^{13}C NMR spectral resonances of (12)

The salt is soluble in diethyl ether and tetrahydrofuran. This compound is a very fine white powder. The oxygen and water sensitivity of (12) is similar to the other Li salts. Electrospray ionization mass spectrometry contained the parent ion at 195 m/z. Elemental analysis confirmed the purity of this product.

4.2.3 Synthesis of $(dda)_3TiCl$ (13)

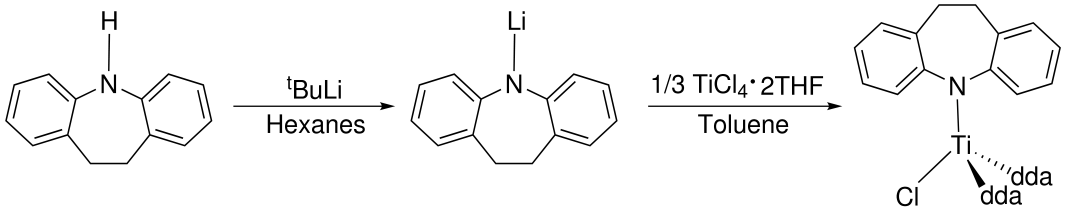

Scheme 4.4: The synthesis of $(dda)_3TiCl$ (13)

The synthesis of (13) is achieved in the same way as $(dpa)_3TiCl$ and $(dpta)_3TiCl$ complexes. The chloride is produced when three molar equivalents of (12) are added to one equivalent of $TiCl_4 \cdot 2THF$. This reactions yields $(dda)_3TiCl$ in approximately 80% yield. The reaction mixture is recrystallized from a mixture of toluene and hexane, and produces a microcrystalline orange

powder. The synthesis of $(dda)_3TiCl$ is shown in Scheme 4.4.

4.2.4 Room temperature NMR studies of (13)

The aromatic region of the ^1H spectrum of (13) is difficult to assign due to extensive coupling of the protons on the aromatic ring, seen in Figure 4.2. There is coupling between H_a and H_b. There is also coupling between H_b and H_c, and H_c and H_d. There is also long range coupling between H_a and H_c, and H_d and H_b. This kind of system is known as the four spin system ABCD.[141]

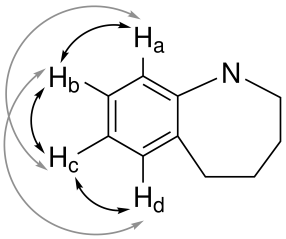

Figure 4.2: H,H couplings in dda ligand

Due to the extensive coupling amongst the protons on the dda ligand, the ^1H spectrum consists of one doublet and one large multiplet in the aromatic region, and two broad singlets in the aliphatic region. The resonances in the aromatic region of the ^1H spectrum of (13) were unable to be assigned by traditional methods. Simulation methods were then attempted on the complex in order to assign coupling constants to the protons in the ^1H spectrum.

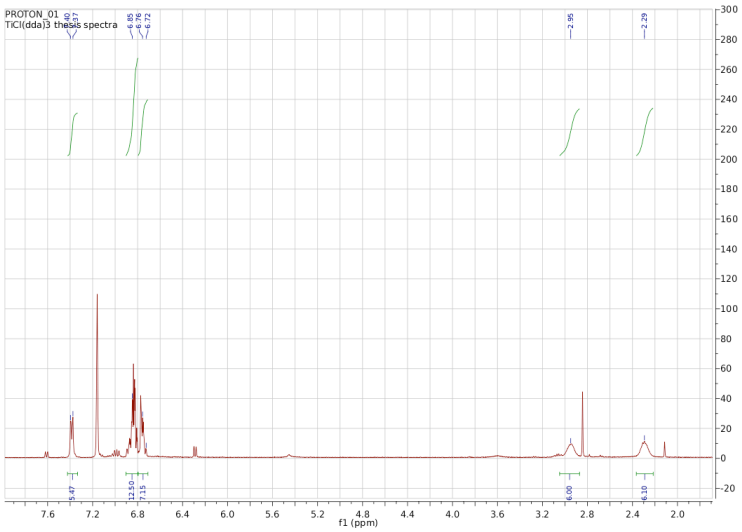

Figure 4.3: ^1H spectrum of (13)

Spinworks[159] was used to simulate the spectrum in collaboration with Dr. Iain Day and Dr. Ian Crossley in order to assign the coupling constants for the ^1H spectrum. This simulation used a line

broadening of 1.8 Hz and the following parameters were derived from initial approximations. The simulations were then iterated against the experimental spectrum of (13), seen in Figure 4.3. The best convergence attained with this simulation was an RMS deviation of 13%, which is obviously very poor. The following problems can be attributed to the poor convergence-poor resolution of the sample, poor shimming by the spectrometer, and presence of (12) in the ^{1}H aromatic region. By changing the parameters many times, one set of resonances would begin to converge in agreement, but then the other resonances would diverge. The simulation data is shown below in Figure 4.4.

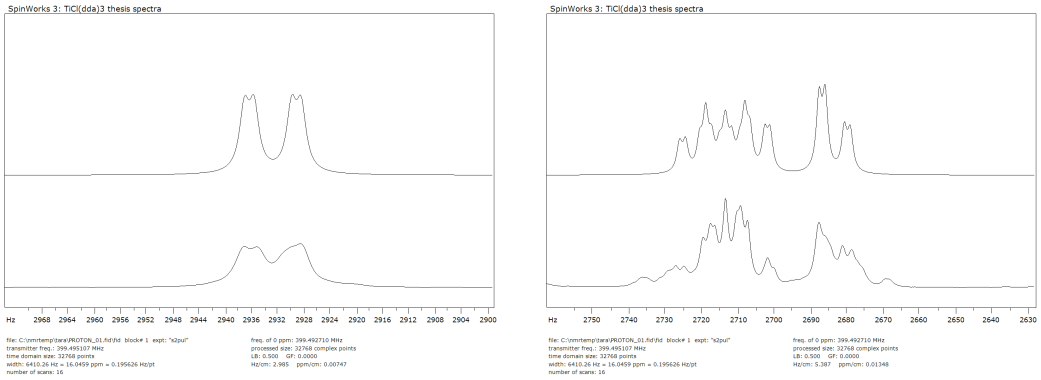

(a) (b)

Figure 4.4: (a): Real and simulated spectra for resonance assigned H_a and (b): Real and simulated spectra for resonances assigned H_b, H_c, and H_d

The resonance assignments produced from the simulation are collated below in Table 4.2. The coupling constants are collated below in Table 4.3. Unfortunately, these coupling constants can not be stated as fact, due to the poor agreement between the simulated and actual spectrum. Simulation data with perfect agreement can still only be reported as one possible solution. In theory, many combinations could provide the same simulation data. A ^{1}H spectrum of a few different samples of (13) was run on the 400 MHz and 600 MHz spectrometers in order to achieve a better resolution for simulation data. Unfortunately, these samples did not produce spectroscopic data with better resolution.

Proton Assignment	δ/ppm	Coupling Pattern
H_a	7.3	multiplet
H_b	6.8	multiplet
H_c	6.7	multiplet
H_d	6.7	multiplet

Table 4.2: Simulation data for the ^{1}H NMR spectral resonances of (13)

Coupling constant assignment	H-H coupling constant/Hz
J_{ab}	7.2
J_{ac}	1.5
J_{ad}	0.0
J_{bc}	5.6
J_{bd}	1.5
J_{cd}	6.9

Table 4.3: Simulation data for the ^{1}H NMR spectral resonances of (13)

The numbering system that will be used for the assignment of protons in further dda systems can be seen in Figure 4.5. The ^{1}H spectrum of $(dda)_3TiCl$ has resonances in the conventional aromatic region, one of which can be resolved, and three which cannot. The resonance at 7.3 ppm is assigned to H_a, and the resonance at 6.7 ppm is assigned to H_d. The multiplet between 6.7 ppm and 6.9 ppm is assigned to H_b and H_c. This multiplet cannot be resolved into single resonances. The nitrogen containing ring has four hydrogen atoms on the backbone of the ring, represented by H_e. Two of these protons are in the *cis* configuration, and the other two are in the *trans* configuration. These hydrogen atoms are represented in the aliphatic region of the spectrum. The resonances at 2.2 ppm and 2.9 ppm are assigned to H_e. These two resonances are very broad due to extensive coupling between the *cis* and *trans* protons. The ^{1}H spectrum is shown below in Figure 4.3, and the resonances are collated in Table 4.4.

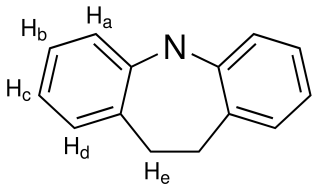

Figure 4.5: Numbering system for the proton assignment of (12)

Proton Assignment	δ/ppm	Coupling Pattern
H_a	7.3	multiplet
H_b, H_c	6.7-6.9	multiplet
H_d	6.7	multiplet
H_e	2.2, 2.9	singlet

Table 4.4: ^{1}H NMR spectral resonances of (13)

Two dimensional spectroscopic data was consulted for assignment of the carbon resonances. The HSQC spectrum for this compound is shown in Figure 4.6. The resonance at 151.1 ppm is assigned to C_6, shifted downfield due to its close proximity to the nitrogen atom. Because the proton resonances can not be resolved to specifically assign H_b and H_c, the carbon atoms correlated to these protons can not be assigned either. The resonances at 126.3 ppm and 126.8 ppm are therefore assigned to C_2 and C_3. The resonance at 126.1 ppm is assigned to C_1, and the resonance at 130.6 is assigned to C_4. The upfield resonance at 31.6 ppm is assigned to C_5 The resonance assignments are collated in Table 4.5.

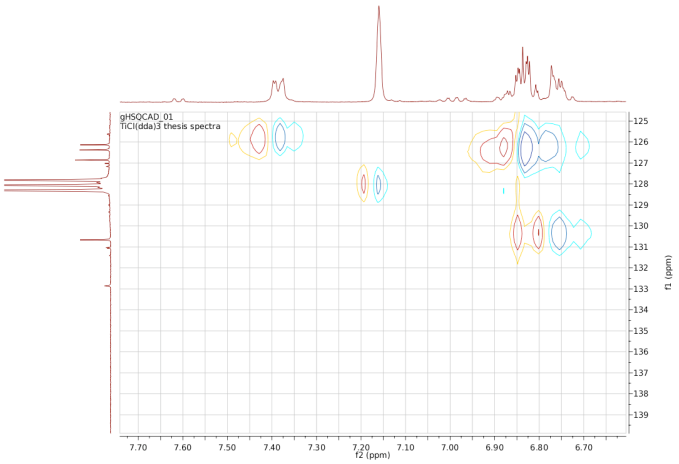

Figure 4.6: The HSQC spectrum of (13)

This product is soluble in ethers, not soluble in hydrocarbon solvents, and slightly soluble in benzene and toluene. Electrospray ionization mass spectrometry also confirmed the purity of this product. The parent ion was found at 666 m/z. The spectral resonances are assigned in Table 4.5. Elemental analysis confirmed the purity of this product.

Carbon Assignment	δ/ppm
C_1	126.1
C_2, C_3	126.8, 126.3
C_4	130.6
C_5	31.6
C_6	151.1
C_7	132.8

Table 4.5: ^{13}C NMR spectral resonances of (13)

4.2.5 Synthesis of $(dda)_3TiMe$ (14)

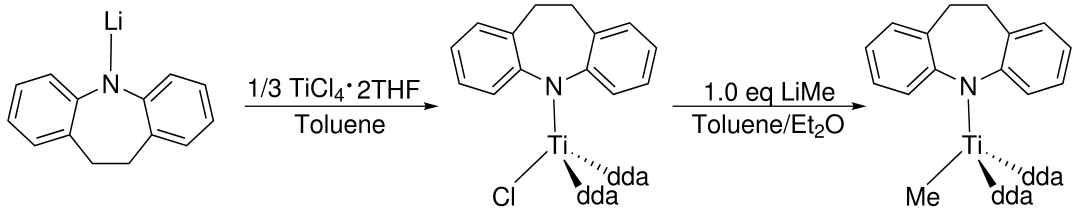

Scheme 4.5: The synthesis of $(dda)_3TiMe$ (14)

The synthesis of (14) is accomplished in a one-step metathesis reaction from (13). One equivalent of LiMe is slurried in toluene, with a few drops of Et_2O added to increase the solubility. A toluene slurry of (13) is prepared, at which time both of these reactants are placed in the -40°C freezer for at least an hour. After an hour, the LiMe/toluene/Et_2O mixture is added to the $(dda)_3TiCl$/toluene mixture. The $(dda)_3TiCl$ solution is dark orange in colour before addition of LiMe. After addition, the solution is bright orange. The mixture is allowed to warm to room temperature while being stirred for a period of three hours. The solution is then filtered through a fine frit to remove any excess LiCl. The bright orange solution is then concentrated to half its volume, at which time an equal amount of hexane is added to the solution. The solution is put in the -40°C freezer overnight, at which time, a bright orange microcrystalline powder precipitates out of solution. The solution is then filtered, and the product is formed in approximately 50% yield. The synthesis of (14) is shown in Scheme 4.5.

4.2.6 Room temperature NMR studies of (14)

The ^1H spectrum of (14) is similar to the ^1H spectrum of (13). The assignment of the various resonances is very difficult due to the coupling between the protons on the rings. This spectrum also appears to contain resonances from a small amount of (13) as an impurity. The 2D spectroscopic data analysed was unable to help with the assignment of the proton resonances. The resonance at 7.2 ppm is assigned to H_a, and the resonance at 6.8 is assigned to H_d. The resonance at 6.9 ppm is assigned to H_b and H_c. The resonances at 2.4 ppm and 3.0 ppm are assigned to H_e. The resonance at 0.5 ppm is assigned to the protons of the methyl group bound to the titanium. The ^1H spectrum is shown below in Figure 4.7, and the resonances are collated in Table 4.6.

Two dimensional spectroscopic data was consulted for the assignment of the carbon resonances. The HSQC spectrum for this compound is shown in Figure 4.8. The resonance at 32.1 ppm, is assigned to C_5. The resonance at 61.5 ppm is assigned to the carbon of the methyl group bound to titanium. The resonance at 125.7 ppm is assigned to C_1, and the resonance at 130.8

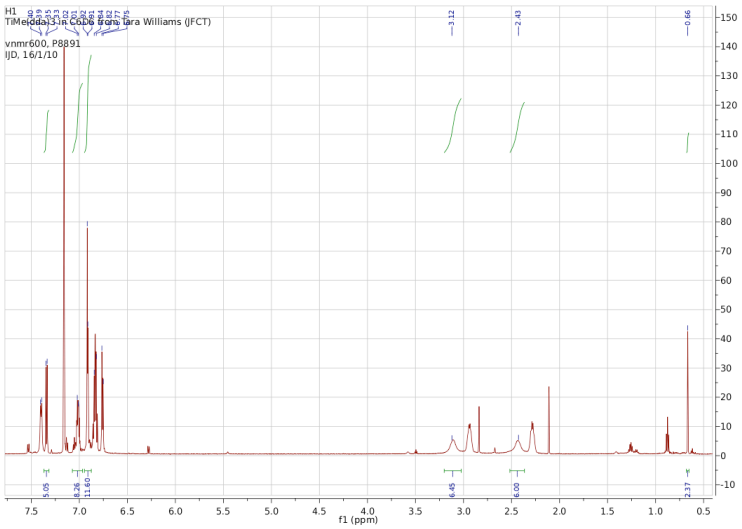

Figure 4.7: ^{1}H spectrum of (14)

Proton Assignment	δ/ppm	Coupling Pattern
H_a	7.2	multiplet
H_b, H_c	6.9	multiplet
H_d	6.8	multiplet
H_e	2.4, 3.1	singlet
methyl	0.6	singlet

Table 4.6: ^{1}H NMR spectral resonances of (14)

ppm is assigned to C_4. The resonances at 126.3 ppm and 126.8 ppm are assigned to C_2 and C_3. *ortho* carbon is also shifted downfield due to its closer proximity to the nitrogen atom. The resonance at 150.2 ppm is assigned to C_6 and the resonance at 134.0 is assigned to C_7. The resonance assignments are collated in Table 4.7.

This product has similar solubility to (13). It is soluble in ethers, insoluble in hydrocarbon solvents, and slightly soluble in benzene and toluene. Elemental analysis confirmed the purity of this product.

4.2.7 Molecular structure of (14)

Single crystals of (14) were also obtained by slow-cooling of a saturated solution of toluene and hexane to -40°C in the glovebox. The molecular structure is shown in Figure 4.9. The lattice parameters for the crystal structure are outlined in Table 4.8. This complex crystallises in space group $Pa\bar{3}$.

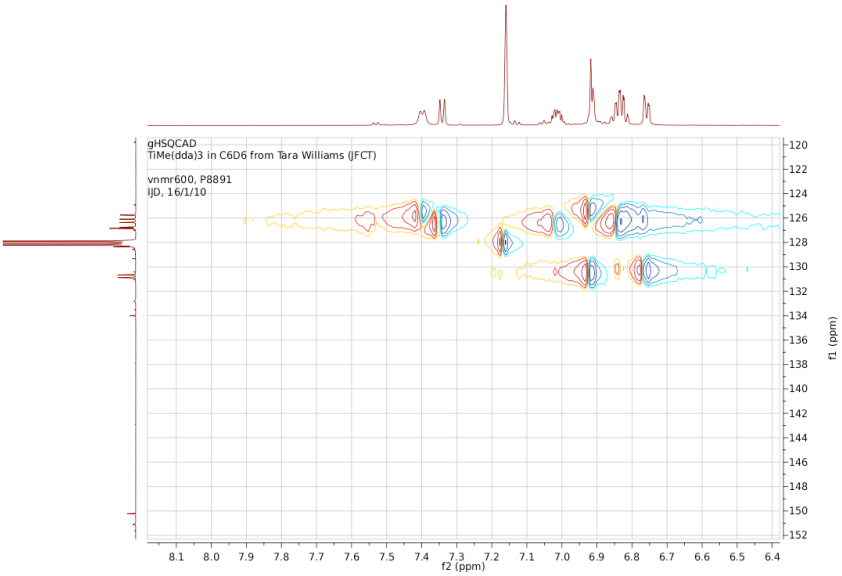

Figure 4.8: The HSQC spectrum of (14)

Carbon Assignment	δ/ppm
C_1	125.7
C_2, C_3	126.3, 126.8
C_4	130.8
C_5	32.1
C_6	150.2
C_7	134.0
methyl	61.5

Table 4.7: ^{13}C NMR spectral resonances of (14)

Lattice parameters and constants			
a	18.9130(2) Å	Space group	$Pa\bar{3}$
b	18.9130(2) Å	V_{cell}	6765.21(12) Å^3
c	18.9130(2) Å	Z	8
α, β, γ	90°		

Table 4.8: Salient structural parameters for the crystal structure of (14)

Similar to (13), this complex is also a *pseudo* tetrahedral molecule with C_3 symmetry. The C_3 symmetry of (14) is emphasised in Figure 4.9(b). The molecule itself is a C_3 axis, which is shown in the asymmetric unit, in Figure 4.9(a). This complex is also a four-coordinate titanium centre.

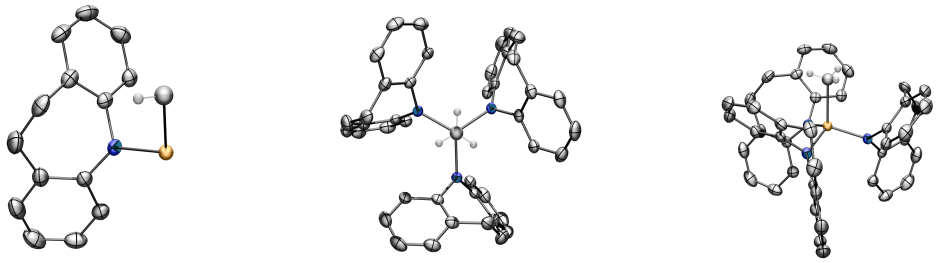

(a) (b) (c)

Figure 4.9: (a): The asymmetric unit of (14); (b): a view along the C_3 axis in the molecular structure of (14) and (c): the molecular structure of (14)

It is ligated by three dda ligands, and a methyl group. Important bond lengths for this structure along with their deviation from the average are collated in Table B.1. Important bond lengths for this structure and their deviation from a tetrahedral angle of 109.5°are collated in Table B.2. Both of these tables are located in Appendix B.

The Ti−N bond length of (14) is also within the average range of four-coordinate Ti−NR_2 complexes found in the CCSD.[143] The average Ti−N bond length found in the CCSD for four-coordinate Ti−NR_2 complexes ranges from 1.83 Å, to 2.05 Å. The Ti−N bond length for (14) was found to be 1.9221 Å. All of the Ti−N bond lengths for (14) are unexceptional, and fall within this range. The Ti−CH_3 bond length for $(dda)_3$TiMe is 2.1142 Å. A search of the CCSD[143] found the average Ti−CH_3 bond length for four-coordinate Ti complexes to be 2.106 Å. The Ti−CH_3 bond for this complex is therefore found in the average range. Approximately 3% of the crystals show contamination with (13) indicating unresolved effects such as substitional disorder. The H−C−Ti bond angle in (14) is therefore a bit smaller due to this contamination. The methyl group was "normal," meaning no agostic interaction was seen. The N−Ti−CH_3 bond angle is 107.55°, deviating more from tetrahedral geometry than the (13). The N−Ti−N bond angles also deviate slightly with the bond angle being given as 111.32°. Even though these angles deviate slightly from 109.5°, *pseudo*-tetrahedral geometry is still seen at the Ti centre of (14).

Structural comparison between $(dda)_3$TiCl (13) and $(dda)_3$TiMe (14)

Previous work in the group by Andrew Colvin[160] has yielded the structure of (13), which also possesses a strong C_3 symmetry around the Ti-X vector.

With such a symmetric molecular packing, both crystallise in high symmetry space groups. The Ti-N bonds in the methyl complex are longer than in the chloride *viz* 1.909 Å, in the chloride in comparison with 1.9221 Å, in the methyl which is consistent with the presence of the more

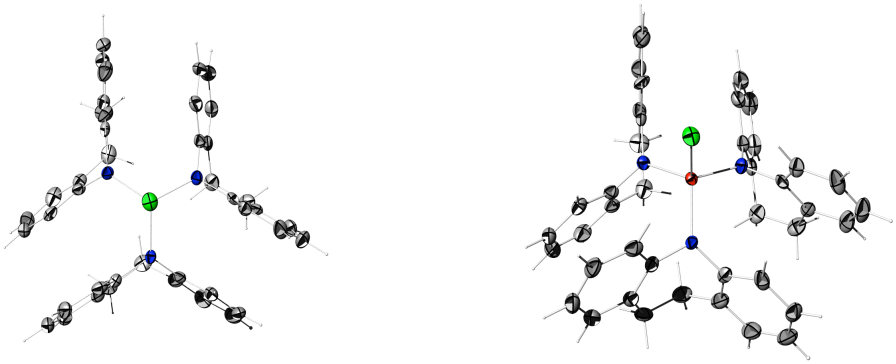

(a) (b)

Figure 4.10: (a): A view along the C_3 axis in the molecular structure of (13) and (b): The molecular structure of (13)

electronegative chloride moiety.

4.2.8 Synthesis of $(dda)_3TiBH_4$ (15)

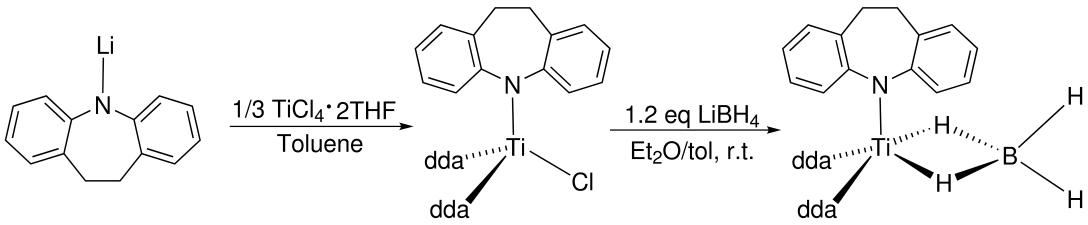

Scheme 4.6: The synthesis of $(dda)_3TiBH_4$ (15)

The synthesis of (15) is accomplished in a metathesis reaction from (13). 1.2 equivalents of $LiBH_4$ is slurried in toluene, with a few drops of Et_2O added to increase the solubility. A toluene slurry of (13) is prepared, at which time the $LiBH_4$/toluene/Et_2O mixture is added to the $(dda)_3TiCl$/toluene mixture. The solution of (13) is dark orange in colour before addition of $LiBH_4$. After addition, the solution is bright orange. The mixture is allowed to stir for a period of twenty-four hours. The solution is then filtered through a fine frit to remove any excess LiCl. The bright orange solution is then concentrated to half its volume, at which time an equal amount of hexane is added to the solution. The solution is put in the -40°C freezer overnight, at which time, a bright orange microcrystalline powder precipitates out of solution. The solution is then filtered, and the product is formed in approximately 65% yield. The synthesis of (15) is shown in Scheme 4.6.

4.2.9 Room temperature NMR studies of (15)

The ^{1}H spectrum of (15) is also similar to the ^{1}H spectrum of (13). The broad resonance from 1.1 ppm to 2.0 ppm is assigned to the four protons of the BH_4 group. The resonance at 7.3 ppm is assigned to H_a, and the resonance at 6.8 ppm is assigned to H_d. The resonance at 6.8 ppm is assigned to H_b and H_c. The broad singlets at 2.3 ppm and 3.0 ppm are assigned to H_e. The ^{1}H spectrum is shown below in Figure 4.11, and the resonances are collated in Table 4.9.

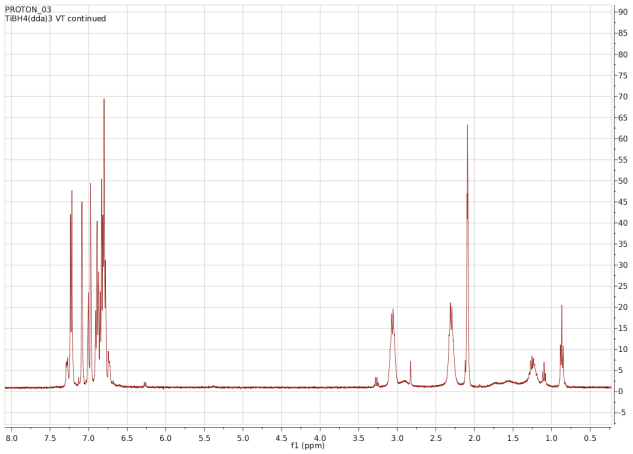

Figure 4.11: ^{1}H spectrum of (15)

Proton Assignment	δ/ppm	Coupling Pattern
H_a	7.3	multiplet
H_b, H_c	6.8	multiplet
H_d	6.8	multiplet
H_e	2.3, 2.9	singlet
BH4	1.1-2.0	multiplet

Table 4.9: ^{1}H NMR spectral resonances of (15)

The protons on the BH_4 group in this complex are unresolvable at room temperature. Common nuclei used in NMR experiments such as ^{1}H and ^{13}C have an I of 1/2. The equation commonly used to find the number of lines in a multiplet, or multiplicity, is $M = 2In + 1$, where n is the number of equivalent neighbour nuclei. This equation then simplifies to $M = n + 1$ for proton and carbon experiments. For these nuclei, the intensities within each multiplet correspond to a binomial series, which is obtained from Pascal's triangle.[141] For ^{11}B however, the I = 3/2. Nuclei with I higher than 1/2 tend to make analysis more difficult due to unusual multiplicities. Nuclei with a large nuclear spin quantum number also tend to have a large quadrupole moment, causing significant

broadening in the NMR spectrum of the nuclei, and in the spectrum of the nuclei directly attached. The quadrupole moment for tetrahedral molecules, such as BH_4, is small or zero, however. There is significant broadening seen in the ^1H spectrum of (15). For the BH_4 signal in this complex, the multiplicity is calculated to be a quartet, using $M = (2)(3/2)(1) + 1 = 4$. In this experiment, $LiBH_4$ was used as the borohydride source. Due to the tetrahedral symmetry of this compound, there is no line broadening in the ^1H spectrum, and a perfect quartet is seen at room temperature. When the BH_4 group is bound to the titanium, the four protons lose tetrahedral symmetry as they are bound μ^2 to the titanium atom, the coordination of which was found in the solid state structure. This loss of symmetry causes the broadening seen in the ^1H spectrum (*vide infra*).[161] The coordination geometry of the BH_4 group will be discussed in the next paragraph. This experiment was also repeated using $NaBH_4$ instead of $LiBH_4$ in order to check the deuterium spectrum to verify the structure of the compound. One equivalent of $NaBH_4$ was added to one equivalent of $(dda)_3TiCl$ in h_6-toluene in a Young's tube. A deterium spectrum was collected on the product. The spectrum showed one only resonance, indicating that the deuteriums were in the same environment.

Infrared spectroscopy is also a useful tool when examining the structure of transition metal borohydride complexes. Vibrational spectroscopy is used to discern how the BH_4 ligand is coordinated to the transition metal centre, as hydrogen atoms are often difficult to locate using only X-ray diffraction methodology. There are three possible ligation geometries for BH_4 which are monodentate, bidentate, and tridentate, examples of which are shown in Figure 4.12. For a monodentate structure, the terminal B−H stretches are found around 2375 cm^{-1}. The bridging stretch is typically found around 2000 cm^{-1}, and the BH_2 deformation around 1075 cm^{-1}. For a bidenate structure with C_{2v} symmetry, there are 12 normal modes of vibration. Terminal B−H stretches, both symmetric and antisymmetric are usually found in the range of 2400 to 2600 cm^{-1}. Bridging B−H stretches, both symmetric and antisymmetric are typically found as overlapped bands around 2000 cm^{-1}. Two other bands, one for a the second bridging stretch is found around 1400 cm^{-1}, and one stretch for BH_2 deformation is observed at 1100 cm^{-1}. For a tridenate structure with C_{3v} symmetry, there are 8 normal modes of vibration. A sharp bridging terminal stretch is typically found at 2560 cm^{-1}, whereas the bridging B−H stretch is typically found at 2100 cm^{-1}. A bridge deformation stretch is also found around 1200 cm^{-1}. The location of the different infrared bands and their shape can consequently identify the ligand coordination of a transition metal borohydride.[162]

Two dimensional spectroscopic data was consulted for the assignment of the carbon resonances. The resonance at 31.6 ppm is assigned to C_5, and the resonance at 126.2 is assigned to C_1. The resonances at 126.3 ppm and 126.7 ppm are assigned to C_2 and C_3. The resonance at 130.7

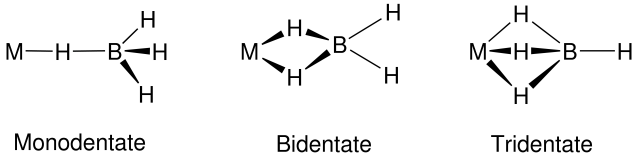

Figure 4.12: Possible coordination geometries of BH_4 transition metal complexes

ppm is assigned to C_4 and the resonance at 132.4 ppm is assigned to C_7. The resonance at 154.9 is assigned to C_6. The HSQC spectrum for this compound is seen in Figure 4.13. The resonance assignments are collated in Table 4.10.

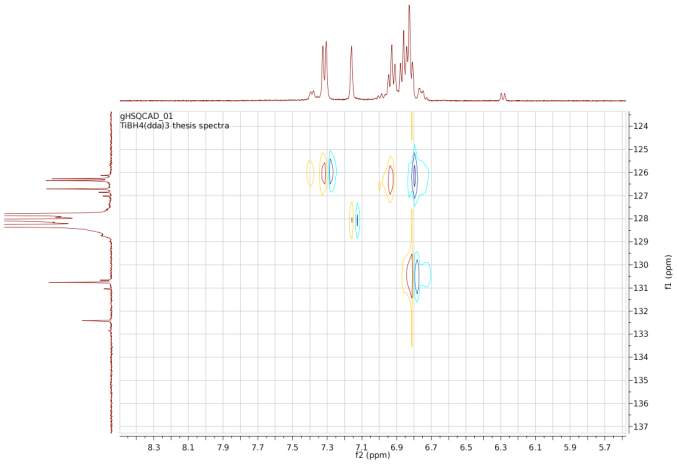

Figure 4.13: The HSQC spectrum of (15)

This product has similar solubility to (13). It is soluble in ethers, insoluble in hydrocarbon solvents, and slightly soluble in benzene and toluene. Electrospray ionization mass spectrometry also confirmed the purity of this product. The parent ion was found at 644 m/z. Elemental analysis confirmed the purity of this product.

Carbon Assignment	δ/ppm
C_1	126.2
C_2, C_3	126.7, 126.3
C_4	130.7
C_5	31.6
C_6	154.9
C_7	132.4

Table 4.10: ^{13}C NMR spectral resonances of (15)

4.2.10 Variable temperature NMR studies of (15)

Variable temperature ^{1}H NMR experiments were performed on (15) in order to resolve the broad resonance between 1.0 ppm and 2.0 ppm. This resonance is representative of the four protons of the BH_4 group. All of the experiments were performed on the same sample, dissolved in d_8 toluene. These data from these experiments are shown below in Figure 4.14 and Figure 4.15.

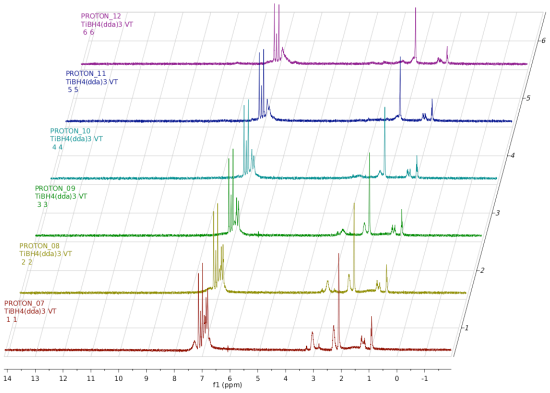

Figure 4.14: The low temperature ^{1}H stacked plot of $(dda)_3TiBH_4$ from -30°C (bottom) to -80°C (top)

In the low temperature data, the experiments performed at -30°C and -40°C still show a broad multiplet between 1.0 ppm and 2.0 ppm. From -50°C to -80°C, the multiplet for the BH_4 protons disappears, and the spectrum completely flattens between 1.0 ppm and 2.0 ppm. In the high temperature stack plot, the spectrum on the bottom is representative of the experiment at 50 °C. The multiplet begins to resolve at 50 °C, and has completely resolved into a quartet at 100 °C.

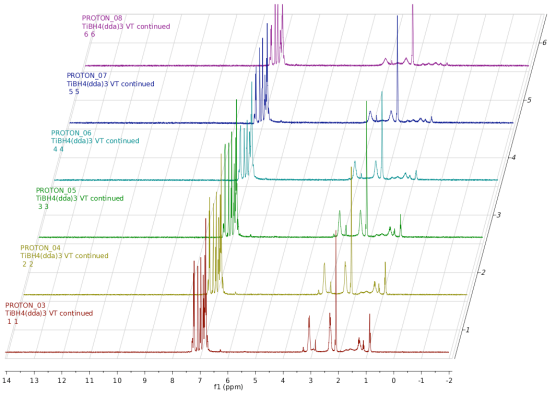

Figure 4.15: The high temperature ^{1}H stacked plot of $(dda)_3TiBH_4$ from 50°C (bottom) to 100°C (top)

The high temperature averaging and broad nature of the resonances at room temperature are in

accord with the solid state structure of the system, which shows an η^2-BH_4 unit. This structure was resolved at the University of Tennessee by Andy Colvin.[160] The molecular structure is shown in Figure 4.16.

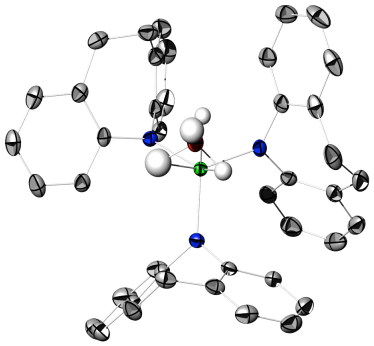

Figure 4.16: The molecular structure of (15)

4.3 Synthesis of $(dda)_3TiH$

4.3.1 Recent work on transition metal formates

As mentioned in the overview for this chapter, transition metal hydrides are very important in the possible syntheses of transition metal oxygenates. The insertion of CO_2 into a M−H bond for the formation of a metalloformate has been studied extensively over the years.[163–169] Studies have found that an important step in the hydrogenation of CO_2 involves the formation of a metalloformate, of the form, LnM−OC(O)H. Two examples showing the insertion of CO_2 into a M−H bond are discussed below.

The use of thallium complexes in transition metal metathesis has been studied by Parkin *et. al.*[170] Dialkyl zinc complexes, ZnR_2, were metathesised with Tl[^{tBu}Tp], where [^{tBu}Tp], is *tris*-(3-*tert*-butylpyrazolyl)hydroborato in order to form four-coordinate monoalkyl zinc complexes. This reaction scheme is shown in Scheme 4.7.

These monomeric four-coordinate alkyl zinc complexes were the first zinc alkyl derivatives supported by a η^3-*tris* Tp ligand.[171–173] [^{tBu}Tp]ZnMe was characterised by NMR spectroscopy in order to monitor its reaction with other reagents. A deposition of Tl accompanies this reaction due to the decomposition of unstable TlR, which is an irreversible process. This decomposition provides an effective driving force for this reaction to occur.[174] As the use of the Tp ligand was successful in supporting the monomeric zinc alkyl derivatives in the synthesis of four-coordinate alkyl zinc complexes, this method was performed to try and isolate the [^{tBu}Tp]ZnH. The trans-

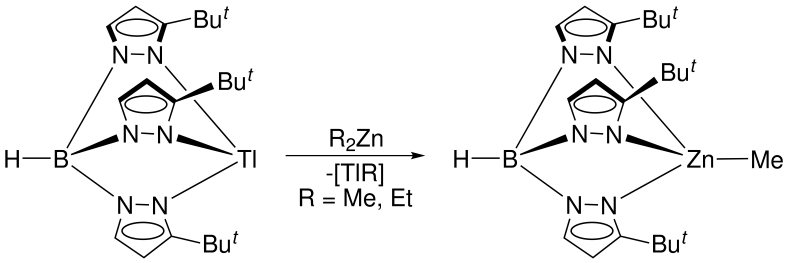

Scheme 4.7: Metathetical reaction between Me_2Zn and Tl[^{tBu}Tp]

ition metal hydride, [^{tBu}Tp]ZnH was successfully synthesised by metathetically using ZnH_2 and Tl[^{tBu}Tp]. This reaction is shown in Scheme 4.8.

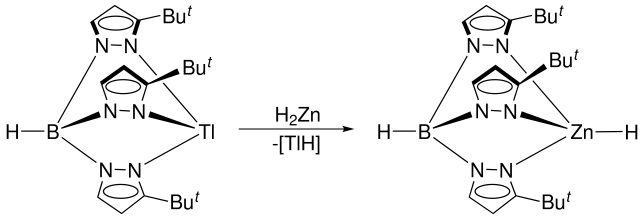

Scheme 4.8: Metathetical reaction between H_2Zn and Tl[^{tBu}Tp]

The molecular structure of this complex was determined by X-ray diffraction. The hydrogen atom bound to the ligand was not located by X-ray diffraction. The hydride resonance was observed at 5.36 ppm in the ^{1}H spectrum, however. This zinc-hydride functionality was tested with a number of substrates. The reaction of the [^{tBu}Tp]ZnH with CO_2 is shown in Scheme 4.9.

The insertion of CO_2 into the Zn−H species produced the η^1-formate derivative. The Zn−Me species, however, was unreactive with the addition of CO_2. [^{tBu}Tp]Zn(η^1−(O_2CH)), was also characterised by NMR spectroscopy. This complex exhibits a resonance at 8.91 ppm in the ^{1}H spectrum, and a resonance at 166.7 ppm in the ^{13}C spectrum. There is no molecular structure of this complex. The complex has been designated as an η^1-formate after examination of the infrared data. The large difference, around 365 cm^{-1}, in the symmetric and asymmetric CO_2 stretch is indicative of η^1 coordination. The insertion of CO_2 into the Zn−H bond indicates that a Zn−H bond is more reactive than a Zn−C bond with respect to four-coordinate transition metal centres.

The tantalaziridine-hydride complex, Ar[^{t}BuCH_2]N)$_2$(κ^2−CH_2C(Me)$_2$CH_2NAr)TaH, was recently synthesised by Rankin and Cummins.[175] This complex was synthesised for the insertion of CO_2 to form the transition metal formate species. Bimetallic methylene diolate complexes were formed instead. These bridging intermediates have been hypothesised to be intermediates between the formation of the formate from the hydride, yet the isolation of these complexes have remained

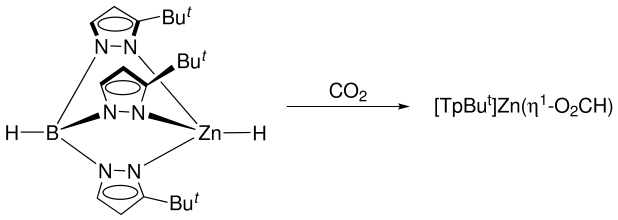

Scheme 4.9: Insertion of CO_2 into Zn−H bond

limited.[176–188]

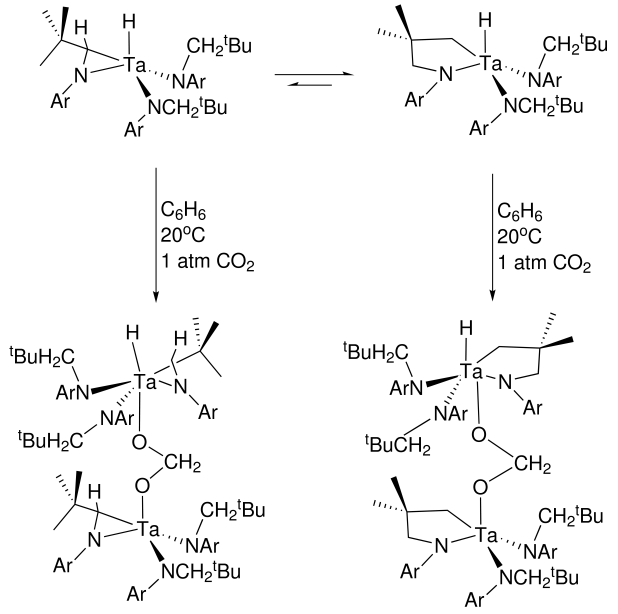

Scheme 4.10: Formation of Ar[^{t}BuCH$_2$]N)$_2$(κ^2−CH$_2$C(Me)$_2$CH$_2$NAr)Ta)$_2$(μ−OCH$_2$O)

The hydride was successfully synthesised following a previous route to a Nb−H complex.[189] The resonance for the Ta−H was found at 17.1 ppm in the ^{1}H NMR spectrum, and an absorbance of 1756 cm^{-1} was found in the infrared spectrum. This spectroscopic data was in agreement with previously published terminal hydride complexes.[190–193] The hydride complex undergoes conversion to an isomeric hydride complex in solution. Exposure of the hydride to one atmosphere of CO_2 led to the formation of Ar[^{t}BuCH$_2$]N)$_2$(κ^2−CH$_2$C(Me)$_2$CH$_2$NAr)Ta)$_2$(μ−OCH$_2$O). This synthesis is shown in Scheme 4.10. These products were determined to be a diastereomeric mixture. Combustion analysis supported this formulation. Analysis of the ^{13}C and ^{1}H spectroscopic data also confirmed the formation of the methylene diolate complex.

4.3.2 Synthetic routes to $(dda)_3TiH$

There are many routes towards the syntheses of transition metal hydrides; only the routes implemented in this chapter will be mentioned here. The synthetic routes performed for the synthesis of $(dda)_3TiH$ are outlined in Scheme 4.11. The first route is the direct metathesis from a hydride source. Hydrogenation of a transition metal alkyl is another route to the hydride. The third route is the abstraction of a BH_3 group from a transition metal borohydride. Direct metathesis for the formation of a transition metal formate was also attempted, with the intention of first forming the formate, and then subsequently forming the hydride. The attempted synthetic routes to the complex, $(dda)_3TiH$, are detailed in the following sections.

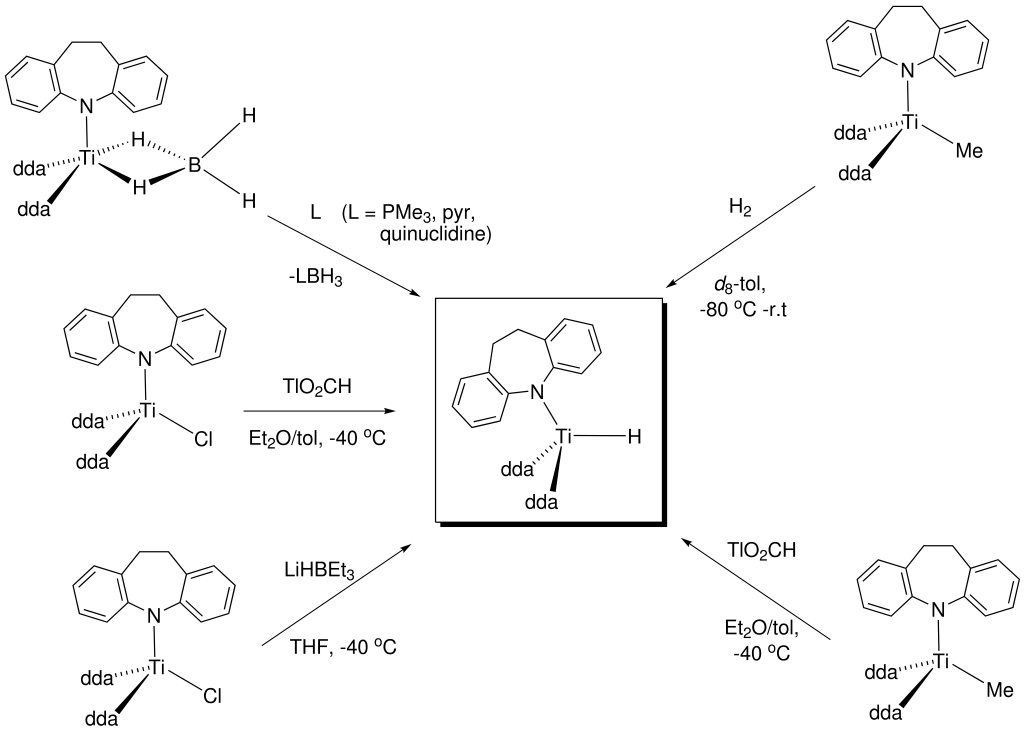

Scheme 4.11: The synthetic routes to $(dda)_3TiH$

4.3.3 Direct metathetical synthesis of $(dda)_3TiH$ using a hydride source

The first route to the $(dda)_3TiH$ investigated was the metathetical reaction of (13) with a hydride source. This synthesis is shown in Scheme 4.12. The hydride source chosen was $LiEt_3BH$. One equivalent of $LiEt_3BH$ in THF was added to one equivalent of (13) in THF. These reactants were cooled to $-40°C$ for an hour before addition. The reaction was allowed to warm up to room temperature after the addition was complete. The dark yellow solution was allowed to stir for twelve hours, at which time it was filtered, and the solvent was removed under reduced pressure. The first time this reaction was attempted, and allowed to stir at room temperature, the reaction

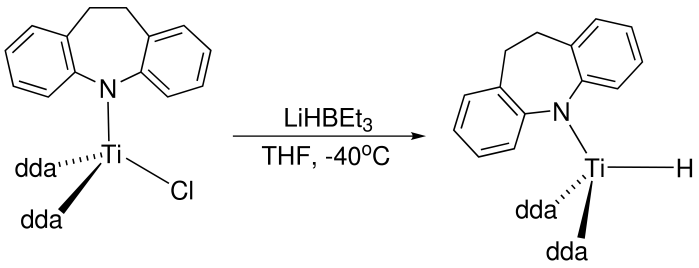

Scheme 4.12: Direct metathetical syntheses of $(dda)_3TiH$ using a hydride source

mixture darkened to a brown colour, during the twelve hour period. When the reaction was worked up, it was found that the dark brown colour change was an indicator for thermal decomposition. The reaction was run subsequent times and kept in the freezer. Even at low temperature, the reaction mixture always decomposed to a dark solution, with a gummy black precipitate. A ^1H spectrum of this compound was able to be recorded when this reaction was performed in a Young's tube, on a very small scale. One equivalent of (13), 0.0056 g, was added to a Young's valved tube in the glovebox. Deuterated THF was condensed into the tube, the solution was allowed to thaw and a ^1H spectrum of this compound was collected for comparison. The tube was taken back into the glovebox and 8.40 μL of $LiEt_3BH$ was added to the tube. The tube was shaken to ensure complete reaction and another ^1H spectrum was collected.

Since such a small amount of $LiEt_3BH$ was needed for the Young's tube reaction, the sample was dominated with (13), indicated in the ^1H spectrum. When comparing the ^1H spectrum before addition of $LiEt_3BH$ and then after addition, there does not seem to be a change observed in the aromatic region. Two new resonances do appear however. The first resonance is observed at 4.5 ppm , which is indicative of the presence of H_2. Resonances for H_2 typically appear between 4.40 ppm and 4.7 ppm.[194] There is another resonance at -1.2 ppm which is indicative of the presence of the $(dda)_3TiH$ species. There are also resonances at 0.7 ppm and 0.03 ppm for $LiEt_3BH$ still in the ^1H spectrum indicating that this reaction has not gone fully to completion. The presence of H_2 in the ^1H spectrum does however, indicate that the $(dda)_3TiH$ was formed, which is confirmed by the resonance for the hydride at -1.2 ppm. The reaction then proceeded forward to give off H_2. Figure 4.17 shows a stacked plot of (13) and (13) + $LiEt_3BH$. Even though this reaction did go to completion, and $(dda)_3TiH$ was successfully synthesised, the product was too unstable to be isolated.

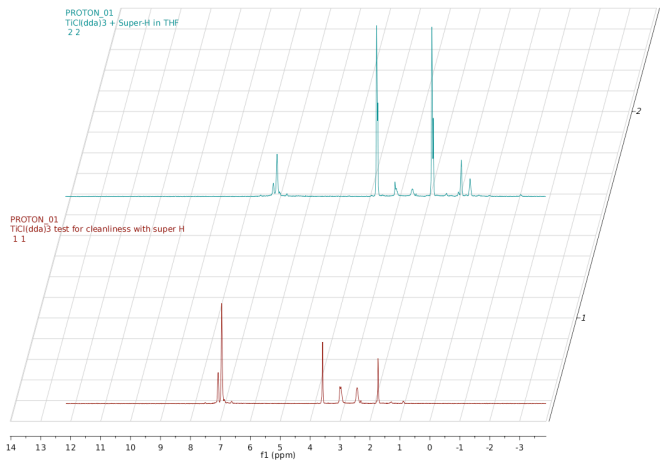

Figure 4.17: Stacked plot of the ^{1}H spectrum of (13) and (13) + $LiEt_3BH$

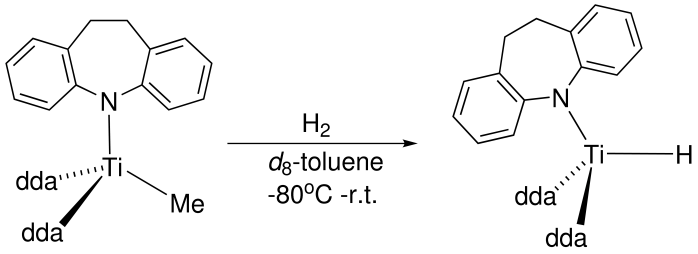

Scheme 4.13: Direct hydrogenation of $(dda)_3TiMe$ for the synthesis of $(dda)_3TiH$

4.3.4 Direct hydrogenation of (14) for the synthesis of $(dda)_3TiH$

The second route to the $(dda)_3TiH$ investigated was the direction hydrogenation of (14). This reaction is shown in Scheme 4.13. The reaction was performed small scale using a Toepler pump to ensure that exactly one equivalent of H_2 was condensed in the Young's tube. One equivalent of (14), 0.0490 g, was added to a Young's valved tube in the glovebox. Approximately 0.6 mL of deuterated toluene was condensed in to the tube. The solution was allowed to thaw and a ^{1}H spectrum of this compound was collected for comparison. The Young's tube was frozen in a -80°C slush bath, and subsequently the headspace of the tube was pumped out thoroughly. One equivalent of H_2, 0.85 bar, was condensed in to the tube and the solution was allowed to thaw. The Young's tube was shaken thoroughly to ensure reaction, and a ^{1}H spectrum was collected immediately.

In order to add one equivalent of H_2 to the Young's tube for the reaction to occur, a large amount of (14) was required stoichiometrically. The sample was therefore quite saturated with (14), and the aromatic region of the ^{1}H spectrum is unresolvable. However, the aromatic region of

this sample appears identical to the aromatic region of the (14) in d_8 toluene. There is a resonance at 4.5 ppm, which is due to free H_2. The CH_3 resonance, located at 0.5 ppm, of (14) has shifted slightly to 0.5 ppm. The resonance at 0.2 is assigned to be CH_4 gas indicating that the reaction has taken place very quickly and then decomposed to give off H_2. Figure 4.18 shows a stacked plot of (14) and (14) + H_2.

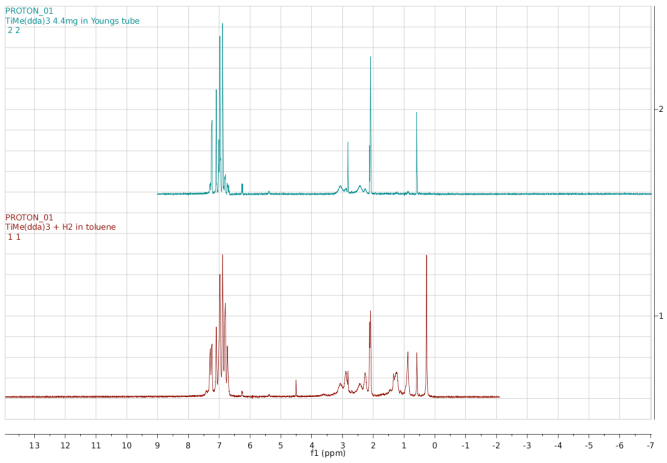

Figure 4.18: Stacked plot of the ^{1}H spectrum of (14) and (14) + H_2

4.3.5 Abstraction of BH_3 from (15) for the synthesis of $(dda)_3TiH$

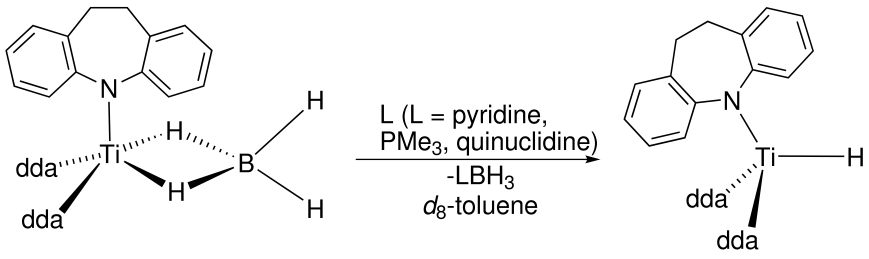

Scheme 4.14: Abstraction of BH_3 from (15) for the synthesis of $(dda)_3TiH$

The third route to the $(dda)_3TiH$ investigated was the abstraction of BH_3 from (15). The three abstracting agents used in the syntheses were pyridine, quinuclidine and triphenylphosphine. The reaction scheme for the abstraction routes is shown in Scheme 4.14. Each of the abstraction routes is outlined separately below.

The first abstracting agent investigated was trimethylphosphine, (PMe_3). One equivalent of (15), 0.0250 g, was added to a Young's valved tube in the glovebox. Deuterated toluene was then condensed in to the tube, the solution was allowed to thaw and a ^{1}H spectrum was collected for

comparison. The tube was taken back in to the glovebox, and one equivalent of PMe_3, 4.0 μL, was added to the reaction mixture. The tube was shaken to ensure reaction, and a ^1H spectrum was collected.

The aromatic region of the ^1H spectrum of (15) + PMe_3 is identical to the aromatic region of (15). There is a new resonance at 0.8 ppm which is assigned to free PMe_3. The broad resonance between 1.0 ppm and 2.0 ppm assigned to the BH_4 protons in the ^1H spectrum of (15) is observed in this spectrum with no change in chemical shift. The observations from the ^1H spectrum of (15) before and after the addition of PMe_3 indicate that a reaction does not occur. Figure 4.19 shows a stacked plot of (15) and (15) + PMe_3.

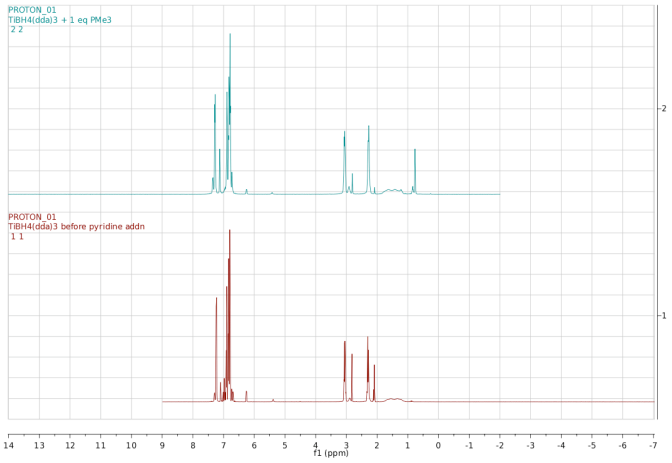

Figure 4.19: Stacked plot of the ^1H spectrum of (15) and (15) + PMe_3

The second abstracting agent to be investigated was pyridine, or C_5H_5N. One equivalent of (15), 0.0250 g, was added to a Young's valved tube in the glove box. Deuterated toluene was condensed in to the tube, the solution was allowed to thaw and a ^1H spectrum was collected for comparison. The tube was taken back in to the glovebox, and one equivalent of C_5H_5N, 3.0 μL, was added to the reaction mixture. The tube was shaken to ensure reaction, and a ^1H spectrum was collected.

The aromatic region of the ^1H spectrum of (15) + C_5H_5N is very similar to the aromatic region of (15). There is a new resonance, however, at 8.4 ppm, which is assigned to free C_5H_5N. The broad resonance between 1.0 ppm and 2.0 ppm assigned to the BH_4 protons in the ^1H spectrum of (15), is observed in this spectrum with no change in chemical shift. The observations from the ^1H spectrum of (15) before and after the addition of C_5H_5N indicate that a reaction does not occur. Figure 4.20 shows a stacked plot of (15) and (15) + C_5H_5N.

The third abstracting agent to be investigated was quinuclidine, or $C_7H_{13}N$. One equivalent of (15), 0.0142 g, was added to a Young's valved tube in the glove box. Deuterated toluene was

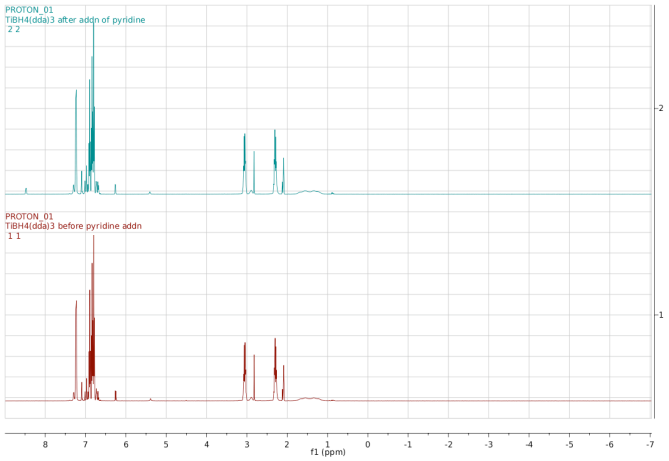

Figure 4.20: Stacked plot of the ^{1}H spectrum of (15) and (15) + C_5H_5N

condensed in to the tube, the solution was allowed to thaw, and a ^{1}H spectrum was collected for comparison. The tube was taken back in to the glovebox, at which time one equivalent of $C_7H_{13}N$, 0.0025 g, was then added to the reaction mixture. The tube was shaken to ensure reaction, and a ^{1}H spectrum was collected.

The aromatic region of the ^{1}H spectrum of (15) + $C_7H_{13}N$ is very similar to the aromatic region of (15). There is a new resonance at 8.2 ppm, which is assigned to a small impurity in the $C_7H_{13}N$. The broad resonance between 1.0 ppm and 2.0 ppm assigned to the BH_4 protons in the ^{1}H spectrum of (15), is observed in this spectrum but this resonance has decreased in size. A new resonance does appear at 4.5 ppm. The two new resonances in the aliphatic spectrum, 1.2 ppm and 0.9 ppm, are assigned to quinuclidine, indicating that this reaction has not gone fully to completion. The presence of H_2 in the ^{1}H spectrum does however, indicate that the $(dda)_3TiH$ was possibly formed, and then proceeded forward to give off H_2. Figure 4.21 shows a stacked plot of (15) and (15) + $C_7H_{13}N$.

4.3.6 Direct metathetical syntheses of $(dda)_3TiO_2CH$

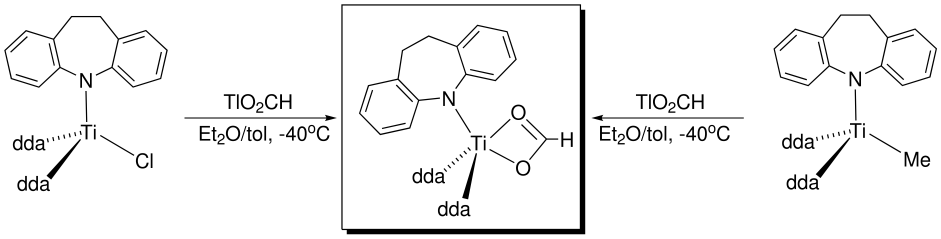

Scheme 4.15: Direct metathetical syntheses of $(dda)_3TiO_2CH$

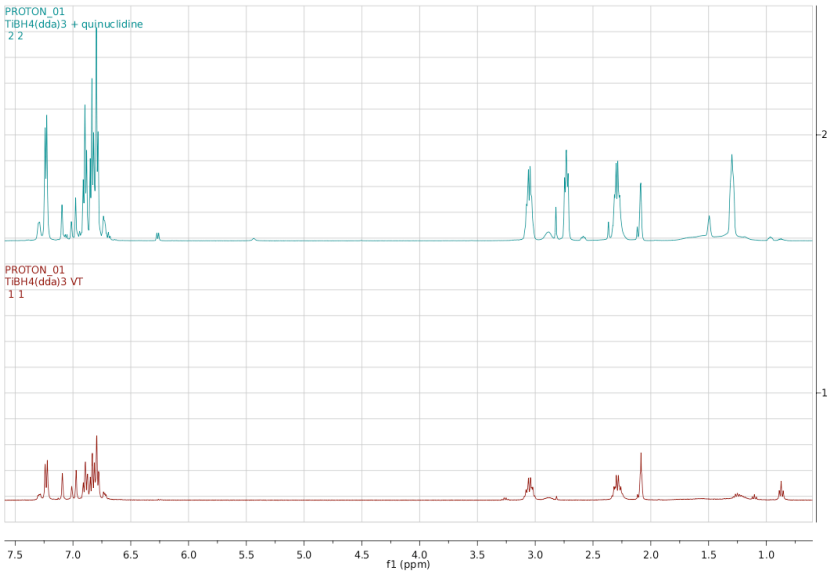

Figure 4.21: Stacked plot of the ^{1}H spectrum of (15) and (15) + $C_7H_{13}N$

The route to the $(dda)_3TiO_2CH$ investigated was the metathetical reaction of (13) or (14) with thallium formate. These reactions are shown in Scheme 4.15. One equivalent of $TlCHO_2$, either 0.0027 g or 0.0014 g, was reacted with one equivalent of (13), 0.0055 g, or (14), 0.0035 g in a Young's tube, in d_8-THF. Deuterated THF was chosen in order to increase the solubility of CHO_2Tl which is insoluble in most solvents. The CHO_2Tl was ground into a fine powder before it was added to the Young's tube. The tube was shaken to ensure reaction. There was a visible amount of CHO_2Tl, unreacted in the tube, so the tube was placed in a sonicator to ensure that the CHO_2Tl had completely dissolved in the reaction mixture.

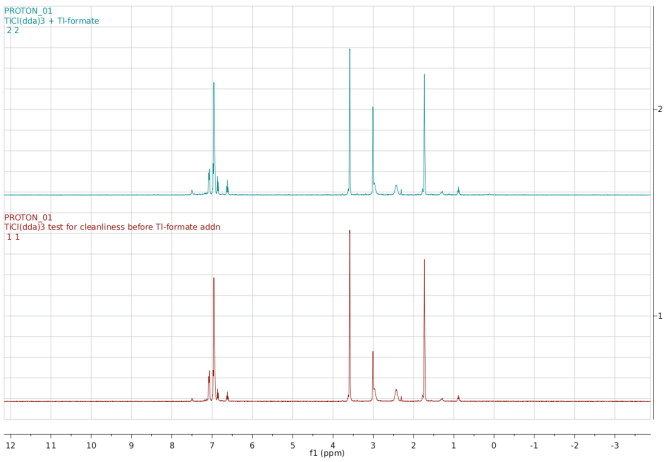

Figure 4.22: Stacked plot of the ^{1}H spectrum of (13) and (13) + $TlCHO_2$

No reaction was observed in the ^{1}H spectrum of (13) or (14). A stacked plot for each of the

reactions is shown in Figure 4.22 and Figure 4.23. These reactions were repeated large-scale but no visible change in the ^{1}H spectrum was observed. These observations indicate that a reaction does not occur with the addition of CHO_2Tl to $(dda)_3TiMe$ or $(dda)_3TiCl$.

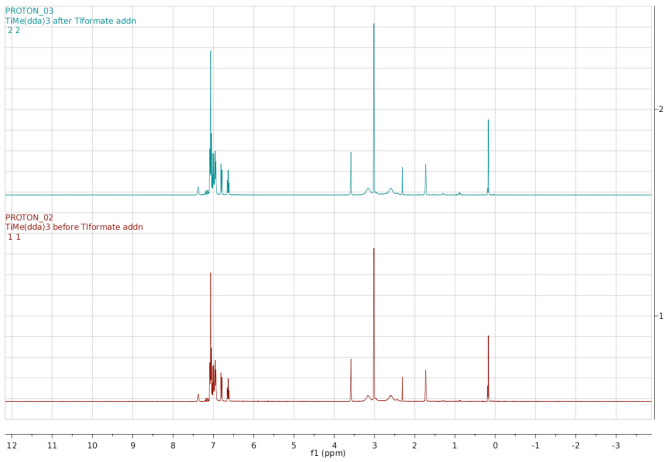

Figure 4.23: Stacked plot of the ^{1}H spectrum of (14) and (14)+ $TlCHO_2$

4.3.7 Synthesis of $(dda)_3Ti$ (16)

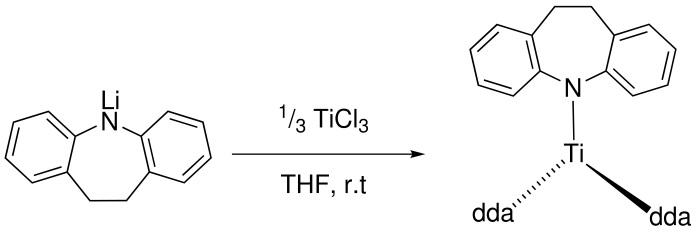

Scheme 4.16: Synthesis of $(dda)_3Ti$ (16)

$(dda)_3Ti$, is synthesised following *via* metathesis of $TiCl_3 \cdot 3THF$. Three molar equivalents of ddaLi were added to one equivalent of $TiCl_3 \cdot 3THF$. This reaction yields (16) in approximately 75% yield. The reaction mixture is recrystallised from a mixture of toluene and hexane, and produced a microcrystalline gold powder. The synthesis of (16) is shown in Scheme 4.16. This complex is extremely light sensitive.

A ^{1}H spectrum of (16) was collected and is shown below in Figure 4.24. As(16) is a titanium (III) complex, it is unsurprising that this spectrum indicates paramagnetic activity. As none of the other routes to the hydride produced a paramagentic ^{1}H spectrum, these reactions do not follow the decomposition pathway in Scheme 4.18 *vide infra*.

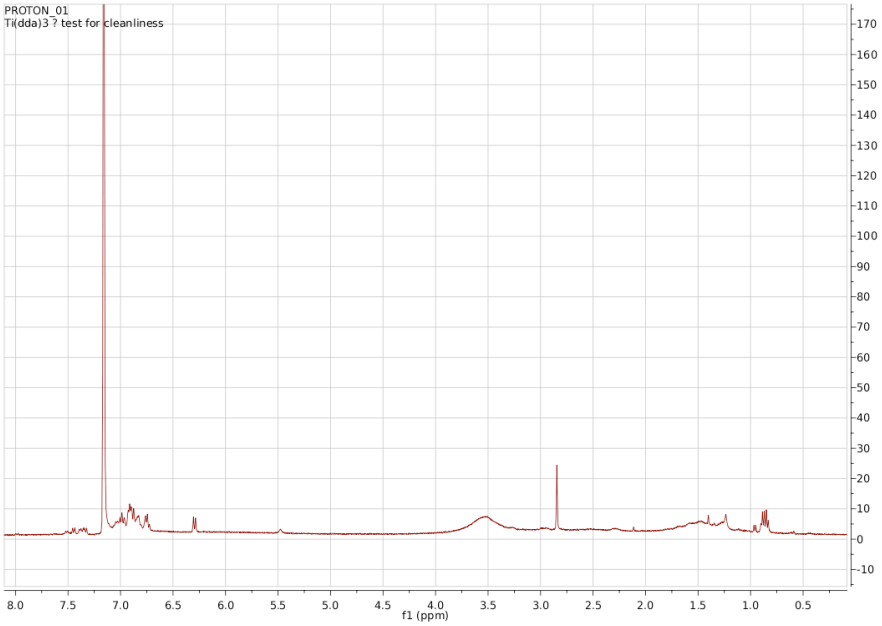

Figure 4.24: The ^{1}H spectrum of $(dda)_3Ti$

4.4 The use of $[(dda)_3Ti]^+[B(C_6F_5)_4]^-$ as a propene polymerisation catalyst

4.4.1 Synthesis of $[(dda)_3Ti]^+[B(C_6F_5)_4]^-$ (17)

The successful polymerisation of the *tris* amido complexes in Chapter 3 led to the investigation of the amide ligand, dda, to be used in the synthesis of a possible polymerisation catalyst. The cationic species, (17), was synthesised in a similar manner to the complexes, $[(dpa)_3Ti]^+[B(C_6F_5)_4]^-$ and $[(dpta)_3Ti]^+[B(C_6F_5)_4]^-$. The synthesis of $[(dda)_3Ti]^+[B(C_6F_5)_4]^-$ is achieved in the same way as $[(dpa)_3Ti]^+[B(C_6F_5)_4]^-$. One equivalent of $KB(C_6F_5)_4$, is dissolved in benzene, and added to one equivalent of (13) in benzene. Upon addition, the solution turns from a bright orange to a dark orange. The solution was stirred at room temperature for three hours, at which time it was stopped, and allowed to settle. The solution was then filtered to remove any remaining KCl, and the frit was washed two times with hexane. The solvent was removed under reduced pressure, producing a dark orange solid in approximately 40% yield. This product is also extremely air, water and ether sensitive. The synthesis of (17) is shown in Figure 4.17.

The ^{1}H spectrum of (17) is shown in Figure 4.25. The same numbering scheme used for complexes (13), (14), and (15) will be used to assign the resonances for (17). The resonances at 2.2 ppm and 3.0 ppm are assigned to the protons, labelled H_e. The resonance at 7.3 ppm is assigned to H_a, and the resonance at 6.7 ppm is assigned to H_d. The resonance at 6.8 is assigned to the H_b and H_c. This spectrum also contains resonances in the aliphatic region, similar

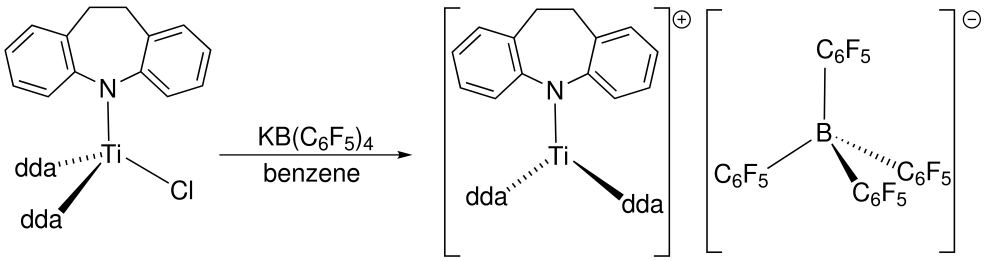

Scheme 4.17: The synthesis of (17)

to $[(dpa)_3Ti]^+[B(C_6F_5)_4]^-$ and $[(dpta)_3Ti]^+[B(C_6F_5)_4]^-$. These resonances have the same chemical shift in all of the ^{1}H spectroscopic data. These resonances do not correlate to any carbon resonances in the ^{13}C spectrum however. The proton assignments are collated in Table 4.11.

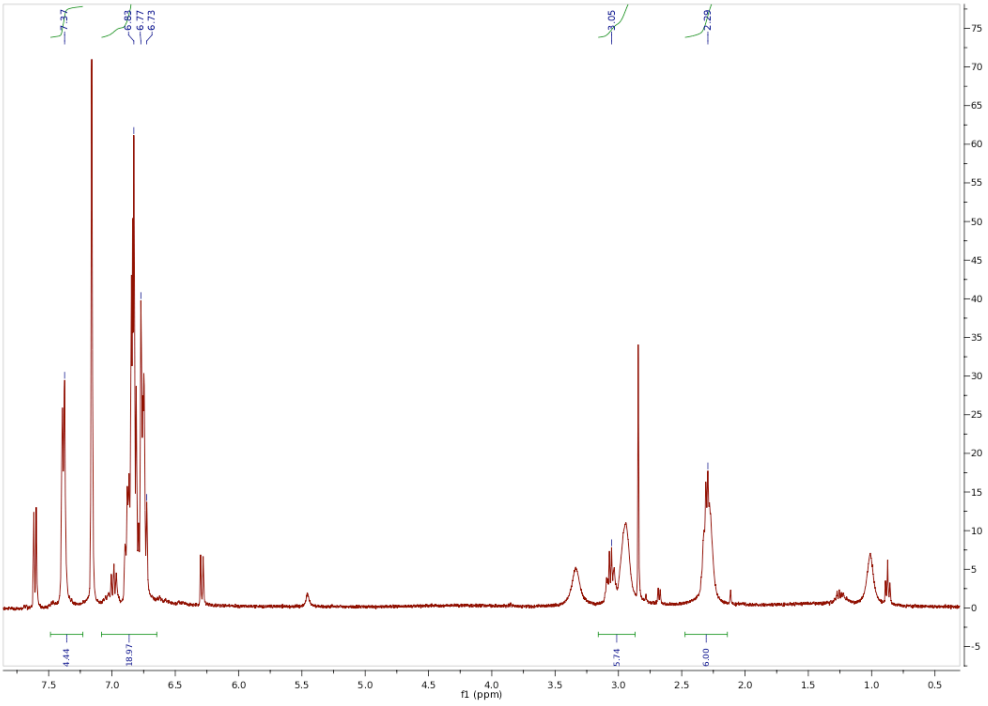

Figure 4.25: The ^{1}H spectrum of $[(dda)_3Ti]^+[B(C_6F_5)_4]^-$

Proton Assignment	δ/ppm	Coupling Pattern	H-H coupling constant/Hz
H_a	7.3	multiplet	-
H_b, H_c	6.8	multiplet	-
H_d	6,7	multiplet	-
H_e	2.2, 3.0	multiplet	-

Table 4.11: ^{1}H NMR spectral resonances of (17)

Two dimensional spectra were consulted for the assignment of the carbon resonances. The HSQC spectrum for this compound is shown in Figure 4.26. The resonance at 31.3 ppm is assigned to C_5, and the resonance at 125.1 ppm is assigned to C_1. The resonances at 125.6 ppm and 126.4 ppm are assigned to C_2 and C_3. The resonance at 130.2 ppm is assigned to C_4. The resonance at 132.4 ppm is assigned to C_7, while the resonance at 150.7 ppm is assigned to C_6. The resonance assignments are collated in Table 4.12.

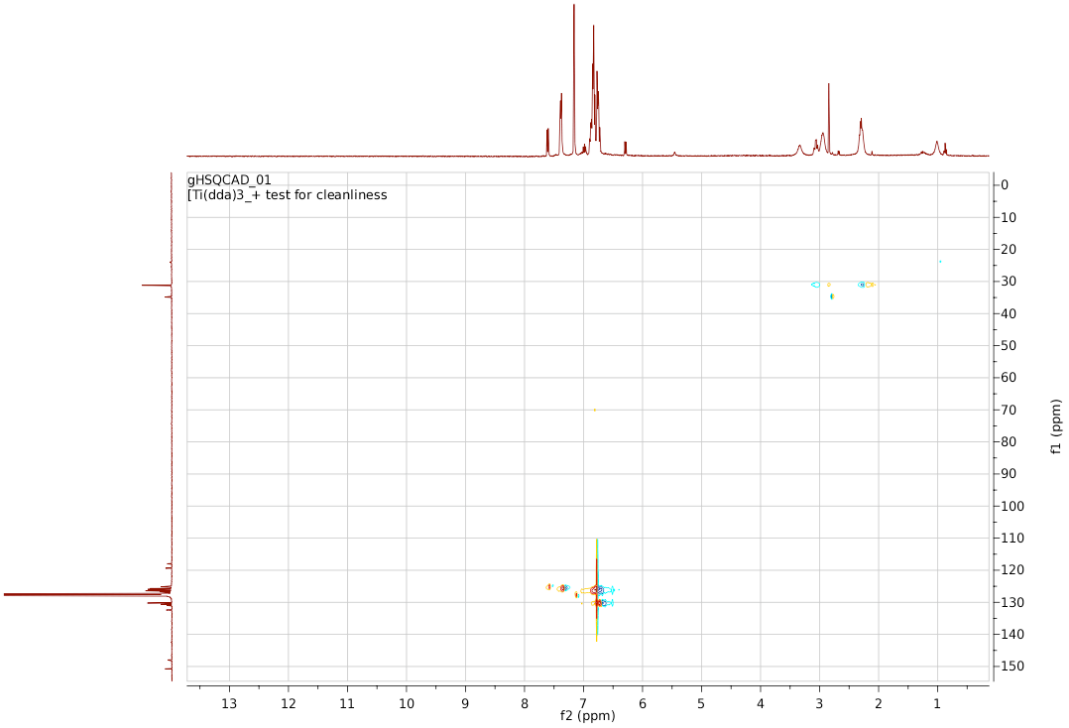

Figure 4.26: The HSQC spectrum of (17)

This complex is very ether sensitive. This complex is soluble in toluene, and slightly soluble in most other hydrocarbon solvents. Mass spectrometry was unable to find the parent ion for this complex, due to immediate decomposition in air. Elemental analysis confirmed the purity of this product.

4.5 Polymerisation reaction data

39.3 mg, 3.0 x 10^{-5} mol, of the cationic complex, $[(dda)_3Ti]^+[B(C_6F_5)_4]^-$ was added to a volume calibrated ampoule. The ampoule was evacuated under high vacuum (10^6 mbar) and 33.17 g (38.26 mL) of toluene was vacuum distilled into the ampoule, 30.4 mmol of propene without purification, was expanded into the line with a volume of 961 mL at a pressure of 718 mbar. The frozen solution was allowed to thaw and warm to 0.0°C. The colour of the activated catalyst in solution

Carbon Assignment	δ/ppm
C_1	125.1
C_2, C_3	126.3, 126.8
C_4	130.8
C_5	32.1
C_6	150.2
C_7	134.0

Table 4.12: ^{13}C NMR spectral resonances of (17)

was dark orange. The gas was expanded into the ampoule, and the temperature was kept at 0.0°C during the experiment. When the catalyst is exposed to the monomer, the pressure drops 165 mbar and polymerisation ensues. A plot of the time versus rate of polymerisation of propene can be seen in Figure 4.27. The polymerisation reaction yielded 40.0 mg of polypropene. Figure 4.28 shows the ln pressure over time for the polymerisation experiment of $[(dda)_3Ti]^+[B(C_6F_5)_4]^-$.

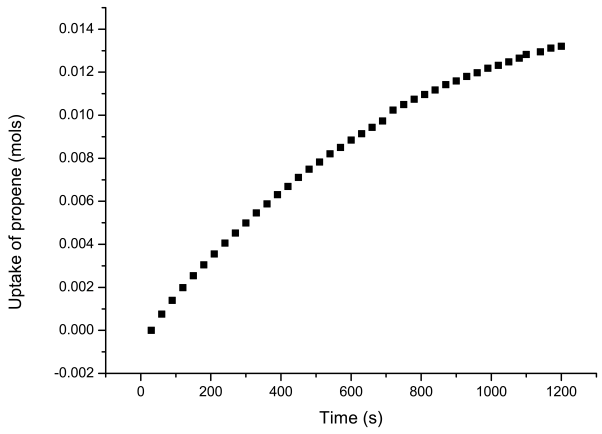

Figure 4.27: Rate of propene consumption with $[(dda)_3Ti]^+[B(C_6F_5)_4]^-$

4.6 Conclusions

The complexes (13), (14), and(15) were synthesised and characterised using NMR spectroscopy. The ^{1}H spectroscopic data of these complexes is very difficult to assign because they are four-spin AA'BB' systems. There is extensive coupling amongst the protons on the rings, and coupling between the *cis* and *trans* protons on the backbone of the nitrogen containing ring. Simulation data was used in order to try to assign the resonances, only a small amount of convergence was

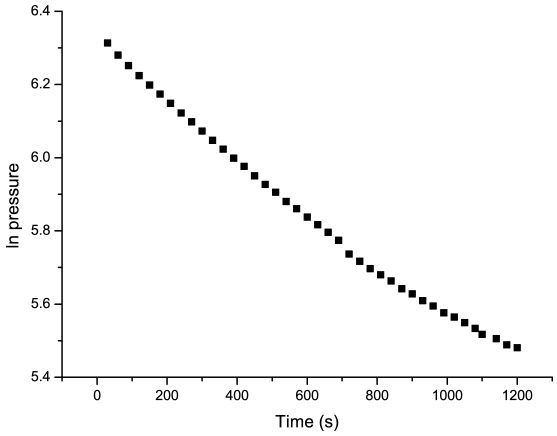

Figure 4.28: ln pressure vs. time plot for the catalyst $[(dda)_3Ti]^+[B(C_6F_5)_4]^-$

found. HSQC spectroscopic data was used to assign the carbon resonances of all three complexes.

The molecular structure was also elucidated for (13), (14), and (15). The complexes, (13) and (14) were found to be *pseudo* tetrahedral molecules with C_3 symmetry. The Ti−N bond lengths for these complexes fall within the average range found for four-coordinate Ti−NR_2 complexes. The N−Ti−N bond angles of (13) and (14) deviate slightly from a perfect tetrahedral angle of 109.45°. The N−Ti−Cl bond angle of (13) and N−Ti−C bond angle of (14) only deviate slightly from 109.45°as well.

The equilibrium is important in the investigation of the formation of transition metal formates. In the complexes synthesised by Parkin and Cummins *vide supra*, the equilibrium lies to the right of the reaction, allowing for the formation of the transition metal formate. In the hydride complex synthesised by Parkin, the irreversible decomposition of TlR, leading to the deposition of Tl, provided a driving force for the formation of the hydride. All of the routes investigated towards the $(dda)_3TiH$ in this chapter were also irreversible processes involving the evolution of either CH_4 or LiCl. There is enough driving force for the formation of $(dda)_3TiH$, yet the product is too unstable to be isolated and cannot be further reacted with CO_2 to form the formate complex.

Various routes to the synthesis of $(dda)_3TiH$ were attempted. Three of the reactions implemented for this purpose, the reaction of superhydride with (13), the reaction of quinuclidine with (15) and the direct hydrogenation of (14) produced results indicating the $(dda)_3TiH$ complex had been formed during reaction. This fact implies that the formation of $(dda)_3TiH$ is not dependent on the synthetic route used.

The formation of $(dda)_3TiH$ was observed in the reaction of $LiEt_3BH + (13)$. The resonance observed at -1.2 ppm in the ^1H spectrum is assigned to the Ti−H. The ^1H spectrum also contained resonances for the starting material, $LiEt_3BH$ and H_2. The fact that the product formed contains resonances assigned to $LiEt_3BH$, H_2, and $(dda)_3TiH$ indicates that this reaction proceeds very

quickly, and that the $(dda)_3TiH$ complex is exceedingly unstable.

The ^1H spectroscopic data for the reaction of quinuclidine with (15) and the direct hydrogenation of (14) are similar to the reaction of $LiEt_3BH + (13)$ except there is no direct observation of a resonance for the $(dda)_3TiH$. Their data contain resonances at approximately 4.5 ppm, which is indicative of the presence of H_2. The introduction of an H_2 resonance in the ^1H spectrum of these compounds is indicative that the reaction was successful, but the $(dda)_3TiH$ is so unstable that the reaction moves forward very quickly, producing H_2 as the final product. The spectroscopic data also show the presence of starting material resonances, indicating that while the reaction itself is slow, the formation of $(dda)_3TiH$ occurs quickly. A possible reaction mechanism for the decomposition pathway of $(dda)_3TiH$ is shown in Scheme 4.18. In order to verify the proposed pathway, (16) was synthesised.

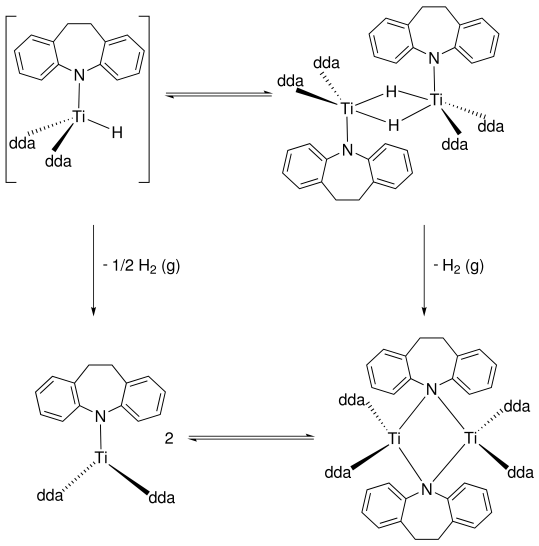

Scheme 4.18: Dihydrogen formation of a transient hydride

A *tris* amido cationic complex, (17), similar to those in Chapter 2, was synthesised. This complex was spectroscopically characterised by NMR spectroscopy and elemental analysis. The polymerisation reaction is an "effective" first-order kinetic reaction. The tacticity and molecular weight of the polymer produced is unknown at this time. The polymer needs to be produced on a larger scale in order to be studied. This catalyst is not as active as those synthesised in Chapter 2; the yield of rate constant for this reaction is $0.0007s^{-1}$. The dda ligands used for this catalyst have more steric bulk than the dpa or dpta ligands. One possibility for the decrease in catalytic activity when using (17) is that the single site for polymerisation is crowded by the sterically bulky dda ligands.

Chapter 5

Experimental

5.1 Experimental procedures

All solvents used in synthetic procedures were pre-dried over 4 Å (1.6mm) molecular sieves before reflux over the appropriate drying agent, which are collated in Table 5.1.

Solvent	Drying agent
Diethyl ether	NaK_3
Tetrahydrofuran	K
Dimethoxyethane	K
Dioxane	Na
Benzene	K
Toluene	Na
Xylenes	Na
Pentanes	NaK_3
Hexanes	K
Cyclohexane	K
Heptanes	Na
Methylcyclohexane	Na

Table 5.1: Drying agents for solvents

Anhydrous solvent was collected in an ampoule containing a potassium mirror (for hydrocarbons) or 4Å molecular sieves (for ethers). Solvents used for NMR spectroscopy were dried over the appropriate drying reagent prior to reflux for approximately one week, before being vacuum transferred into an ampoule containing a potassium mirror. These solvents were then freeze, pump, thaw, degassed at least three times before use.

Air or moisture sensitive samples for NMR spectroscopy were prepared by vacuum transfer on the high-vacuum line of the appropriate NMR solvent into an NMR tube sealed with Young's tap.

All air or moisture sensitive solids and solutions were handled using standard Schlenk techniques under argon, or in an argon-filled glove box, with concentrations of H_2O and O_2 less than 0.1 ppm. Glassware was dried in a 130° oven after being cleaned thoroughly in a base and acid bath. Recrystallizations were performed in a glove box freezer ($-40\,^\circ$C), or in a chest freezer (-30° C) or in a -80° C freezer. Reactions were conducted in standard Schlenk ware, vials or high-vacuum ampoules.

NMR spectra were recorded on a 400 MHz, 500 MHz, or 600 MHz Varian spectrometer, with resonant frequencies for different nuclei given in Table 5.2

B_0 / T	7.0333	9.3778	14.0667
Nucleus	Frequency / MHz	Frequency / MHz	Frequency / MHz
^{1}H	300	400	600
^{13}C	75.4351	100.5801	150.8701
^{11}B	96.2519	128.3359	192.5038
^{19}F	282.2820	376.3760	564.5641
^{15}N	30.4103	40.5471	60.8206

Table 5.2: NMR frequencies

^{15}N and N,H Correlation experiments were performed by Dr. Iain Day on the 600 MHz Varian spectrometer.

Mass spectroscopy was performed by Dr. A.K. Abdul-Sada at the University of Sussex, on a VG autospec Fisons instrument (electron impact ionization at 70eV).

Elemental analyses were carried out by Stephen Boyer at London Metropolitan University.

Single crystal X-Ray data were collected and solved by Dr. Peter Hitchcock or Dr. Martyn Coles at the University of Sussex, or Onome Swader at the University of Tennessee.

Polymerisation experiments were performed by Brad Miller at the University of Tennessee.[156]. GPC was run on a Polymer Laboratories GPC-220 in trichlorobenzene at 145°C with refractive index (RI), Light Scattering (LS15 and LS90), and viscometer detector (UV). Samples were prepared at a concentration of 1.0 mg/ml. DSC was run on a Mettler-Toledo DSC821 from -50°C to 250 °C at a ramp 10°C/min. Each sample was run three times to eliminate thermal history. The NMR experiments were done on the Bruker 400MHz spectrometer in trichlorobenzene spiked with deuterated DMSO as the lock solvent at 120 °C.

Diarylamines were recrystallized on the Schlenk line from hot toluene or xylenes before vacuum distillation.

$TiCl_4.2\,THF$ was prepared by adding 2 molar equivalents of THF in dichloromethane to a solution of $TiCl_4$ in the same solvent at $-80\,°C$, followed by cold filtration with a filter cannula and drying under reduced pressure.

$TiCl_3.3\,THF$ was prepared using the method by Arnold *et. al.*[195]

Alkali metals and alkali metal hydrides were freed of hydrocarbon oil by extensive washing with hexane.

^{t}BuLi was received as a nominal 1.6 M solution in pentane. The solution was filtered through a fine frit and then evaporated in the glove box to yield a white crystalline solid that was stored at $-40\,°C$.

All other reagents were used as received unless specified in the preparation.

5.2 General Syntheses of complexes

5.2.1 Synthesis of dpaLi (1)

1.9324 g (0.0114 mol, 1 eq) of diphenylamine was dissolved in 50 mL of hexane. 0.8778 g (0.0137 mol, 1.2 eq) of t-butyl lithium was added to the diphenylamine over a period of one hour. The diphenylamine solution formed a white precipitate immediately after the t-butyl lithium was added. The solution was allowed to stir overnight, and then filtered. The resulting white solid was washed three times with approximately 20 mL of pentane, and then dried under reduced pressure.

^{1}H NMR (d_8-THF): δ / ppm: 6.79 (t, 2H, *J*=7.1 Hz), 6.68 (d, 2H, *J*=7.7 Hz), 6.13 (t, 1H, *J*=6.5 Hz).

^{13}C NMR (d_8-THF): δ / ppm: 112.65, 119.70, 129.06, 159.98.

Yield: 1.8556 g/ 92.8%.

Anal. Calcd: C, 82.29; H, 5.75; N, 8.00. Found: C, 82.37; H, 5,63; N, 7.95.

MS (EI): *m/z* = 168 (M^+ - Li)

5.2.2 Synthesis of $(dpa)_3TiCl$ (2)

4.8252 g (0.026 mol, 3 eq) of dpaLi was slurried in toluene, and added to a slurry of 2.8394 g (0.009 mol, 1 eq) of $TiCl_4 \cdot 2THF$ in toluene. The solution turned dark red within the first few drops of Lidpa, and was allowed to stir overnight. The dark red solution was allowed to settle and was filtered. The solvent was removed under reduced pressure, recrystallization from toluene/hexane yields a dark red solid.

^{1}H NMR (d_8-THF): δ / ppm: 6.82 (d, 2H, *J*=7.9 Hz), 6.98 (t, 2H, *J*=7.3 Hz), 7.11 (t, 2H, *J*=7.7 Hz).

^{13}C NMR (d_8-THF): δ / ppm: 124.60, 127.01, 130.36, and 151.19 ppm.

Yield: 3.998 g/ 80.0%.

MS (EI): *m/z* = 587 (M^+, 100%).

5.2.3 Synthesis of dptaLi (3)

1.9741 g (0.0101 mol, 1 eq) of di-*p*-tolylamine was dissolved in 50 mL of hexane. 0.7793 g (0.0122 molm 1.2 eq) of t-butyl lithium was added to the di-*p*-tolylamine over a period of one hour. The di-*p*-tolylamine solution formed a cream precipitate immediately after the t-butyl lithium was added. The solution was allowed to stir overnight, and then filtered. The resulting cream-colored solid was washed three times with approximately 20 mL of pentane, and then dried under reduced pressure.

^{1}H NMR (d_8-THF): δ / ppm: 7.90 (d, 1H, *J*=7.6 Hz).

^{13}C NMR (d_8-THF): δ / ppm: 19.73, 118.40, 128.58, and 156.87.

Yield: 1.8521 g/ 92.6%.

Anal. Calcd: C, 82.75; H, 6.94; N, 6.89. Found: C, 82.62; H, 7.00; N, 6.72.

MS (EI): *m/z*: = 196 (M^+ - Li)

5.2.4 Synthesis of $(dpta)_3TiCl$ (4)

1.1050 g (4.69 x 10^{-3} mol, 3.0 eq) of dptaLi was slurried in toluene and added to a slurry of 0.5232 g (1.57 x 10^{-3} mol, 1 eq) of $TiCl_4 \cdot 2THF$ in toluene. The solution turned light red within the first few drops of Kdpta, and was allowed to stir overnight. The red solution was allowed to settle and was then filtered through a fine frit. The solvent was removed under reduced pressure. Recrystallization from toluene/hexane yields a bright red solid.

^{1}H NMR (d_6-benzene): δ / ppm: 1.96 (s, 6H), 6.81 (d, 2H, *J*=8.1 Hz), 7.07 (d, 2H, *J*=8.3 Hz).

^{13}C NMR (d_6-benzene): δ / ppm: 20.26, 123.54, 129.84, 134.70, and 147.02 ppm.

Yield: 1.0361 g/ 98.4%.

Anal. Calcd: C, 75.05; H, 6.30; N, 6.25 Found: C, 74.86; H, 6.34; N, 6.12.

MS (EI): *m/z* = 673 (M^+, 100%).

5.2.5 Synthesis of $(dpa)_3TiMe$ (5)

0.5001 g (8.51 x 10^{-4} mol, 1 eq) of $(dpa)_3TiCl$ was dissolved in toluene and put in the -40°freezer for one hour in which time 0.0187 g (8.51 x 10^{-4} mol, 1 eq) of MeLi suspended in toluene at

-40°C was added. This reaction was allowed to warm to room temperature and to stir overnight. This tea-colored solution was then filtered through a frit and washed with toluene. The solvent was removed under reduced pressure, producing a bright orange solid.

^{1}H NMR (d_8-toluene): δ / ppm: 0.40 (s, 3H), 6.84 (t, 1H, *J*=7.3 Hz), 7.04 (t, 2H, *J*=7.7 Hz), 7.10 (d, 2H, *J*=7.5 Hz).

^{13}C NMR (d_8-toluene): δ / ppm: 65.16, 117.83, 120.66, 123.63, 129.08, 129.53, and 147.81.

Yield: 0.4093 g/ 84.8%.

Anal. Calcd: C, 78.30; H, 5.86; N, 7.40 Found: C, 78.18; H, 5.72; N, 7.28.

MS (EI): *m/z* = 568 (M^+, 7%), 553 (M^+-Me, 99%).

5.2.6 Synthesis of $(dpta)_3$TiMe (6)

0.0500 g (7.4 x 10^{-4} mol, 1 eq) of $(dpta)_3$TiCl was dissolved in toluene and put in the -40°freezer for one hour in which time 0.0169 g (7.5 x 10^{-4} mol, 1 eq) of MeLi suspended in toluene at -40°C was added. This reaction was allowed to warm to room temperature and to stir overnight. This tea-colored solution was then filtered through a frit and washed with toluene. The solvent was removed under reduced pressure, producing a bright orange solid.

^{1}H NMR (d_8-toluene): δ / ppm: 0.20 (s, 3H), 2.01 (s, 3H), 6.92 (d, 2H, *J*=8.1 Hz), 7.22 (d, 2H, *J*=8.3 Hz).

^{13}C NMR (d_8-toluene): δ / ppm: 19.66, 62.56, 117.94, 123.75, 129.53, 130.23, 141.44, and 145.40.

Yield: 0.4848 g/ 66.0%.

Anal. Calcd: C, 79.25; H, 6.96; N, 6.45 Found: C, 78.95; H, 6.94; N, 6.40.

MS (EI): *m/z* = 652 (M^+, 9%), 636 (M^+-Me, 99%).

5.2.7 Synthesis of $(dpa)_3TiMeB(C_6F_5)_3$ (7)

0.2000 g (3.52 x 10^{-4} mol, 1 eq) of $(dpa)_3$TiMe was dissolved in hexane, at which time 0.1804 g (3.52 x 10^{-4} mol, 1 eq) of $B(C_6F_5)_3$ dissolved in a 90:10 mixture of hexane/benzene was added dropwise. The color of the solution went from dark red to purple after the addition of $B(C_6F_5)_3$ was complete. The reaction was allowed to stir for three hours, at which time the solvent was removed under reduced pressure, producing a dark red/purple powder.

^{1}H NMR (d_8-toluene): δ / ppm: 0.96 (s, 3H), 6.68 (m, 30H).

^{13}C NMR (d_8-toluene): δ / ppm: 76.79, 122.73, 123.49, 130.69, and 152.71.

^{19}F NMR (d_8-toluene): δ / ppm: -166.07, -160.16, -142.06, -131.69, -128.51, and -85.12.

^{11}B NMR (d_8-toluene): δ / ppm: -13.97.

Yield: 0.27848 g/ 79.0%

Anal. Calcd: C, 61.51; H, 3.23; N, 3.84 Found: C, 61.25; H, 3.20; N, 4.00

5.2.8 Synthesis of $(dpta)_3TiMeB(C_6F_5)_3$ (8)

0.2000 g (3.07 x 10^{-4} mol, 1 eq) of $(dpta)_3TiMe$ was dissolved in hexane, at which time 0.1573 g (3.07 x 10^{-4} mol, 1 eq) of $B(C_6F_5)_3$ dissolved in a 90:10 mixture of hexane/benzene was added dropwise. The color of the solution went from bright red to purple after the addition of $B(C_6F_5)_3$ was complete. The reaction was allowed to stir for three hours, at which time the solvent was removed under reduced pressure, producing a dark red/purple powder.

^{1}H NMR (d_8-toluene): δ / ppm: 0.90 (s, 3H), 6.80 (m, 24H).

^{13}C NMR (d_8-toluene): δ / ppm: 20.33, 75.87, 122.58, 123.31, 130.76, and 131.01, 138.07, and 144.05.

^{19}F NMR (d_8-toluene): δ / ppm: -165.54, -161.53, -154.66, -147.14, -132.22, and -129.80.

^{11}B NMR (d_8-toluene): δ / ppm: -13.96.

Yield: 0.2829 g/ 80.3%.

Anal. Calcd: C, 63.23; H, 4.02; N, 3.57 Found: C, 63.27; H, 3.94; N, 3.48.

5.2.9 Synthesis of $[(dpa)_3Ti]^+[B(C_6F_5)_4]^-$ (9)

0.4665 g (6.50 x 10^{-4} mol, 1 eq) of $KB(C_6F_5)_4$ was dissolved in benzene, and added dropwise to a solution of 0.3819 g (6.50 x 10^{-4} mol, 1 eq) of $(dpa)_3TiCl$. The dark red/purple solution was allowed to stir for three hours when 50 mL of hexane was added to precipitate out KCl. The red/purple solution was filtered and washed with 10 mL of pentane 3 times. The solvent was removed under reduced pressure, producing a dark/purple solid.

^{1}H NMR (d_6-benzene): δ / ppm: 6.80 (t, 1H, *J*=7.3 Hz), 6.96 (t, 2H, *J*=7.7 Hz), 7.03 (d, 2H, *J*=7.6 Hz).

^{13}C NMR (d_6-benzene): δ / ppm: 123.42, 125.57, 129.42, and 150.00.

Yield: 0.2970 g/ 37.1%.

Anal. Calcd: C, 58.52; H, 2.46; N, 3.41 Found: C, 58.36; H, 2.31; N, 3.28.

5.2.10 Synthesis of $[(dpta)_3Ti]^+[B(C_6F_5)_4]^-$ (10)

0.4366 g (6.48 x 10^{-4} mol, 1 eq) of $KB(C_6F_5)_4$ was dissolved in benzene, and added dropwise to a solution of 0.4081 g (6.47 x 10^{-4} mol, 1 eq) of $(dpta)_3TiCl$. The dark red/orange solution was allowed to stir for three hours when 50 mL of hexane was added to precipitate out KCl. The

orange/red solution was filtered and washed with 10 mL of pentane 3 times. The solvent was removed under reduced pressure, producing a orange/red solid.

^{1}H NMR (d_6-benzene): δ / ppm: 2.01 (s, 3H), 6.87 (d, 2H, *J*=8.1 Hz), 7.13 (d, 2H, *J*=8.3 Hz).

^{13}C NMR (d_6-benzene): δ / ppm: 20.26, 123.54, 129.84, 134.70, and 147.02.

Yield: 0.4404 g/ 55.1%.

Anal. Calcd: C, 60.25; H, 3.22; N, 3.19 Found: C, 60.10; H, 3.25; N, 3.30.

5.2.11 Synthesis of $KB(C_6F_5)_4$ (11)

5.7752 g (0.0161 mol, 1 eq) of $Mg(C_6F_5)_2$, 1.0143 g (8.06 x 10^{-3} mol, 0.50 eq) of KBF_4, and 0.1532g (0.0016 mol, 10 mol %) were added to a heavy walled ampoule with 100 mL THF. This solution was allowed to reflux for 33 days at 80° C. The solution was then filtered and the solvent was removed under reduced pressure, producing a sticky brown solid. The solid was then washed 7 times with 50 mL portions pentane, producing a fine, cream powder.

^{19}F NMR (d_6-benzene): δ / ppm: -133.14, -154.79, and -162.82.

^{13}C NMR (d_6-benzene): δ / ppm: 136.72, 140.46, and 147.79.

^{11}B NMR (d_6-benzene): δ / ppm: 2.55.

Yield: 3.5568 g/ 59.1%.

MS (EI):*m/z* = 679 (M^+-K).

5.2.12 Synthesis of ddaLi (12)

10.0 g (0.0512 mol, 1 eq) of iminodibenzyl was dissolved in 200 mL hexane. 3.9363 g (0.0615 mol, 1.2 eq) of t-butyl lithium was added to the iminodibenzyl very slowly. The iminodibenzyl solution formed a cream precipitate shortly after the first portion of t-butyl lithium was added. The solution was allowed to stir overnight, and then filtered. The resulting cream-colored solid was washed three times with approximately 50 mL of pentane, and then dried under reduced pressure.

^{1}H NMR (d_8-THF): δ / ppm: 2.89 (s, 4H), 6.05 (t, 3H), 6.48 (d, 2H), 6.56 (d, 2H), 6.63 (t, 2H).

^{13}C NMR (d_8-THF): δ / ppm: 40.17, 112.55, 124.04, 126.87, 130.76, 132.70, and 165.63.

Yield: 9.8252 g/ 95.4%.

Anal. Calcd: C, 83.58; H, 6.01; N, 6.96. Found: C, 83.44; H, 5.87; N, 6.85.

MS (EI): *m/z* = 195 (M^+-Li).

5.2.13 Synthesis of $(dda)_3TiCl$ (13)

8.7241 g (0.043 mol, 3 eq) of ddaLi was slurried in toluene, and added to a slurry of 4.8261 g (0.0145 mol, 1 eq) of $TiCl_4 \cdot 2THF$ in toluene. The solution turned dark orange within the first few drops of LiNdda, and was allowed to stir overnight. The dark orange solution was allowed to settle and was filtered. The solvent was removed under reduced pressure, recrystallization from toluene/hexane yields an orange crystalline powder.

^{1}H NMR (d_8-toluene): δ / ppm: 2.30 (m, 6H), 2.94 (m, 6H), 6.83 (m, 24H).

^{13}C NMR (d_8-toluene): δ / ppm: 31.02, 125.69, 125.94, 126.42, 130.23, 132.42, and 150.74.

Yield: 9.0731 g/ 94.2%.

Anal. Calcd: C, 75.73; H, 5.45; N, 6.31 Found: 75.84; H, 5.38; N, 6.16.

MS (EI): *m/z* = 666 (M^+, 100%).

5.2.14 Synthesis of $(dda)_3TiMe$ (14)

0.5001 g (7.50 x 10^{-4} mol, 1 eq) of $(dda)_3TiCl$ was dissolved in toluene and put in the -40°freezer for one hour in which time 0.0168 g (7.64 10^{-4} mol, 1.2 eq) of MeLi suspended in toluene/Et_2O at -40°C was added. This reaction was allowed to warm to room temperature and to stir overnight. This orange solution was then filtered through a frit and washed with toluene. The solvent was removed under reduced pressure, producing a bright yellow solid.

^{1}H NMR (d_8-toluene): δ / ppm: 0.55 (s, 3H), 2.43 (m, 6H), 3.06 (m, 6H), 6.88 (m, 24H).

^{13}C NMR (d_8-toluene): δ / ppm: 31.92, 60.97, 125.74, 127.21, 131.06, 133.59, and 149.76.

Yield: 0.2237 g/ 46.2%.

Anal. Calcd. C, 79.99; H, 6.09; N, 6.51 Found: C, 79.83; H, 6.11; N, 6.31.

5.2.15 Synthesis of $(dda)_3TiBH_4$ (15)

0.5000 g (7.51 x 10^{-4} mol, 1 eq) of $(dda)_3TiCl$ was slurried in toluene, at which time 0.0195 g (8.95 x 10^{-4}mol, 1.2 eq) of $LiBH_4$ slurried in toluene/diethyl ether was added dropwise, and allowed to stir for twenty-four hours. The solution was pale orange in color. The solution was allowed to settle and was filtered through a fine frit. The solvent was removed under reduced pressure, producing a light orange solid. Recrystallization from toluene/hexane yield light orange crystals.

^{1}H NMR (d_8-toluene): δ / ppm: 2.29 (m, 6H), 3.05 (m, 6H), 6.80 (m, 24H).

^{13}C NMR (d_8-toluene): δ / ppm: 31.16, 125.64, 126.23, 126.38, 130.27, and 132.07, and 153.43.

Yield: 0.3356 g/ 69.3%.

Anal. Calcd: C, 78.14; H, 6.25; N, 6.51 Found: C, 78.03; H, 6.16; N, 6.49.

MS (EI): *m/z* = 644 (M^+, 5%), 631 (M^+-BH_4, 99%).

5.2.16 Synthesis of $(dda)_3Ti$ (16)

0.9854 g (4.90 x 10^{-3} mol, 3 eq) of ddaLi was slurried in THF, and was added to a slurry of 0.6053 g (1.63 x 10^{-3} mol, 1 eq) of $TiCl_3 \cdot 3THF$ in THF. The solution turned dark green within the first few drops of Lidda, and was allowed to stir overnight. The dark green solution was allowed to settle, and was filtered through a fine frit. The solvent was removed under reduced pressure. Recrystallization from toluene/hexane yielded a bright golden yellow solid.

Yield: 0.7795 g/ 75.7%.

Anal Calcd: C, 79.99; H, 5.75; N 6.66 Found: C, 79.86; H, 5.60; N, 6.37.

5.2.17 Synthesis of $[(dda)_3Ti]^+[B(C_6F_5)_4]^-$ (17)

0.2500 g (3.48 x 10^{-4} mol, 1 eq) of $KB(C_6F_5)_4$ was dissolved in benzene, and added dropwise to a solution of 0.2319 g (3.48 x 10^{-4} mol, 1 eq) of $(dda)_3TiCl$. The dark orange solution was allowed to stir for three hours when 50 mL of hexane was added to precipitate out KCl. The dark orange solution was filtered and washed with 10 mL of pentane 3 times. The solvent was removed under reduced pressure, producing a orange solid.

^{1}H NMR (d_6-benzene): δ / ppm: 1.54 (m, 6H), 2.30 (m, 6H), 5.97 (m, 24H).

^{13}C NMR (d_6-benzene): δ / ppm: 31.34, 125.17, 125.68, 126.41, 130.22, 132.41, and 150.73.

^{19}F NMR (d_6-benzene): δ / ppm: -162.81, -154.56, and -133.07.

Yield: 0.4375 g/ 43.8%.

Anal Calcd: C, 60.53; H, 2.77; N, 3.21. Found: C, 60.96; H, 2.81; N, 3.28.

5.2.18 Synthesis of MgC_6F_5Br

10.0 g (0.0400 mol, 5.047 mL, 1 eq) of C_6F_5Br was added to 1.181 g (0.0485 mol, 1.2 eq) of Mg in 150 mL diethyl ether to make the Grignard, C_6F_5BrMg. The halide was added to the Mg slowly and the brown solution C_6F_5BrMg was allowed to stir overnight. The solution was then filtered.

5.2.19 Synthesis of $[Mg(C_6F_5)_2(Et_2O)(dioxane)]$

13.7801 g (0.0558 mol, 6.9561 mL, 1 eq) of C_6F_5Br was added to 1.6274 g (0.0670 mol, 1.2 eq) of Mg in 150 mL diethyl ether to make the Grignard, C_6F_5BrMg. The halide was added to the Mg slowly and the C_6F_5BrMg was allowed to stir overnight. The solution was then filtered and 4.76 mL dioxane (0.0558 mol, 2 eq) in 50 mL of diethyl ether was added to the C_6F_5BrMg. The

solution began to precipitate immediately and was allowed to settle overnight. The solution was filtered, and the solvent was removed under reduced pressure, producing a fine, white powder.

^{19}F NMR (d_6-benzene): δ / ppm: -114.04, -157.10, and -161.28.

^{13}C NMR (d_6-benzene): δ / ppm: 14.97, 65.44, and 66.24.

Yield: 5.7752 g/ 57.8%.

5.2.20 Synthesis of Methylaluminoxane (MAO)

6.4550 g (0.0026 mol, 4 eq) of $CuSO_4 \cdot 5H_2O$ was dissolved in 200 mL of toluene in a 1L round-bottom Schlenk flask and placed in a 0.0°C ice bath. 5.17 mL (0.05 mol, 1 eq) of $AlMe_3$ was diluted with 150 mL of toluene in a large Schlenk flask. The $AlMe_3$ solution was added drop-wise to the $CuSO_4$ solution, stirring vigorously, over a period of three hours. Upon the addition of the first drop of $AlMe_3$, the flask became cloudy, and began gaving off large amounts of gas. After the addition was complete, the flask was kept cool for an additional five hours, after which time the reaction was allowed to stir at room temperature overnight under a flow of argon gas to allow methane to vent from the flask. The solution was allowed to settle for a few hours, at which time the solution was filtered into a large Schlenk flask, the residue was washed with toluene, and the solvent was removed under reduced vacuum. Once all of the solvent had been removed, a sticky, cream-colored solid remained. The product was dried for twelve hours on the high-vacuum line.

Yield: 4.84 g/ 75.0%.

Bibliography

[1] Chen, E. Y.; Marks, T. J. *Chemical Reviews* **2000**, *100*, 1391–1434.

[2] Boor, J. J. *Ziegler-Natta Catalysts and Polymerizations*; Academic Press, 1979.

[3] Chien, J. C. W. *Coordination Polymerization*; Academic Press, 1975.

[4] Natta, G.; Pasquon, I.; Zambelli, A. *Journal of the American Chemical Society* **1962**, *84*, 1488–1490.

[5] Doi, Y.; Ueki, S.; Keii, T. *Macromolecules* **1979**, *12*, 814–819.

[6] Muthukumaru, S., Pillari; Ravindranathan, M.; Sivaram, S. *Chemical Reviews* **1986**, *86*, 353–399.

[7] Keim, W.; Kowaldt, F.; Goddard, R.; Kruger, C. *Angew. Chem. Int. Ed. English* **1978**, *17*, 466–467.

[8] Breslow, D.; Newburg, N. *Journal of the American Chemical Society* **1957**, *79*, 5072–5073.

[9] Breslow, D. *U.S. Patent* **1955**, 537039.

[10] Natta, G.; Pino, P.; Mazzanti, G.; Lanzo, R. *Chim. Ind.* **1957**, *39*, 1032–1033.

[11] Natta, G.; Pino, P.; Mazzanti, G.; Giannini, U.; Mantica, E. *Polymer Science* **1957**, *26*, 120–123.

[12] Natta, G.; Pino, P.; Mazzanti, G.; Giannini, U. *Journal of the American Chemical Society* **1957**, *79*, 2975–2976.

[13] Long, W.; Breslow, D. *Journal of the American Chemical Society* **1960**, *82*, 1953–1957.

[14] Breslow, D.; Newburg, N. *Journal of the American Chemical Society* **1959**, *81*, 81–86.

[15] Long, W. *Journal of the American Chemical Society* **1959**, *81*, 5312–5316.

[16] Chien, J. *Journal of the American Chemical Society* **1959**, *81*, 86–92.

[17] Skupinska, J. *Chemical Reviews* **1991**, *91*, 613–648.

[18] Sinn, H.; Kaminsky, W. *Advances in Organometallic Chemistry* **1980**, *18*, 99–149.

[19] Arlman, E.; Cossee, P. *Journal of Catalysis* **1964**, *3*, 99–104.

[20] Cossee, P. *Journal of Catalysis* **1964**, *3*, 80–88.

[21] Cossee, P. *Tetrahedron Letters* **1960**, *12*, 12–16, 17–21.

[22] Zefirova, A.; Shilov, A. *E. Dokl. Akad Nauk. SSSR* **1961**, *136*, 599–602.

[23] Dyachkovskii, F. S.; Shilova, A.; Shilov, A. *Journal of Polymer Science Part C* **1967**, *16*, 2333–2339.

[24] Reichert, K.; Meyer, K. *Makromolecular Chemistry* **1973**, *169*, 163–176.

[25] Long, W.; Breslow, D. *Liebigs Ann. Chem.* **1975**, 463–469.

[26] Andresen, A.; Cordes, H.; Herwig, H.; Kaminsky, W.; Merk, A.; Mottweiler, R.; Pein, J.; Sinn, H.; Vollmer, H. *Angew. Chem. Int. Ed. English* **1976**, *15*, 630–632.

[27] Sinn, H.; Kaminsky, W. *Advances in Organometallic Chemistry* **1980**, *18*, 99–149.

[28] Sinn, H.; Kaminsky, W.; Vollmer, H.; Woldt, R. *Angew. Chem. Int. Ed. English* **1980**, *19*, 390–392.

[29] Kaminsky, W.; Kulper, K.; Brintzinger, H.; Wild, F. *Angew Chem. Int. Ed. English* **1985**, *24*, 507–508.

[30] Barron, A. *Comments on Inorganic Chemistry* **1993**, *14*, 123.

[31] Sinn, H.; Kaminsky, W.; Hoker, H. *Macromolecular Symposia 97* **1995**.

[32] Srinivasa, R. S.; Sivaram, S. *Progress in Polymer Science* **1995**, *20*, 309–367.

[33] Pasynkiewicz, S. *Polyhedron* **1990**, *9*, 429.

[34] Oliver, J.; Kuman, R. *Polyhedron* **1990**, *9*, 409.

[35] Atwood, J.; Hrneir, D.; Priester, R.; Rogers, R. *Organometallics* **1983**, *2*, 985.

[36] Mason, M. R.; Smith, J. M.; Bott, S. C.; Barron, A. R. *Journal of the American Chemical Society* **1993**, *115*, 4971–4984.

[37] Apblett, A.; Warren, A.; Barron, A. *Chemical Materials* **1992**, *4*, 167.

[38] Power, M.; Barron, A. *Journal of the Chemical Society Chemical Communications* **1991**, 1315.

[39] Benn, R.; Jannsen, E.; Lehmkul, H.; Rufinska, A.; Angermund, K.; Betz, P.; Goddard, R.; Kruger, C. *Journal of Organometallic Chemistry* **1991**, *411*, 37.

[40] Power, M.; Ziller, J.; Barron, A. *Organometallics* **1992**, *11*, 2783.

[41] Massey, A.; Park, A. *Journal of Organometallic Chemistry* **1964**, *2*, 245–250.

[42] Chambers, R.; Chivers, T. *Organometallic Chemistry Reviews* **1996**, *3*, 279–304.

[43] Chambers, R.; Chivers, T. *Journal of the Chemical Society* **1965**, 3933.

[44] Yang, X.; Stern, C.; Marks, T. J. *Journal of the American Chemical Society* **1994**, *116*, 10015–10031.

[45] Ewen, J.; Elder, M. *European Patent* **1991**, 0427697.

[46] Ewen, J.; Elder, M. *U.S. Patent* **1996**, 5561092.

[47] Yang, X.; Stern, C.; Marks, T. J. *Journal of the American Chemical Society* **1991**, *113*, 3623–3625.

[48] Parks, D.; Spence, R.; Piers, W. *Angew. Chem. International Edition English* **1995**, *34*, 809–811.

[49] Piers, W. E.; Chivers, T. *Chemical Society Reviews* **1997**, *26*, 345–353.

[50] Chen, Y.; Yang, S.; Stern, C.; Marks, T. J. *Journal of the American Chemical Society* **1996**, *118*, 12451–12452.

[51] Li, L.; Marks, T. J. *Organometallics* **2000**, *19*, 3332–3337.

[52] Li, L.; Marks, T. J. *Organometallics* **1998**, *17*, 3996–4003.

[53] Marks, T. J.; Stevens, J. In *Topics in Catalysis*; Baltzer: Amsterdam, 1999; Vol. 15, pp 97–103.

[54] Jia, L.; Yang, X.; Stern, C.; Marks, T. J. *Organometallics* **1997**, *16*, 842–857.

[55] Chien, J.; Tsai, W.; Rausch, M. *Journal of the American Chemical Society* **1991**, *113*, 8570–8571.

[56] Ewen, J.; Elder, M. *European Patent* **1991**, 0,426,637.

[57] Elder, M.; Ewen, J. *European Patent Application* **1993**, 0,573,403.

[58] Jia, L.; Yang, X.; Ishihara, A.; Marks, T. J. *Organometallics* **1995**, *14*, 3135–3137.

[59] Jelinek, T.; Baldwin, P.; Schedit, W.; Reed, C. *Inorganic Chemistry* **1993**, *32*, 1982–1990.

[60] Strauss, S. *Chemical Reviews* **1993**, *93*, 927–942.

[61] Seppelt, K. *Angew. Chem. Int. Ed. English* **1993**, *32*, 1025–1027.

[62] Bochmann, M. *Angew. Chem. Int. Ed. English* **1992**, *31*, 1181–1182.

[63] Chien, J.; Tsai, W.; Rausch, M. *Journal of the American Chemical Society* **1991**, *113*, 8570–8571.

[64] Jordan, R.; Bajgur, C.; Dasher, W.; Rheingold, A. *Organometallics* **1987**, *6*, 1041–1051.

[65] Turner, H.; Hlatky, G. *European Patent Application* **1988**, EP 2211004.

[66] Lin, Z.; Le Marechal, J.; Sabat, M.; Marks, T. J. *Journal of the American Chemical Society* **1987**, *109*, 4127–4129.

[67] Trotter, J. *The Chemistry of the Carbon-Halogen Bond*; Wiley, 1973.

[68] Deck, P.; Marks, T. J. *Journal of the American Chemical Society* **1995**, *117*, 6128–6129.

[69] Siedle, A.; Newmark, R. *Journal of Organometallic Chemistry* **1995**, *497*, 119–125.

[70] Jeske, G.; Lauke, H.; Mauermann, H.; Schumann, H.; Marks, T. J. *Journal of the American Chemical Society* **1985**, *107*, 8111–8118.

[71] Schumann, H.; Meese-Marktscheffel, J.; Esser, L. *Chemical Reviews* **1995**, *95*, 865–986.

[72] Schaverien, C. *Advances in Organometallic Chemistry* **1994**, *36*, 283–362.

[73] Greenwood, N.; Earnshaw, A. *Chemistry of the Elements*, 2nd ed.; BH, 1998.

[74] Elschenbroich, C.; Salzer, A. *Organometallics*, 2nd ed.; VCH Publishers, 1992.

[75] McKnight, A.; Waymouth, R. *Chemical Reviews* **1998**, *98*, 2587–2598.

[76] Sinn, H.; Kaminsky, W. *Advanced Organometallic Chemistry* **1980**, *18*, 99–149.

[77] Kaminsky, W.; Miri, M.; Sinn, H.; Woldt, R. *Makromolecular Chemistry Rapid Communications* **1983**, *4*, 417–421.

[78] Bercaw, J. *3rd Chemical Congress of North America.*

[79] Shapiro, P.; Bunel, E.; Schaefer, W.; Bercaw, J. *Organometallics* **1990**, *9*, 867–869.

[80] Okuda, J. *Chemische Berichte* **1990**, *123*, 1649.

[81] Canich, J. *U.S. Patent* **1991**, 5,026,798.

[82] Canich, J.; Licciardi, G. *U.S. Patent* **1991**, 5,057,475.

[83] Canich, J. *European Patent Application* **1991**, 0 420 436 A1.

[84] Stevens, J.; Timmers, F.; Wilson, D.; Schmidt, G.; Nickias, P.; Rosen, R.; Knight, G.; Lai, S. *European Patent Application* **1991**, 0416815A2.

[85] Stevens, J.; Neithamer, D. *European Patent Application* **1991**, 0 416 815 A2.

[86] Canich, J. *European Patent Application* **1991**, 0 420 436 A1.

[87] Stevens, J.; Timmers, F.; Wilson, D.; Schmidt, G.; Nickias, P.; Rosen, R.; Knight, G.; Lai, S. *European Patent Application* **1991**, 0 416 815 A2.

[88] Pannell, C. J., R.B.; Hlatky, G. *PCT International Application* **1994**, WO 94/00500.

[89] Canich, J. *U.S. Patent Application* **1992**, 5,096,867.

[90] Brant, P.; Canich, J. *PCT Internation Application* **1993**, WO 93/12151.

[91] Brant, P.; Canich, J.; Merrill, N. *PCT Internation Application* **1993**, WO 93/21242.

[92] Brant, P.; Canich, J.; Dias, A.; Bamberger, R.; Licciardi, G.; Henrichs, P. *PCT International Patent Application* **1994**, 94/07930.

[93] Canich, J. *PCT International Patent Application* **1996**, WO 96/00244.

[94] LaPointe, R.; Rosen, R.; Nickias, P. *European Patent Application* **1992**, 0 495 375 A2.

[95] LaPointe, R.; Stevens, J.; Nickias, P.; McAdon, M. *European Patent Application* **1992**, 0 520 732 A1.

[96] Lai, S.; Wilson, J.; Knight, G.; Stevens, J. *PCT International Patent Application* **1993**, WO 93/08221.

[97] Rosen, R.; Nickias, P.; Devore, D.; Stevens, J.; Timmers, F. *U.S. Patent* **1994**, 5,374,696.

[98] Devore, D.; Crawford, L.; Stevens, J.; Timmers, F.; Mussell, R.; Wilson, D.; Rosen, R. *PCT International Patent Application* **1995**, WO 95/00526.

[99] Nickias, P.; McAdon, M.; Patton, J. *PCT International Patent Application* **1997**, 97/15583.

[100] Harrington, B. *PCT International Patent Application* **1996**, WO 96/40806.

[101] Harrington, B.; Hlatky, G.; Canich, J.; Merrill, N. *U.S. Patent* **1997**, 5,635,573.

[102] Devore, D. *European Patent Application* **1992**, 0 514 828 A1.

[103] Sernetz, F.; Muelhaupt, R.; Waymouth, R. *Macromolecular Chemistry and Physics* **1996**, *197*, 1071–1083.

[104] Xu, G. *Macromolecules* **1998**, *31*, 2395–2402.

[105] Stevens, J. *Studies in Surface Science and Catalysis* **1996**, *101*, 11–20.

[106] Mani, R.; Burns, C. *Macromolecules* **1991**, *24*, 5476.

[107] Soga, K.; Lee, D.; Yangihara, H. *Polymer Bulletin* **1988**, *20*, 237.

[108] Kakugo, M.; Miyatake, T.; Mizunuma, K. *Studies of Surface Science Catalysis* **1990**, *56*, 517.

[109] Miyatake, K.; Mizunuma, M.; Kakugo, M. *Makromol. Chem., Marcromol. Symp.* **1993**, *66*, 203.

[110] Oliva, L.; Caporaso, L.; Pellecchia, C.; Zambelli, A. *Marcomolecules* **1995**, *28*, 4665.

[111] Scollard, J.; McConville, D.; Payne, N.; J.J., V. *Macromolecules* **1996**, *29*, 5241.

[112] Scollard, J.; McConville, D. *Journal of the American Chemical Society* **1996**, *118*, 10008–10009.

[113] Longo, P.; Oliva, L.; Grassi, A.; Pellecchia, C. *Makromol. Chem.* **1989**, *190*, 2357.

[114] Herfert, N.; Fink, G. *Makromol. Chem.* **1992**, *193*, 773.

[115] Williams, D.; Schofield, M.; Anhaus, J.; Schrock, R. *Journal of the American Chemical Society* **190**, *112*, 6728.

[116] Glueck, D.; Green, J.; Michelman, R. I.; Wright, I. *Organometallics* **1992**, *11*, 4560.

[117] Williams, D.; Schofield, M.; Schrock, R. *Organometallics* **1993**, *12*, 4560.

[118] Gibson, V. *J. Chem. Soc., Dalton Trans.* **1994**, 1607.

[119] Bolton, P.; Adams, N.; Clot, E.; Cowley, A.; Wilson, P.; Schroder, M.; Mountford, P. *Organometallics* **2006**, *25*, 5549–5565.

[120] Jolly, P.; Wilke, G. *The Organic Chemistry of Nickel*; Academic, 1975.

[121] Bogdanovic, B. *Advances in Organometallic Chemistry* **1979**, *17*, 105.

[122] Peuckert, M.; Keim, W. *Organometallics* **1983**, *2*, 594–597.

[123] Keim, W. *Angew. Chem. Int. Ed. Engl.* **1990**, *29*, 235–244.

[124] Johnson, L.; Killian, C.; M., B. *Journal of the American Chemical Society* **1995**, *117*, 6414–6415.

[125] Small, B.; Brookhart, M.; Bennett, A. *Journal of the American Chemical Society* **1998**, *120*, 4049.

[126] Small, L.; Brookhart, M. *Journal of the American Chemical Society* **1998**, *120*, 7143–7144.

[127] Britovsek, G.; Gibson, V.; Kimberly, B.; Maddox, P.; McTavish, S.; Solan, G.; White, A.; Williams, D. *Chemical Communications* **1998**, 849.

[128] Ziegler, K. *Advanced Organometallic Chemistry* **1968**, *6*, 1.

[129] Cossee, P. *Transactions of the Faraday Society* **1962**, *58*, 1226.

[130] Henrici, O. G.; Olive, S. *Angew. Chem. Ed. Engl.* **1967**, *6*, 790.

[131] Purcell, K.; Kotz, J. C. *Inorganic Chemistry*; W.B. Saunders Company, 1977.

[132] Brookhart, M.; L.H. Green, M. *Journal of Organometallic Chemistry* **1983**, *250*, 395–408.

[133] Dawoodi, Z.; L.H. Green, M.; Mtetwa, V.; Prout, K. *Journal of the Chemical Society, Chemical Communications* **1982**, 802.

[134] Dawoodi, Z.; L.H. Green, M.; Mtetwa, V.; Prout, K. *Journal of the Chemical Society, Dalton Transactions* **1986**, 1629.

[135] Cotton, F.; Frenz, B.; Hunter, D. *Journal of the American Chemical Society* **1974**, *96*, 4820.

[136] Calligaris, M.; Mitchelli, F.; Nardin, G.; Randaccio, L. *Journal of Chemical Society. A.* **1971**, 2720.

[137] Moseley, P.; Shearer, H. *Journal of the Chemical Society, Dalton Transactions* **1973**, 64.

[138] Green, M. L. H. *Journal of Organometallic Chemistry* **1995**, *500*, 127–148.

[139] DePue, J. S.; Collum, D. B. *Journal of the American Chemical Society* **1988**, *110*, 5518–5524.

[140] DePue, J. S.; Collum, D. B. *Journal of the American Chemical Society* **1988**, *110*, 5524–5533.

[141] Friebolin, H. In *Basic One and Two-Dimensional NMR Spectroscopy*; Wiley-VCH, 2005; Chapter 1, pp 30–31.

[142] Keeler, J. *Understanding NMR Spectroscopy*; Wiley, 2005.

[143] Allen, F. *Acta Cryst. B58*, 380–388.

[144] March, J. *Advanced Organic Chemistry*, 4th ed.; Wiley Interscience, 1996.

[145] Dury, M.; Priou, C.; Richard, J. *U.S. Patent* **2004**, 6,700,019.

[146] Lorber, C.; Choukroun, R.; Vendier, L. *Organometallics* **2008**, *27*, 5017–5024.

[147] R. Galsworthy, J.; L. H. Green, M.; Maxted, N.; Muller, M. *J. Chem. Soc., Dalton Trans.* **1998**, 387–392.

[148] Sasaki, T.; Johoji, H.; Shiraishi, H.; Miyoshi, Y. *Japenese Patent Application, year = 1992, pages = JP 92-104168.*

[149] Nicco, A.; Aboulafia, J. *European Patent Application* **1964**, FR 1358503.

[150] Yoshida, T.; Yuguchi, S. *European Patent Application* **1963**, JP 42011646.

[151] Giannini, U.; Longi, P.; Deluca, D.; Pivotto, B. *European Patent Application* **1971**, DE 2030753.

[152] Giannini, U.; Longi, P.; Deluca, D.; Pivotto, B. *European Patent Application* **1969**, IT 867243.

[153] Hefner, J. G. *European Patent Application* **1988**, EP 320169.

[154] Adrien, N.; Joseph, A. *Compositions catalytiques de polymerisation d'alpha olefins*; 1963.

[155] Hefner, J. *Transition metal amides as catalysts for the polymerization of olefins*; 1989.

[156] Miller, B. *Polymerisation Data*; Technical Report, 2010.

[157] Keller, K. M.; Turner, J. F. C. *Unpublished Results*.

[158] Labinger, J. A.; Bercaw, J. E. *Nature* **2002**, *417*, 507–514.

[159] Marat, K. *Spinworks 3.0*, University of Manitoba, 2008.

[160] Colvin, A. J.; Turner, J. F. C. *Unpublished Results*.

[161] Zanger, M.; Moyna, G. *Journal of Chemical Education* **2005**, *82*, 1390.

[162] Marks, T. J.; Kennelly, W. J.; Kolb, J. R.; Shimp, L. A. *Inorganic Chemistry* **1972**, *11*, 2540–2546.

[163] Leitner, W. *Angew. Chem. Int. Ed. Engl.* **1995**, *34*, 2207–2221.

[164] Jessop, P.; Ikariya, T.; Noyori, R. *Chemical Reviews* **1996**, *96*, 259–272.

[165] Marks, T. J. *Chemical Reviews* **2001**, *101*, 953–996.

[166] Aresta, M.; Dibenedetto, A. *Dalton Trans.* **2007**, *28*, 2975–2992.

[167] Fachinetti, G.; Floriani, C.; Roselli, A.; Pucci, S. *Chemical Communications* **1978**, *6*, 269–270.

[168] Gamboretta, S.; Strologo, S.; C., F.; Chiesi-Villa, A.; Guastini, C. *Journal of the American Chemical Society* **1985**.

[169] Cutler, A.; Raja, M.; Todaro, A. *Inorganic Chemistry* **1987**, *26*, 2877–2881.

[170] Looney, A.; Han, R.; Gorrell, I.; Cornebise, M.; Yoon, K.; Parkin, G. *Organometallics* **1995**, *14*, 274–288.

[171] Gorrell, I.; Looney, A.; Parkin, G. *J. Chem. Soc. Chem. Commun.* **1990**, 220–222.

[172] Gorrell, I.; Looney, A.; Parkin, G.; Rheingold, A. *Journal of the American Chemical Society* **1990**, *112*, 4068–4069.

[173] Han, R.; Gorrell, I.; Looney, A.; Parkin, G. *J. Chem. Soc., Chem. Commun.* **1991**, 717–719.

[174] Gilman, H.; Jones, R. *Journal of the American Chemical Society* **1946**, *68*, 517–520.

[175] Rankin, M. A.; Cummins, C. C. *Journal of the American Chemical Society* **2010**, *132*, 10021–10023.

[176] Fisher, I.; Bell, A. *Journal of Catalysis* **1997**, *172*, 222–237.

[177] Fisher, I.; Bell, A. *Journal of Catalysis* **1998**, *178*, 153–173.

[178] Frank, B.; Jentoft, F.; Soerijanto, H.; Krohnert, J.; Schlogl, R.; Schomacker, R. *Journal of Catalysis* **2007**, *246*, 177–192.

[179] Matsuo, T.; Kawaguchi, H. *Journal of the American Chemical Society* **2006**, *128*, 12362–12363.

[180] Schlorer, N.; Berger, S. *Organometallics* **2001**, *20*, 1703–1704.

[181] Schlorer, N.; Cabrita, E.; Berger, S. *Angew. Chem. Int. Ed.* **2002**, *41*, 107–109.

[182] Riduan, S.; Zhang, Y.; Ying, J. *Angew. Chem. Int. Ed.* **2009**, *48*, 3322–3225.

[183] Tardif, O.; Hashizume, F.; Hou, A. *Journal of the American Chemical Society* **2004**, *126*, 8080–8081.

[184] Berthet, J.; Ephritikhine, M. *New Journal of Chemistry* **1992**, *16*, 767–768.

[185] Day, V.; Fredrich, M.; Klemperer, W.; Liu, R. *Journal of the American Chemical Society* **1979**, *101*, 491–492.

[186] Murugesu, M.; Abboud, K.; Christou, G. *Polyhedron* **2004**, *23*, 2779–2788.

[187] Chakov, N.; Zahkharov, L.; Rheingold, A.; Abboud, K.; Christou, G. *Inorganic Chemistry* **2005**, *44*, 4555–4567.

[188] Fursova, E.; Romanenko, G.; Ovcharenko, V. *Russian Chemical Bulletin International Edition* **2005**, *54*, 811–813.

[189] Figueroa, J.; Cummins, C. C. *Journal of the American Chemical Society* **2003**, *125*, 4020–4021.

[190] Kaesz, H.; Daillant, R. *Chemical Reviews* **1972**, *72*, 231–281.

[191] Fryzuk, M. D.; MacKay, B.; Patrick, B. *Journal of the American Chemical Society* **2003**, *125*, 3234–3235.

[192] Gavenonis, J.; Tilley, T. D. *Organometallics* **2004**, *23*, 31–43.

[193] Watanabe, T.; Ishida, Y.; Matsuo, T.; Kawaguchi, H. *Journal of the American Chemical Society* **2009**, *131*, 3474–3475.

[194] Fulmer, G. R.; Miller, A. J.; Sherden, N. H.; Gottlieb, H. E.; Nudelman, A.; Stoltz, B. M.; Bercaw, J. E.; Goldberg, K. I. *Organometallics* **2010**, *29*, 2176–2179.

[195] Jones, N. A.; Liddle, S. T.; Wilson, C. A.; Arnold, P. L. *Organometallics* **2007**, *26*, 755–757.

Appendix A

^{1}H and ^{13}C NMR Spectra

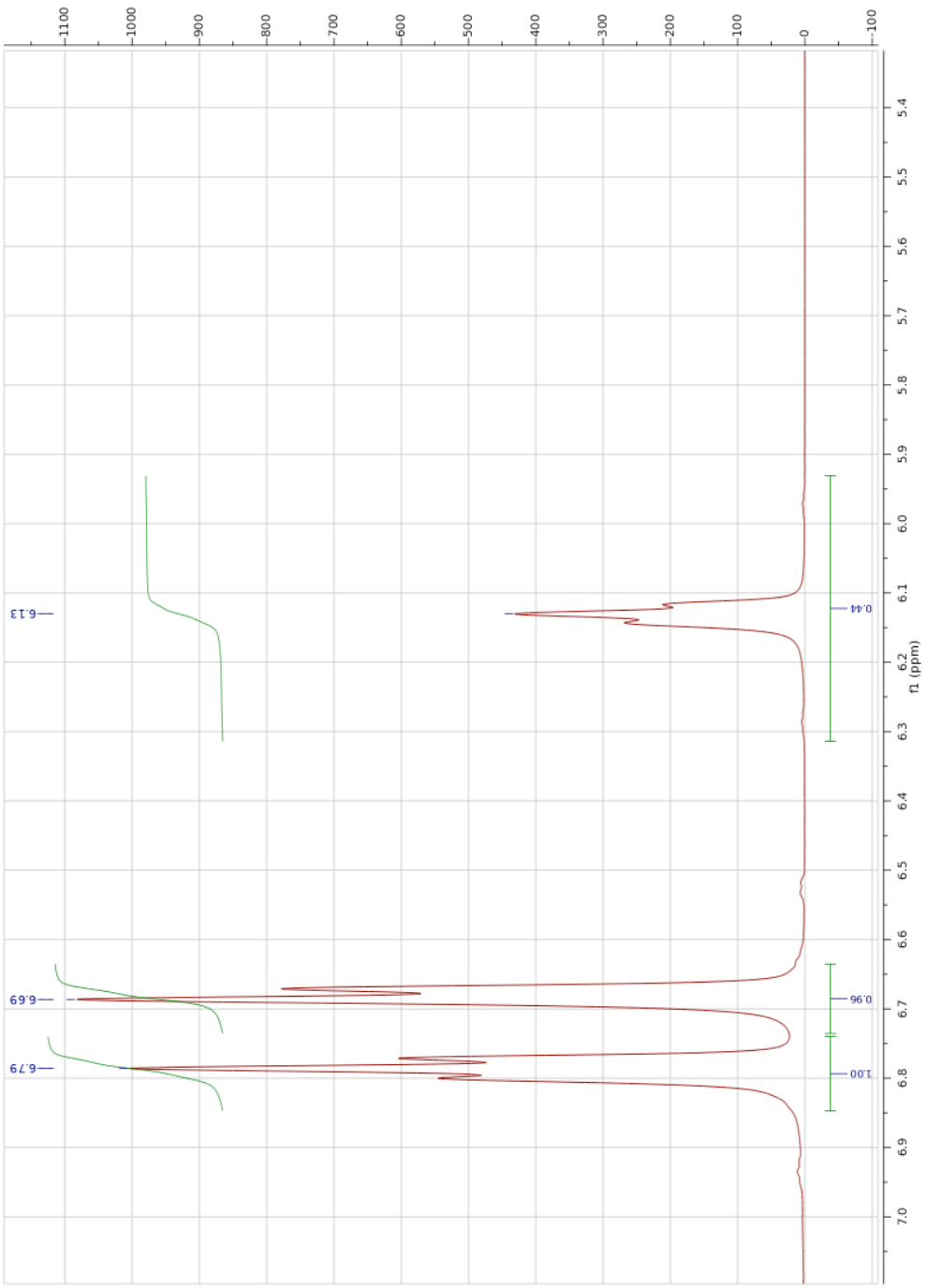

Figure A.1: The aromatic region of the ^{1}H spectrum of dpaLi

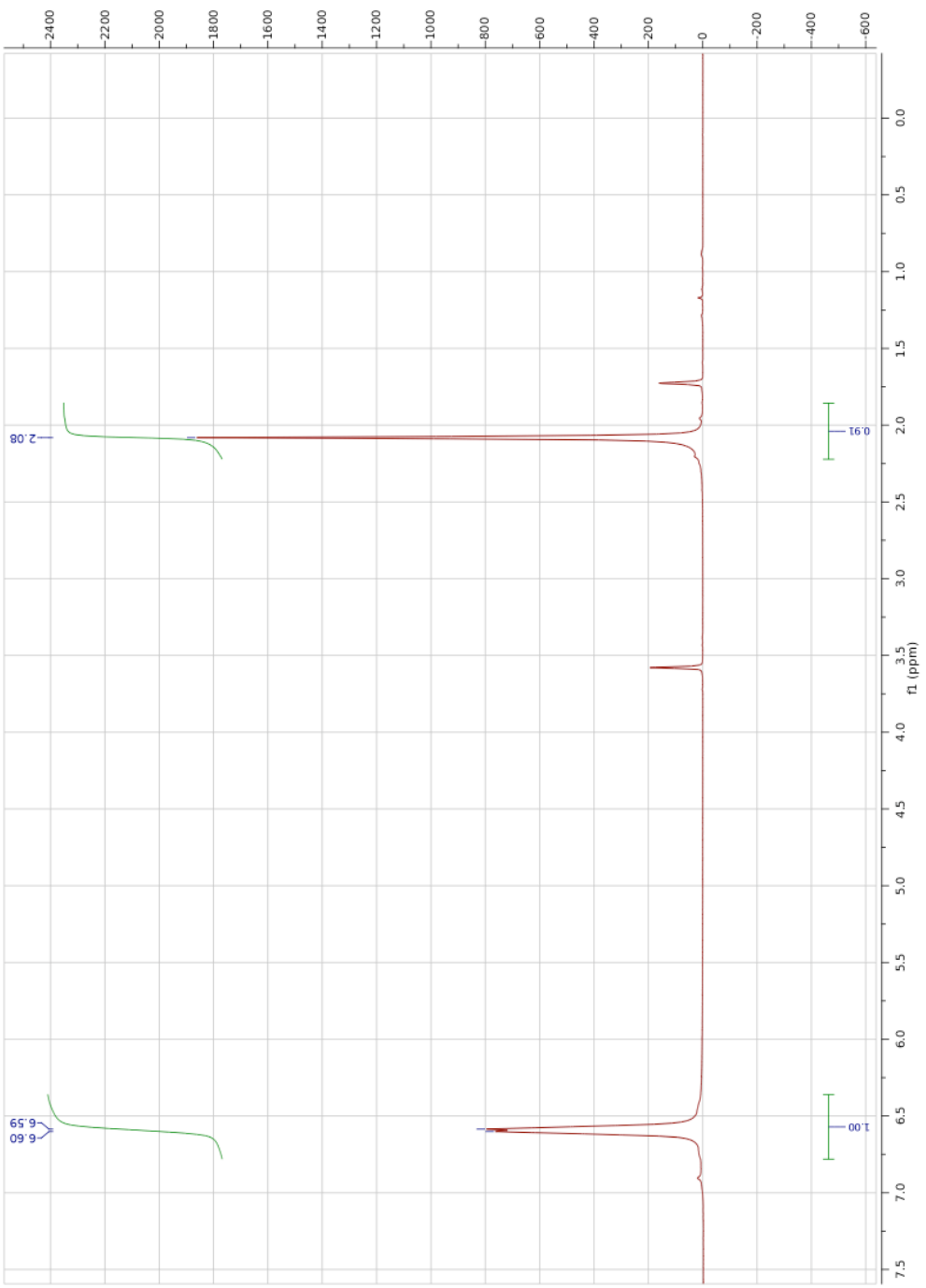

Figure A.2: The ^{1}H spectrum of dptaLi

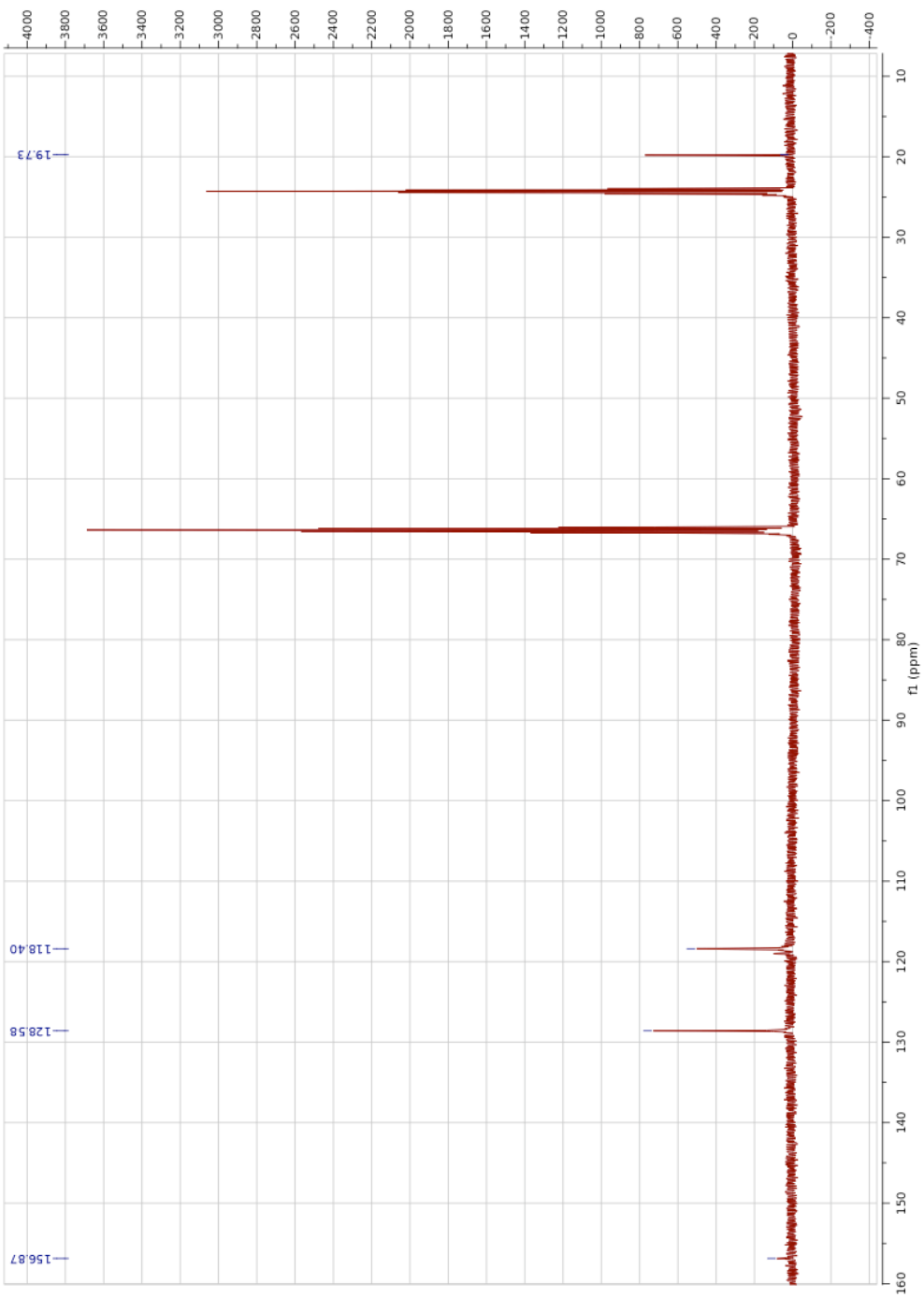

Figure A.3: The ^{13}C spectrum of dptaLi

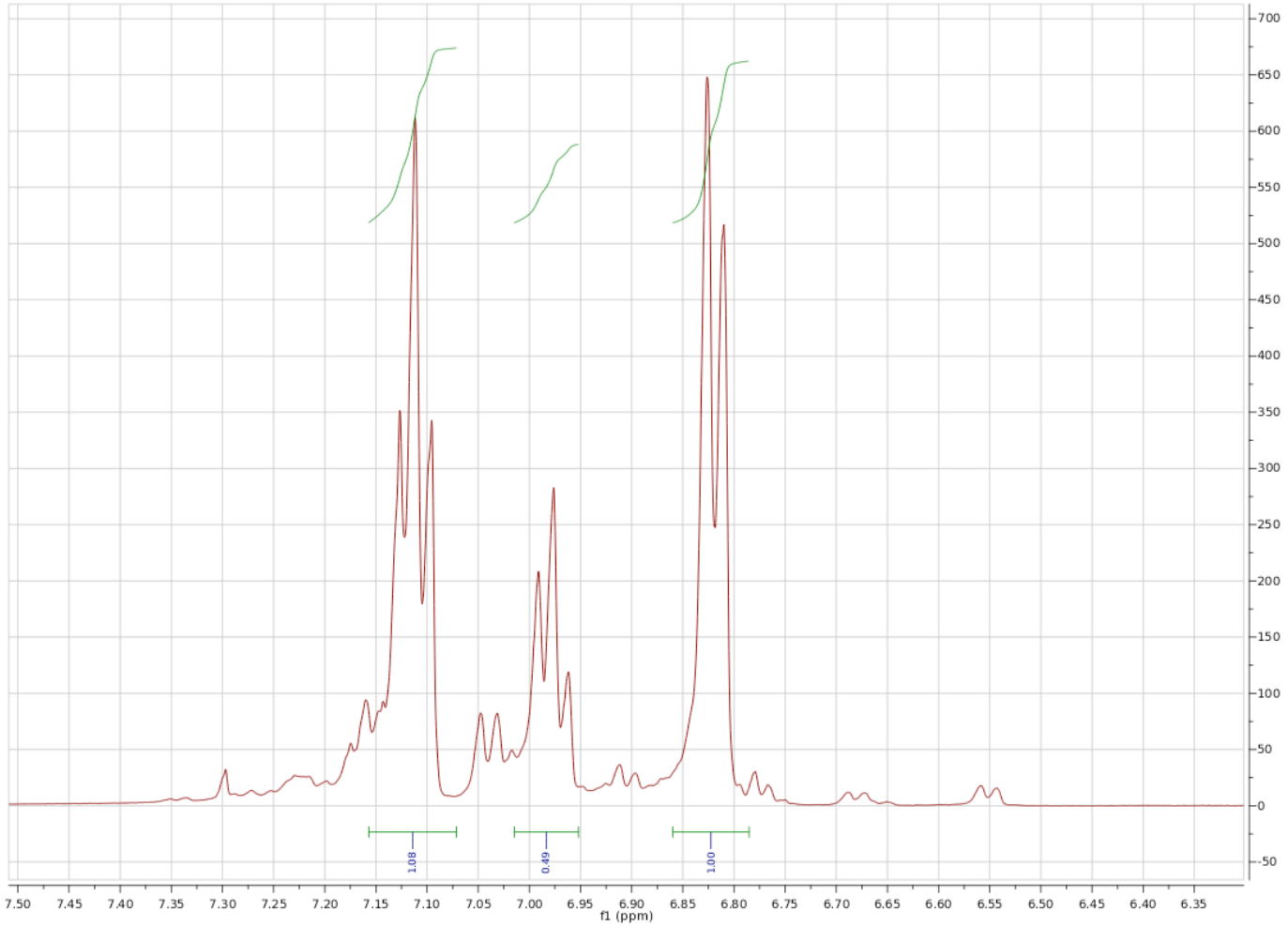

Figure A.4: The ^{1}H spectrum of $(dpa)_3TiCl$

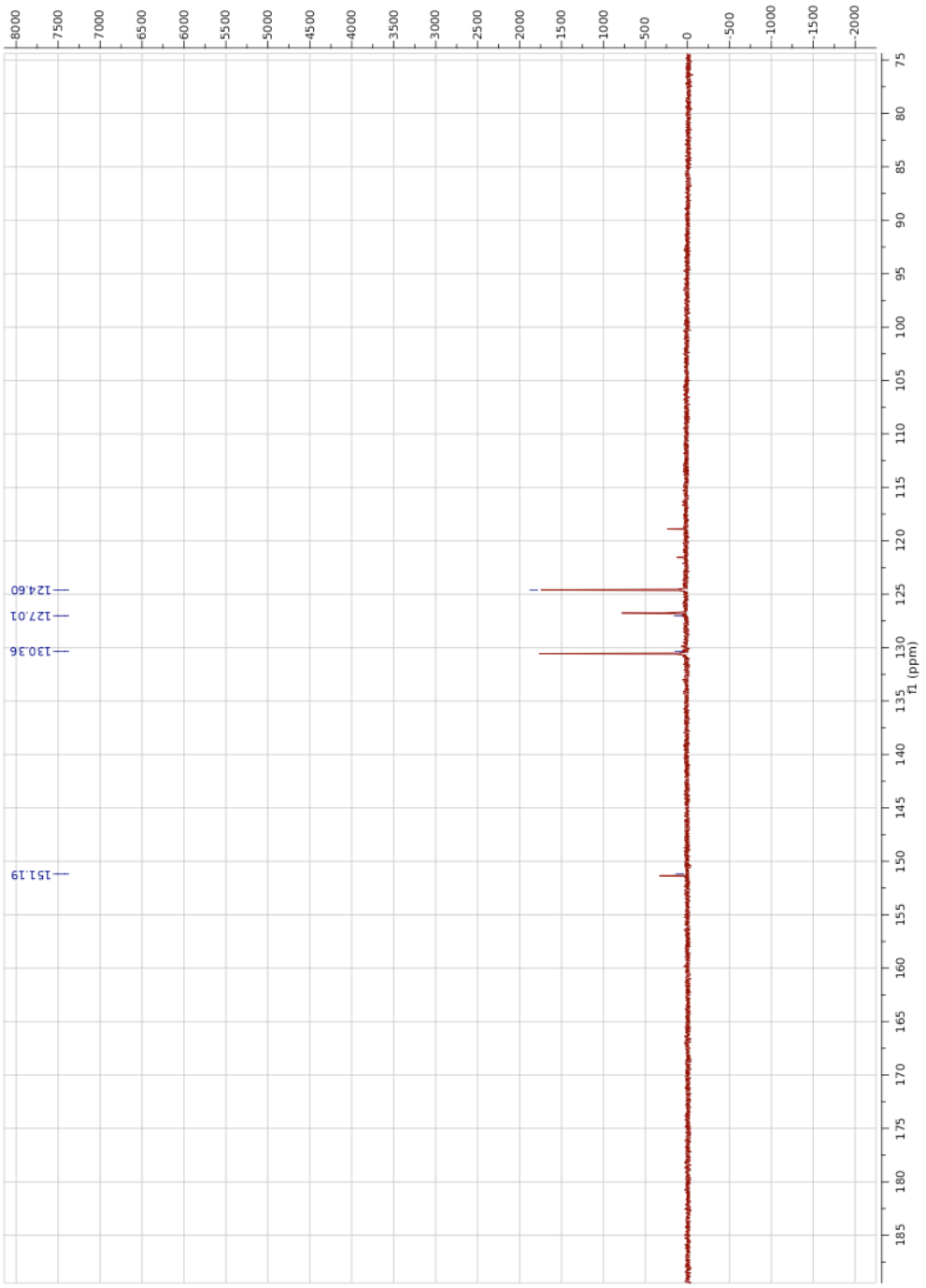

Figure A.5: The ^{13}C spectrum of $(dpa)_3$ TiCl

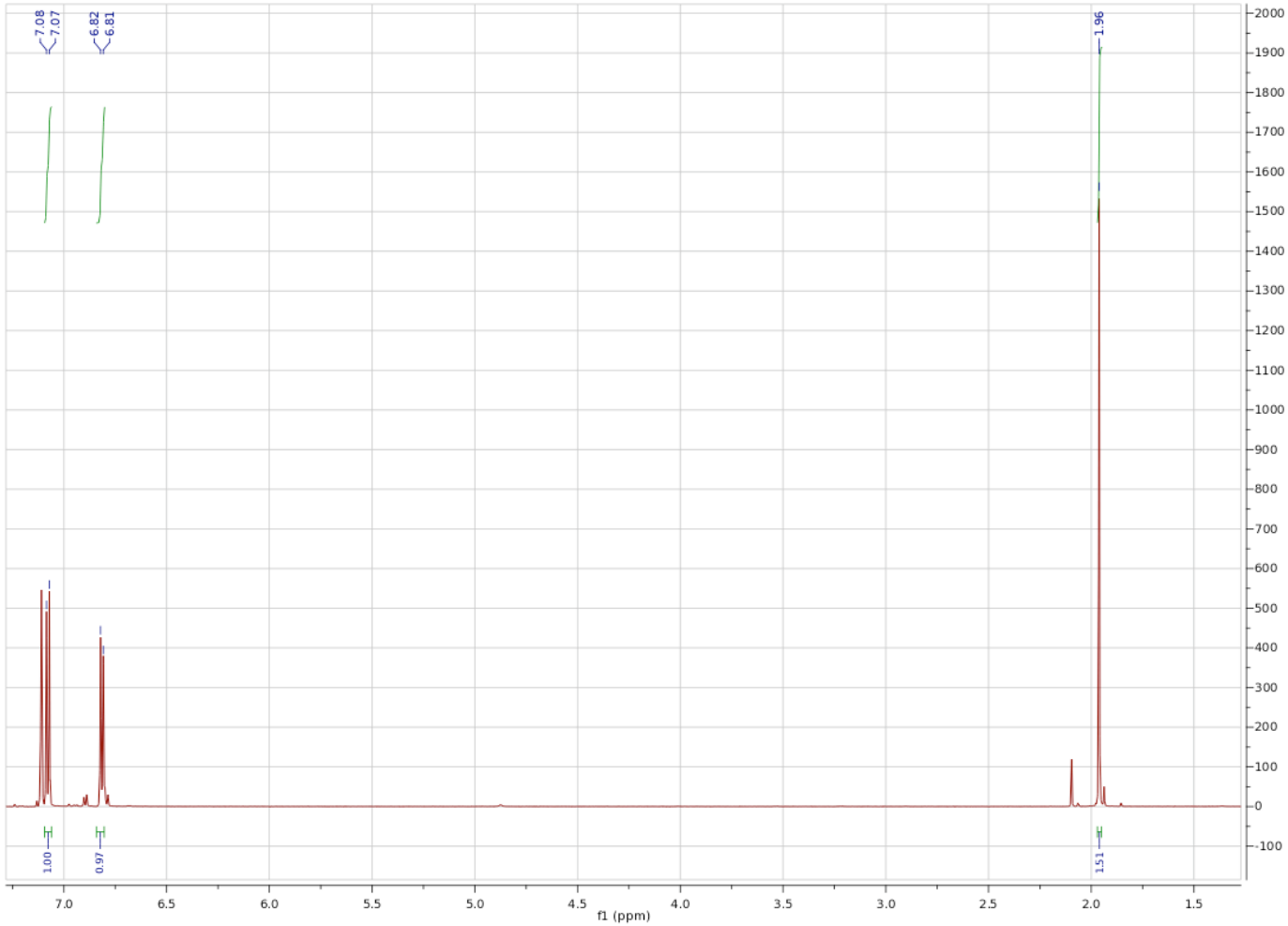

Figure A.6: The ^{1}H spectrum of $(dpta)_3TiCl$

Figure A.7: Aromatic region of the ^{1}H spectrum of $(dpta)_3TiCl$

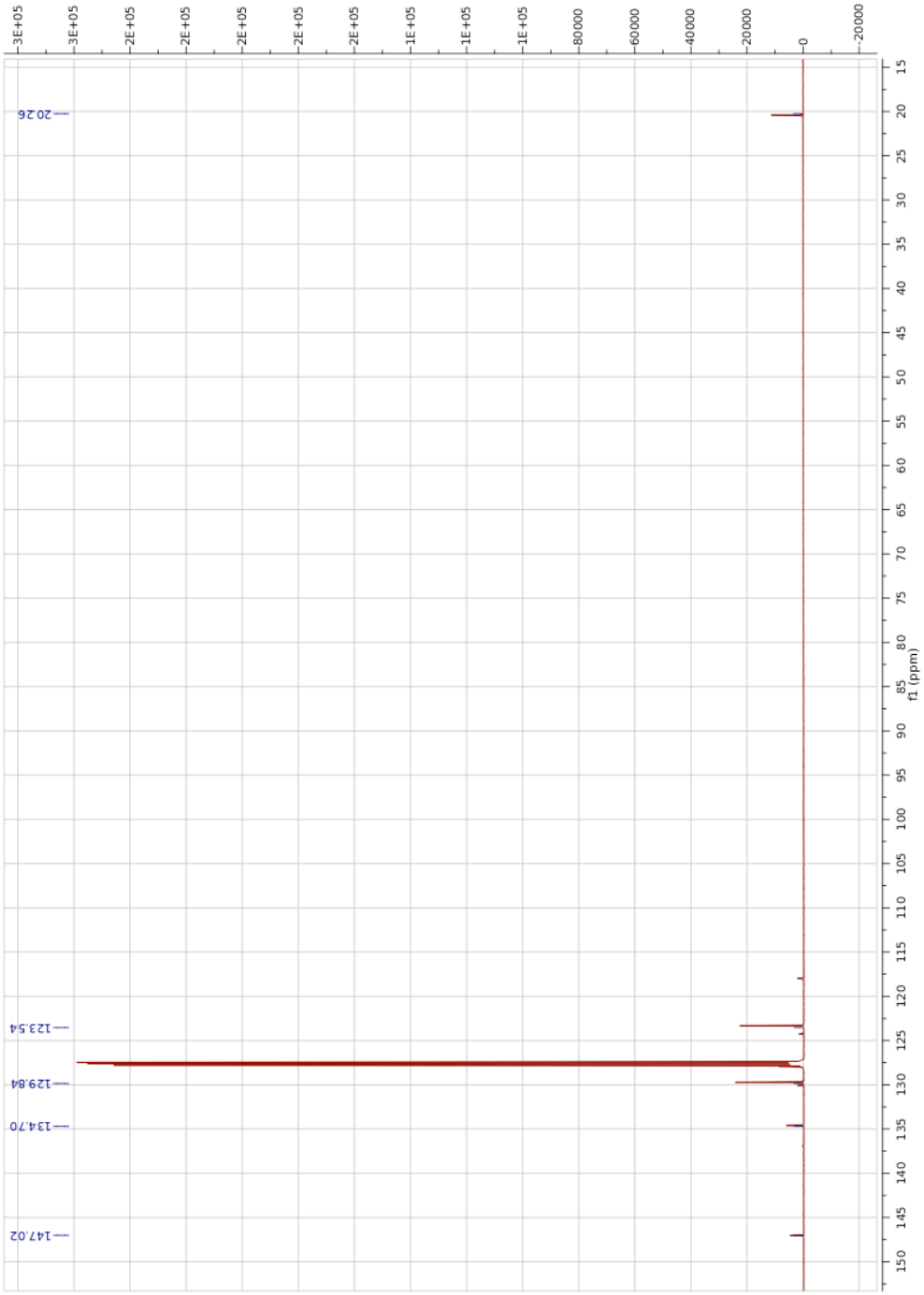

Figure A.8: The ^{13}C spectrum of $(dpta)_3TiCl$

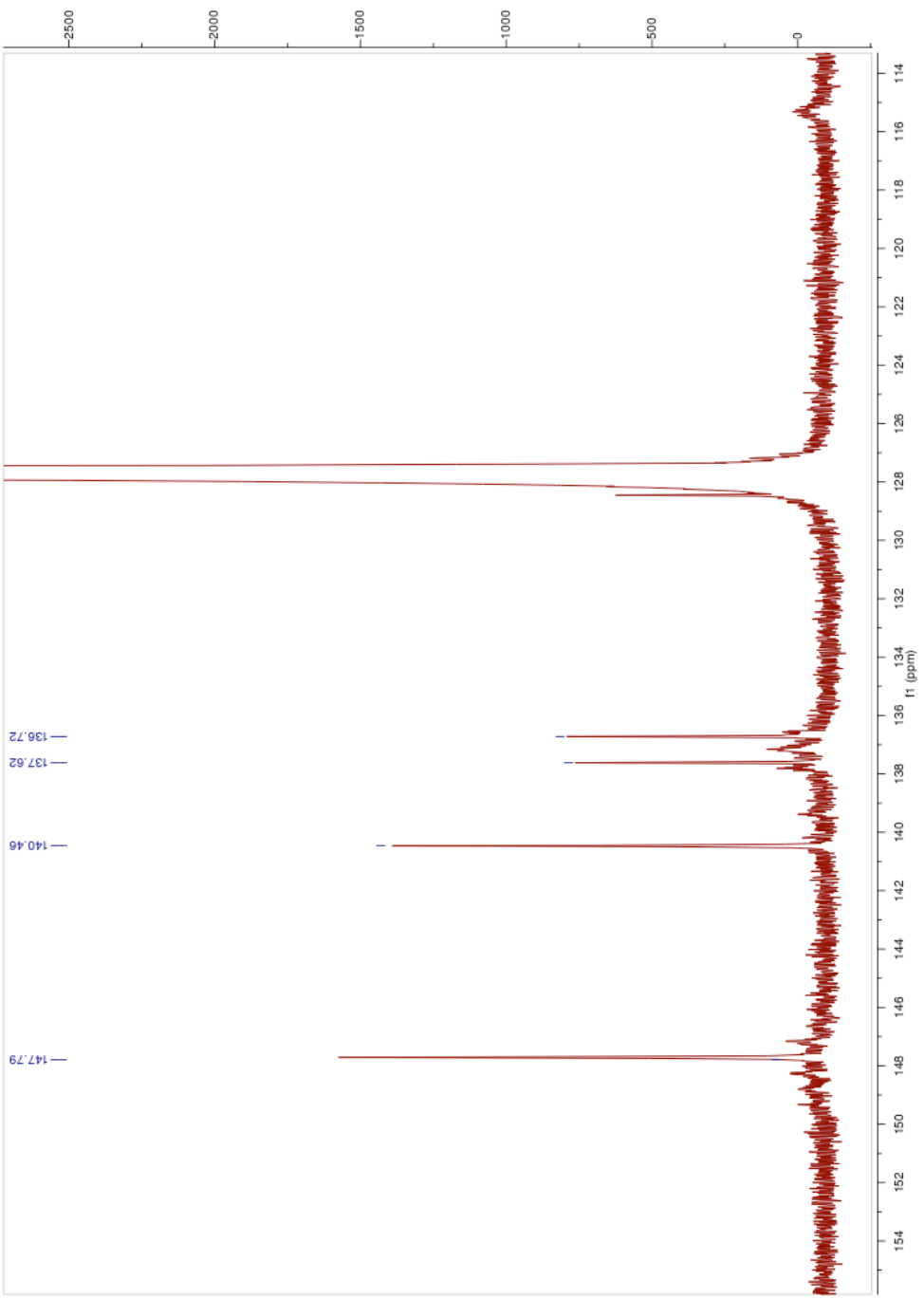

Figure A.9: The ^{19}F spectrum of $KB(C_6F_5)_4$

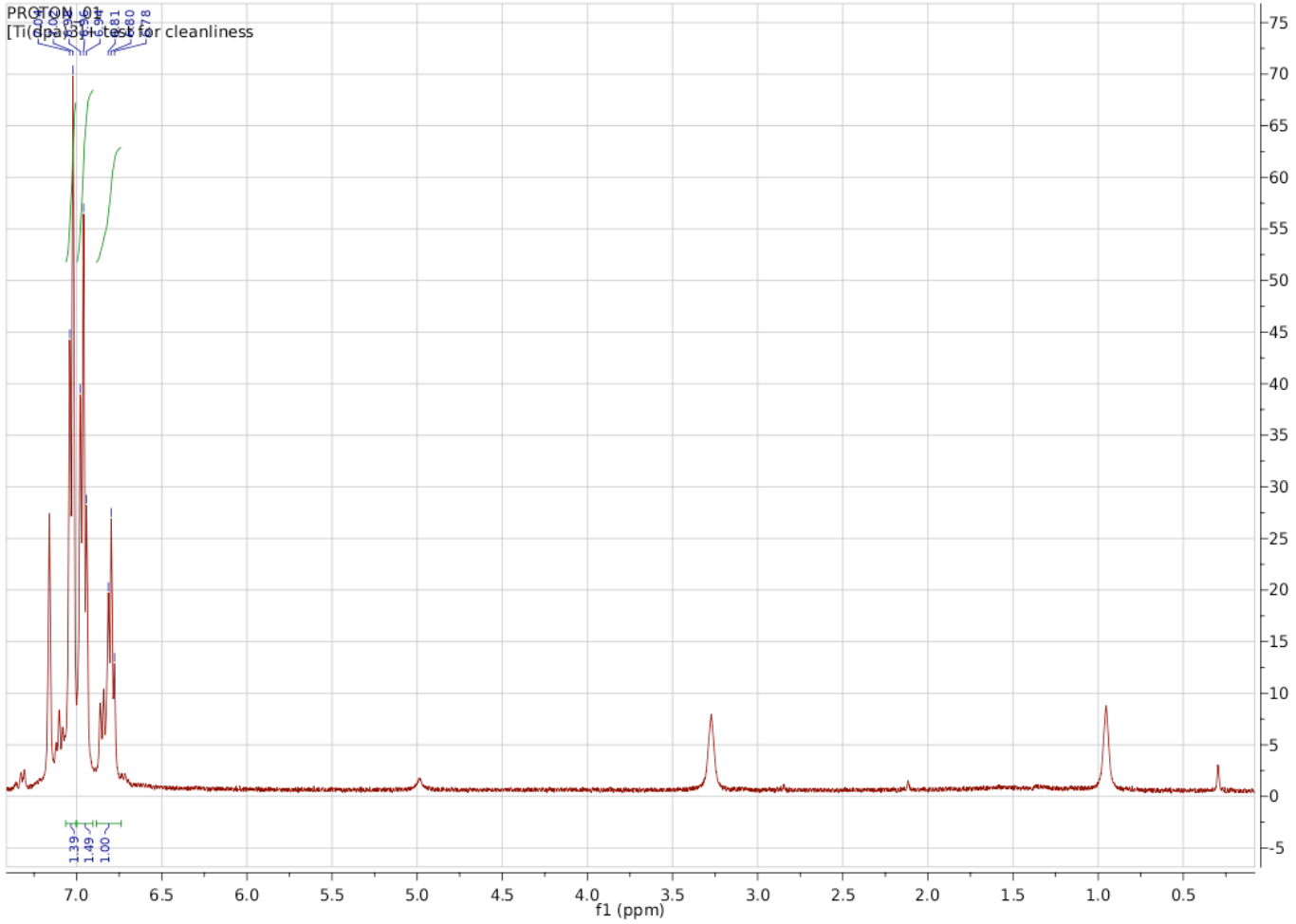

Figure A.10: The ^{1}H spectrum of $[(dpa)_3Ti]^{+}[B(C_6F_5)_4]^{-}$

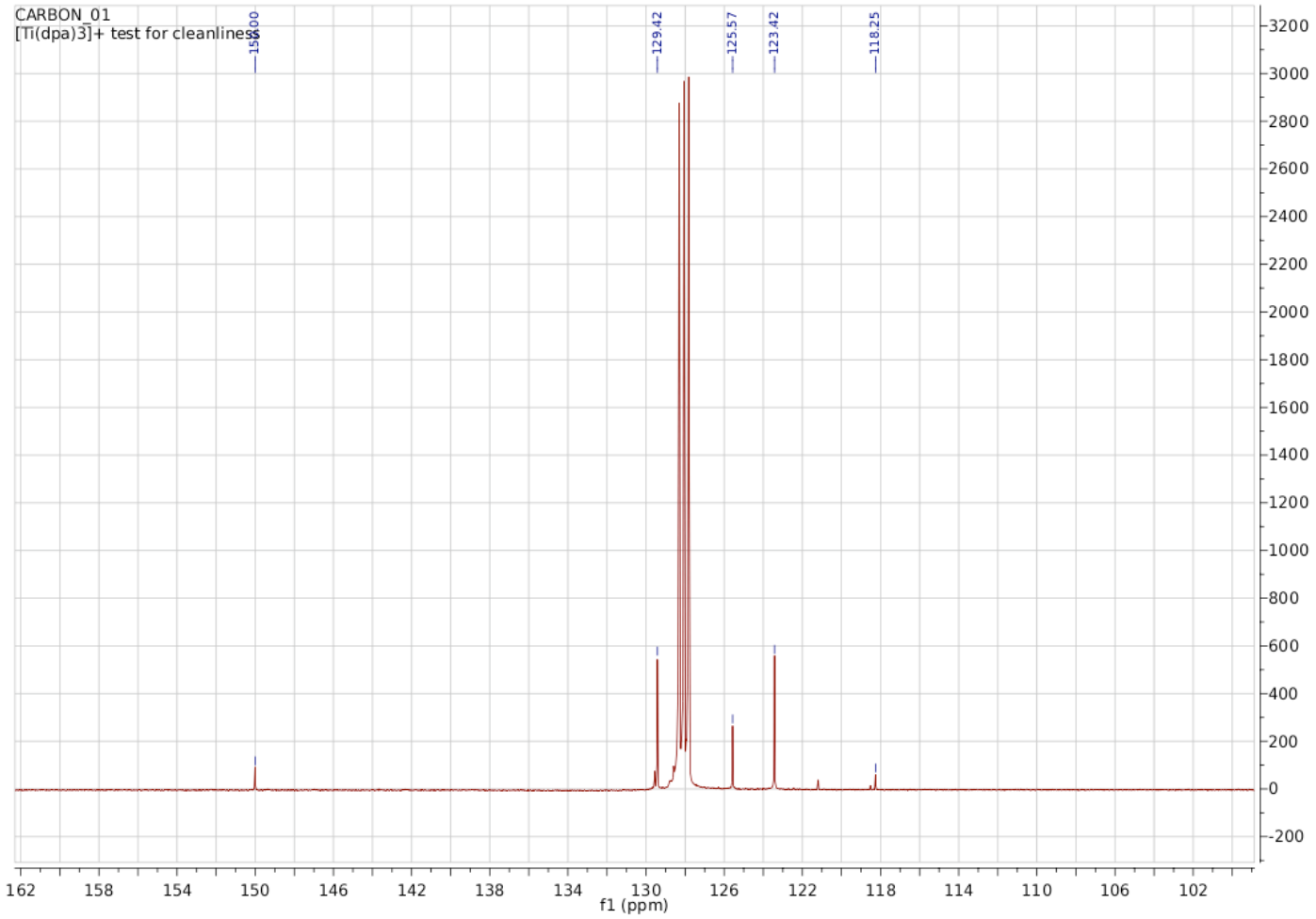

Figure A.11: The ^{13}C spectrum of $[(dpa)_3Ti]^+[B(C_6F_5)_4]^-$

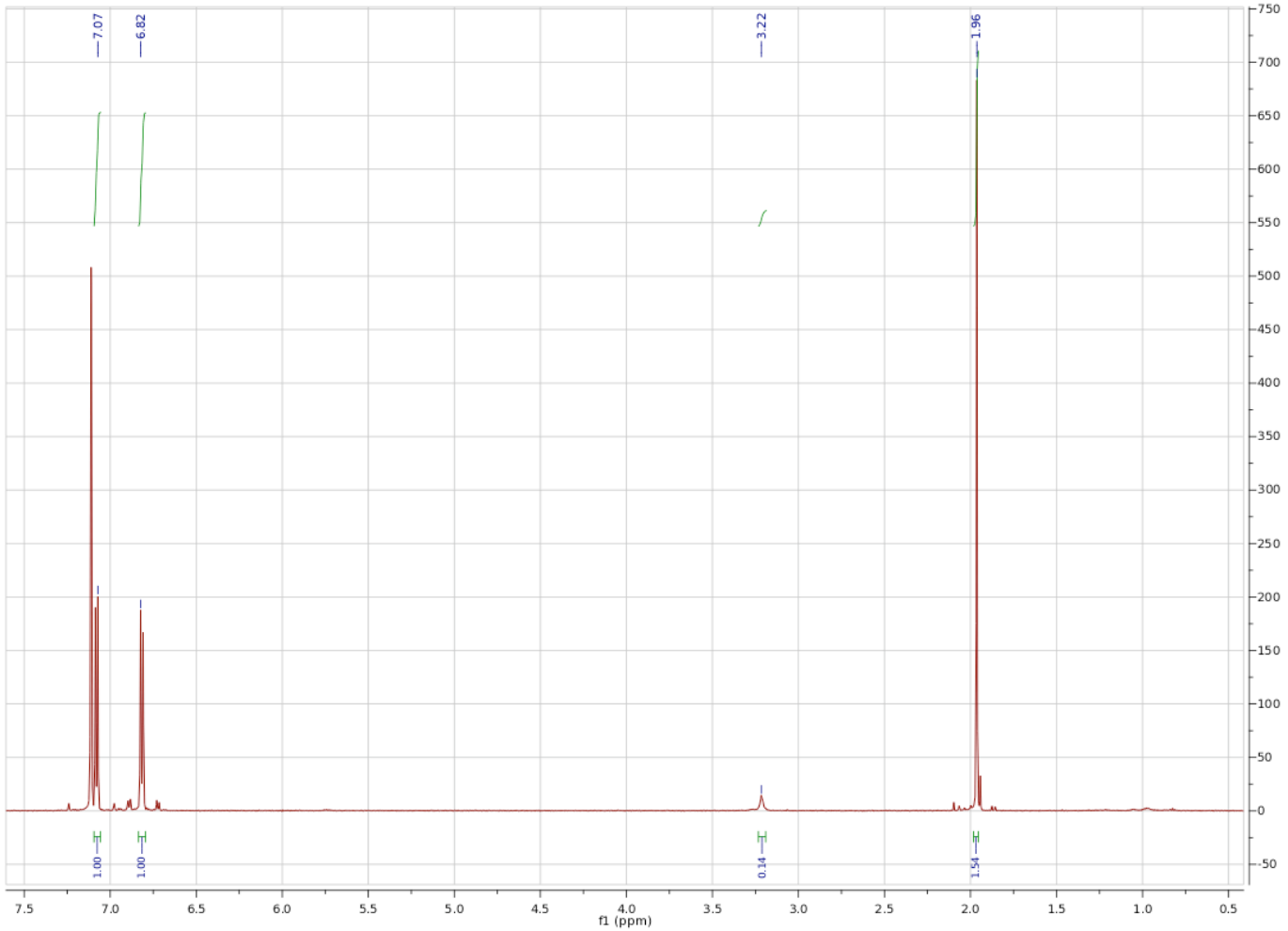

Figure A.12: The ^{1}H spectrum of $[(dpta)_3Ti]^{+}[B(C_6F_5)_4]^{-}$

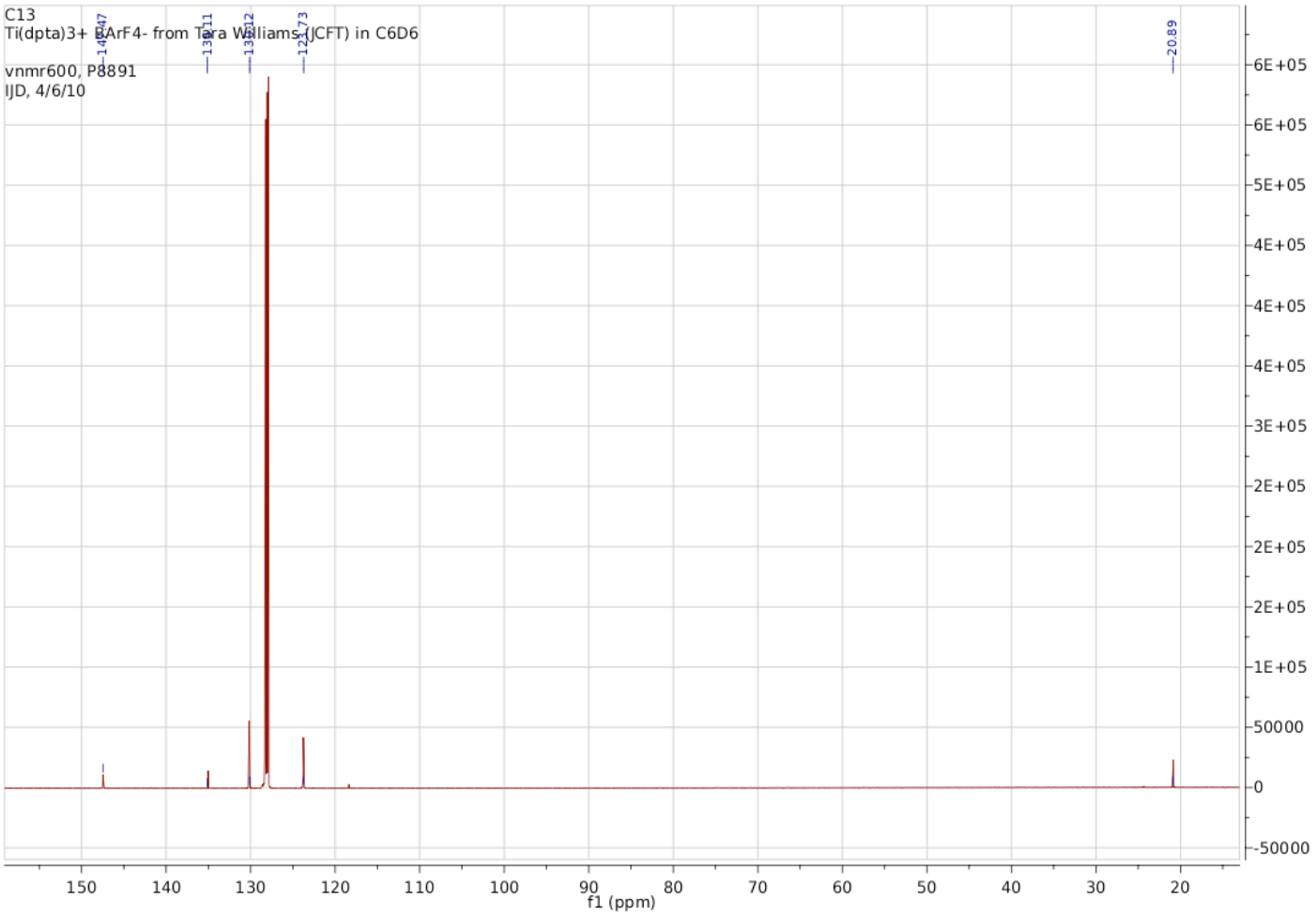

Figure A.13: The ^{13}C spectrum of $[(dpta)_3Ti]^+[B(C_6F_5)_4]^-$

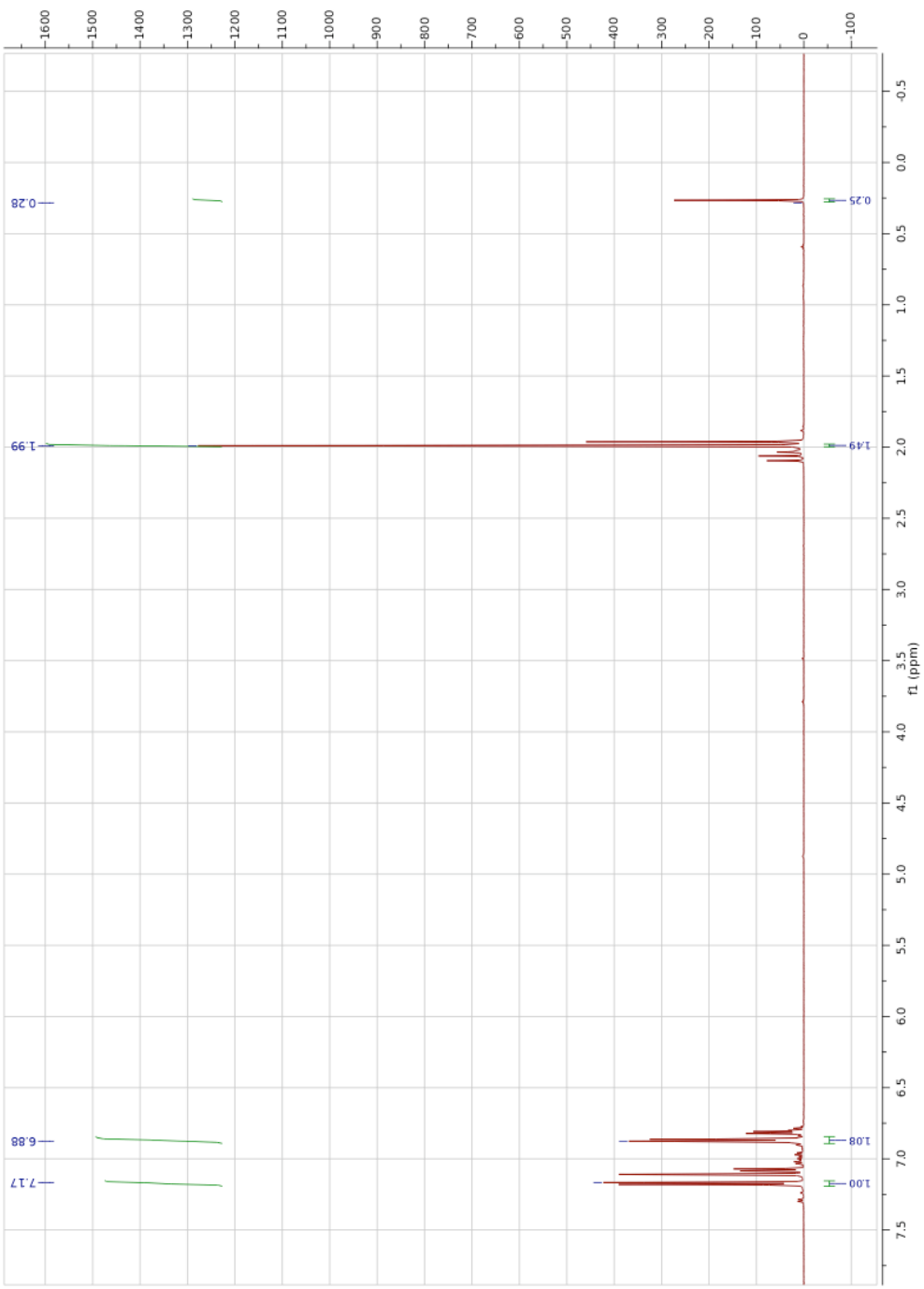

Figure A.14: The ^{1}H spectrum of $(dpta)_3$TiMe

Figure A.15: The ^{13}C spectrum of $(dpta)_3TiMe$

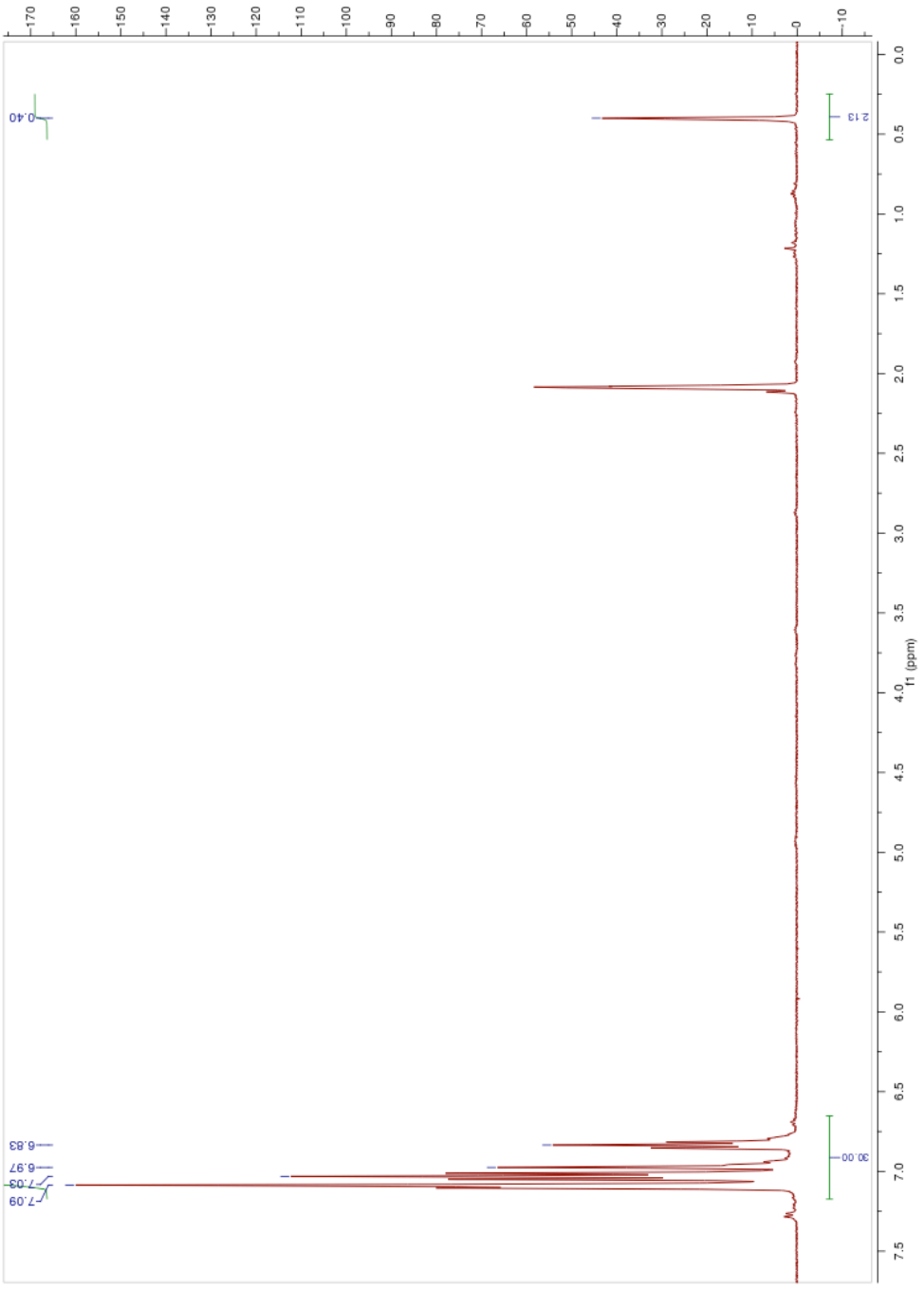

Figure A.16: The ^{1}H spectrum of $(dpa)_3TiMe$

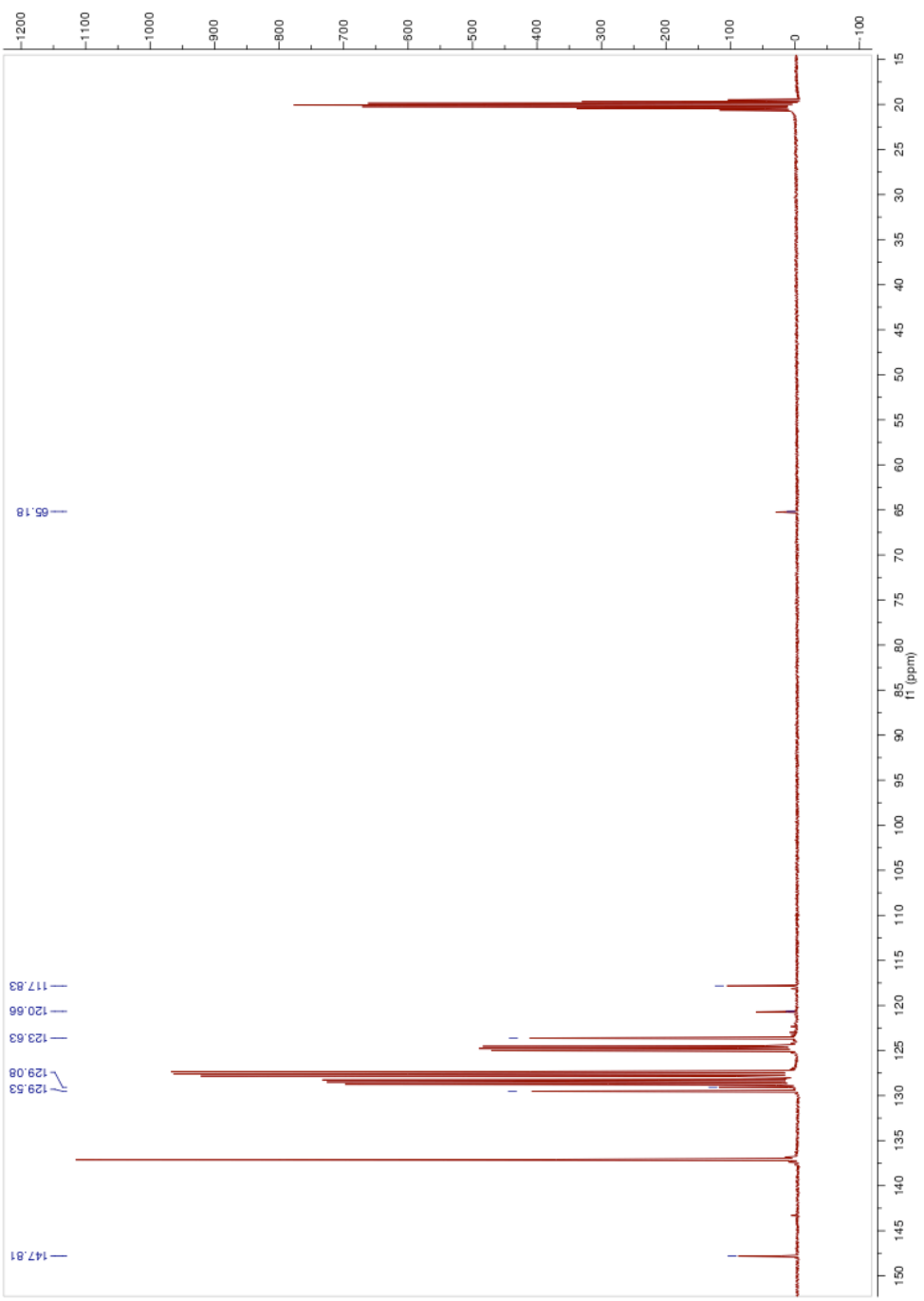

Figure A.17: The ^{13}C spectrum of $(dpa)_3TiMe$

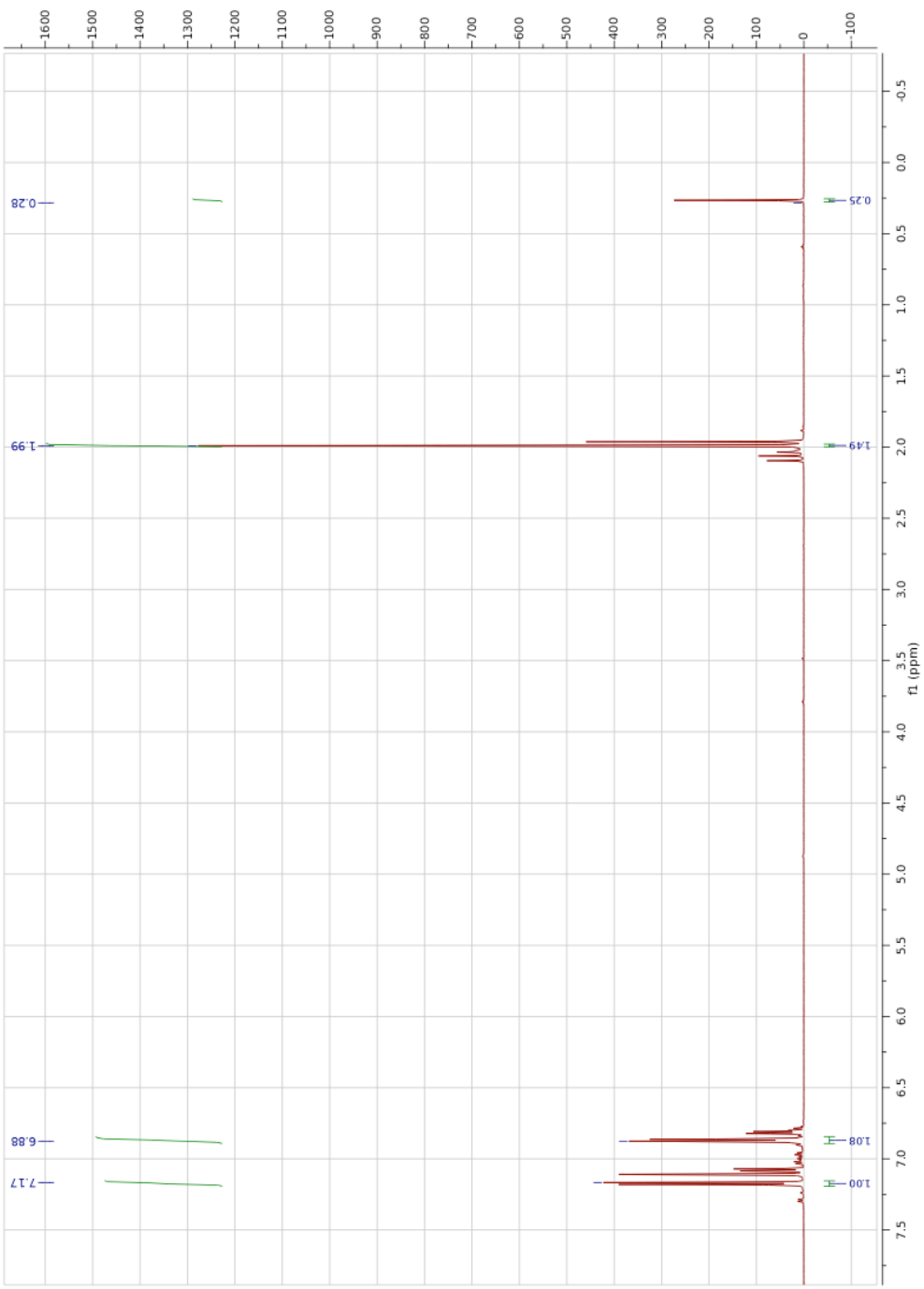

Figure A.18: The ^{1}H spectrum of $(dpta)_3TiMe$

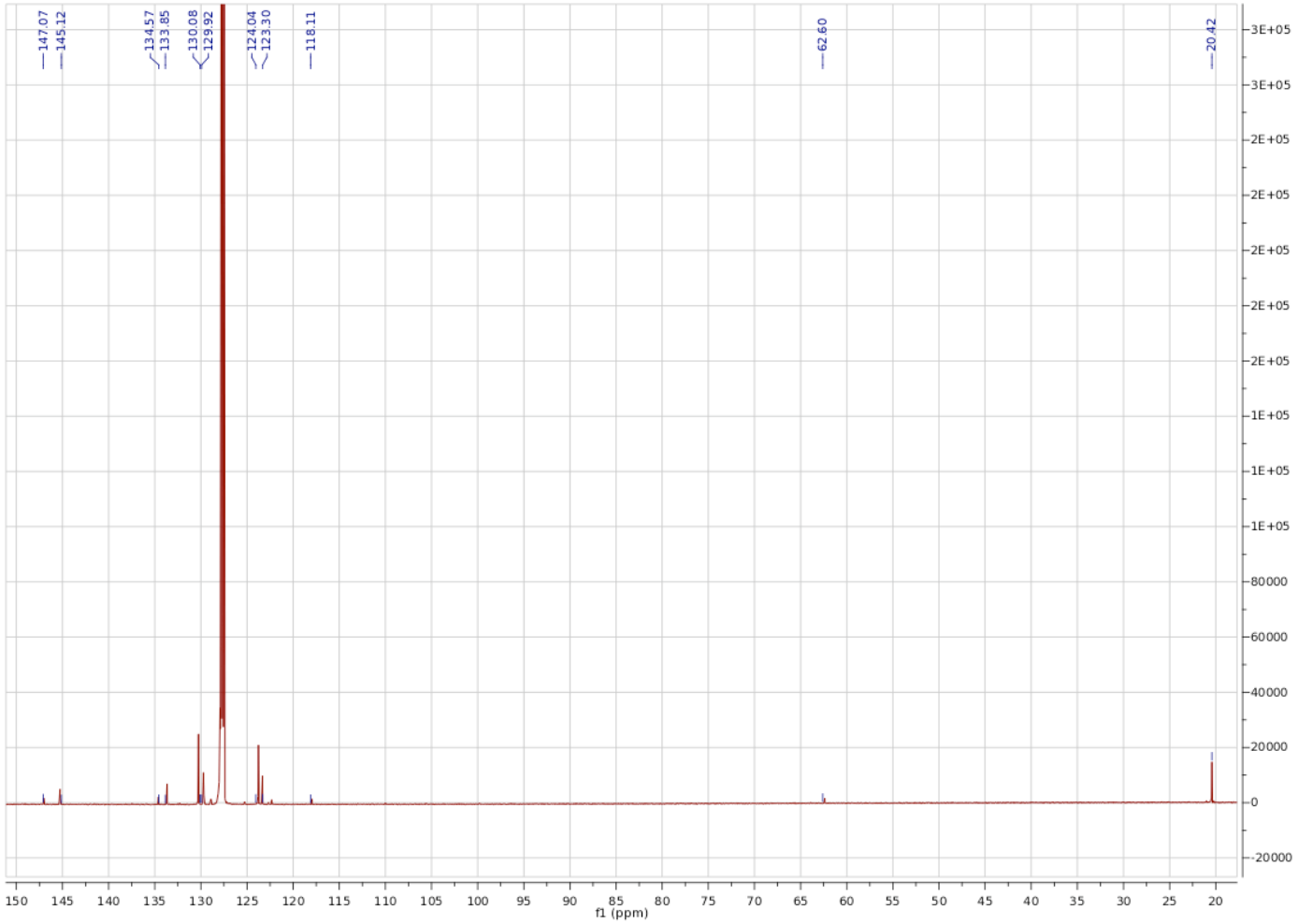

Figure A.19: The ^{13}C spectrum of $(dpta)_3TiMe$

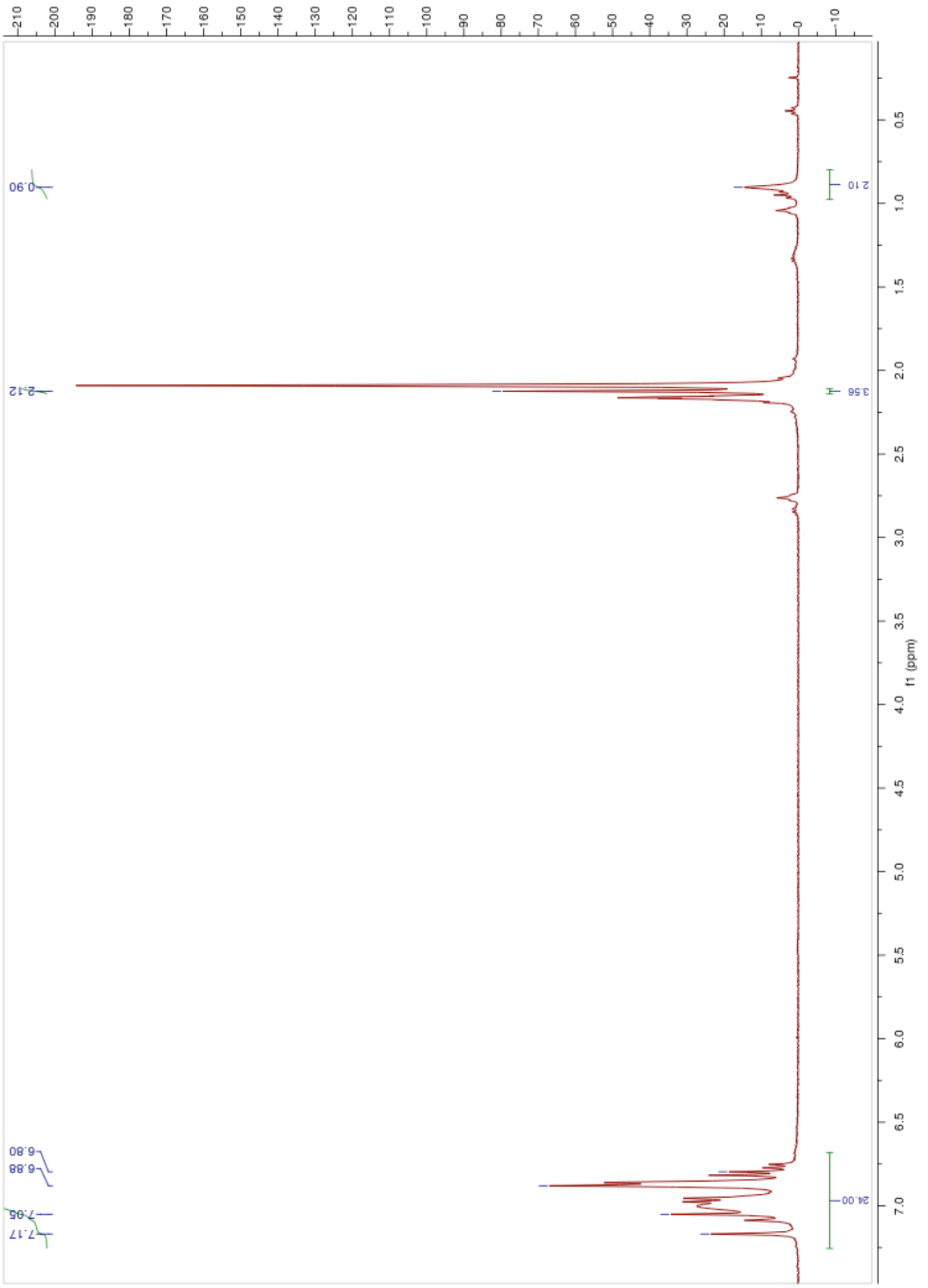

Figure A.20: The ^{1}H spectrum of $(dpta)_3TiMeB(C_6F_5)_3$

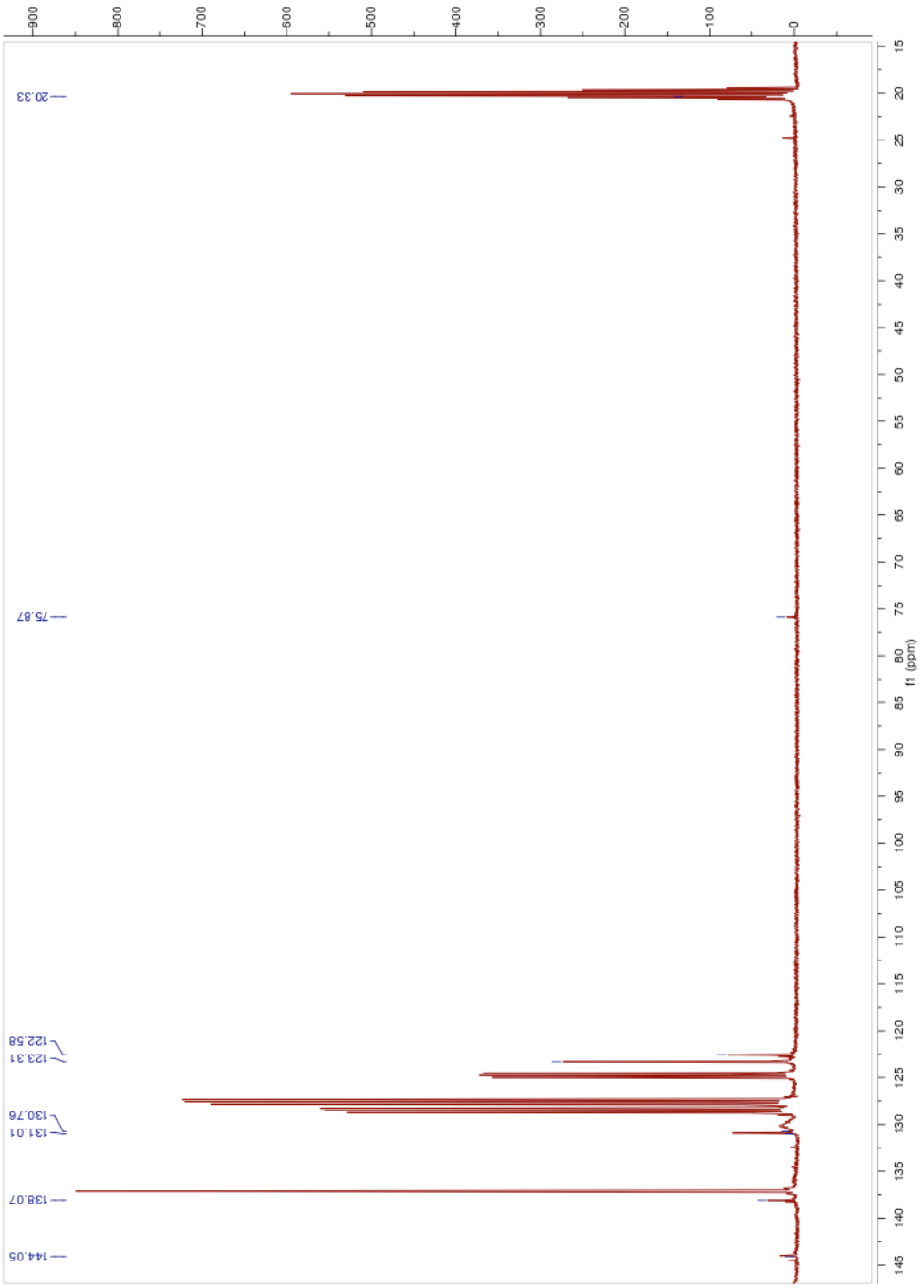

Figure A.21: The ^{13}C spectrum of $(dpta)_3TiMeB(C_6F_5)_3$

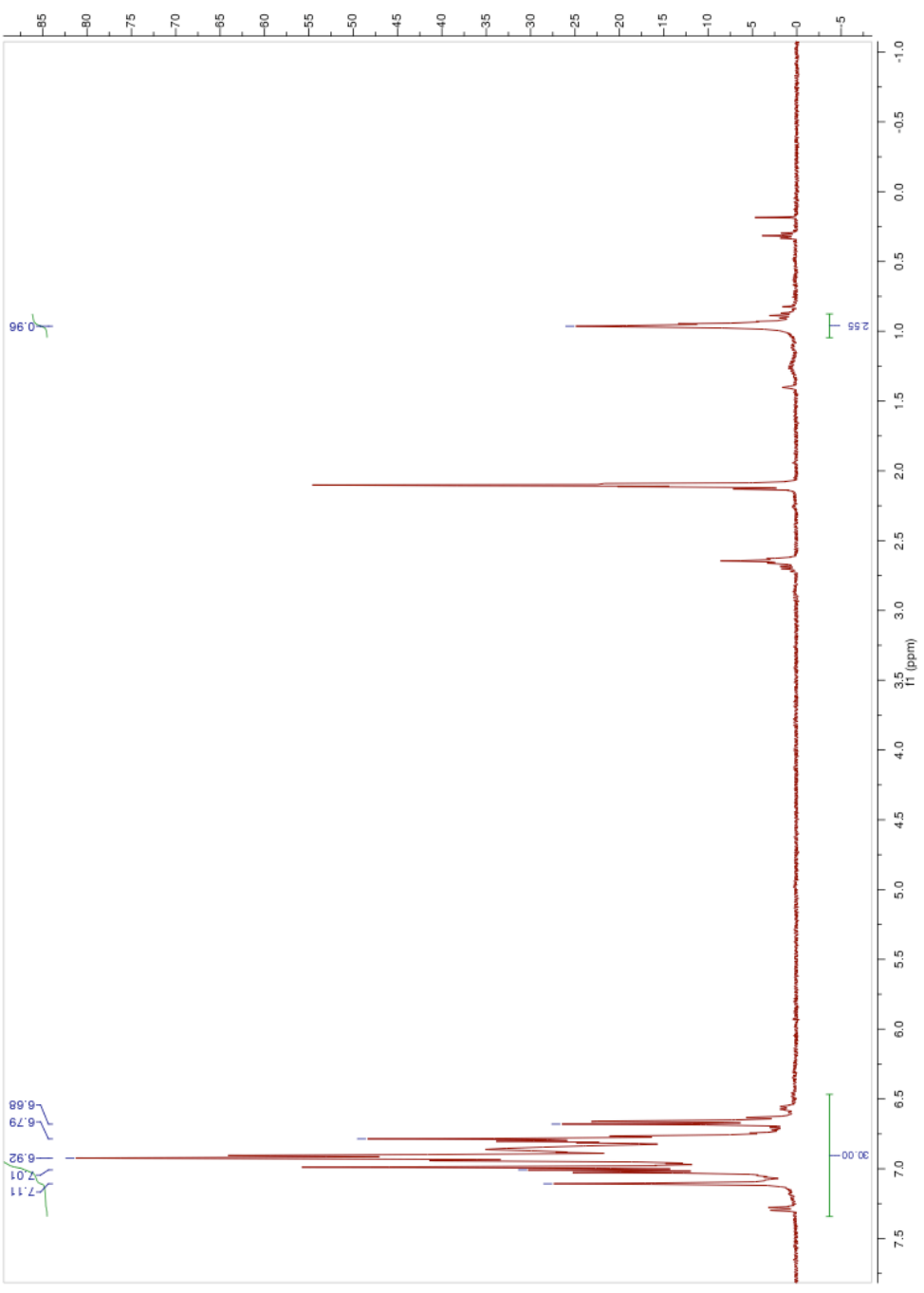

Figure A.22: The ^{1}H spectrum of $(dpa)_3TiMeB(C_6F_5)_3$

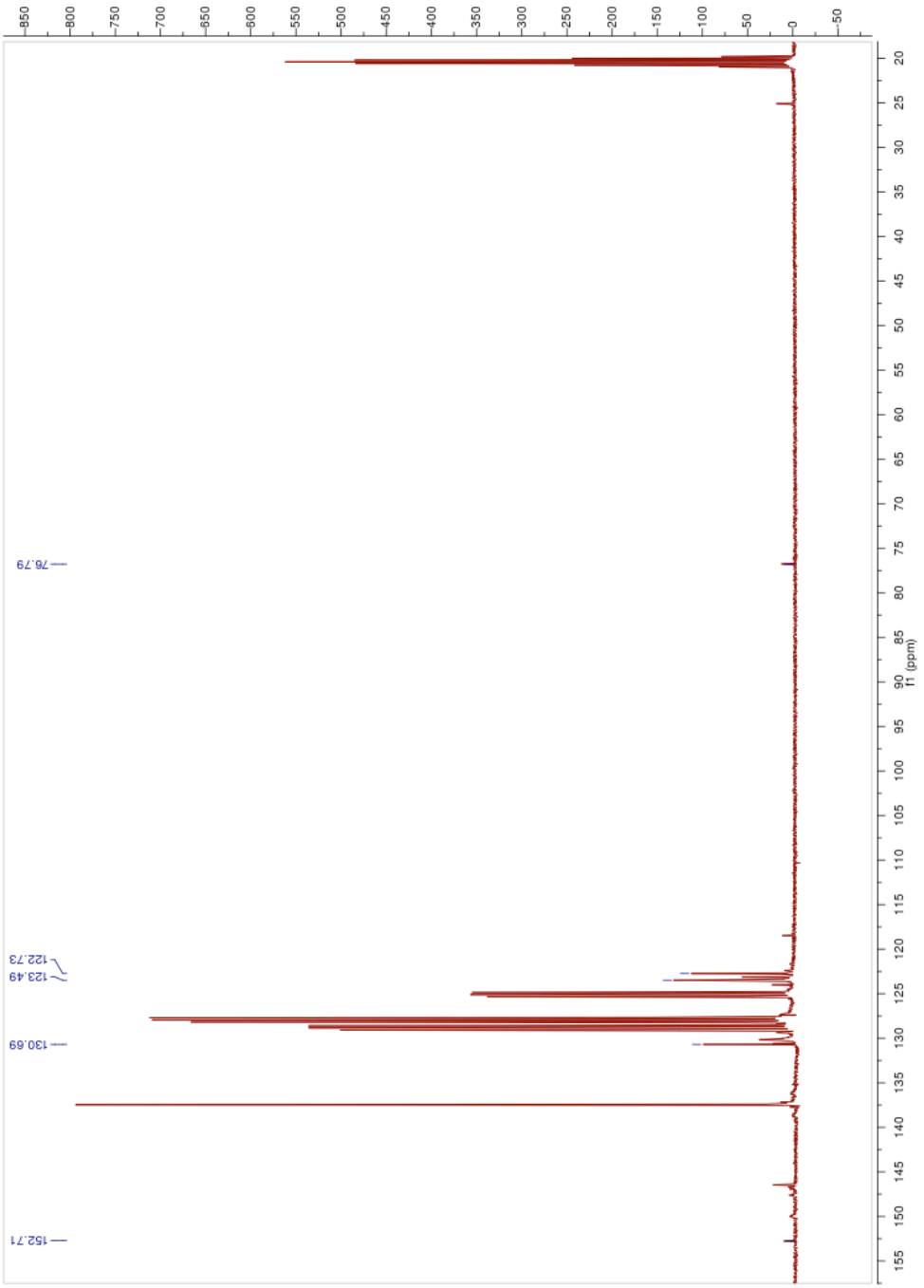

Figure A.23: The ^{13}C spectrum of $(dpa)_3TiMeB(C_6F_5)_3$

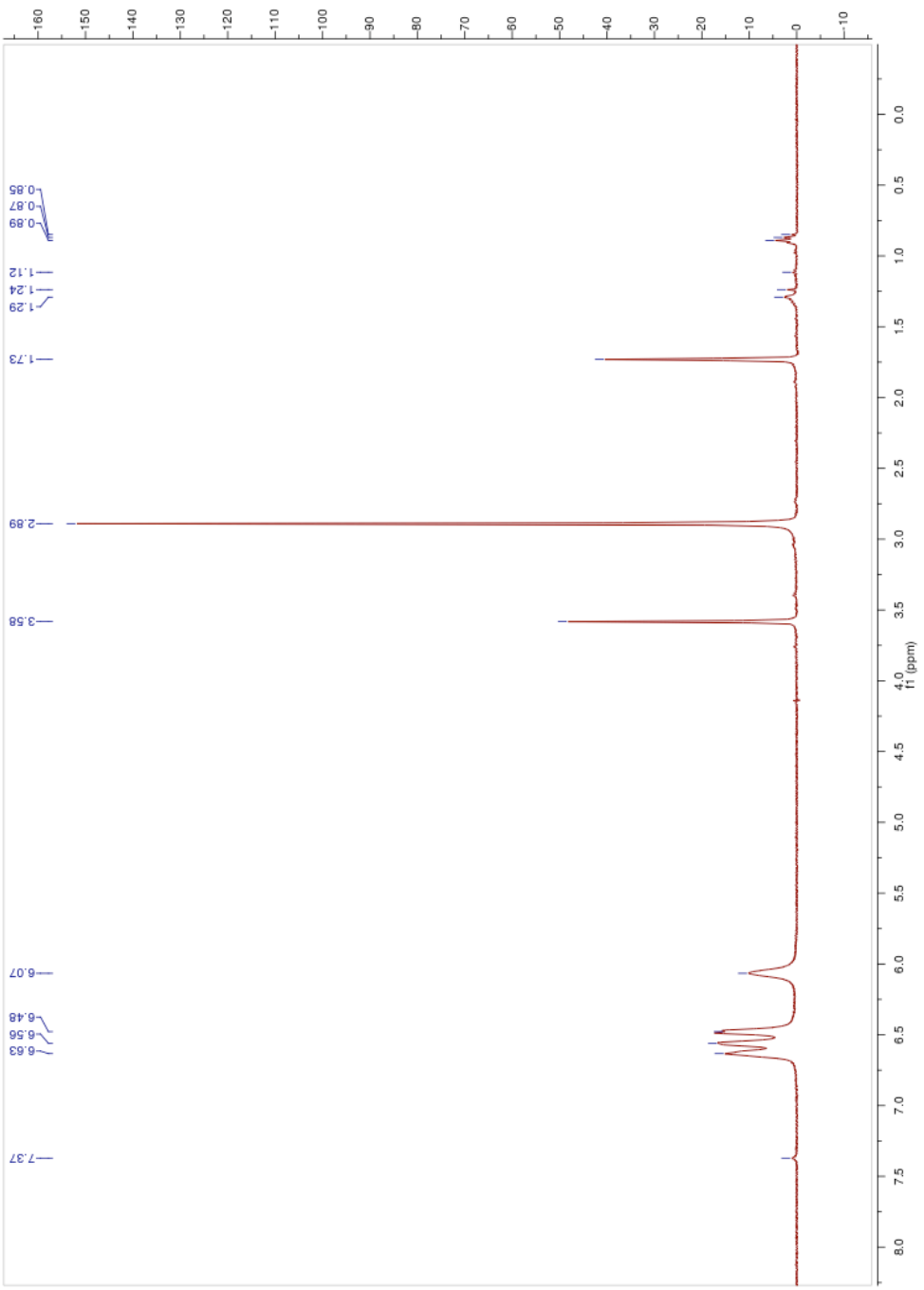

Figure A.24: The ^{1}H spectrum of ddaLi

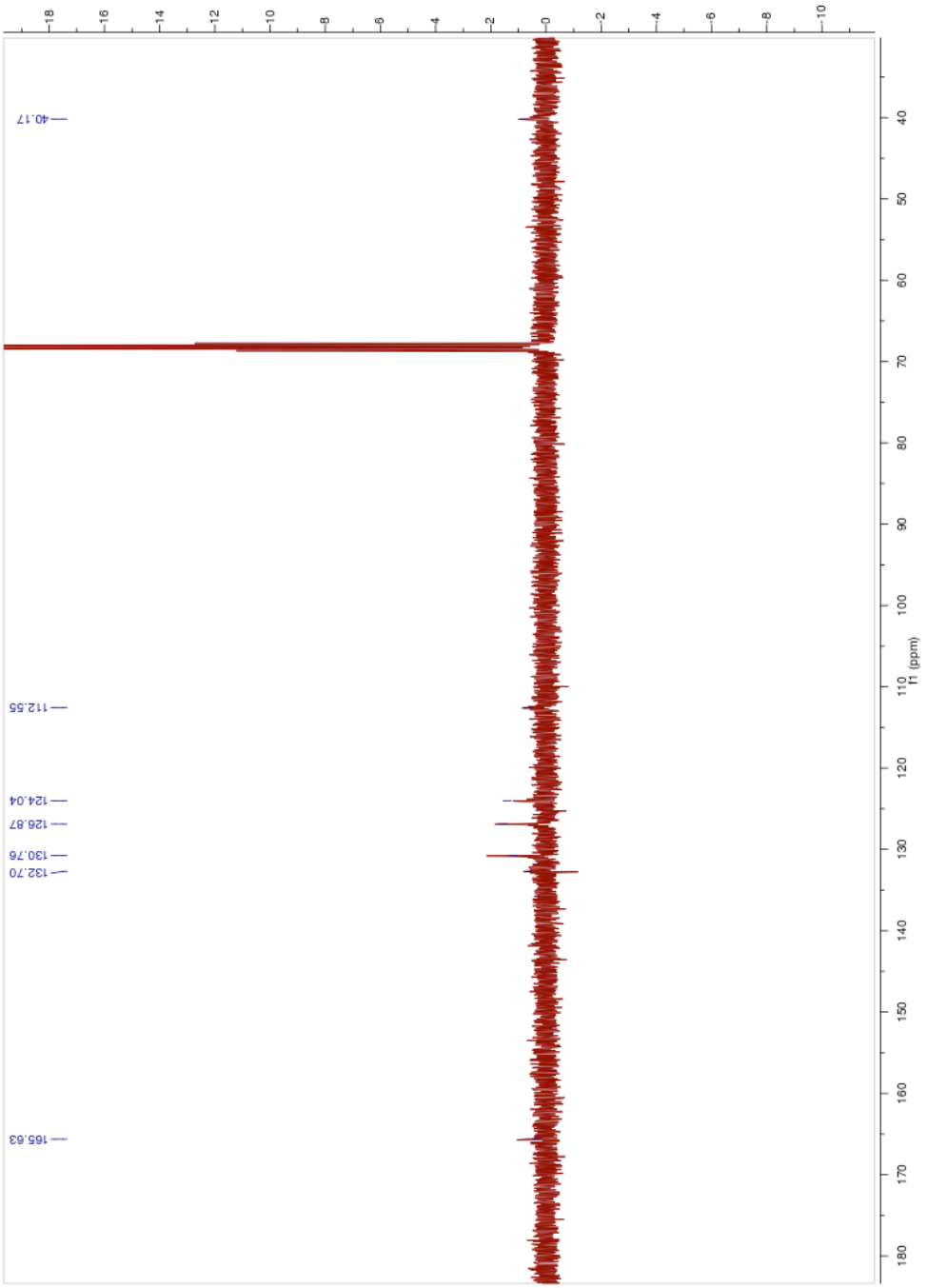

Figure A.25: The ^{13}C spectrum of ddaLi

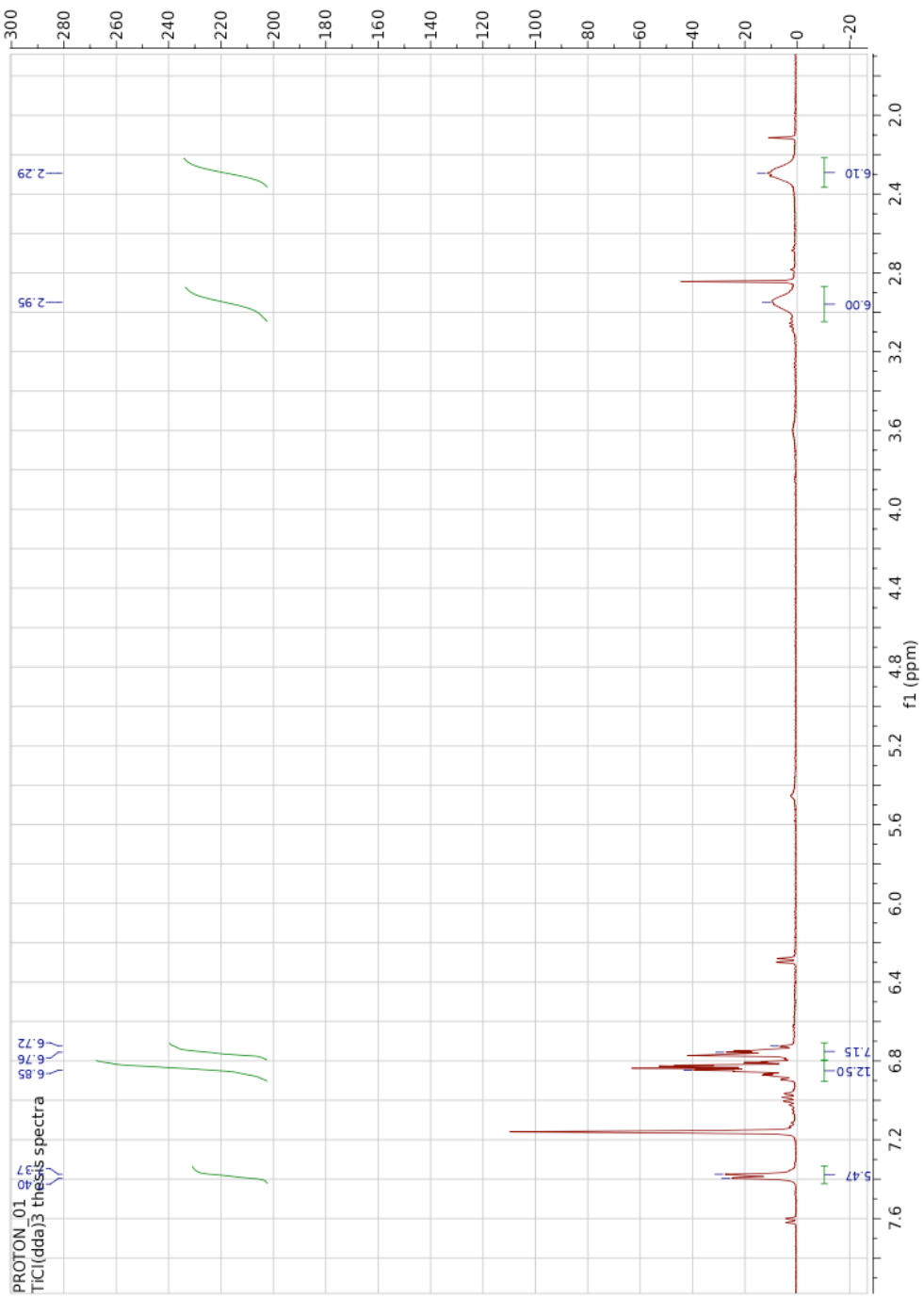

Figure A.26: The ^{1}H spectrum of $(dda)_3$TiCl

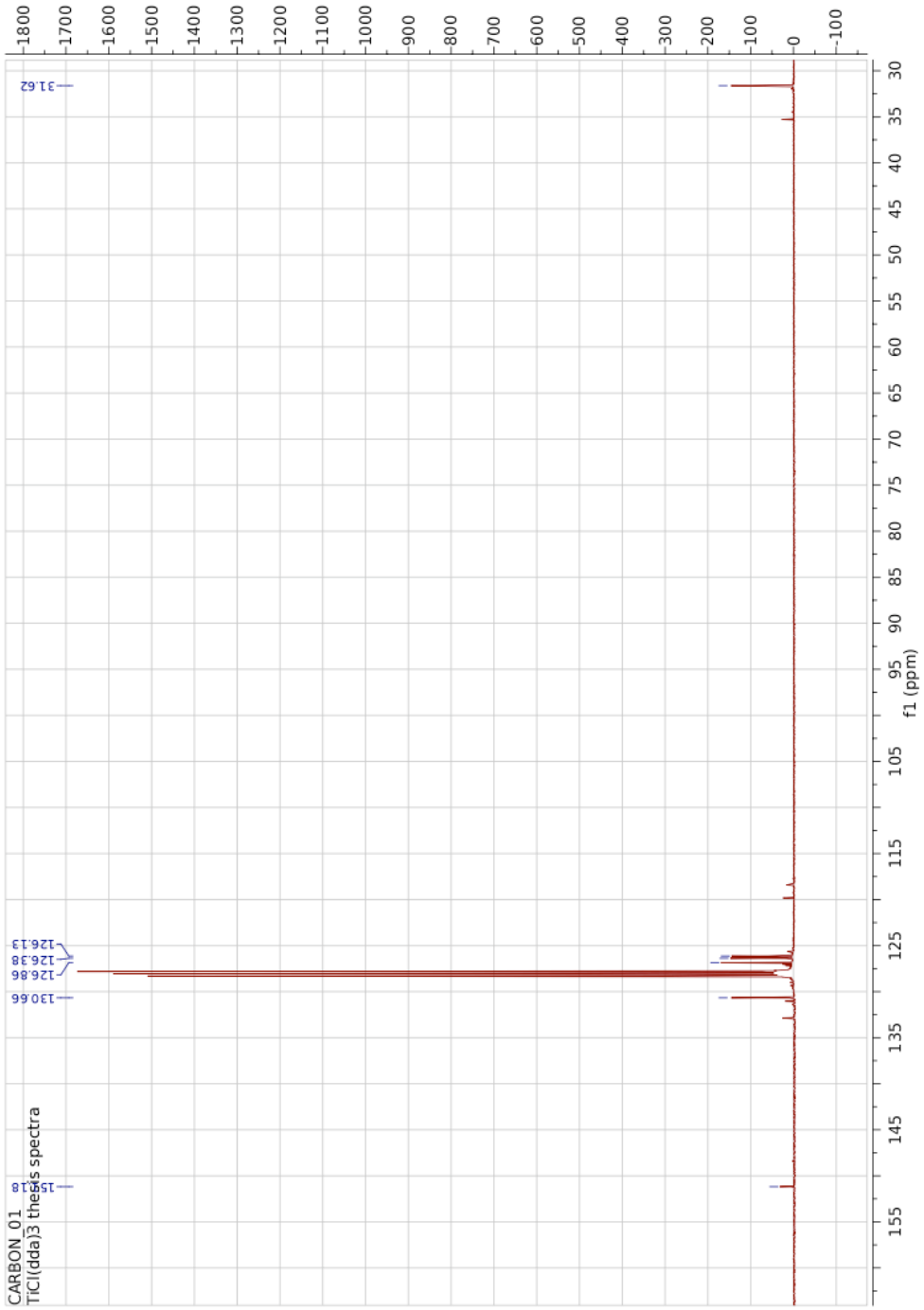

Figure A.27: The ^{13}C spectrum of $(dda)_3TiCl$

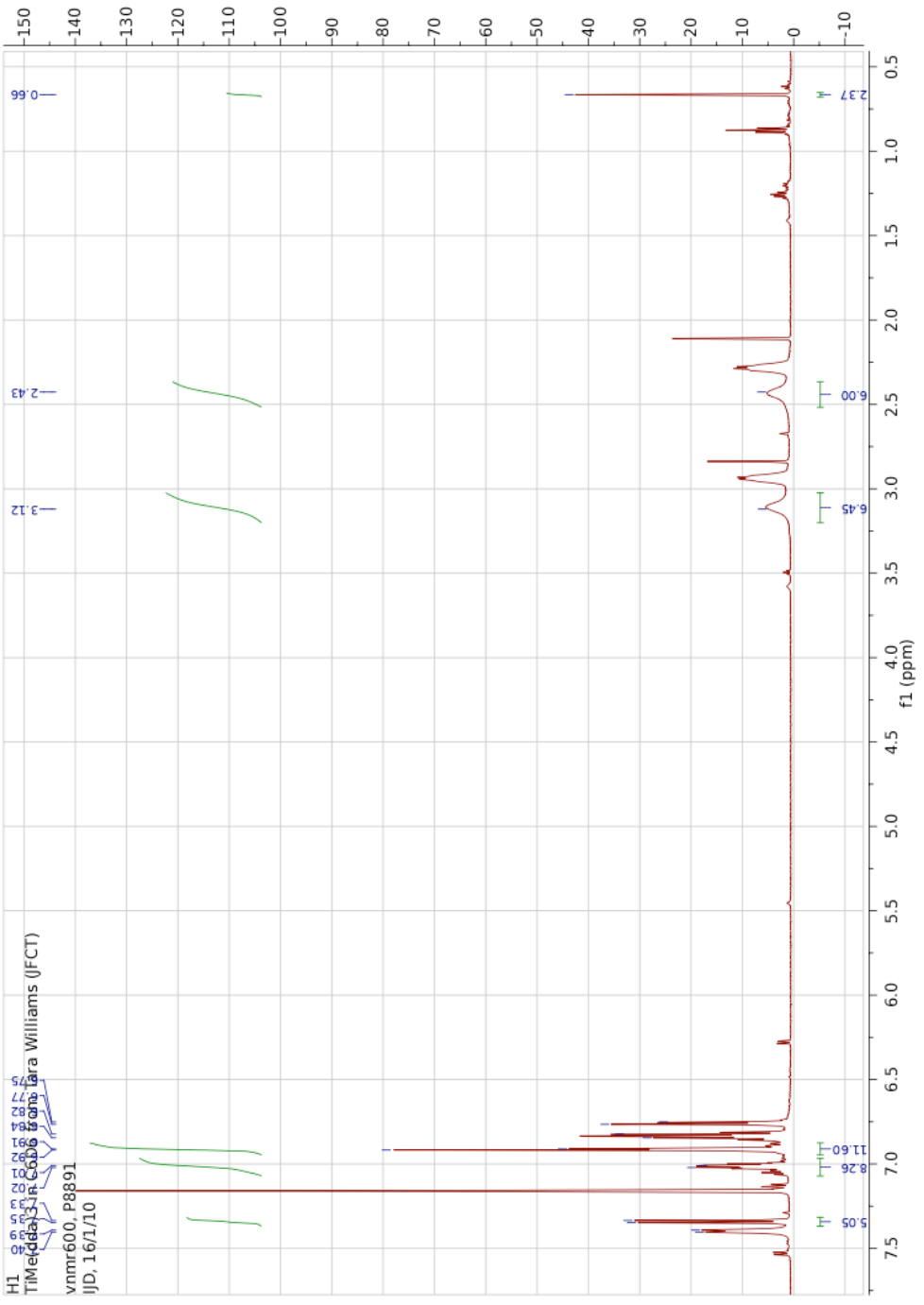

Figure A.28: The ^{1}H spectrum of $(dda)_3$TiMe

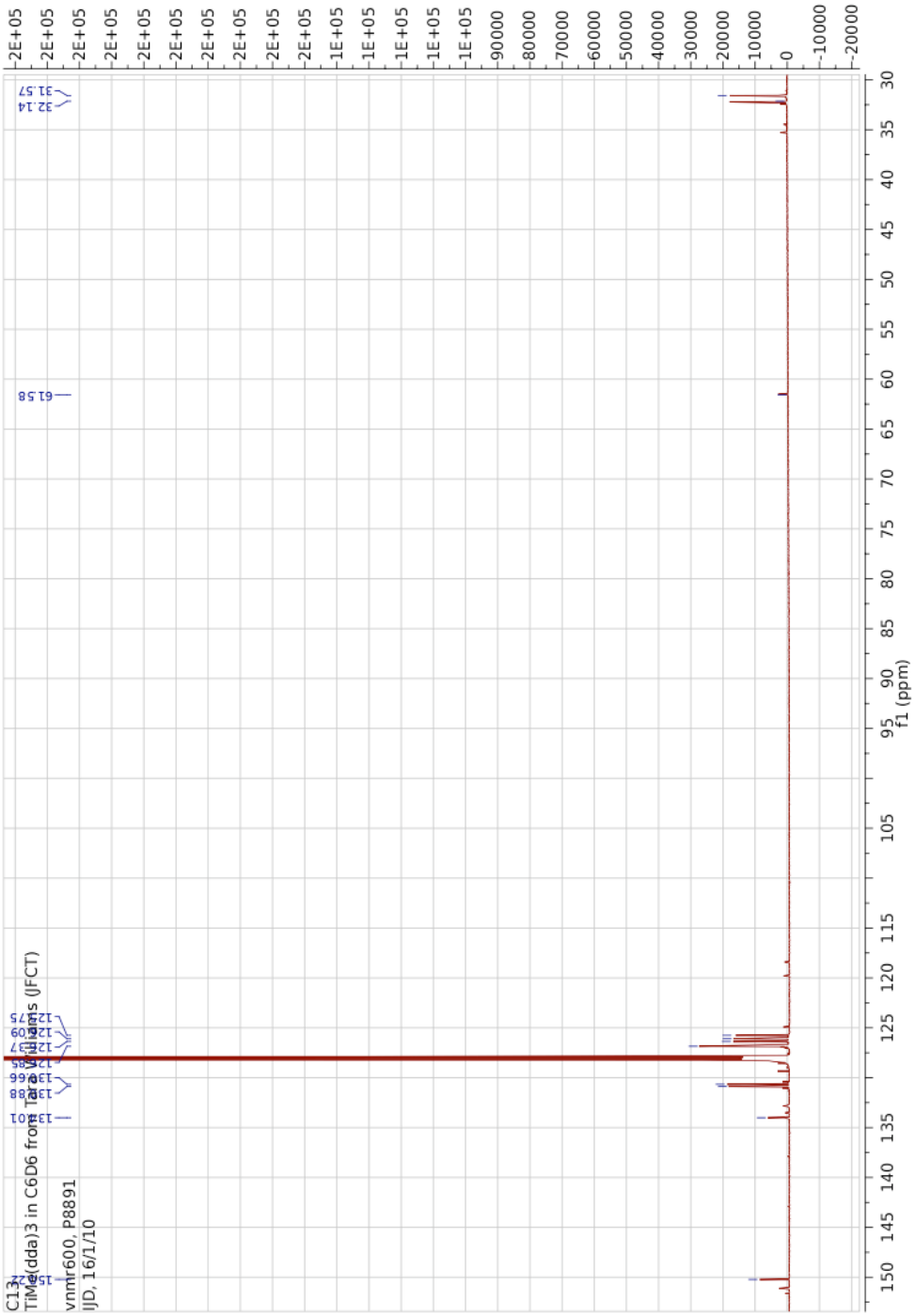

Figure A.29: The ^{13}C spectrum of $(dda)_3$TiMe

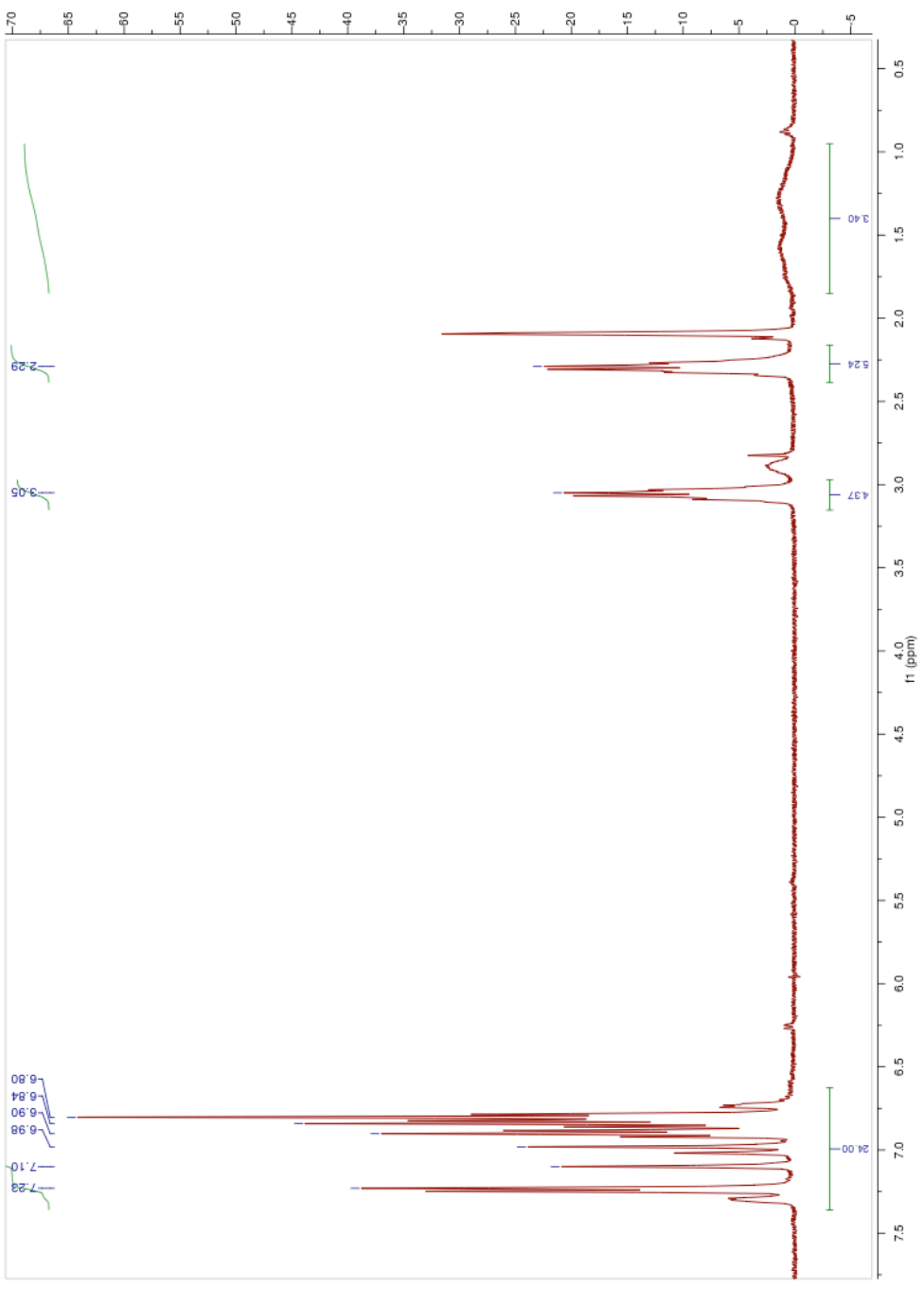

Figure A.30: The ^{1}H spectrum of $(dda)_3TiBH_4$

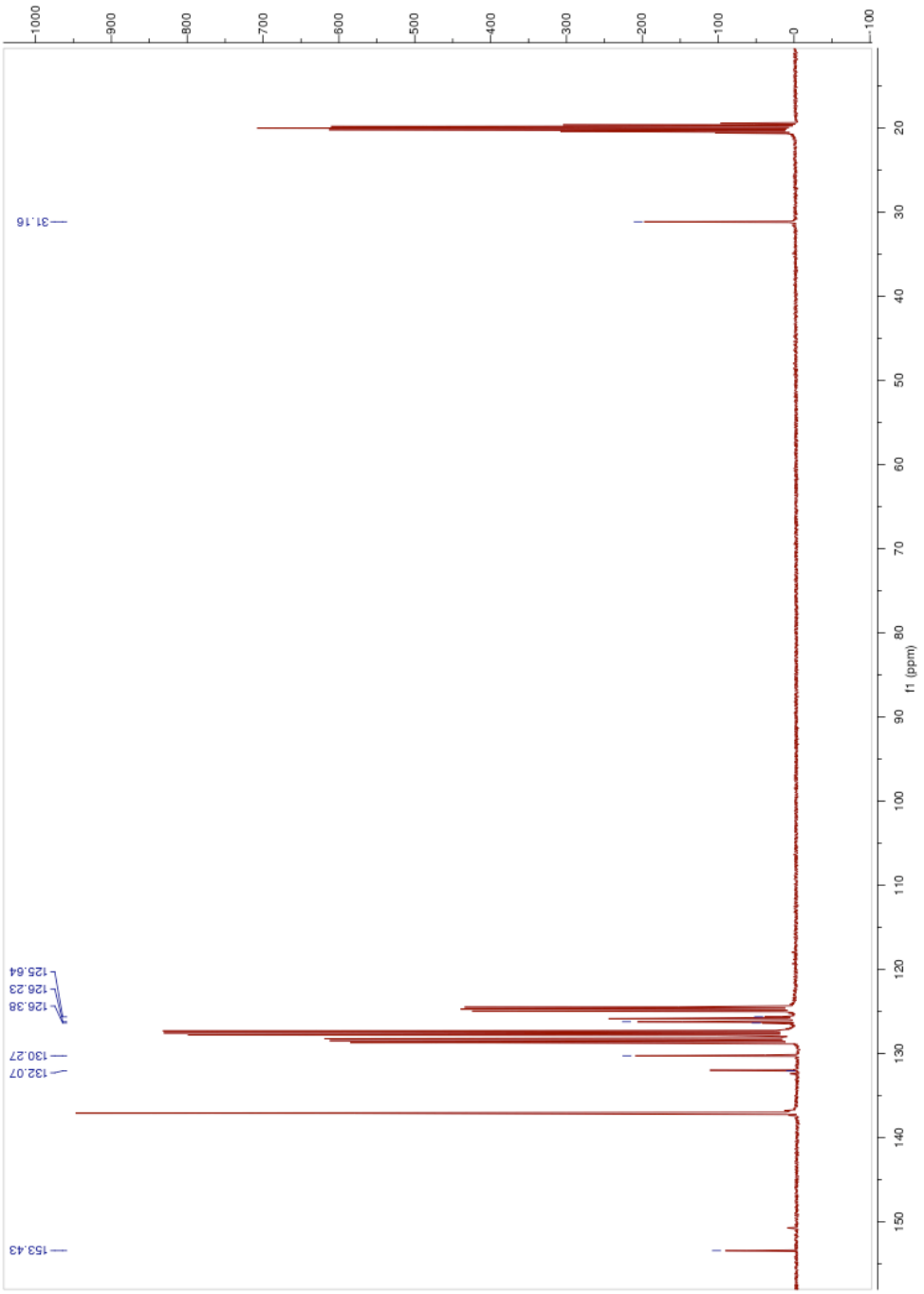

Figure A.31: The ^{13}C spectrum of $(dda)_3TiBH_4$

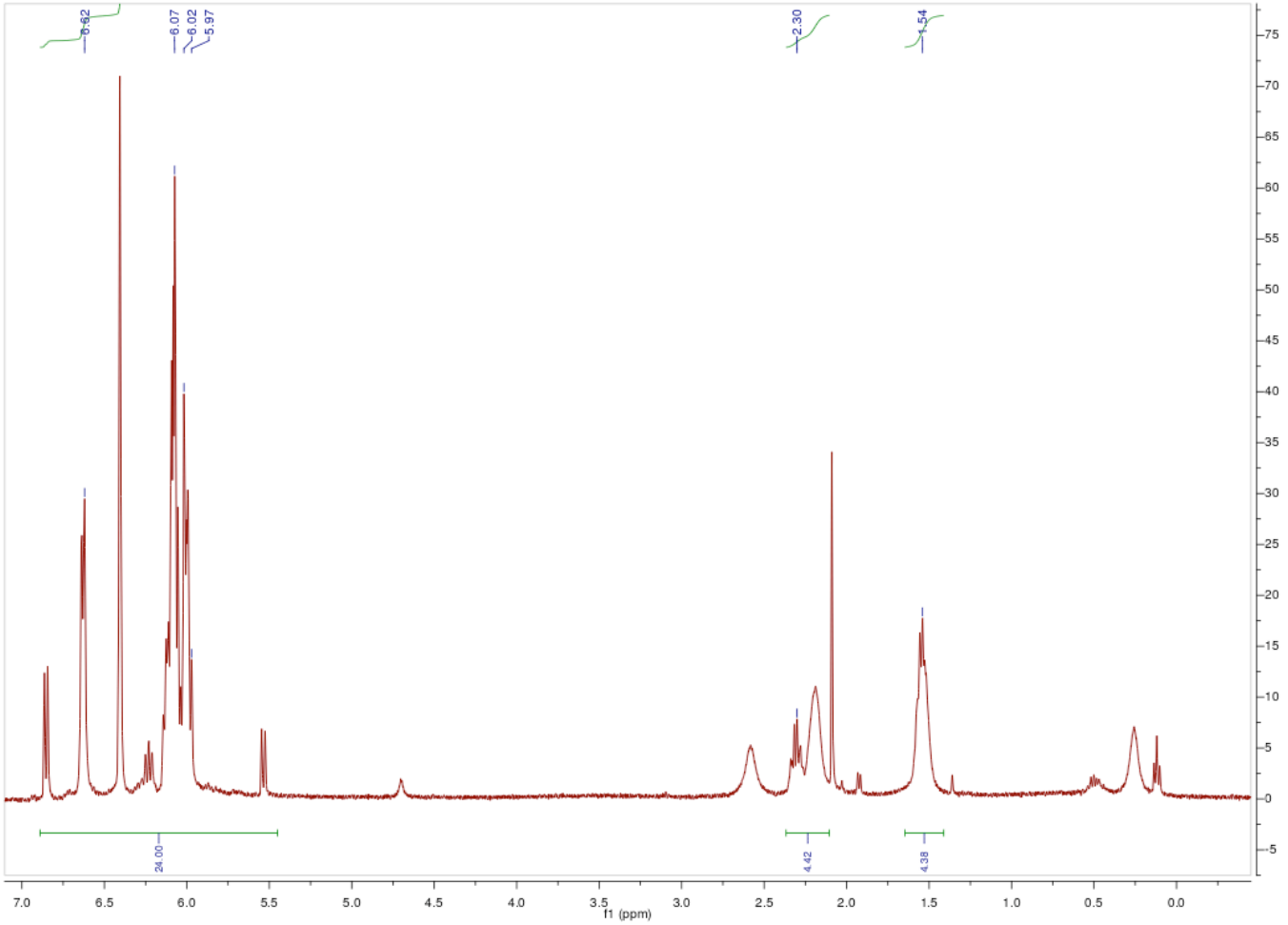

Figure A.32: The ^{1}H spectrum of $(dda)_3Ti]^{+}[B(C_6F_5)_4]^{-}$

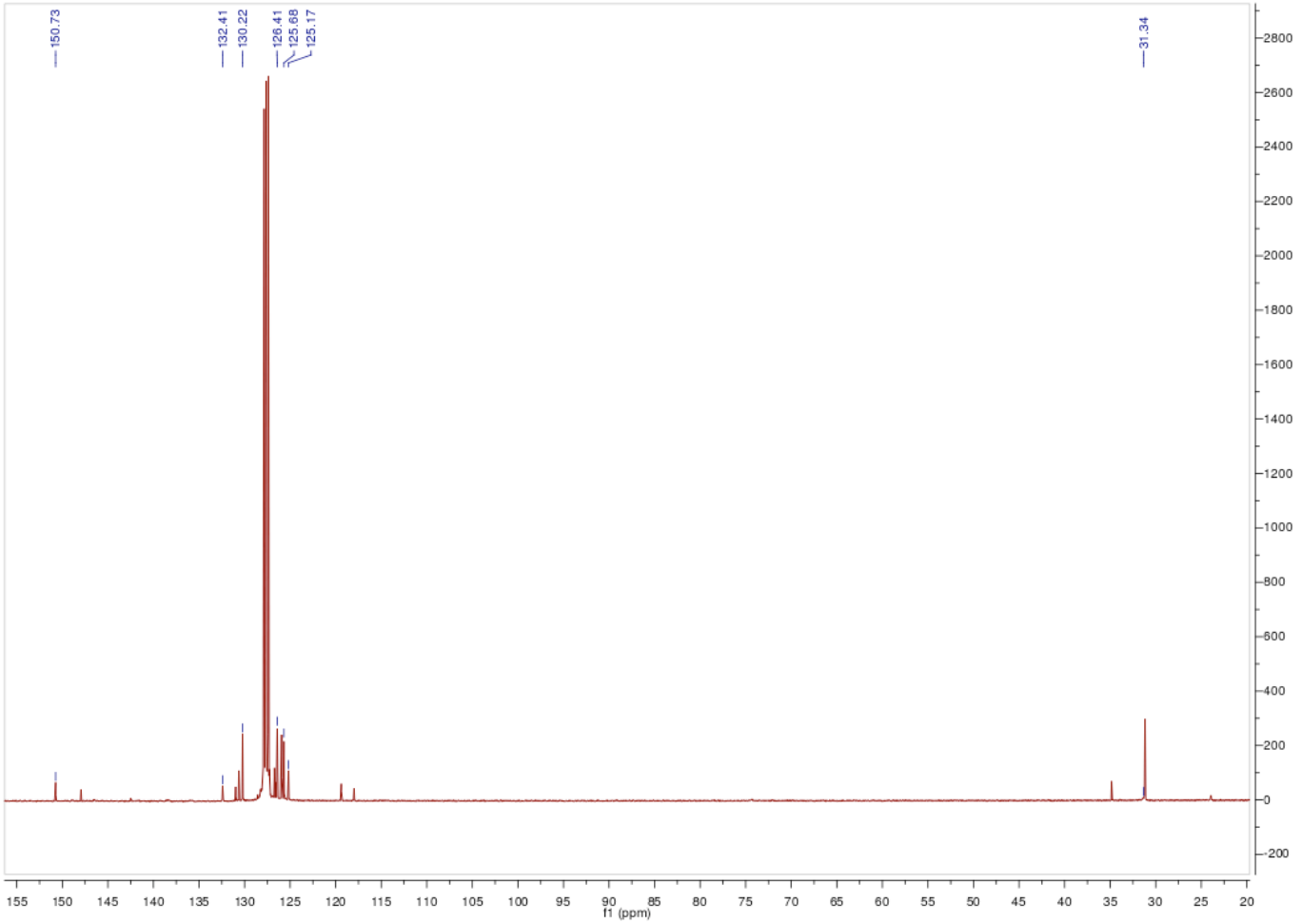

Figure A.33: The ^{13}C spectrum of $(dda)_3Ti]^+[B(C_6F_5)_4]^-$

Appendix B

Tables of Important bond lengths and angles for molecular structures

Atom vector *i*	Atom vector *j*	r_{ij}/Å
Ti	N	1.9221(14)
Ti	C(15)	2.114(3)
N	N(14)	1.432(2)
N	C(1)	1.443(2)
C(1)	C(2)	1.387(3)
C(1)	C(6)	1.402(2)
C(2)	C(3)	1.391(3)
C(3)	C(4)	1.374(3)
C(4)	C(5)	1.378(3)
C(5)	C(6)	1.395(3)
C(6)	C(7)	1.496(3)
C(7)	C(8)	1.521(3)
C(8)	C(9)	1.519(3)
C(9)	C(10)	1.390(3)
C(9)	C(14)	1.407(3)
C(10)	C(11)	1.378(4)
C(11)	C(12)	1.375(3)
C(12)	C(13)	1.381(3)
C(13)	C(14)	1.399(3)

Table B.1: Important bond lengths for the crystal structure of $(dda)_3TiMe$

Interatomic angle *i*	Interatomic angle *j*	Interatomic angle *k*	θ_{ijk} /°
N'	Ti	N	111.32(4)
N'	Ti	C(15)	107.55(4)
C(14)	N	C(1)	115.52(13)
C(14)	N	Ti	133.72(11)
C(1)	N	Ti	110.26(11)
C(2)	C(1)	C(6)	1120.53(17)
C(2)	C(1)	N	119.76(15)
C(6)	C(1)	N	119.69(15)
C(1)	C(2)	C(3)	119.70(18)
C(4)	C(3)	C(2)	119.9(2)
C(3)	C(4)	C(5)	120.8(2)
C(4)	C(5)	C(6)	120.47(19)
C(5)	C(6)	C(1)	118.55(18)
C(5)	C(6)	C(7)	122.52(17)
C(1)	C(6)	C(7)	118.92(17)
C(6)	C(7)	C(8)	111.93(17)
C(9)	C(8)	C(7)	118.23(18)
C(10)	C(9)	C(14)	117.68(19)
C(10)	C(9)	C(8)	116.30(18)
C(14)	C(9)	C(8)	126.01(18)

Table B.2: Important bond angles in the crystal structure of $(dda)_3TiMe$

Appendix C

Plots of $\ln P$ *vs.* t for Chapter 3

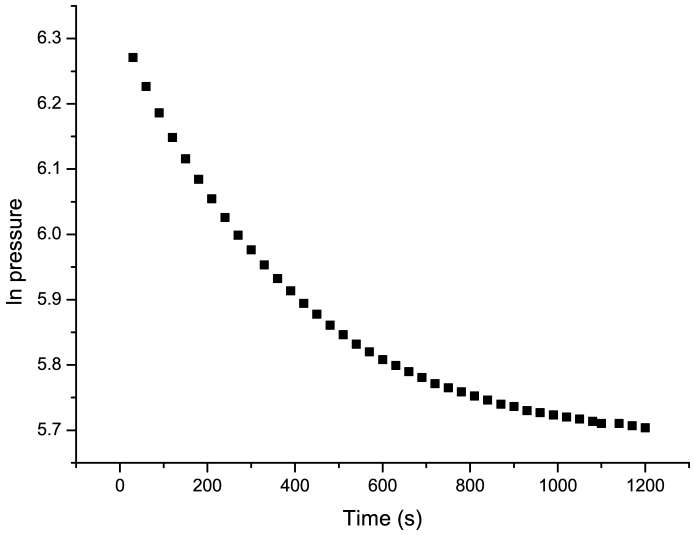

Figure C.1: ln pressure vs. time for the catalyst $TiCl(dpta)_3 + KB(C_6F_5)_4$

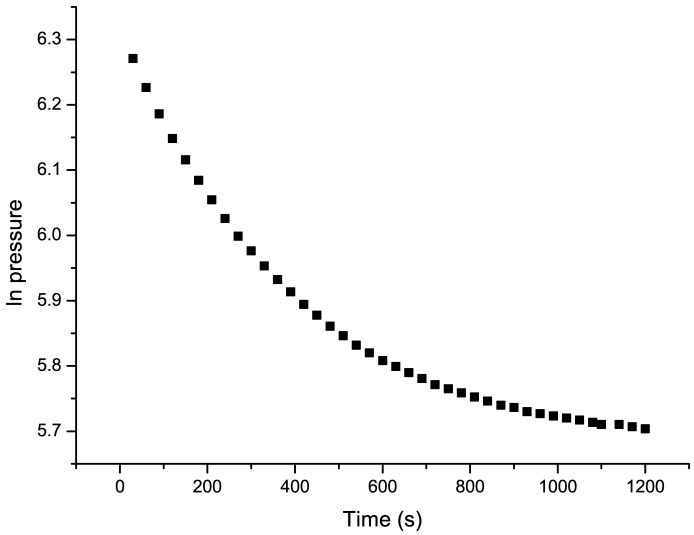

Figure C.2: ln pressure vs. time for the catalyst $TiCl(dpa)_3 + KB(C_6F_5)_4$

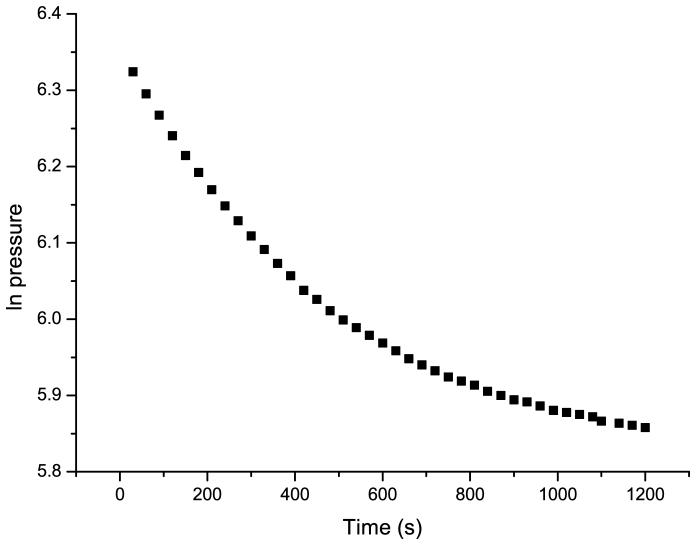

Figure C.3: ln pressure vs. time for the catalyst $[Ti(dpta)_3]^+[B(C_6F_5)_4]^-$

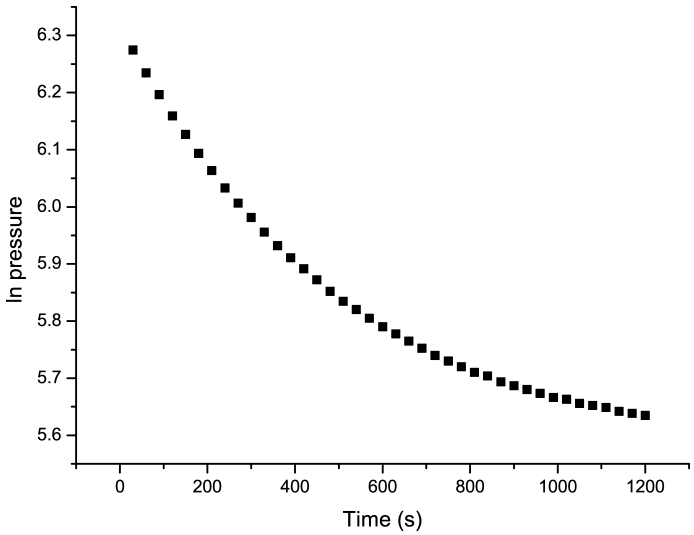

Figure C.4: ln pressure vs. time for the catalyst $[Ti(dpa)_3]^+[B(C_6F_5)_4]^-$

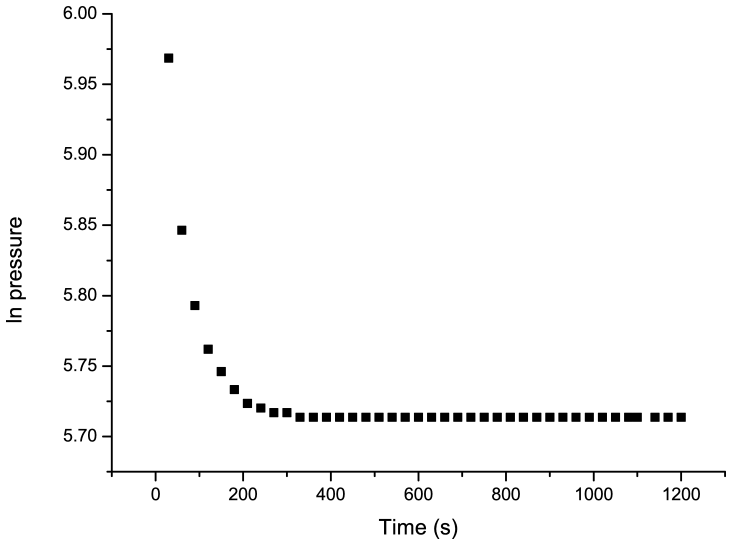

Figure C.5: ln pressure vs. time for the catalyst $TiCl(dpa)_3 + MAO$

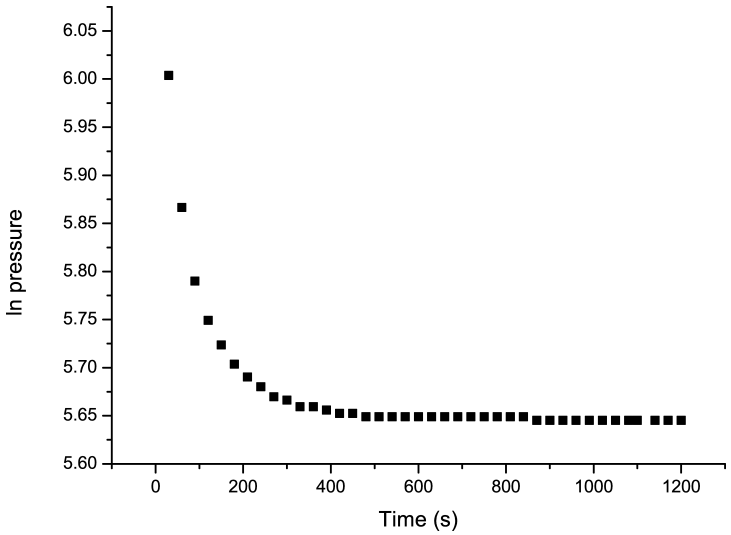

Figure C.6: ln pressure vs. time for the catalyst $TiCl(dpta)_3 + MAO$

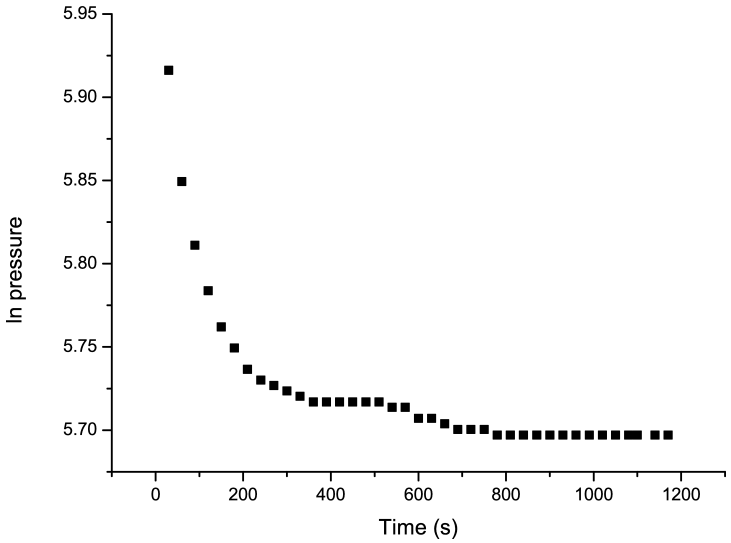

Figure C.7: ln pressure vs. time for the catalyst $TiCl(dpa)_3 + B(C_6F_5)_3$

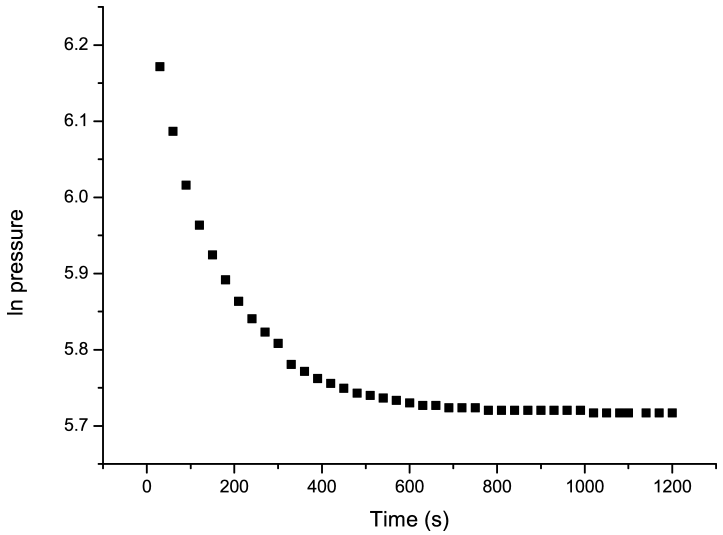

Figure C.8: ln pressure vs. time for the catalyst $TiCl(dpta)_3 + B(C_6F_5)_3$

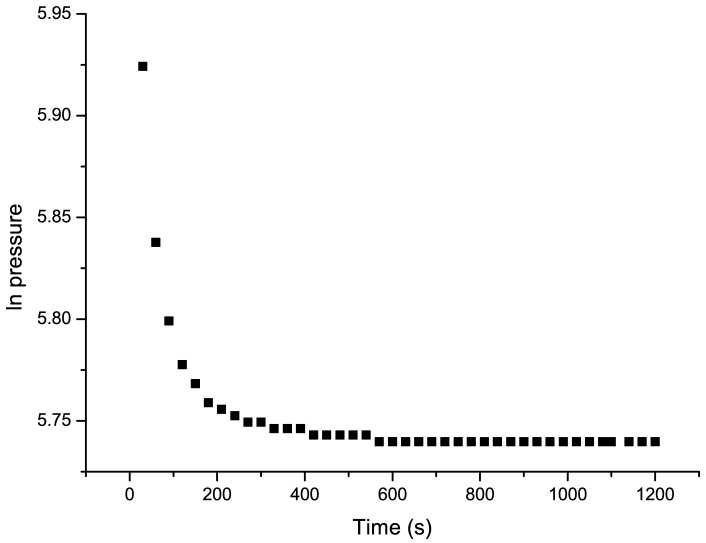

Figure C.9: ln pressure vs. time for the catalyst $TiMe(dpa)_3B(C_6F_5)_3$

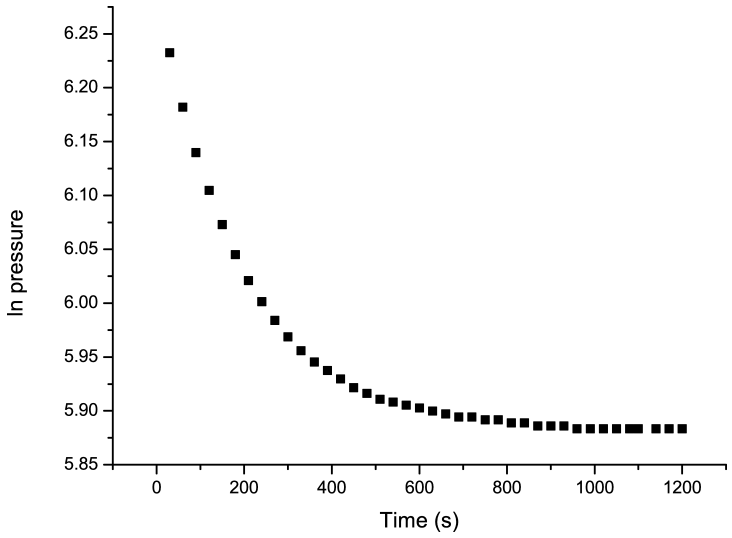

Figure C.10: ln pressure vs. time for the catalyst $TiMe(dpta)_3B(C_6F_5)_3$